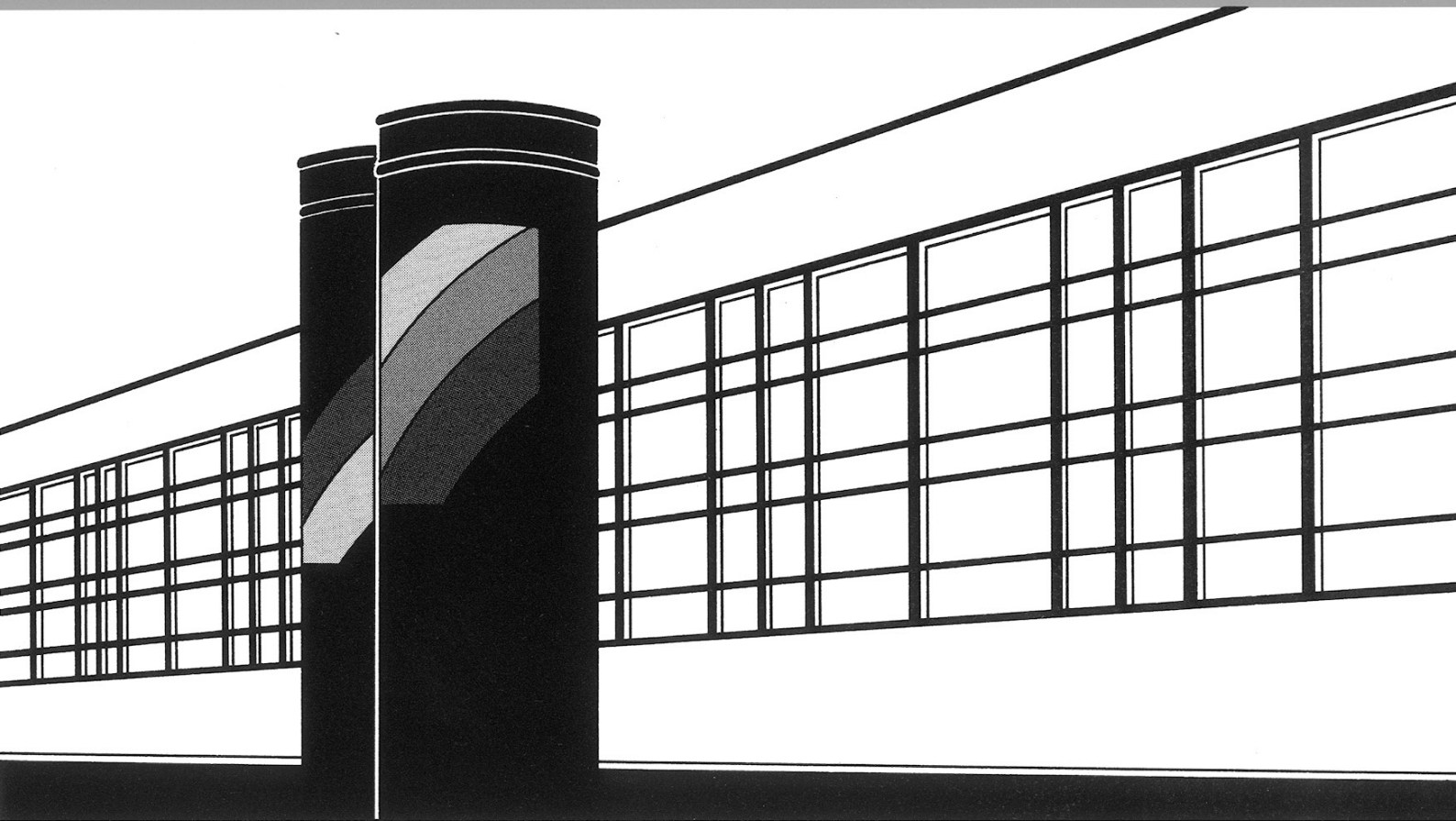


Universität Stuttgart



Institut für Wasser- und Umweltsystemmodellierung

Mitteilungen



Heft 213 Karin Maria Erbertseder

A Multi-Scale Model for Describing
Cancer-Therapeutic Transport in
the Human Lung

A Multi-Scale Model for Describing Cancer-Therapeutic Transport in the Human Lung

Von der Fakultät Bau- und Umweltingenieurwissenschaften der
Universität Stuttgart zur Erlangung der Würde eines
Doktor-Ingenieurs (Dr.-Ing.) genehmigte Abhandlung

Vorgelegt von
Karin Maria Erbertseder
aus Pfarrkirchen

Hauptberichter: Prof. Dr.-Ing. Rainer Helmig
Mitberichter: Prof. Dr.-Ing. Patrick Jenny
Prof. Dr. rer. nat. Peter Scheurich

Tag der mündlichen Prüfung: 16. Februar 2012

Institut für Wasser- und Umweltsystemmodellierung
der Universität Stuttgart
2012

Heft 213 A Multi-Scale Model for
Describing Cancer-Therapeutic
Transport in the Human Lung

von
Dr.-Ing.
Karin Maria Erbertseder

D93 A Multi-Scale Model for Describing Cancer-Therapeutic Transport in the Human Lung

Bibliografische Information der Deutschen Nationalbibliothek

Die Deutsche Nationalbibliothek verzeichnet diese Publikation in der Deutschen Nationalbibliografie; detaillierte bibliografische Daten sind im Internet über <http://www.d-nb.de> abrufbar

Erbertseder, Karin Maria:

A Multi-Scale Model for Describing Cancer-Therapeutic Transport in the Human Lung / von Karin Maria Erbertseder. Institut für Wasser- und Umweltsystemmodellierung, Universität Stuttgart. - Stuttgart: Institut für Wasser- und Umweltsystemmodellierung, 2012

(Mitteilungen Institut für Wasser- und Umweltsystemmodellierung, Universität Stuttgart: H. 213)

Zugl.: Stuttgart, Univ., Diss., 2012

ISBN 978-3-942036-17-7

NE: Institut für Wasser- und Umweltsystemmodellierung <Stuttgart>: Mitteilungen

Gegen Vervielfältigung und Übersetzung bestehen keine Einwände, es wird lediglich um Quellenangabe gebeten.

Herausgegeben 2012 vom Eigenverlag des Instituts für Wasser- und Umweltsystemmodellierung

Druck: Document Center S. Kästl, Ostfildern

Danksagung

Hiermit möchte ich all denen meinen Dank aussprechen, die mich bei der Entstehung dieser Arbeit unterstützt und zu ihrem Gelingen beigetragen haben. In diesem Zusammenhang sei dem Bundesministerium für Bildung und Forschung (BMBF) und dem Stuttgarter Research Centre for Simulation Technology (SimTech) für die finanzielle Unterstützung und Förderung gedankt.

Sehr großer Dank gebührt meinem Hauptberichter Rainer Helmig. Kennengelernt habe ich Rainer auf der Ferienakademie 2007 in Sarntal. Im Jahr 2008 habe ich Rainers Angebot, an seinem Lehrstuhl zu provieren, mit Freude angenommen. Rainer hat es verstanden mich durch seine gezielten Fragen stets in meiner Arbeit voranzubringen. Die großen Freiheiten, die er mir bei meiner Forschung gewährt hat, sind eine große Motivation für mich gewesen und haben die Grundlage für die Freude an der Arbeit gebildet. Weiter möchte ich mich bei den Mitberichtern Patrick Jenny und Peter Scheurich bedanken. Patrick Jenny hat mir die Möglichkeit geboten für drei Monate an seinem Lehrstuhl an der ETH Zürich zu forschen. Diese wunderschöne Zeit werde ich nie vergessen, ebenso wenig wie die fachlichen Diskussionen mit Patrick. Seine schnelle Auffassungsgabe hat mich immer wieder zutiefst beeindruckt. Peter Scheurich hat es verstanden seine Faszination für die Biologie auf mich zu übertragen. Peter hat stets Zeit gefunden für meine Fragen und Anliegen. Mein besonderer Dank richtet sich auch an Holger Class und Bernd Flemisch. Holger und Bernd haben so manches Mal Licht ins Dunkel gebracht.

Johannes Reichold und Jan Hasenauer danke ich für die Zurverfügungstellung ihrer Simulationsprogramme, sowie für die sehr hilfreichen Diskussionen und Denkanstöße während meiner Promotion. Es ist mir eine sehr große Freude gewesen mit Johannes und Jan zusammenzuarbeiten. Des Weiteren gebührt ein besonderer Dank allen meinen Kollegen und Kolleginnen: Katherina Baber, Yufei Cao, Melanie Darcis, Anozie Ebigo, Rainer Enzenhöfer, Benjamin Faigle, Jochen Fritz, Andreas Geiges, Christoph Grüninger, Veronica Heiß, Vishal Jambhekar, Alexander Kissinger, Jonas Koch, Andreas Kopp, Anna Kuhlmann, Hartmut Kuhnke, Andreas Lauser, Philipp Leube, Julian Mehne, Klaus Mosthaf, Jennifer Niessner, Wolfgang Nowak, Philipp Nuske, Sergey Oladyshkin, Maren Paul, Nicolas Schwenck, Alexandru Tatomir, Janina Theresa Ulmer, Lena Walter, Markus Wolff und Irina Zizina. Die tolle Atmosphäre in der Arbeitsgruppe werde ich sehr vermissen. Besonders bedanken möchte ich mich für die großartige Aufführung am Tag meiner Promotionsprüfung. Ich werde diesen wunderschönen Tag nie vergessen. Meine beiden Zimmerkolleginnen Melanie Darcis und Lena Walter sind während meiner Zeit am Lehrstuhl zu wahren Freundinnen geworden. Prudence Lawday und Maria Costa Jornet danke ich für Ihre Hilfe bei allen organisatorischen Angelegenheiten, sowie David Werner und Michelle Hartnick für Ihre Unterstützung bei jeglichen Problemen im Bereich Hard- und Software. Unvergesslich bleiben die Mädelsabende mit Melanie, Lena und Maria.

Jedoch ohne die Unterstützung meiner Familie wäre ich nicht soweit gekommen. Ich bedanke mich bei meinen Eltern, Anneliese und Robert, die immer für mich da sind und mir mein Studium ermöglicht haben, und bei meinem Bruder Thomas, der sich für meine Anliegen immer Zeit nimmt und einfach der beste Bruder auf der Welt ist. Meinem Lebensgefährten Christian danke ich für dessen Rückhalt, die Unterstützung und sein Verständnis in den vergangenen Jahren.

*"Tue erst das Notwendige, dann das Mögliche
und plötzlich schaffst du das Unmögliche"*

Franz von Assisi.

Contents

Notation	IX
Abstract	a
Zusammenfassung	c
1 Introduction	1
1.1 Motivation	1
1.2 Structure of the Thesis	2
2 Biological/Medical Background	3
2.1 Anatomy of the Lung	3
2.2 Cardiovascular System of the Lung	5
2.3 Composition and Function of the Body Fluid Blood	8
2.4 Types of Tissues	9
2.4.1 Structure and Function of the Connective Tissue	9
2.4.1.1 Connective Tissue Cells	10
2.4.1.2 Intercellular Substances - Extracellular Matrix	10
2.4.2 Pulmonary Tissue	11
2.5 Characteristics of Tumors	12
2.6 Idea of the Cancer Cell-Selective Apoptogenic Therapy	14
2.6.1 Explanation of the Cell Cycle	14
2.6.2 Process of Apoptosis	15
2.6.3 Induction of the Cancer Cell-Selective Apoptosis by TRAIL	18
2.6.4 Use of the Bifunctional Fusion Protein scFv-TRAIL	20
3 Model Concept for Describing Cancer-Therapeutic Transport in the Lung	21
3.1 Definition of Basic Terms	21
3.2 Definition of Structures and Scales	22
3.3 Definition of Effective Parameters	23
3.4 Definition of Fluid Properties	24
3.5 Definition of Processes	26
3.6 Idea of the Multi-Scale Model	27
4 Vascular Graph Model (VGM)	31
4.1 General Model Concept	31
4.2 Mathematical Model	32
4.3 Numerical Model	35

5	Alveolus Model - A Double-Continuum Approach (DCM)	36
5.1	General Model Concept	36
5.2	Pulmonary Tissue Continuum	38
5.3	Pulmonary Capillary Bed Continuum	40
5.4	Coupling Functions for the Flow and Transport Processes between the Two Continua	43
5.5	Numerical Model	46
6	Low-Dimensional Population Model for TRAIL-Induced Proapoptotic Signaling ([PMTS]_s)	47
6.1	General Model Concept	47
6.2	Governing Equations	48
6.3	Numerical Model	52
7	Coupling of the Individual Models to Each Other	53
7.1	Coupling of the DCM to the VGM	53
7.2	Coupling of the [PMTS] _s to the DCM	55
7.3	Multi-Scale Model for Describing Cancer-Therapeutic Transport in the Lung .	56
8	Model Applications	59
8.1	First Example - Simulating the Flow and the Transport of a Therapeutic Agent within the Lung	59
8.1.1	Simulation Setup	61
8.1.2	Initial and Boundary Conditions	63
8.1.3	Parameters	63
8.1.4	Simulation Results	67
8.2	Second Example - Simulating the Flow, Transport and Reaction of TRAIL Us- ing the Multi-Scale Model	72
8.2.1	Simulation Setup	72
8.2.2	Initial and Boundary Conditions	73
8.2.3	Parameters	73
8.2.4	Optimization of the Work Flow of the Multi-Scale Model for Long- Time Applications	75
8.2.5	Simulation Results	80
8.2.6	Local Sensitivity Analysis of the Multi-Scale Model	86
8.3	Conclusions	93
9	Final Remarks - Summary and Outlook	95
	Bibliography	97
A	Numerical Model	105
A.1	Vascular Graph Model	106
A.1.1	Time Discretization	106
A.1.2	Spatial Discretization	107
A.2	Alveolus Model	109

A.2.1	Time Discretization	109
A.2.2	Spatial Discretization	109
A.2.3	Solving the Non-Linear Problem	117
A.3	Low-Dimensional Population Model for TRAIL-Induced Proapoptotic Signaling	118
A.3.1	Explicit Runge-Kutta Scheme - The Dormand-Prince Method	118
A.3.2	Backward Differentiation Formulas Method	120

List of Figures

1	Lung anatomy (with kind permission of T. Winslow, copyright 2006).	3
2	Part of the bronchial system: showing the dichotomous branching of the bronchial tree (adapted from Tillmann (2005) [97] with kind permission from Springer Science+Business Media).	4
3	Different types of capillaries (adapted from Schiebler and Korf (2007) [85] with kind permission from Springer Science+Business Media). A Continuous capillary: continuous basal membrane. B Fenestrated capillary. C Discontinuous capillary: endothelial cells with intercellular pores; discontinuous basal membrane.	6
4	Bronchial tree and alveoli with bronchial and pulmonary vessels (adapted from Tillmann (2005) [97] with kind permission from Springer Science+Business Media).	7
5	Loose connective tissue (adapted from Schiebler et al. (1999) [84] with kind permission from Springer Science+Business Media).	11
6	Phases of the cell cycle (the information about the duration of the single phases is taken from Koolman and Röhm (2009) [58]).	15
7	Extracellular pathway of apoptosis (according to Alberts et al. (2004) [7]). . .	17
8	Intracellular pathway of apoptosis (according to Alberts et al. (2004) [7]). . . .	17
9	Structure of the TRAIL molecule (adapted by permission from Macmillan Publishers Ltd: [Cell Death and Differentiation] LeBlanc and Ashkenazi (2003) [61], copyright 2003).	18
10	TRAIL signal transduction pathway (adapted by permission from J. Hasenauer, Institute for Systems Theory and Automatic Control - University of Stuttgart).	19
11	Left: from a biological tissue towards a porous medium. Right: definition of the representative elementary volume according to Bear (1972) [19].	22
12	Left: definition of the shear stress. Right: flow behavior of different fluids. . .	25
13	Relevant scales for describing cancer-therapeutic transport in the lung.	27
14	General model concept for describing cancer-therapeutic transport in the lung - solving a multi-scale problem.	28
15	Sequential coupling of the three models for describing cancer-therapeutic transport in the lung.	29
16	Schematic representation of a vascular graph: a collection of nodes i connected by edges ij	31
17	Gravity dependence of the pulmonary blood flow.	33

18	Explanation of the general concept of the double-continuum model.	37
19	Computation of the effective permeability of a REV. Fixed pressures p_1 and p_2 set at all nodes crossing the left and right face normal to x respectively (no-flow boundary condition at all nodes crossing the other four faces). Effective permeability computed from pressure gradient and integral mass flow F_{REV} through the REV's capillary network (reprinted by permission from Macmillan Publishers Ltd: [Journal of Cerebral Blood Flow & Metabolism] Reichold et al. (2009) [81], copyright 2009).	41
20	Generation of a realistic permeability field for the capillary continuum.	42
21	Determination of the permeability tensor for the capillary continuum: hexagonal mesh of pulmonary capillaries embedded in a cuboid.	42
22	Paracellular and transcellular pathways (adapted from Baber (2009) [11] with kind permission of K. Baber).	43
23	Processes and forces of transvascular exchange (adapted from Baber (2009) [11] with kind permission of K. Baber).	44
24	TRAIL signal transduction pathway as modeled by the [PMTS] _s (image from J. Hasenauer, Institute for Systems Theory and Automatic Control - University of Stuttgart).	48
25	Coupling of the DCM to the VGM.	54
26	Coupling of the [PMTS] _s to the DCM.	56
27	Work flow of the multi-scale model.	57
28	Classification of blood vessels according to the Strahler ordering system.	60
29	Visualization of the vascular graph coupled to the DCM. The black lines represent the blood vessels, which form the unstructured grid of the VGM. The red nodes and the blue rectangles symbolize the capillary bed and pulmonary tissue around an alveolus, which are simulated using the DCM. The red nodes are the healthy upscaled nodes and the blue rectangles are the tumorous ones. The blood vessels above / below the alveoli are arteries / veins of the order one to four, with a morphology according to Table 11 respectively.	61
30	Left: Model domain of the alveolus model for a healthy upscaled node consisting of a spherical shell with an inner diameter of 140 μm and an outer diameter of 364 μm (according to Weibel (1991) [101]). Right: Different kind of structures comprised by the model domain of the DCM.	62
31	Visualization of the permeability field of the capillary bed in units of $(\mu\text{m})^2$ for a healthy upscaled node: (a) in x -direction, (b) in xz -direction, (c) in z -direction, in all the other directions the permeability is zero.	65
32	Results of the vascular graph model. (a) Pressure distribution [Pa]. (b) A therapeutic agent is introduced at the arterial root vertex. Drug distribution [mol/mol] after one time step. (c) Drug distribution [mol/mol] after 11 seconds.	68

33	Results for a healthy alveolus (leftmost red node in Figure 29), at the final time step of the simulation. (a) Pressure distribution within the pulmonary capillary bed continuum [Pa]. (b) Drug distribution [mol/mol] within the pulmonary capillary bed continuum. (c) Pressure distribution within the pulmonary tissue continuum [Pa]. (d) Drug distribution [mol/mol] within the pulmonary tissue continuum.	70
34	Results for a tumor alveolus (middle blue rectangle in Figure 29), at the final time step of the simulation. (a) Pressure distribution within the pulmonary capillary bed continuum [Pa]. (b) Drug distribution [mol/mol] within the pulmonary capillary bed continuum. (c) Pressure distribution within the pulmonary tissue continuum [Pa]. (d) Drug distribution [mol/mol] within the pulmonary tissue continuum.	71
35	Model domain of an healthy upscaled node.	72
36	(a) Comparison of the simulation results of the <i>twelve hours simulation</i> with the results of the <i>one hour simulation</i> for the healthy upscaled node 42 and the tumorous upscaled node 58. (b) Comparison of the simulation results of the <i>one hour simulation</i> with the results of the <i>one minute simulation</i> for the healthy upscaled node 42 and the tumorous upscaled node 58.	77
37	Work flow of the multi-scale model for a long-time application.	78
38	Different time scales of the multi-scale model for the long-time application.	79
39	Drug distribution over the model time of twelve hours shown at three different nodes of the vascular graph: the healthy upscaled node 42, the tumorous upscaled node 58 and the root venous node.	80
40	Results for the healthy alveolus (leftmost red node in Figure 29; node 42) after one hour. (a) Pressure distribution within the pulmonary capillary bed continuum [Pa]. (b) Drug distribution [mol/mol] within the pulmonary capillary bed continuum. (c) Pressure distribution within the pulmonary tissue continuum [Pa]. (d) Drug distribution [mol/mol] within the pulmonary tissue continuum.	82
41	Results for the tumorous alveolus (middle blue rectangle in Figure 29; node 58) after one hour. (a) Pressure distribution within the pulmonary capillary bed continuum [Pa]. (b) Drug distribution [mol/mol] within the pulmonary capillary bed continuum. (c) Pressure distribution within the pulmonary tissue continuum [Pa]. (d) Drug distribution [mol/mol] within the pulmonary tissue continuum.	83
42	Average drug distribution in the tissue continuum over the model time of twelve hours for the healthy upscaled node 42 and for the tumorous upscaled node 58.	84
43	Average drug distribution in the tissue continuum over the model time of twelve hours shown for all three tumorous upscaled nodes (left black rectangle = node 57, middle black rectangle = node 58, right black rectangle = node 59).	85
44	Percent of dead cancer cells at the upscaled node 58 (top view on the horizontal cross section through the middle of the model domain).	86

45	Visualization of the maximal normalized local sensitivity matrix for the healthy upscaled node 42. The processes in the capillary continuum are described by the Equations (28) and (29). The transfer equations are defined by the Starling equation (31) and the Stavermann-Kedem-Katchalsky equation (32). The processes in the tissue continuum are described by the Equations (21) and (24). The flow and the transport of TRAIL through the vascular graph is calculated using the Equations (14) and (18).	91
46	Visualization of the maximal normalized local sensitivity matrix for the tumorous upscaled node 58. The processes in the capillary continuum are described by the Equations (28) and (29). The transfer equations are defined by the Starling equation (31) and the Stavermann-Kedem-Katchalsky equation (32). The processes in the tissue continuum are described by the Equations (21) and (24). The flow and the transport of TRAIL through the vascular graph is calculated using the Equations (14) and (18).	92
47	Explicit time discretization.	107
48	Example of a vascular graph.	107
49	Implicit time discretization.	109
50	Vertex centered finite volume method (box method). a) Construction of the grid. b) Division of the box B_i into subcontrol volumes V_k^i . c) computation of the fluxes (according to Baber et al. (2011) [10]).	110

List of Tables

2	Organization of the human airways: generation number G according to the dichotomous branching of the airways (Schiebler et al. (1999) [84]).	4
3	Properties of the human pulmonary circulation (Singhal et al. (1973) [92]). . .	7
4	Composition and properties of blood in a healthy human (modified according to Formiggia et al. (2009) [38]).	8
5	Different types of connective tissue.	10
6	Different characteristics of the two cell death processes.	16
7	Properties of typical vessels for an adult (modified according to Formiggia et al. (2009) [38]).	34
8	Transvascular pathways (Curry (1984) [28]).	44
9	Single cell model for TRAIL-induced proapoptotic signaling (mo = molecules, log = log-normally distributed) (parameter estimation by J. Hasenauer, Institute for Systems Theory and Automatic Control - University of Stuttgart, from experiments of M. Doszczak and P. Scheurich, Institute of Cell Biology and Immunology - University of Stuttgart).	50
10	Log-normally distributed parameters of the low-dimensional population model for TRAIL-induced proapoptotic signaling (values fitted to unpublished experimental data of M. Doszczak and P. Scheurich by J. Hasenauer). .	51
11	Classification of the pulmonary arterial tree (according to Horsfield (1978) [47]) and of the pulmonary venous tree (according to Horsfield and Gordon (1981) [48]) using Strahler's ordering system.	60
12	Model parameters of the alveolus model	64
13	Calculation of permeability field of the cuboid shown in Figure 21.	65
14	Changed model parameters of the alveolus model	74
15	Model parameters varied for the local sensitivity analysis.	90
16	Coefficients of the Backward Differentiation Formulas method up to the order 6 (Ascher and Petzold (1998) [9]).	120

Notation

Symbol	Definition	Dimension
Greek Letters:		
α_i	coefficient of the BDF method	[-]
α_{up}	upwinding parameter	[-]
β_0	coefficient of the BDF method	[-]
Δp	hydrostatic pressure difference	[kg / (m s ²)]
Δp_{ij}	pressure difference between node i and j	[kg / (m s ²)]
$\Delta \pi$	oncotic pressure difference	[kg / (m s ²)]
Δz_{ij}	geometrical distance in z direction between node i and j	[m]
ϵ	residuum	[-]
μ	dynamic fluid viscosity	[kg / (m s)]
μ_{ij}	dynamic fluid viscosity for a vessel segment ij	[kg / (m s)]
μ_l	location parameter	[-]
ν	kinematic viscosity	[m ² / s]
π	mathematical constant describing the ratio of a circle's circumference to its diameter	[-]
π_c	oncotic pressure in a capillary	[kg / (m s ²)]
π_{is}	oncotic pressure in the interstitial space	[kg / (m s ²)]
ρ_{mass}	mass density	[kg / m ³]
$\rho_{i,mass}$	mass density at node i	[kg / m ³]
$\rho_{i,mol}$	molar density at node i	[mol / m ³]
ρ_{mol}	molar density	[mol / m ³]
σ	osmotic reflection coefficient	[-]
σ_f	solvent-drag reflection coefficient	[-]
σ_s	scale parameter	[-]
τ	tortuosity	[-]
$\hat{\tau}$	tortuosity factor	[-]
τ_s	shear stress	[kg / (m s ²)]
ϕ	porosity	[-]
ψ	maximum allowable local error	[-]

Latin Letters:

a_{ss}	coefficient of the Dormand-Prince method	[-]
A	area	[m ²]
A_{ij}	cross-sectional area of a vessel segment ij	[m ²]
$A_{xz,REV}$	cross-section of a REV parallel to the x-axis	[m ²]
$\frac{A_{lymph}}{V_{tissue}}$	surface area of the lymphatic vessels per unit volume of tissue	[1 / m]
$\frac{A_{vessel}}{V_{tissue}}$	surface area of vessels per unit volume of tissue	[1 / m]
b	variate drawn from a normal distribution	[-]
b_s	weight of the Dormand-Prince method	[-]
\mathbf{b}	vector containing the boundary conditions and source and sink terms	
B	box volume	[m ³]
c	concentration	[kg / m ³]
c_s	coefficient of the Dormand-Prince method	[-]
[CARP]	concentration of CARP	[molecules / cell]
[C0]	concentration of TRAIL-receptor complexes	[molecules / cell]
[C1]	concentration of TRAIL-receptor complexes with bounded FADD	[molecules / cell]
[C2]	concentration of the internalized TRAIL-receptor complexes	[molecules / cell]
[C3]	concentration of caspase-3	[molecules / cell]
[C3*]	concentration of activated caspase-3	[molecules / cell]
[C8]	concentration of caspase-8	[molecules / cell]
[C8*]	concentration of activated caspase-8	[molecules / cell]
D	diffusion coefficient	[m ² / s]
D_{eff}	effective diffusion coefficient	[m ² / s]
e	local truncation error	[-]
E	element	[-]
f	subcontrol-volume face	[m ²]
$f_{deadCells}$	percentage of cancer cells undergoing cell death	[-]
f_C	capillary volume fraction	[-]
f_T	volume fraction of tissue	[-]
F	force	[kg m / s ²]
F_{ij}	molar mass flow rate through a vessel segment ij	[mol / s]
[FLIP]	concentration of FLIP	[molecules / cell]
$F_{x,REV}$	flow in x-direction	[m ³ / s]
\mathbf{g}	vector of gravitational acceleration $(0, 0, -g)^T$	[m / s ²]
g	(scalar) gravitational acceleration	[m / s ²]
G	discretized domain	[-]
h_n	time-step size	[s]

J	diffusive flux	[kg / (m ² s)]
k	first order rate constant of a drug	[1 / s]
\mathbf{k}_f	hydraulic conductivity	[m / s]
k_{off}	kinetic constant for the backward reaction	[1 / s]
k_{on}	kinetic constant for the forward reaction	[m ³ / (mol s)]
\mathbf{K}	tensor of (intrinsic) permeability	[m ²]
\mathbf{K}_C	(intrinsic) permeability tensor of a cuboid	[m ²]
\mathbf{K}_{CB}	(intrinsic) permeability tensor of a capillary bed	[m ²]
K_x	(intrinsic) permeability in x-direction	[m ²]
l_{vessel}	length of a capillary	[m]
[L]	ligand concentration	[molecules / cell]
L	length	[m]
L_{ij}	length of a vessel segment ij	[m]
L_{lymph}	hydraulic conductivity of a lymphatic vessel wall	[m ² s / kg]
L_p	hydraulic conductivity of a vessel wall	[m ² s / kg]
$L_{y,REV}$	length of a representative elementary volume (REV) in y-direction	[m]
m	mass	[kg]
M	molar mass	[kg / mol]
n	number of moles	[mol]
\mathbf{n}	normal vector	[m]
n_{nodes}	number of nodes	[-]
n_{steps}	number of steps	[-]
N	shape function	[-]
N_A	Avogadro constant	[-]
N_{vessel}	number of vessels	[-]
\mathbf{o}	m-vector of parameters	[-]
p_c	hydrostatic pressure in a capillary	[kg / (m s ²)]
p_{eff}	effective filtration pressure	[kg / (m s ²)]
p_{is}	hydrostatic pressure in the interstitial space	[kg / (m s ²)]
p_{lymph}	hydrostatic pressure in a lymphatic vessel	[kg / (m s ²)]
p_o	order	[-]
p_1	pressure	[kg / (m s ²)]
p_2	pressure	[kg / (m s ²)]
P	diffusive permeability of a capillary wall	[m / s]
q	source and sink terms	[mol / (m ³ s)]
q_F	coupling variable for describing the exchange of fluid between the two continua	[mol / (m ³ s)]
$q_{i,fDCM}$	coupling of the mass flow between the DCM and the VGM at node i	[mol / s]
$q_{i,xDCM}$	exchange of dissolved therapeutic agent between the DCM and the VGM at node i	[mol / s]
q_o	order	[-]
q_T	coupling variable for describing the exchange of ther- apeutic agent between the two continua	[mol / (m ³ s)]

Q	flow rate	$[\text{m}^3 / \text{s}]$
r	radius of a drug molecule	$[\text{m}]$
$r_{\text{adsorption}}$	sink term for describing the interaction of the drug molecules with the tumor cells	$[\text{mol} / (\text{m}^3 \text{s})]$
r_c	radius of a capillary	$[\text{m}]$
$r_{\text{degradation}}$	sink term for describing the degradation of a therapeutic agent	$[\text{mol} / (\text{m}^3 \text{s})]$
$r_{i,\text{degradation}}$	sink term for describing the degradation of a therapeutic agent at node i	$[\text{mol} / (\text{m}^3 \text{s})]$
r_{ij}	radius of a vessel segment ij	$[\text{m}]$
$r_{\text{inner sphere}}$	radius of the inner sphere	$[\text{m}]$
r_{lymph}	sink term for describing the influence of the lymphatic system	$[\text{mol} / (\text{m}^3 \text{s})]$
$r_{\text{lymph-drug}}$	sink term for describing the reduction of dissolved therapeutic agent by the lymphatic system	$[\text{mol} / (\text{m}^3 \text{s})]$
$r_{\text{outer sphere}}$	radius of the outer sphere	$[\text{m}]$
r_{vessel}	radius of a capillary	$[\text{m}]$
$[R]$	receptor concentration	$[\text{mol} / \text{m}^3]$ or $[\text{molecules} / \text{cell}]$
\mathbf{R}	three-dimensional rotation matrix	$[-]$
R	gas constant	$[-]$
\mathbf{R}^T	transpose of a three-dimensional rotation matrix	$[-]$
$[R \sim L]$	receptor-complex concentration	$[\text{mol} / \text{m}^3]$
R_{ij}	flow resistance of vessel segment ij	$[\text{kg} / \text{m}^4 \text{s}]$
\mathbf{S}	local sensitivity matrix	$[-]$
$\tilde{\mathbf{S}}$	normalized local sensitivity matrix	$[-]$
t	time	$[\text{s}]$
$t_{1/2}$	half-life of a drug	$[\text{s}]$
T	temperature	$[\text{K}]$
T_{ij}	vessel conductance	$[\text{m}^4 \text{s} / \text{kg}]$
u	upscaled node	$[-]$
u_p	primary variable	$[-]$
\mathbf{u}_p	vector of primary variables	$[-]$
v	velocity	$[\text{m} / \text{s}]$
\mathbf{v}_f	Darcy velocity	$[\text{m} / \text{s}]$
V	volume	$[\text{m}^3]$
V_i	volume associated to a node i	$[\text{m}^3]$
W_i	weighting function for node i	$[-]$
x	mole fraction of a therapeutic agent	$[-]$
x_c	mole fraction of a therapeutic agent in a capillary	$[-]$
x_{co}	initial mole fraction of a therapeutic agent	$[-]$
x_i	mole fraction of a therapeutic agent within the volume of a node i	$[-]$
x_{ij}	mole fraction of a therapeutic agent at the physical upstream node	$[-]$

x_{is}	mole fraction of a therapeutic agent in the interstitial space	[-]
X	mass fraction	[-]
X_f	integration point	[-]
[XIAP]	concentration of XIAP	[molecules / cell]
\mathbf{y}	n-vector of output variables	[-]
Y	log-normally distributed random variable	[-]
z	geodetic height	[m]
z_i	distance of a node i to the entry of the pulmonary artery into the lung	[m]

Subscripts:

α	phase α
D	Dirichlet boundary
h	healthy
i	node i
ij	vessel segment ij
j	node j
N	Neumann boundary
s	number of stages
t	tumorous
u	upscaled node u
$up(i, j)$	upstream node

Superscripts:

$\hat{}$	discrete value at a node
C	component of a phase
n	total number of components in a phase
t	old time step
$t + \Delta t$	new time step
*	activated form of a protein

Abstract

According to the World Health Organization, lung cancer kills more people than any other type of cancer and is responsible for 1.4 million deaths worldwide yearly [6]. This thesis proposes a multi-scale model for describing cancer-therapeutic transport in the human lung. The developed multi-scale model represents flow, transport and reaction processes: in the pulmonary macrocirculation on the organ scale, in the capillary bed around an alveolus, in the surrounding pulmonary tissue and in the tumor on the tissue scale, and in the tumor cell population and in the single cancer cells on the cells scale. The model concept is specialized for an alveolar cell carcinoma. The therapeutic agent is administered via a bolus injection into the blood stream.

The relevant processes occurring on these three scales are described by three different numerical models that are sequentially coupled to each other. On the organ scale, the discrete vascular graph model (VGM) simulates the advection and reaction of the blood-dissolved drug within the non-capillary part of the pulmonary vasculature (arteries, arterioles, venules and veins). To determine the amount of administered therapeutic agent that will reach the cancer cells, the VGM is coupled to the alveolus model: a double-continuum approach for porous media (DCM). The processes occurring in the alveolar capillaries and in the surrounding pulmonary tissue are represented by the DCM. The DCM is also used to describe the tumor regions in the lung. The system of equations of the coupled discrete / continuum model contains terms that account for degradation processes of the therapeutic agent, the reduction of the number of drug molecules by the lymphatic system and the interaction of the drug with the tissue cells. Further, the low-dimensional population model for TRAIL-induced proapoptotic signaling ([PMTS]_s) is sequentially coupled to the alveolus model. In this way, the spatiotemporal distribution of the therapeutic agent in the pulmonary tissue is linked with the biochemical reactions occurring on the cells scale. The low-dimensional population model for TRAIL-induced proapoptotic signaling describes the reactions of a heterogeneous cancer cell population to the administered therapeutic agent and calculates the percentage of cancer cells undergoing cell death.

As such, the multi-scale model can predict the spatial and temporal distribution of a drug administered by a continuous bolus injection in the human lung and the reaction of the cancer to the therapeutic agent. The functionality of the developed multi-scale model is demonstrated in example simulations using simplified pulmonary vascular networks.

Zusammenfassung

Die Motivation für diese Arbeit stellt die Entwicklung eines mathematischen und numerischen Modells für die Beschreibung der Verteilung eines Medikaments und dessen therapeutische Wirksamkeit in der menschlichen Lunge zur Lungenkrebstherapie dar. Das entwickelte Modellkonzept zur Beschreibung der Fluss-, Transport- und Reaktionsprozesse in der menschlichen Lunge ist auf das Medikament scFv-TRAIL, einem Fusionsprotein, für die Behandlung eines Alveolarkarzinoms ausgelegt. Gemäß der Weltgesundheitsorganisation (WHO) tötet Lungenkrebs mehr Menschen als jede andere bekannte Krebsart und ist jährlich für ungefähr 1,4 Millionen Tote weltweit verantwortlich (siehe [6]). Ungefähr 80 Prozent aller Lungenkrebserkrankungen werden durch eine über viele Jahre andauernde Inhalation von Zigarettenrauch verursacht. Andere Lungenkrebs verursachende Karzino-gene sind zum Beispiel Asbest, Arsen oder Nickel. Luftverschmutzung, Röntgenstrahlung, Vitaminmangel oder genetische Faktoren sind nur in ungefähr sieben Prozent aller Fälle die Ursache für eine Erkrankung an Lungenkrebs (Frommhold und Gerhardt (1987) [39]).

Die gängigsten Behandlungen von Krebserkrankungen beruhen auf der Entnahme des Tumors durch einen chirurgischen Eingriff, dem Einsatz einer Strahlentherapie oder der Verwendung von Zytostatika (Chemotherapie). Ein großer Nachteil der Strahlentherapie und der Chemotherapie ist, dass diese Behandlungsmethoden zur Apoptose, dem programmierten Zelltod, oder zur Hemmung der Zellteilung und des Zellwachstums von allen sich schnell teilenden Zellen im menschlichen Körper führen: den Krebszellen wie aber auch den Haarzellen, den Zellen im Mund, im Darm und den Knochenzellen. Somit sind die heutzutage üblichen Therapien von Krebserkrankungen mit erheblichen Nebenwirkungen verbunden, wie zum Beispiel Haarausfall, Übelkeit, Erbrechen. Ein weiteres Problem ist, dass durch einen chirurgischen Eingriff selten alle Krebszellen aus dem Körper entfernt werden können und somit nur eine Kombination aus allen drei Behandlungsansätzen zur Heilung des Patienten führen kann. Einen neuen Ansatz in der Behandlung von Krebserkrankungen stellt die Entwicklung von Zytostatika dar, die gezielt nur die Apoptose der Tumorzellen herbeiführen. Hierzu zählt auch das in dieser Arbeit betrachtete Fusionsprotein scFv-TRAIL. Dieses Fusionsprotein bewirkt den programmierten Zelltod von Lungenkrebszellen.

Diese Arbeit befasst sich mit der Entwicklung und Implementierung eines Mehrskalensmodells zur Beschreibung der Fluss-, Transport- und Reaktionsprozesse in der menschlichen Lunge zur Behandlung eines Alveolarkarzinoms mit einem tumorselektiven zytostatischen Therapeutikum.

Entwicklung eines Mehrskalensmodells zur Beschreibung der Fluss-, Transport- und Reaktionsprozesse in der menschlichen Lunge zur Lungenkrebstherapie

Das Zytostatikum zur Behandlung des Alveolarkarzinoms wird durch eine intravenöse Injektion verabreicht. Das im Blut gelöste Medikament wird vom rechten Herzventrikel in diskreten Pulsen in die rechte und linke Lungenarterie gepumpt. Von dort strömt das Blut und der zytostatische Wirkstoff durch ein Netzwerk aus Arterien und Arteriolen zu den Kapillaren. Die Kapillaren umschließen die Lungenbläschen. Nur durch die Gefäßwände der Kapillaren kann das Therapeutikum den Blutkreislauf verlassen und in das umliegende Lungengewebe und somit zu den Krebszellen gelangen. Das Blut und ein Teil des gelösten Wirkstoffes fließt durch ein Netzwerk aus Venulen und Venen zurück zum Herzen. Um die Fluss- und Transportprozesse des verabreichten Medikaments und die Reaktion des Tumors auf diese Zytostatikum zu beschreiben, muss das entwickelte Modell sowohl die Prozesse im Lungenkreislauf, den Austausch von Flüssigkeit und Therapeutikum zwischen dem Kapillarnetz und dem umliegenden Lungengewebe, die Fluss-, Transport- und Reaktionsprozesse im Gewebe und die Reaktion des Tumors und der einzelnen Krebszellen auf das Zytostatikum abbilden. Hierfür wird die Kopplung von drei räumlichen Skalen notwendig.

Auf der Organebene, der räumlich gesehen größten Skala, wird der advective Transport des gelösten Wirkstoffes durch den Lungenkreislauf, genauer durch die Arterien, Arteriolen, Venulen und Venen des Lungenkreislaufs, betrachtet. Ebenso wird der Abbau des Medikaments durch metabolische Transformationsreaktionen und Miktion berücksichtigt. Dazu wird das sogenannte *Vascular Graph Model* (VGM) verwendet. Auf der mittleren Skala, der Gewebeebene, wird der advective und diffusive Transport im Kapillarnetz um ein Lungenbläschen und dem umliegenden Gewebe, sowie die Fluss- und Transportprozesse im Tumor, durch das *Alveolus Model* (DCM), einem Doppelkontinuumsansatz, beschrieben. Das VGM beschreibt die Geometrie der Blutgefäße durch einen diskreten Ansatz. Wohingegen das DCM einen Homogenisierungsansatz verwendet, um die räumliche Anordnung der Kapillaren um ein Lungenbläschen und das umliegende Lungengewebe zu repräsentieren. Ein Lungenbläschen ist von zirka 1800 Kapillarsegmenten umgeben (Renkin et al. (1984) [82]). Die menschliche Lunge besitzt ungefähr 300 Millionen Lungenbläschen (Weibel (1991) [102]) und somit müsste die räumliche Anordnung von $5,4 \cdot 10^{11}$ Kapillarsegmenten beschrieben werden. Um dies zu umgehen und den Rechenaufwand zu reduzieren, verwendet das DCM, wie bereits zuvor erwähnt, einen Homogenisierungsansatz zur Beschreibung der räumlichen Anordnung des Kapillarnetzes und des Lungengewebes. Auf der kleinsten Skala, der Zellebene, wird das *Low-Dimensional Population Model for TRAIL-Induced Proapoptotic Signaling* ([PMTS]_s) eingesetzt. Auf der Zellebene werden sowohl die Reaktionen des Alveolarkarzinoms, als auch die der einzelnen Krebszellen auf das verabreichte Medikament betrachtet. Die Fluss- und Transportprozesse durch die Blutgefäße des Lungenkreislaufs und durch das Lungengewebe spielen sich im Bereich von Sekunden bis hin zu wenigen Minuten ab. Wohingegen die Reaktion des Tumors auf das verabreichte Zytostatikum, die Apoptose der Krebszellen, erst nach mehreren Stunden abgeschlossen ist.

Das entwickelte Mehrskalensmodell besteht aus den drei oben erwähnten Modellen und koppelt sequentiell das VGM mit dem DCM und das DCM mit [PMTS]_s, um die Fluss-, Transport- und Reaktionsprozesse in der gesamten Lunge darzustellen.

Mathematisches Umsetzung des Mehrskalensmodells

Die Aufgabe eines mathematischen Modells ist es das entwickelte konzeptionelle Modell in mathematische Formulierungen zu übertragen. Dies bedeutet, dass die durch das konzeptionelle Modell ausgewählten, relevanten Prozesse nun durch mathematische Gleichungen beschrieben werden.

Das Gleichungssystem des *Vascular Graph Model* basiert auf einem Ein-Phasen Zwei-Komponenten Ansatz. Die strömende Phase besteht aus den beiden Komponenten Blut und verabreichtes Medikament. Das mathematische Modell beruht auf der vereinfachenden Annahmen einer nicht pulsierenden Strömung. Weiter wird angenommen, dass die Strömungsgeschwindigkeiten an den Gefäßwänden Null ist (Haftbedingung). Der Einfluss von Verzweigungen im Blutgefäßbaum auf die Strömungsprozesse wird vernachlässigt. Somit berücksichtigt das VGM keine turbulenten Strömungen. Die betrachtete Phase, bestehend aus Blut und darin gelöstem Medikament, wird als inkompressible, pseudoplastische Flüssigkeit beschrieben. Der Fluss durch die einzelnen Blutgefäße wird mit Hilfe der Kontinuitätsgleichung berechnet. Der advective Transport des gelösten Medikaments durch den Gefäßbaum wird durch die Transportgleichung beschrieben. Die Transportgleichung enthält einen Senkterm, der die Abbauprozesse des Medikaments im Blut berücksichtigt.

Das Gleichungssystem des *Alveolus Model* verwendet für jedes der beiden Kontinua einen Ein-Phasen Zwei-Komponenten Ansatz für starre, poröse Medien. Im Falle des Gewebekontinuums besteht die Phase aus den Komponenten Gewebsflüssigkeit und darin gelöstes Medikament. Die Phase des Kapillarbettkontinuums setzt sich aus Blut und Therapeutikum zusammen. Die beiden Phasen werden als inkompressible, newtonsche Flüssigkeiten betrachtet. Sowohl im Gewebekontinuum, als auch im Kapillarbettkontinuum liegt eine schleichende Strömung vor. Dies bedeutet, dass die Reynolds-Zahl in beiden Kontinua immer kleiner als eins ist und somit das Gesetz von Darcy für die Berechnung der Fließgeschwindigkeiten verwendet werden kann. Der Fluss in den beiden Kontinua wird mit Hilfe von Kontinuitätsgleichungen berechnet. Der advective und diffusive Transport des gelösten Medikaments im Gewebekontinuum und im Kapillarbettkontinuum werden durch Transportgleichungen beschrieben. Die Kontinuitäts- und Transportgleichungen der beiden Kontinua sind über Quell- und Senkterme miteinander gekoppelt. Zusätzlich beinhalten die Gleichungen des Gewebekontinuums Senkterme für die Beschreibung der Einflüsse des Lymphsystems und der Wechselwirkungen der Wirkstoffmoleküle mit den Krebszellen auf die Fluss- und Transportprozesse im Gewebe. Die Transportgleichung im Kapillarbettkontinuum enthält einen weiteren Senkterm. Dieser berücksichtigt die Abbauprozesse des Medikaments im Blut.

Das Gleichungssystem des *Low-Dimensional Population Model for TRAIL-Induced Proapoptotic Signaling* beinhaltet ein Einzelzellmodell zur Abbildung der Reaktionen einer einzelnen Krebszelle auf einen proapoptotischen Stimulus. Das Einzelzellmodell ist in ein heterogenes Zellpopulationsmodell eingebunden. Die heterogene Reaktion aller Krebszellen eines Tumors auf den gleichen Stimulus wird durch das Zellpopulationsmodell abgebildet. Das gewöhnliche Differentialgleichungssystem ist für alle Zellen gleich aufgebaut. Jedoch werden für jede Zelle andere Anfangsbedingungen und Parameterwerte gewählt.

Numerische Implementierung des Mehrskalensmodells

Die entwickelten mathematischen Modelle zur Beschreibung der Fluss-, Transport- und Reaktionsprozesse in der menschlichen Lunge sind analytisch, wenn überhaupt, nur sehr schwer zu lösen. Deshalb werden die Gleichungssysteme der mathematischen Modelle mit Hilfe numerischer Algorithmen gelöst. Dies erfordert die zeitliche Diskretisierung der gewöhnlichen Differentialgleichungen des *Low-Dimensional Population Model for TRAIL-Induced Proapoptotic Signaling* und die räumliche und zeitliche Diskretisierung der partiellen Differentialgleichungen des *Vascular Graph Model* und des *Alveolus Model*. Die durch die zeitliche und räumliche Diskretisierung erhaltenen numerischen Algorithmen der drei verwendeten mathematischen Modelle des Mehrskalensmodells und die numerische Umsetzung der Kopplungen zwischen den Modellen sind unter der Verwendung von drei verschiedenen Simulatoren realisiert worden. Mit Hilfe der implementierten numerischen Algorithmen können die Prozesse, welche durch das konzeptionelle Modell definiert worden sind, berechnet werden.

Das lineare, partielle Differentialgleichungssystem des VGM wird numerisch gelöst nach den beiden Primärvariablen Druck und Molenbruch an gelöstem Medikament. Hierfür wird für die räumliche Diskretisierung des Gleichungssystems ein Finite Differenzen Verfahren und für die zeitliche Diskretisierung ein explizites Euler-Verfahren verwendet. Die Kontinuitätsgleichung, zur Ermittlung des Druckfeldes in den Blutgefäßen, wird entkoppelt von der Transportgleichung, zur Bestimmung der Medikamentenverteilung im Gefäßbaum, gelöst. Das Courant-Friedrichs-Lewy (CFL) Kriterium stellt die Stabilität und die Konvergenz der Lösung sicher, trotz der Verwendung einer expliziten Zeitdiskretisierung. Das nicht-lineare, partielle Differentialgleichungssystem des DCM wird ebenso nach den beiden Primärvariablen Druck und Molenbruch an gelöstem Medikament im Lungengewebe (Kontinuum 1) und nach den beiden Primärvariablen Druck und Molenbruch an gelöstem Medikament im Kapillarbett (Kontinuum 2) gelöst. Für die räumliche Diskretisierung des nicht-linearen Gleichungssystems wird die Box-Methode (siehe Helmig (1997) [45]) verwendet. Die zeitliche Diskretisierung der Gleichungen beruht auf dem impliziten Euler-Verfahren. Das Anfangswertproblem des gewöhnlichen Differentialgleichungssystem des [PMTS]_s wird mit Hilfe eines expliziten Runge-Kutta Verfahrens, der Dormand-Prince Methode, und dem BDF-Verfahren numerisch gelöst.

Für die sequentielle Kopplung des DCM an das VGM wird das sogenannte *Python Subprocess Module* verwendet. Das *Vascular Graph Model* liefert die Anfangs- und Randbedingungen für die beiden Primärvariablen Druck und Molenbruch an gelöstem Medikament im Kapillarbett. Das DCM übergibt an das VGM die Menge an Flüssigkeit und gelöstem Medikament, welche den Blutkreislauf innerhalb eines Simulationzeitschrittes verlassen haben. Die sequentielle Kopplung des [PMTS]_s an das DCM wird durch die Verwendung der MATLAB ENGINE Routine realisiert. Das Doppelkontinuummodell übergibt an das *Low-Dimensional Population Model for TRAIL-Induced Proapoptotic Signaling* die Medikamentenkonzentration im Tumorgewebe. Das [PMTS]_s berechnet die Prozentzahl apoptotischer Krebszellen auf Grund der Wirkstoffkonzentration im Tumor. Diese Information wird an das DCM zurückgegeben.

Simulationsergebnisse und lokale Sensitivitätsanalyse des Mehrskalensmodells

In dieser Arbeit werden zwei verschiedene Simulationsbeispiele gezeigt. Das erste Beispiel zeigt die räumliche und zeitliche Verteilung des verabreichten Medikaments in einem kleinen Ausschnitt der Lunge für eine Modellierungszeit von elf Sekunden.

Das zweite Beispiel stellt die räumliche und zeitliche Verteilung des verabreichten Medikaments in einem kleinen Ausschnitt der Lunge über einen Zeitraum von zwölf Stunden und die Reaktion der Krebszellen auf das Therapeutikum dar.

Die lokale Sensitivitätsanalyse des Mehrskalensmodells zeigt den Einfluss der einzelnen Parameter auf das Modellergebnis auf. Es wird untersucht, wie sich eine Änderung eines einzelnen Parameterwertes auf die Drücke und Molenbrüche in den Blutgefäßen, im Lungengewebe und im Tumor, sowie auf den Anteil apoptotischer Zellen im Tumorgewebe auswirken. Insgesamt ist der Einfluss von 64 Parametern untersucht worden. Als einer der wichtigsten Parameter ist der Durchmesser der Blutgefäße identifiziert worden. Hingegen sind die Senkterme, die den Einfluss des Lymphsystems und die Abbauprozesse des Medikaments beschreiben, eher zu vernachlässigen.

Zusammenfassung und Ausblick

Diese Arbeit stellt ein Mehrskalensmodell zur Beschreibung der Fluss-, Transport- und Reaktionsprozesse in der menschlichen Lunge zur Behandlung von Lungenkrebs vor. Das entwickelte mathematische und numerische Modell verbindet drei unterschiedliche räumliche Skalen und die entsprechenden physikalischen Prozesse jeder Skala miteinander. Es existiert bereits eine Vielzahl von Veröffentlichungen über die Modellierung von Fluss- und Transportprozessen in Tumoren, zum Beispiel: Baxter und Jain (1989) [18], Baxter und Jain (1990) [16], Baxter und Jain (1991) [17], Chapman et al. (2008) [24], Eikenberry (2009) [33] oder Shipley und Chapman (2010) [91]. Ebenso gibt es zahlreiche Publikationen über die Simulation der Strömungsprozesse in den menschlichen Blutgefäßen: Boas et al. (2008) [21], Reichold et al. (2009) [81], Guibert et al. (2010) [40], Lorthois et al. (2011) [65] oder Lorthois et al. (2011) [66]. Auch auf dem Gebiet der Apoptosemodellierung sind bereits viele Veröffentlichungen vorhanden, wie zum Beispiel: Bagci et al. (2006) [13], Eißing et al. (2009) [34] oder Hasenauer et al. (2010) [43]. Das in dieser Arbeit vorgestellte Mehrskalensmodell basiert auf den oben erwähnten Publikationen. Jedoch die Kopplung eines Modells für die Makrozirkulation mit zwei weiteren Modellen, einem für die Mikrozirkulation und dem umliegenden Gewebe und einem zweitem Modell für die Apoptosemodellierung im Tumor, und somit die Repräsentation eines ganzen Organs befallen von einem Tumor sind neu.

Das entwickelte Mehrskalensmodell besteht aus den folgenden drei Modellen: dem *Vascular Graph Model* zur Darstellung der Prozesse in der Makrozirkulation, dem *Alveolus Model* für die Beschreibung der Prozesse im Kapillarbett um eine Alveole und dem umliegenden Lungengewebe, sowie dem *Low-Dimensional Population Model for TRAIL-Induced Proapoptotic Signaling* zur Abbildung der Reaktionen der Krebszellen auf das verabreichte Medikament. Allerdings, sind noch weitere Verbesserungen an den einzelnen Modellen möglich. Bis jetzt bilden das VGM und das DCM noch nicht die zyklischen Druckschwankungen im Blutkreislauf auf Grund des Herzschlags ab. Weiterhin wäre es interessant unterschiedliche Behandlungszyklen zu simulieren, um den Einfluss der Behandlungsdauer und der verabreichten Medikamentendosis auf die Anzahl apoptotischer Zellen im Tumor zu untersuchen.

Zusätzlich ist es von Nöten das bestehende Mehrskalenmodell um ein Tumor-Wachstums-Modell zu erweitern. Um die Vorhersagekraft des Modells zu stärken, ist es unumgänglich hochauflösende Angiographiedaten vom Lungenkreislauf für die Gewinnung realistischer Parameterwerte zu verwenden.

Das in dieser Arbeit vorgestellte Modellkonzept stellt einen ersten Schritt in Richtung eines prädiktiven numerischen Modells dar, das in der Lage wäre die Behandlung eines Alveolarkarzinoms zu leiten. Nur durch die kontinuierliche Verbesserung des bereits bestehenden Mehrskalenmodells kann das Ziel, den Einsatz dieses Modells bei der Behandlung von Lungenkrebspatienten, erreicht werden.

1 Introduction

1.1 Motivation

The motivation for this work is the development of a mathematical and a numerical model, that describe the distribution and the therapeutic efficacy of a targeted protein therapeutic within the human lung for cancer therapy. The therapeutic agent, that is used for this model, is a bifunctional fusion protein, the so-called scFv-TRAIL. The TRAIL molecule is combined with a monoclonal antibody that recognizes the cell surface of the tumor. It binds to the epidermal growth factor receptor that is overexpressed in a number of cancers, especially in lung tumors. The scFv-TRAIL molecule belongs to the targeted protein therapeutics and seems to be the future in cancer treatment.

According to the World Health Organization, lung cancer kills more people than any other type of cancer and is responsible for 1.4 million deaths worldwide yearly [6]. Lung cancer, especially the bronchial carcinoma, is the most frequently occurring malignant tumor in our country. In about 85 percent of all cases, this kind of tumor is induced by the continuous inhalation of tobacco smoke. It is estimated that for every three million cigarettes purchased, a lung cancer follows 35 years later. Lung cancer is a paradigm of carcinogen induced human cancer. Other pulmonary carcinogens are, for example, asbestos, arsenic, and nickel. Air pollution, X-rays, vitamin deficiency and genetic factors are only the cause of lung cancer in about 7 percent of all cases (Frommhold and Gerhardt (1987) [39]).

The delivery of the therapeutic agent to the solid cancer and its selectivity are the decisive factors for a high therapeutic efficacy of the drug. In general, the delivery of the therapeutic agent to the tumor cells involves three processes:

- the transport within the blood vessels,
- the transport across vasculature walls into the surrounding tissues, and
- the transport through the interstitial space towards the cancer cells.

If the tumor exceeds a diameter of about three millimeters, tumor induced angiogenesis will occur (Shijubo et al. (2003) [90]). In this case, a direct transport of the therapeutic agent via the blood vessels to the targeted cells is also possible. The model has to account for all four aforementioned modes of transport. The transport processes are determined by the physiochemical properties of the therapeutic agent (particle size, diffusivity, drug binding) and the biological properties of the tumor (tumor vasculature, tissue structure and composition, interstitial fluid pressure, tumor cell density) (Jang et al. (2003) [54]). Further,

the reaction of the tumor to the administered therapeutic agent has to be taken into account to describe the therapeutic efficacy of the drug.

The development of a mathematical and a numerical model that are suitable to guide lung cancer therapeutic strategies is an ambitious aim. This work does not claim to fully achieve this ultimate goal. However, it is a first step towards it. The developed model is based on the anatomy and histology of the human lung and is specialized in the therapeutic agent scFv-TRAIL.

1.2 Structure of the Thesis

Following these introductory comments, the anatomy, the histology and the cardiovascular system of the human lung are described in Chapter 2. An overview about the properties and the composition of blood is also given. Further, the characteristics of tumors and the cancer cell-selective apoptogenic therapy are explained. Chapter 2 provides the basis for Chapter 3: the model concept for describing cancer-therapeutic transport in the lung. The description of the flow, transport and reaction processes in the lung is a multi-scale problem. Therefore, three different models are used. Chapter 3 gives an overview about the individual models and how these models interact with each other. The therapeutic agent is administered via a bolus injection into the blood stream. The vascular graph model (VGM) represents the processes occurring in the pulmonary circulation: the arteries, arterioles, venules and veins. In Chapter 4, the underlying assumptions, the balance equations and the numerical implementation of the VGM are explained. The vascular graph model is coupled to the alveolus model, a double-continuum approach. The alveolus model represents the flow, transport and reaction processes in the capillary bed around a single alveolus and the surrounding pulmonary tissue. Chapter 5 introduces the idea and the reason for using a double-continuum model. Furthermore, the balance equations for each continuum, the coupling functions for the flow and transport processes between the two continua, and the numerical implementation of the alveolus model are described. The alveolus model is coupled to the low-dimensional population model for TRAIL-induced proapoptotic signaling ([PMTS]_s). This model describes the reaction of the cancer cells to the present concentration of the therapeutic agent in the pulmonary tissue. In Chapter 6, the model concept, the system of ordinary differential equations and the numerical implementation of the [PMTS]_s are explained. Chapter 7 describes in detail the coupling of the three individual models that have been introduced in Chapter 4, Chapter 5 and Chapter 6. In Chapter 8, two different scenarios are presented to demonstrate the functionality and the capabilities of the developed model concept for describing cancer-therapeutic transport in the lung. A local sensitivity analysis is performed to determine the impact of the individual parameters on the model results. Chapter 9 summarizes the important points of this thesis and gives an outlook to possible enhancements. In the appendix of this thesis, a more detailed overview about the numerical implementation of the VGM, the DCM and the [PMTS]_s is given.

2 Biological/Medical Background

2.1 Anatomy of the Lung

The lungs are a pair of cone-shaped breathing organs: the left lung and the right lung. They bring oxygen into the body when breathing in and take out carbon dioxide when breathing out. The lungs are arboreal segmentations of the bronchi with a vascular system that are united by connective tissue. Figure 1 shows the anatomy of a human lung.

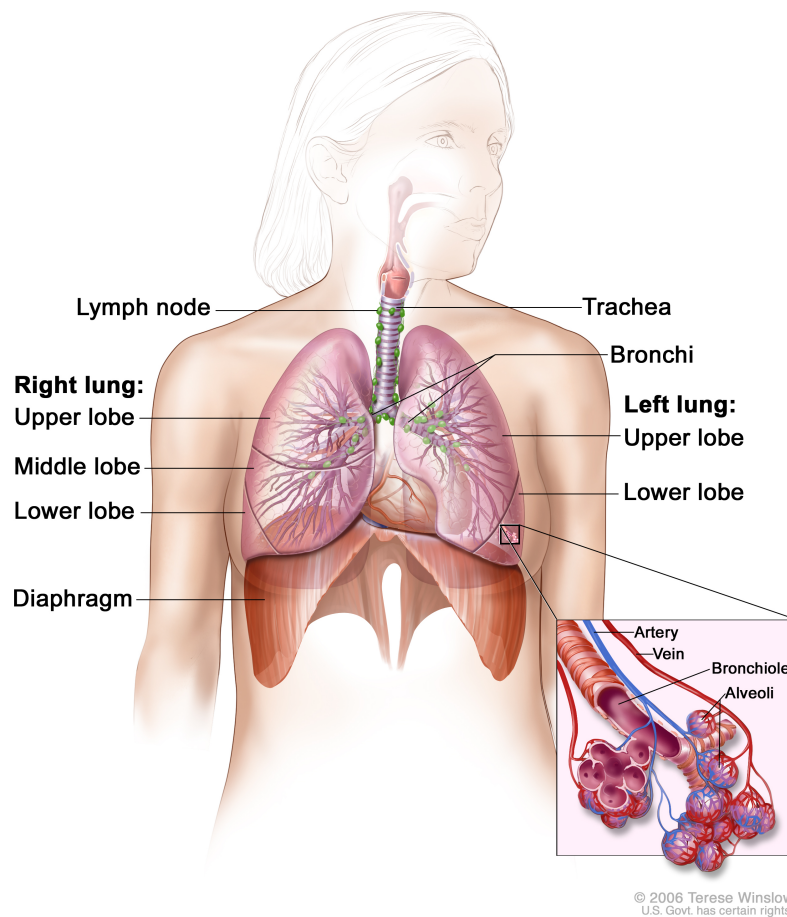


Figure 1: Lung anatomy (with kind permission of T. Winslow, copyright 2006).

Each lung has sections called lobes. The left lung has two lobes and the right lung, which is slightly larger, has three. The lobes are further subdivided into smaller segments, the

so-called lobules. A thin membrane named the pleura surrounds the lungs. The bronchial system consists of air conducting and respiratory sections. The branching of the bronchial tree occurs strictly by dichotomy (see Figure 2). However, the branching is irregular. Diameters and lengths of daughter branches vary and terminal branches are reached after a diverse number of generations. Table 2 shows in detail the subdivision of the human bronchial tree. The average number of generations is about 23 for human airways (Weibel (1991) [102]). The trachea (zeroth generation of airways) divides into the two main bronchi (first generation of airways) that lead to the right and the left lung. Each bronchi is further subdivided and gives rise to the bronchioles. The bronchioles lead to the alveolar sacs. A single alveolar sac consists of a cluster of alveoli. In the alveoli the gas exchange occurs. In total, the lung contains about 300 million alveoli (Schiebler et al. (1999) [84]). The respiratory bronchioles, alveolar ducts and alveolar sacs which originate from a single terminal bronchiole (terminal part of the non respiratory bronchioles) are referred to as acinus (see Figure 2). A single acinus contains about 2000 alveoli (Des Jardins (2008) [55]).

Table 2: Organization of the human airways: generation number G according to the dichotomous branching of the airways (Schiebler et al. (1999) [84]).

G^2	air conducting sections					respiratory sections ¹							
	trachea	bronchi		bronchioles				alveolar system					
		lobar	segmental	non respiratory	respiratory			AD ³		AS ⁴			
	0	1	2	3	4 → 15	16	17	18	19	20	21	22	23

¹ sites of gas exchange

² G : generation number

³ AD: alveolar ducts

⁴ AS: alveolar sacs

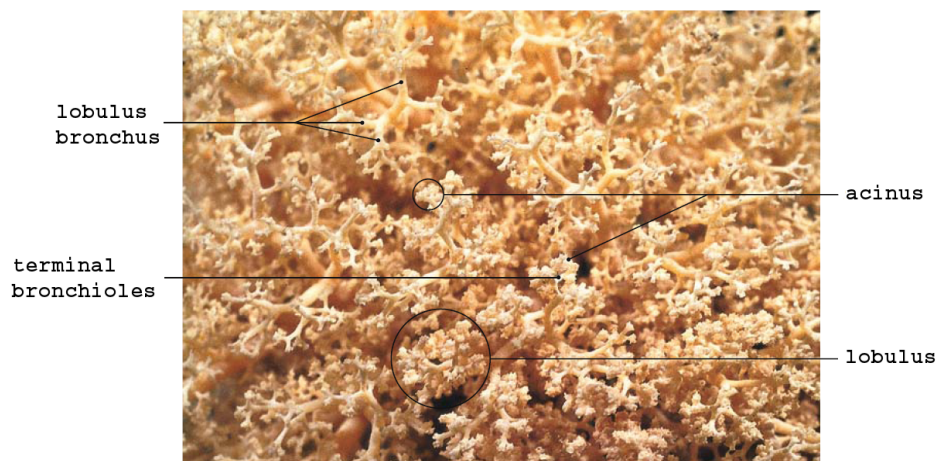


Figure 2: Part of the bronchial system: showing the dichotomous branching of the bronchial tree (adapted from Tillmann (2005) [97] with kind permission from Springer Science+Business Media).

2.2 Cardiovascular System of the Lung

The cardiovascular system of the human body is divided into the systemic circulation supplied by the left heart ventricle and the pulmonary circulation supplied by the right ventricle (Formiggia et al. (2009) [38]). The pulmonary blood circuit, as well as the systemic blood circuit, are composed of arteries, arterioles, capillaries, venules and veins (Des Jardins (2008) [55]). Every vessel that transmits blood away from the heart is called artery. Its end section is termed arteriole. Veins are all vessels that lead the blood back to the heart. The smallest type of veins are the so-called venules, that end in the veins. According to Formiggia et al. (2009) [38], venules can be classified into microvenules (diameter of 15-100 μm), minivenules (diameter of 100-300 μm) and venules (diameter 300-500 μm).

The blood supply of the lung occurs by a dual vascular supply: the bronchial vessels and the pulmonary vessels. The pulmonary vessels belong to the pulmonary circulation while the bronchial vessels are related to the systemic circulation. The main task of the pulmonary blood circuit is the arterialization¹ of the venous blood. Further, all structures distal² to the terminal bronchioles are supplied with nutrients by the pulmonary vascular system. Blood is ejected from the right heart ventricle in discrete pulses where it flows through a network of branching arteries of decreasing size to the arterioles and then to the capillaries. From the capillaries, blood returns to the heart through a network of venules and veins. The arteries and veins have a pure conduit function: the delivery of blood to and from the capillary beds. Whereas, the pulmonary capillaries are responsible for the perfusion of the tissue with oxygen and nutrients, the removal of carbon dioxide and catabolites, and the oxygenation of blood (Formiggia et al. (2009) [38]). The pulmonary capillaries which surround the alveoli form a hexagonal network around the single alveoli (Weibel (1963) [101]). Capillaries are muscular free endothelial tubes. The structure of the capillary wall is organ-specific and therefore function-related. The capillary wall consists of the glycocalyx, the endothelium, the basal membrane and the pericytes. The glycocalyx covers the entire surface of the endothelium and the intercellular gaps. It forms the first contact between the blood and the vessel wall. The glycocalyx is highly hydrated and extends up to 100 nm into the lumen of the vessel. Due to the charged surface of the glycocalyx, it provides the first barrier to transport of substances from the intravascular space across the vessel wall into the surrounding tissue (Formiggia et al. (2009) [38]). The endothelium is the main constituent of the vessel wall forming the interface between the flowing blood and the vessel wall. It can be distinguished between capillaries with thin endothelial cells (0.1-0.2 μm) and thick endothelial cells (0.3-1.0 μm). The basal membrane appears as a closed layer in the lateral direction and can be discontinuous in the longitudinal direction. It is 30-60 nm thick. The pericytes are flat cells with strongly branched appendices, that finger-shaped encompass the endothelial tube. The pericytes are covered by the basal membrane. As it is shown in Figure 3, there are three types of capillaries: continuous, fenestrated and discontinuous. Continuous capillaries do not have inter- or intracellular gaps (see Section 5.4). The endothelial cells overlap and are closely linked by tight junctions (mean pore radius of 4 to 5 nm (Schmidt and Lang

¹Arterialization means the conversion of the venous blood into arterial blood during its passage through the lungs by the absorption of oxygen and the release of carbonic acid gas into the inspired air.

²An adjective used for a body part that is further away from another part, referring, for example, to the trunk (Marcovitch (2005) [68]).

(2007) [87])). The endothelium of fenestrated capillaries is penetrated by intracellular pores (fenestrations). These pores have a diameter of 50 to 60 nm (Schmidt and Lang (2007) [87]). The vessel wall of discontinuous capillaries is characterized by wide gaps between the cells, a discontinuous basal lamina, and numerous fenestrations in the endothelium (Baber (2009) [11]). In the lung there are only continuous, non-fenestrated capillaries (Tillmann (2005) [97]).

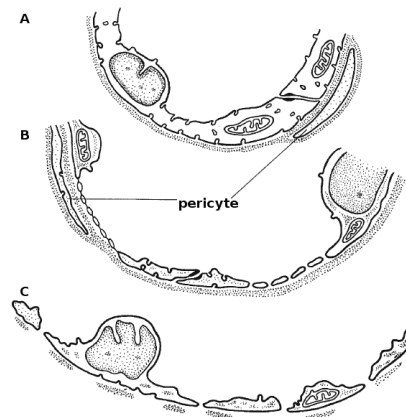


Figure 3: Different types of capillaries (adapted from Schiebler and Korf (2007) [85] with kind permission from Springer Science+Business Media). **A** Continuous capillary: continuous basal membrane. **B** Fenestrated capillary. **C** Discontinuous capillary: endothelial cells with intercellular pores; discontinuous basal membrane.

The two pulmonary arteries that originate from the pulmonary trunk enter the corresponding lung through the pulmonary hilum³. The branching of the pulmonary artery occurs by an irregular dichotomy. Each artery divides into 2 daughter branches of unequal length and diameter until the alveolar capillaries are reached (Milnor (1972) [71]). The arterial tree runs and branches in parallel to the tracheobronchial tree. The venous tree also shows a dichotomous branching behavior. In contrast to the arteries, the veins run away from the bronchial tree and take a more direct way to the hilus of the lung. The veins of each lung merge into two large veins so that blood of four pulmonary veins is drained into the left atrium of the heart (Des Jardins (2008) [55]). In Table 3, the properties of the human pulmonary circulation are summarized.

The bronchial vessels, the second blood vessel system in the lung, are a part of the systemic circulation and have a purely nutritive function. The bronchial vessels are responsible for the supply of oxygen to the bronchi up to the terminal bronchioles, the tissue of the pulmonary artery walls, and the peribronchial tissue (Larsen and Ziegenfuß (2009) [60]). The blood flow through the bronchial arteries and veins is about one per cent of the total blood flow through the lungs. The bronchial arteries follow the tracheobronchial tree up to the terminal bronchioles. There, the bronchial arteries merge with the pulmonary arteries and

³Pulmonary hilum denotes the location where the pulmonary artery, the pulmonary vein, the main bronchus, nerves and lymphatic vessels penetrate the lung.

Table 3: Properties of the human pulmonary circulation (Singhal et al. (1973) [92]).

diameter range [mm]	number of vessels	volume [ml]	mean velocity [mm/s]
30 (main pulmonary artery)	1	64	110
8-30	10	21	155
1-8	10^3	37	104
0.1-1	$0.25 \cdot 10^6$	19	44
0.02-0.1	$20 \cdot 10^6$	5	23
0.01 (capillaries)	$300 \cdot 10^6$	5	2

capillaries that are part of the pulmonary vascular system. One third of the bronchial venous blood returns to the right atrium through the azygos, hemiazygos and intercostal veins. The other two-thirds of the bronchial venous blood drain into the pulmonary circulation via bronchopulmonary anastomoses⁴ and return to the left atrium through the pulmonary veins (Des Jardins (2008) [55]). Figure 4 depicts a part of the bronchial tree showing the division of the bronchial and pulmonary vessels.

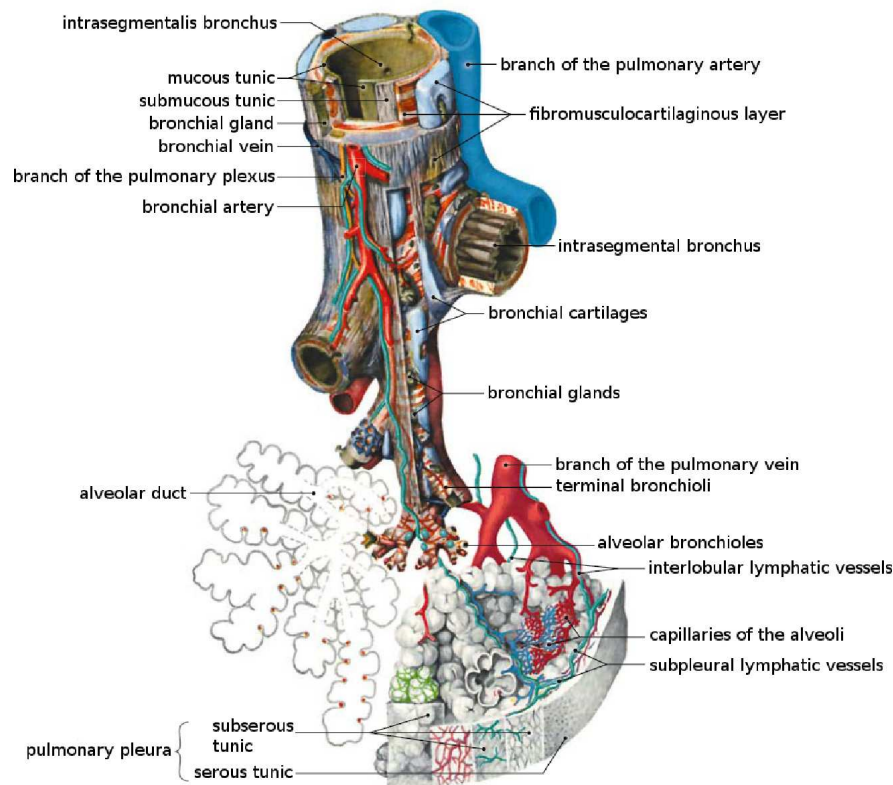


Figure 4: Bronchial tree and alveoli with bronchial and pulmonary vessels (adapted from Tillmann (2005) [97] with kind permission from Springer Science+Business Media).

⁴An anastomosis is a direct connection between different branches of veins or arteries without any intervening network of capillaries (Marcovitch (2005) [68]).

2.3 Composition and Function of the Body Fluid Blood

The body fluid blood is a suspension of erythrocytes (red blood cells), leukocytes (white blood cells) and thrombocytes (blood platelets) in blood plasma. The portion of cells is about 45 percent and the portion of blood plasma amounts to 55 percent (Schiebler (1999) [84]). The volume fraction of cells is termed the hematocrit. Blood can be described as a liquid organ with several different functions like the transport and distribution of oxygen, carbon dioxide, cells, nutrients, hormones, metabolites, vitamins, mineral nutrients, and temperature. Certain organs control and change the chemical and physical properties of blood, that the concentration of dissolved components, the pH value and the temperature stay constant. Further functions of blood are the hemostasis (blood clotting) and the immune defense (Schmidt and Lang (2007) [87]).

Blood plasma is composed of about 90 percent water. The remaining ten percent consist of proteins (about eight percent), electrolytes, food substances, respiratory gases, hormones, vitamins and waste products (Des Jardins (2008) [55]). Albumins amount to 60 percent of

Table 4: Composition and properties of blood in a healthy human (modified according to Formiggia et al. (2009) [38]).

composition	unit	value	function
erythrocytes	number per mm ³	4.2 – 6.3 · 10 ⁶	transport of O ₂ and CO ₂
leukocytes	number per mm ³	4 – 10 · 10 ³	
neutrophils	%	40-70	phagocytosis of bacteria
eosinophils	%	1-2	defense against parasites, participation in allergic reactions
basophils	%	0.5-1	release of histamine (causes allergic reactions) and heparin (for fat metabolism)
lymphocytes	%	20-40	immune defense
monocytes	%	2-10	phagocytosis, movement into the tissue and differentiation into macrophages
blood platelets	number per mm ³	2 – 4 · 10 ⁵	blood clotting
ions	mEq/l	295-310	
protids	g/l	70-80	
lipids	g/l	5-7	
glucids	g/l	0.8-1.1	
properties	unit	value	
density	kg/m ³	1040-1060	
hematocrit	%	40-50	
osmotic pressure	mOsm	280-300	
pH		7.39-7.41	

the proteins. The remainder of proteins is composed of globulins and fibrinogen (Schiebler (1999) [84]).

Erythrocytes, the red blood cells, consist of a bilipid membrane and a membrane cytoskeleton that surrounds a solution called hemoglobin. Hemoglobin is a protein that shows a high affinity for oxygen. The red blood cells have a biconcave discoid shape with a diameter of about 8 μm and a thickness of approximately 2 μm . Erythrocytes are highly deformable (Formiggia et al. (2009) [38]). Thrombocytes, the blood platelets, have a diameter in the range of 2 to 4 μm . Thrombocytes are anuclear cells and play an important role in the coagulation of blood. Red blood cells as well as blood platelets are not able to cross the vessel walls of the circulatory system whereas leukocytes, the white blood cells, can pass through the walls of venules (Schiebler (1999) [84]). Leukocytes are involved in the immune defense of the body. Due to the structural and chemical properties of leukocytes, the different kind of leukocytes are grouped into granulocytes and agranulocytes. Neutrophils, eosinophils and basophils belong to the granulocytes. These cells contain granules⁵ in their cytoplasm. Lymphocytes and monocytes lack granules and belong to the agranulocytes (Des Jardins (2008) [55]). The precise composition and the properties of blood, as well as the functions of the different cells, are specified in Table 4.

2.4 Types of Tissues

A tissue is an assembly of cells and intercellular substances. Depending on the function of the tissue, it is termed parenchyma or stroma. Parenchyma means all kinds of tissue in an organ that have special, organ-specific functions. If the tissue mainly forms the supporting structure of the organ it will be termed stroma. In many cases, it cannot be distinguished between parenchyma and stroma. In the human body, four basic types of tissue can be found: epithelial tissue, muscular tissue, nerve tissue and connective tissue. The cells that belong to the same kind of tissue are characterized by special morphological properties and functions. The epithelial tissue is a cellular layer that forms the lining of internal and external surfaces. The epithelium fulfills functions like resorption, absorption, transport and secretion of substances. The muscular tissue is characterized by cells whose primary function is contraction. The nervous tissue is composed of neurons, neuroglia, nerves and nerve fibers. The neurons transmit the electrical impulses and the neuroglia provide a support system for the neurons. Nervous tissue is necessary for the selective communication between, and the control of, body parts. For in-depth information about the structure and the functions of the different types of tissue, the reader is referred to Schiebler (1999) [84] and Junqueira et al. (2002) [56]. The tissue of the lung consists mainly of connective tissue. The structure and function of the connective tissue will be explained in the following subchapter.

2.4.1 Structure and Function of the Connective Tissue

The connective tissue is a type of tissue made up of fibers forming a framework and support structure for body tissues and organs. The connective tissue is allotropic and its structure

⁵A granule is a small particle. The release of granules is called degranulation.

depends on the local demands. It can be differentiated between formed and unformed connective tissue (see Table 5). The unformed tissue is not able to hold its shape in contrast to the formed one. However, all kinds of connective tissue consist of connective tissue cells and intercellular substances.

Table 5: Different types of connective tissue.

unformed connective tissue	formed connective tissue
mesenchyme	tendons and ligaments
mucous connective tissue	cartilage
spinocellular connective tissue	bone
reticular connective tissue	dentin
loose connective tissue	
dense connective tissue	
adipose tissue	

2.4.1.1 Connective Tissue Cells

There are different types of connective tissue cells:

- fixed connective tissue cells, which are attached to a certain place, for example fibrocytes, adipocytes, reticulum cells and
- mobile connective tissue cells, for example macrophages, lymphocytes, plasma cells, and granulocytes. The mobile connective tissue cells belong predominantly to the immune system.

Fixed connective tissue cells stabilize the tissue and provide the matrix for the exchange of metabolites. Mobile connective tissue cells are able to change their positions but they do not take part in the production of intercellular substances.

2.4.1.2 Intercellular Substances - Extracellular Matrix

The intercellular substances fill the free spaces in the tissue and consist mainly of:

- fibers of different structures and physical properties (formed intercellular substance),
- amorphous ground substance and
- interstitial fluid.

Collagen fibers, reticular fibers and elastic fibers are the different types of fibers of the formed intercellular substance. Collagen fibers are the main component of the loose and the dense connective tissue (see Table 5). The mechanical properties of the connective tissue are determined by the arrangement of the collagen fibers. The reticular fibers generate a

scaffold of fibers in hematopoietic (blood-forming) organs. They are found on the surface of muscle cells, capillaries and some epithelial cells. The reticular fibers give the tissue a certain stiffness. The elastic fibers are cross-linked and form a three dimensional network. Normally, elastic fibers are found together with collagen fibers. In the lung the amount of elastic fibers is relatively high. The elasticity of the tissue is defined by these fibers.

The amorphous ground substance consists mainly of proteins and polysaccharides. The strength of the intercellular substance depends on the degree of polymerization of the polysaccharides.

The interstitial fluid is predominantly bound to the amorphous ground substance and forms a hydrational shell there. The amount of mobile interstitial fluid is very small and has a similar composition like blood plasma (see Section 2.3). A part of the blood plasma filtrates from the arterial part of the capillaries into the surrounding tissue where it becomes the interstitial fluid. Compared to blood plasma the concentration of proteins is lower in the interstitial fluid (Schmidt and Lang (2007) [87]).

2.4.2 Pulmonary Tissue

The loose connective tissue will be called stroma if it connects the individual parts of an organ. In the case of the lung these individual parts are the lobules, bronchi, bronchioles and alveolar sacs. The stroma contains mainly collagen fiber bundles. The number of elastic and reticular fibers is smaller. The wide intercellular spaces, the large number of mobile connective tissue cells, and large amounts of amorphous ground substance are characteristic for the loose connective tissue of the lung. An illustration of the stroma of the lung can be seen in Figure 5.

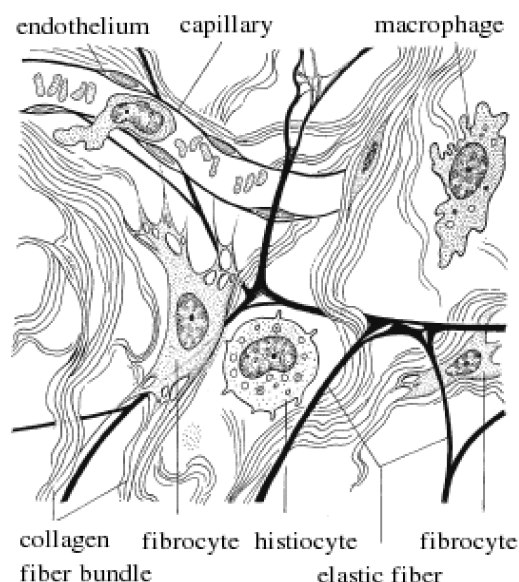


Figure 5: Loose connective tissue (adapted from Schiebler et al. (1999) [84] with kind permission from Springer Science+Business Media).

2.5 Characteristics of Tumors

The expression tumor stands for a swelling or lesion due to an abnormal growth of previously normal cells. The abnormal proliferation of cells (neoplasia) results in a structure known as a neoplasm (Reiche (2003) [79]).

A tumor can be benign or malignant. A benign tumor pushes the surrounding tissue away, but it does not invade other tissues and does not seed to other parts of the body via the lymphatics or the bloodstream (metastasis). A malignant tumor is also called cancer. This kind of tumor is harmful and potentially lethal because the malignant tumor locally erodes the tissue and spreads either by direct growth or by metastasis (Marcovitch (2005) [68]). The malignant cells are characterized by the following six capabilities, the hallmarks of cancer according to Hanahan and Weinberg (2000) [41]:

- the ability to evade apoptosis,
- the self-sufficiency in growth signals,
- the insensitivity to anti-growth signals,
- the sustained angiogenesis,
- the limitless replicative potential and
- the invasion of tissue and metastasis.

The cancer is classified according to the organ of its origin as well as the type of cell from which it is derived:

- carcinoma: A type of cancer developing from cells found in the surface layer of an organ (epithelial tissue).
- sarcoma: Sarcomas are malignant tumors of the connective tissue.
- lymphoma and leukemia: These tumors are derived from hematopoietic cells.
- blastoma: Blastoma is a tumor that arises in the embryonic tissue.

A solid tumor is spatially heterogeneous with large differences in the vasculature. The tumor vasculature varies in function and morphology from the vasculature in the normal tissue. The blood vessels of the tumor are larger in size and more permeable. The tumor vasculature has pores between 100 and 2000 nanometers, whereas the pore size of the normal vasculature is between two and six nanometers (Dreher and Chilkoti (2007) [31]).

A large tumor can be divided into three regions:

- a necrotic region in the tumor core,
- a semi-necrotic region and
- a well vascularized region in the outer border area.

Most of the cells are dead in the center of the tumor, the necrotic core. The outer region of the tumor has rapidly dividing cells, a large blood supply and an abundance of exchange vessels (Baxter and Jain (1989) [18]). Due to an inadequate supply with nutrients, cells of the semi-necrotic region enter the G_0 -phase (see Section 2.6.1). They are quiescent. However, these cells can start dividing again. Cytotoxic therapeutic agents cannot affect quiescent cells. In consideration of this fact, a single chemotherapy will never be successful (Dingermann et al. (2002) [29]).

Small tumors (tumor diameter smaller than two millimeters) are perfused by the vasculature that originates from the surrounding host tissue. If a small avascular tumor exceeds this critical diameter, tumor-induced angiogenesis will occur, because the normal tissue vasculature is no longer able to support the growth of the tumor. Angiogenesis is defined as the process of new blood vessel development from an existing vasculature through endothelial cell sprouting, proliferation and fusion (McDougall et al. (2006) [70]).

The extracellular matrix of a tumor is characterized by (Jain (1987) [50]):

- a large interstitial space,
- a high collagen concentration,
- a low proteoglycan and hyaluronate concentration,
- a high interstitial fluid pressure,
- an absence of an anatomically well-defined, functional lymphatic network and
- a large hydraulic conductivity.

The physiological functions of the extracellular matrix in the normal tissue are to stabilize the spatial and functional relations between the cells, to pose as a barrier to bacterial invasion and to regulate the transport of macromolecules through the interstitium. However, the amorphous ground substance of the tumor tissue is seen as the source of the physical resistance for the drug transport due to the high collagen concentration (Jang et al. (2003) [54]).

The adenocarcinoma, the squamous carcinoma, the large-cell carcinoma and the small-cell carcinoma comprise 80 percent of all known lung cancers. The adenocarcinoma is a tumor that originates in glandular tissue and grows mainly in the pulmonary periphery. The squamous carcinoma is usually found in the lung center, either in a lobe or in one of the bronchi. It can grow to large sizes and forms cavities in the lung. The squamous cells are formed from the reserve cells. These are round cells that replace injured or damaged cells in the epithelium of the bronchi. The large-cell carcinomas are all tumors that cannot be identified as squamous cell cancers or adenocarcinomas. They occur very seldom and have a huge necrotic core. The large cells are the characteristic feature of this cancer. The small-cell carcinoma is characterized by a rapid and invasive growth. Therefore, the process of metastasis starts very soon (Komietzko et al. (1994) [57]).

2.6 Idea of the Cancer Cell-Selective Apoptogenic Therapy

From animal experiments it is known that a certain dose rate of a cytotoxic therapeutic agent will lead to the cell death of a relatively constant fraction of cancer cells. Normally 99.99 percent of the tumor cells will undergo cell death. For a tumor with about 10^{11} cells this means that 10^7 cells will survive the treatment. Therefore, the tumor should be treated as early as possible. However, most of the cancer diseases cannot be diagnosed before the tumor has reached a certain size. Assuming the development of a tumor from a single, malignant cell and an exponential growth behavior of the cell, the tumor reaches two centimeters in size after 30 duplications (10^9 cells). Depending on the type of cancer, this can take one day, two weeks, several months, or more than one year. A tumor consisting of 10^9 cells needs only ten further duplications to reach the critical tumor mass of 10^{12} cells. Now the tumor has a diameter of 20 cm and this leads to the death of the patient in most cases. Three quarters of the time, from the cancer development to the death of the patient, the tumor will not be diagnosed (Dingermann et al. (2002) [29]). There is only a very limited time frame for a successful cancer therapy. The large majority of today's cancer therapies are based on the removal of solid tumor masses by surgery, and a plethora of physical and chemical treatments like chemo- and radiotherapy, that induce the death of all particularly sensitive or rapidly growing cells. These approaches are variously combined in order to optimize the therapeutic efficiency. It is common knowledge that today's cancer therapies have serious side effects. One reason for this is that neither cancer cells nor the cancer cause are directly targeted. A new approach in cancer therapy is the development of a treatment that targets the cause of a cancer. The TRAIL based apoptogenic therapy seems to be a great promise in tumor targeting therapy. It combines high cell killing potential with tumor cell selectivity.

2.6.1 Explanation of the Cell Cycle

A cell proliferates by a tightly linked series of events (see Figure 6). These events can be divided in two periods: the interphase and the M-phase. The interphase consists of the G_0/G_1 -phase, the S-phase and the G_2 -phase. A fully differentiated cell only rarely divides or not at all. It leaves the G_1 -phase and enters the G_0 -phase, the so-called quiescent state of a cell. During the two other G-phases, G_1 and G_2 (G indicating gap), the cell has time to grow and it is ensured that the preparations for the subsequent S-phase or M-phase are finished. The DNA of the cell is duplicated during the S-phase (synthesis phase). The M-phase starts with the division of the nucleus, the so-called mitosis. The cell division is complete after the division of the cytoplasm, the cytokinesis. The progression through the cell cycle is regulated by the assembly of the single phases and the activation of the cell cycle regulatory complexes comprised of cyclins and cyclin-dependent protein kinases (Cdks) (Alberts et al. (2004) [8]). To initiate a particular step in the cell cycle, the protein kinases are activated and deactivated by the binding of the cyclins and additional phosphorylation. The enzymatic activity of the Cdks rises and falls in a cyclic manner due to the cyclic concentration variations of the proteins cyclins during one cell cycle. Cyclins do not have to be enzymatically activated themselves. Further, two checkpoints in the G_1 - and G_2 -phase guarantee the right chronological sequence of the events during one cell cycle and give the cell the possibility to

repair DNA damages before and after the replication of the DNA. At these checkpoints the cell cycle can be stopped and will not enter the next phase of the cell cycle until the cell is prepared. The G_1 checkpoint ensures favorable extracellular conditions for cell proliferation and an intact DNA. Unfavorable extracellular conditions lead to a slowed progress through the G_1 -phase and sometimes the cell enters a specialized resting state, the G_0 -phase. Before the M-phase starts, the G_2 checkpoint guarantees that damaged DNA is repaired and the DNA duplication is complete (Alberts et al. (2004) [7]).

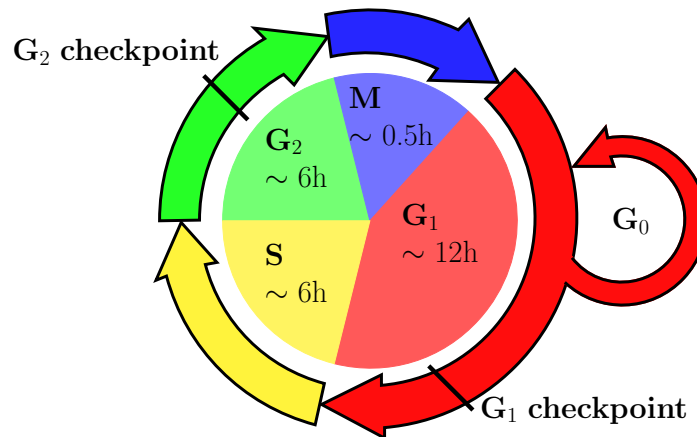


Figure 6: Phases of the cell cycle (the information about the duration of the single phases is taken from Koolman and Röhme (2009) [58]).

If the cells divide with a defect in the DNA (deoxyribonucleic acid) this process can cause cancer or other diseases in the human organism. Therefore, the cells with a DNA defect try to induce the programmed cell death (apoptosis) to stop the replication of the genetic misinformation.

2.6.2 Process of Apoptosis

Apoptosis is a process in which the cells actively participate in their own death. It is a programmed cell death in multicellular organisms. During the apoptosis the cell starts to shrink and gets denser. The cytoskeleton and the nuclear membrane collapse and the DNA is fragmented. The cell surface is changed in such a way that the moribund cell is phagocytized before the intracellular content can be released into the surrounding tissue. Therefore, the programmed cell death does not cause acute inflammation reactions in the body.

Necrosis, the second cell death mechanism in multicellular organisms, always leads to inflammation reactions. Necrosis serves to remove damaged cells from an organism and is a passive process. This kind of cell death is not based on, and regulated by, cell signals. During the necrosis the cell and the mitochondria swell. This causes the rupture of the membranes and thus the inflammation in the organism.

Table 6 shows the different characteristics of the two major cell death processes: apoptosis and necrosis.

Table 6: Different characteristics of the two cell death processes.

apoptosis	necrosis
membrane blebbing, no loss of integrity	loss of membrane integrity
shrinking of cytoplasm	swelling of cytoplasm and mitochondria
alteration of membrane asymmetry	preservation of membrane asymmetry
condensation of nucleus	-
mono- and oligonucleosomal length fragmentation of nuclear DNA	random digestion of DNA
ends with fragmentation of cell into smaller bodies	ends with total cell lysis
activation of caspases	-
involves two different pathways	-
no inflammatory response	inflammatory response

The apoptosis can be triggered by endogenous stimuli, such as the deprivation of the growth factor, or by exogenous stimuli, like the ultraviolet- and the γ -irradiation or other DNA damaging agents. The programmed cell death is based on the cysteine proteases, the so-called caspases (c for cysteine and asp for aspartic acid). The caspases are enzymes that are involved in the digestion of long protein chains into short fragments. They cleave the target proteins at specific aspartic acids. The inactive form of the caspase, the procaspase, is present in the cytosol and is activated by the proteolytic cleavage at specific aspartate residues. Each caspase molecule is able to activate other procaspases. In this way, an initial activation of a small number of procaspase molecules can lead, via an amplifying chain reaction (a cascade), to the explosive activation of a large number of procaspase molecules. The different properties of the caspases allow the classification of these enzymes into the initiators (caspase-8, caspase-9 and caspase-10) and the executioners (caspase-3, caspase-6 and caspase-7) of the apoptosis (Alberts et al. (2004) [7]).

The programmed cell death can be activated in two ways: extracellular (death receptor pathway) or intracellular (mitochondrial apoptotic pathway). The procaspase activation from the outside of the cell is realized by the activation of the death receptors on the cell surface. A death receptor is a transmembrane protein and consists of an extracellular ligand-binding domain, a single transmembrane domain, and an intracellular death domain. The Fas ligand binds to the death receptor protein Fas on the surface of the target cell. This leads to a aggregation of the Fas receptors. The clustered Fas proteins recruit the intracellular adaptor proteins FADD (Fas-associated death domain). These adaptor proteins bind and aggregate procaspase-8 molecules, procaspase-10 molecules, or both, that cleave and activate one another. The complex consisting of the death domain of the Fas death receptor, the intracellular adaptor protein FADD and the procaspase-8 or -10 is termed death-inducing signaling complex (DISC). The initiator caspase-8 and caspase-10 activate downstream procaspases to induce apoptosis (see Figure 7) (Alberts et al. (2004) [7]).

The cell can also kill itself by triggering the procaspase activation from within the cell: the

intracellular pathway of apoptosis (see Figure 8). This will occur if the cell is damaged or stressed. With the help of Bcl proteins like Bad, Bak, Bax and Bid, the outer mitochondrial⁶ membrane is permeabilized. This causes the release of cytochrome c into the cytosol, the intracellular fluid. The cytochrome c binds and activates an adaptor protein Apaf-1 and Apaf-1 activates procaspase-9. The caspase-9 cleaves downstream caspases that lead to apoptosis (Alberts et al. (2004) [8]).

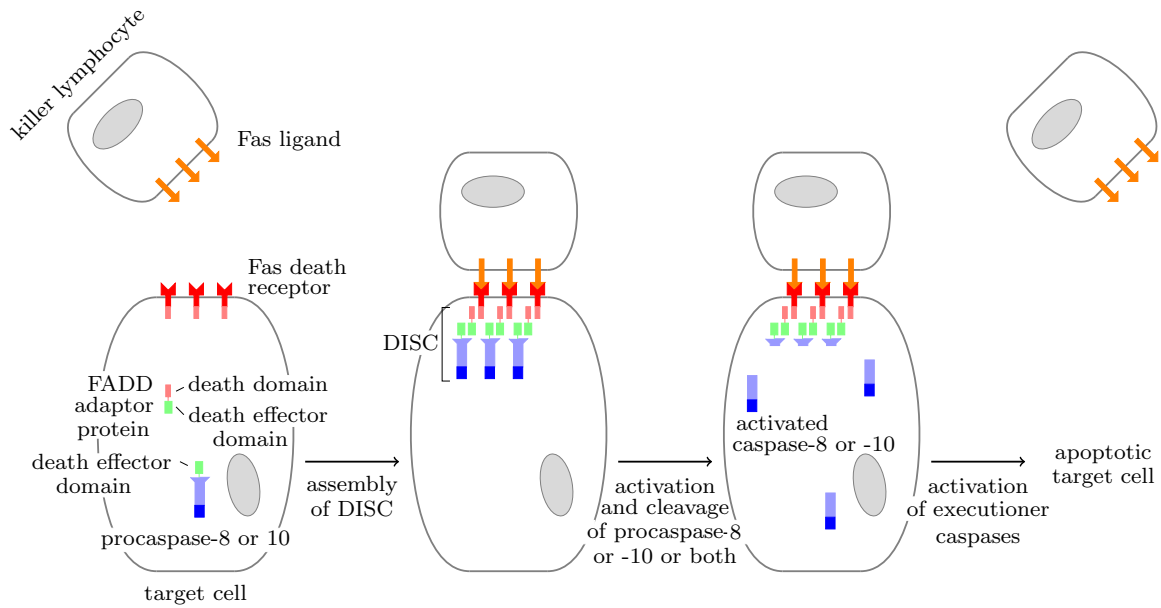


Figure 7: Extracellular pathway of apoptosis (according to Alberts et al. (2004) [7]).

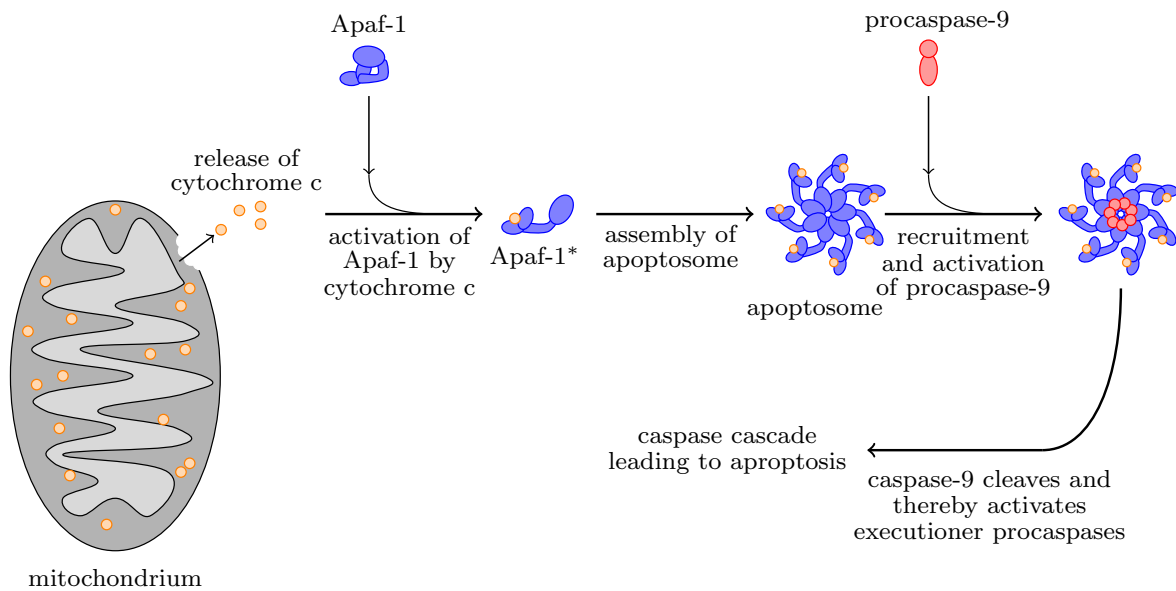


Figure 8: Intracellular pathway of apoptosis (according to Alberts et al. (2004) [7]).

⁶The mitochondrion is a membrane-enclosed organelle - a subunit of the cell (Koolman and Röhm (2009) [58]).

2.6.3 Induction of the Cancer Cell-Selective Apoptosis by TRAIL

The new therapeutic concept, the induction of cancer cell-selective apoptosis by TRAIL, is similar to chemotherapy at inducing an efficient cancer cell kill but has a large, if not exclusive, selectivity for tumor cells. This concept uses a system already existing in the human body that is involved in the tumor surveillance by the innate immune system.

The abbreviation TRAIL stands for tumor necrosis factor (TNF)-related apoptosis-inducing ligand. TRAIL is a type II transmembrane protein and member of the TNF-superfamily. The TNF-superfamily refers to a group of cytokines that are essential in host defense mechanisms and the control of inflammatory processes (Hehlgans and Pfeffer (2004) [44]). A transmembrane protein is located on the cell surface. If it binds to a receptor this protein will be activated and will start a cascade of intracellular signals.

The TRAIL molecule is a homotrimer that can bind to three single receptors. The binding of TRAIL to the death receptors DR4 (TRAIL-R1) and DR5 (TRAIL-R2) results in the apoptosis of the cancer cell. The TRAIL molecule can also bind to three other receptors: DcR1 (TRAIL-R3), DcR2 (TRAIL-R4) and a soluble receptor called osteoprotegerin (OPG). These three receptors act as decoys. As they have a close homology to the extracellular domains of DR4 and DR5, but are not able to induce the apoptosis. The DcR2 receptor has a truncated, non-functioning death domain and the DcR1 receptor lacks the transmembrane and the death domain. The overexpression of these two receptors protects the cell from the apoptosis induction by TRAIL (LeBlanc and Ashkenazi (2003) [61]).

The structure of the TRAIL molecule bound to receptor molecules is shown in Figure 9. The receptor subunits are shown in gray, the three TRAIL subunits are colored, and the single zinc atom is represented by the red sphere. The zinc atom is essential for optimal biological activity like solubility and stability.

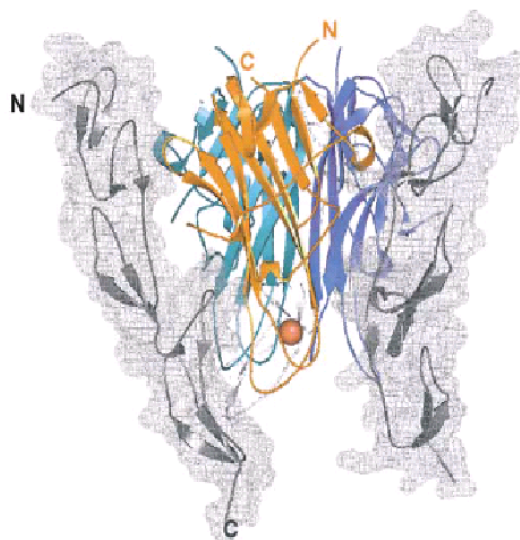


Figure 9: Structure of the TRAIL molecule (adapted by permission from Macmillan Publishers Ltd: [Cell Death and Differentiation] LeBlanc and Ashkenazi (2003) [61], copyright 2003).

Figure 10 illustrates the apoptotic signaling cascade induced by the TRAIL molecule. The binding of TRAIL to DR4 or DR5 results in the aggregation of the receptors and the death inducing signaling complex DISC is formed. The adapter protein FADD (Fas-associated death domain) moves and interacts with the death domain of the receptor. FADD binds the procaspase-8 molecule. This leads to the activation of caspase-8 and so the caspase cascade and the programmed cell death is initiated by the activation of executioner caspases like caspase-3 (Falschlehner et al. (2007) [35]).

Additionally, caspase-8 also cleaves Bid and this starts the intrinsic pathway of apoptosis (see Figure 10). Thus, the intracellular pathway of apoptosis is connected to the extracellular pathway and can amplify the extracellular pathway. The truncated Bid (tBid) interacts with Bax and leads to the release of cytochrome c and Smac. The cytochrome c activates the adaptor protein Apaf-1. Further, cytochrome c binds to the activated adaptor protein Apaf-1 and procaspase-9 forming the apoptosome⁷ which activates caspase-9. Then, the caspase-9 cleaves downstream caspases that leads to the apoptosis of the cell. The protein Smac that is also released from the mitochondrion into the cytosol promotes the cell death by blocking the inhibitor protein XIAP (X-linked inhibitor of apoptosis). Normally, XIAP inactivates caspase-3 by binding to the activated form of caspase-3 and can so delay or even stop the

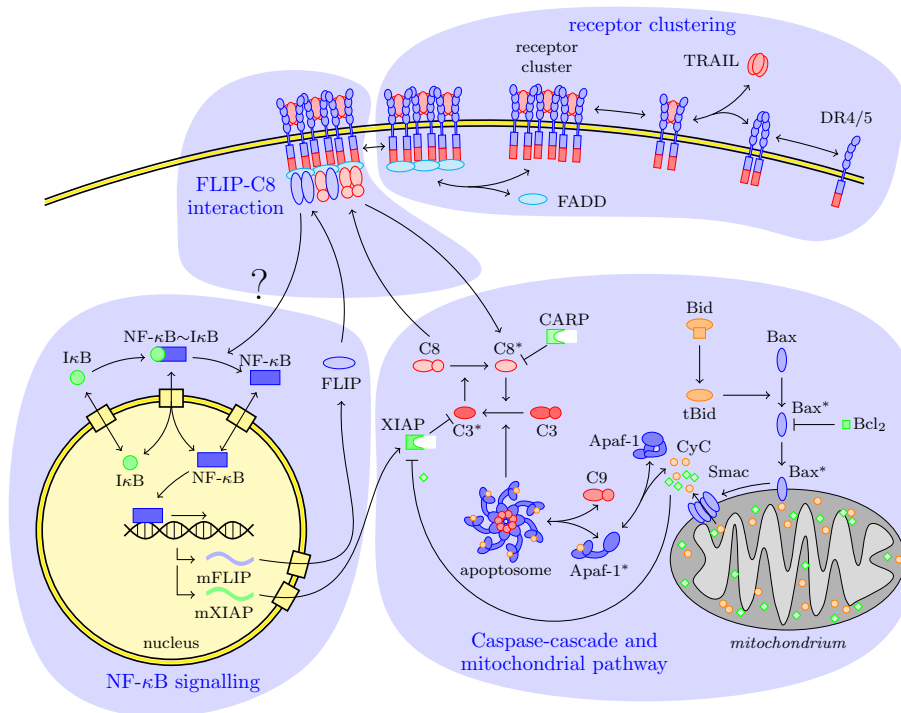


Figure 10: TRAIL signal transduction pathway (adapted by permission from J. Hasenauer, Institute for Systems Theory and Automatic Control - University of Stuttgart).

⁷Complex consisting of Apaf^{*}-1, cytochrome c and procaspase-9; some scientists already use the term apoptosome for the complex containing only Apaf^{*}-1 and cytochrome c (Alberts et al. (2004) [7])

caspase cascade leading to the death of the cell. The proteins Bcl₂⁸ and CARP⁹ also counteract the triggering of the apoptotic signaling pathway by blocking the activation of Bax and the inactivation of caspase-8. A further protein that inhibits the apoptotic signaling cascade is FLIP. FLIP competes with the procaspase-8 proteins for the binding to the adapter protein FADD. Therefore, FLIP reduces the recruitment of procaspase-8 to the death inducing signaling complex DISC and the propagation of apoptotic signals (Cretney et al. (2007) [27]). Until now, the activation of the NF- κ B signaling pathway by TRAIL and its influence on the cell fate by enhancing cell development or proliferation are not well understood (symbolized by the question mark in Figure 10). NF- κ B is known to play an important role in the regulation of the immune reaction, cell proliferation and apoptosis. The predominance of the TRAIL-induced anti- or proapoptotic effects of NF- κ B seems to be dependent on the different cell types. The NF- κ B signaling pathway regulates the expression of the anti-apoptotic proteins XIAP and FLIP (Falschlehner et al. (2007) [35]).

2.6.4 Use of the Bifunctional Fusion Protein scFv-TRAIL

To increase further the therapeutic efficacy and selectivity of TRAIL, the TRAIL molecule is combined with a monoclonal antibody that recognizes cell surface markers specific for cancer cells or tumor stroma cells. This allows TRAIL to exert its apoptotic action only within the tumor. A single-chain fusion protein scFv-TRAIL is created that binds to the epidermal growth factor receptor (EGFR). Fusion proteins are by definition synthetic molecules that do not occur in this composition in nature. Monoclonal antibodies are antibodies which have been artificially produced to recognize a single epitope of a specific antigen. They only bind to their target antigens. In general, antibodies are proteins that attach to foreign material in the body and are released by certain cells of the immune system. Any foreign substance that can induce the immune system to release antibodies is called an antigen. The epidermal growth factor receptor is a cell surface receptor and belongs to the ErbB family. The ErbB protein family consists of four structurally related receptor tyrosine kinases: ErbB-1 (EGFR), ErbB-2, ErbB-3 and ErbB-4. EGFR is overexpressed in a number of cancers, including lung tumors. The monoclonal antibodies block the extracellular ligand binding domain of the EGFRs. If the binding sites are blocked the signal molecules can no longer attach there and activate the tyrosine kinase. The tyrosine kinase is an enzyme that is important for the signal transduction and so the tumor proliferation can be stopped.

⁸This protein belongs to the Bcl₂ protein family. The Bcl₂ protein family consists of about 20 members that can be classified into four groups: the “effectors” Bax or Bak whose oligomerization creates pores in the mitochondrial membrane; the “inhibitors” of the effectors such as Bcl₂, Bcl_{xL} or Bcl_w; the “activators” of Bax and Bak as Bid and Bim; and the “sensitizers” for example Bad, Bik and Noxa which counteract antiapoptotic Bcl₂-like proteins (Spencer and Sorger (2011) [93]).

⁹CARPs (caspase-8 and caspase-10 associated RING proteins) are proteins that interact with caspase-8 and caspase-10 and provide the cancer cells with a resistance mechanism against death ligand-induced apoptosis by the inhibition of the caspase activation (McDonald and El-Deiry (2004) [69]).

3 Model Concept for Describing Cancer-Therapeutic Transport in the Lung

The basis of every numerical simulation of a physical process is the development of a suitable model concept. The model concept reduces the complex system and its physical processes to the relevant ones. The following section introduces the developed model concept for describing cancer-therapeutic transport in the lung, which is a multi-scale problem. Further, the theoretical fundamentals on which the developed multi-scale model is based on are briefly summarized.

3.1 Definition of Basic Terms

Phase

The term phase stands for a region with a homogeneous chemical composition and physical state. Normally, a phase is either solid, liquid or gaseous. Under the assumption of a thermodynamic equilibrium, the Gibbs' phase rule defines the maximum number of coexisting phases.

Component

A phase is composed of at least one component. A component can be a pure chemical substance or a combination of different chemical substances with similar properties such as the pseudo-components interstitial fluid or blood.

Mass- and Mole Fraction

The composition of a multi-component system can be described by mass or mole fractions. The mass fraction of a component C in a phase α , X_α^C , is defined as the mass m_α^C of the component C in the phase α , divided by the total mass of all components n in the phase $\sum_{k=1}^n m_\alpha^k$:

$$X_\alpha^C = \frac{m_\alpha^C}{\sum_{k=1}^n m_\alpha^k}. \quad (1)$$

Similarly, the mole fraction of the component C in the phase α can be calculated by:

$$x_\alpha^C = \frac{n_\alpha^C}{\sum_{k=1}^n n_\alpha^k}, \quad (2)$$

where n_α^C is the number of moles of the component C in the phase α . The sum of all the mass or mole fractions of a phase add always up to one. In this thesis, mole fractions are used to describe the composition of the considered phases.

Reaction Rate

The reaction rate represents the number of particles that are consumed during a chemical reaction per time. Among others, the reaction rate depends on the concentration of the reactants, the temperature and the presence of catalysts.

3.2 Definition of Structures and Scales

There are two main possibilities to describe the flow and transport processes in a biological system: the molecular approach and the continuum approach. The molecular approach considers the movement of single molecules or particles and their interactions under external influences. A continuum approach assumes that the fluid is continuously distributed over the whole space. The continuum approach is based on the averaging over a huge amount of molecules. Due to the high number of molecules in fluids, the molecular approach is inappropriate for the solution of fluid flow problems (Helmig (2008) [46]). In this thesis, the fluid phases considered by the vascular graph model and the alveolus model are always described with a continuum approach.

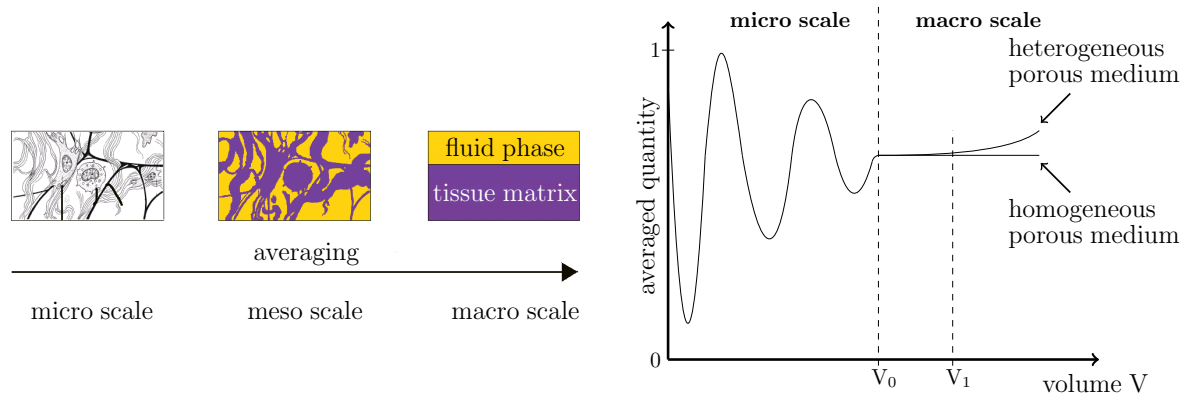


Figure 11: Left: from a biological tissue towards a porous medium. Right: definition of the representative elementary volume according to Bear (1972) [19].

The structure of the biological system can also be considered either in a discrete or a continuous fashion. In the case of the VGM, the structure of the pulmonary circulation is described with a discrete approach, whereas the alveolus model uses a continuum approach to represent the structure of the capillary bed and the pulmonary tissue around an alveolus. Figure 11 shows the continuum approach for the pulmonary tissue on the different scales. The left picture in this figure shows the pulmonary tissue on the micro scale. The individual components can be easily identified. The right picture belongs to the macro scale. On the macro scale it is no longer possible to identify the discontinuities that can be seen on the micro scale. The connection between the micro and the macro scale is the so-called meso scale. On

the meso scale the solid components of the tissue are united and build the porous network. It is no longer differentiated between the individual solid components. The pores are filled with the interstitial fluid. To come from the micro scale to the macro scale an averaging of the properties of the porous medium within a representative elementary volume (REV) is necessary. The representative elementary volume has to be chosen in such a way that the averaged property is not influenced by the REV, see Figure 11. This is the case between V_0 and V_1 . If the REV is smaller than V_0 the averaged quantity will show strong oscillations. For volumes greater than V_1 the averaged quantity will only change in a heterogeneous medium. However, the representative elementary volume should always be smaller than the model domain, so that the characteristic properties of the material points do not get lost. The averaging process creates new effective parameters like porosity, permeability or tortuosity.

3.3 Definition of Effective Parameters

As already mentioned in Section 3.2, an averaging of the properties of the porous medium within a representative elementary volume is necessary to come from the micro scale to the macro scale. This averaging process creates new effective parameters like the porosity or the permeability. In the following, all effective parameters relevant for this thesis will be explained.

Porosity

The porosity ϕ is defined as follows:

$$\phi = \frac{\text{volume of the pore space within the REV}}{\text{total volume of the REV}}. \quad (3)$$

Due to the fact that the porosity ϕ is an effective parameter, it exists only on the macro scale. On smaller scales, the pore space has to be described discretely.

Permeability

The permeability of a porous medium characterizes the ability of the material to allow fluids to pass through it. It is a measure of the resistance of a porous matrix to the flowing fluid. The intrinsic permeability \mathbf{K} is derived from Darcy's law (see Equation (20)) and is defined as follows:

$$\mathbf{K} = -\frac{Q \mu L}{\Delta p A}, \quad (4)$$

where Q represents the flow rate of a fluid with the dynamic viscosity μ through a porous medium with the flow area A over the length L driven by the pressure difference Δp (Class (2001) [25]). The intrinsic permeability \mathbf{K} is strongly related to the hydraulic conductivity \mathbf{k}_f :

$$\mathbf{k}_f = \mathbf{K} \frac{\rho_{mass} g}{\mu}, \quad (5)$$

where ρ_{mass} is the density of the fluid and g is the gravitational constant. The intrinsic permeability \mathbf{K} and the hydraulic conductivity \mathbf{k}_f are both tensors. The intrinsic permeability \mathbf{K} is only a property of the porous medium, whereas the hydraulic conductivity \mathbf{k}_f is related to the porous substance and the flowing fluid.

Tortuosity

The tortuosity τ takes into account the shape of the pores and characterizes the way in which the pores of the considered material are connected. Tortuosity is physically defined as the ratio of the length of the actual path of a traveled species through a porous medium to the unit length of this medium (Shen and Chen (2007) [89]). The tortuosity characterizes the degree of sinuousness of the routes of transport within the porous medium.

In this thesis, the solid matrix of the considered porous media is assumed to behave as a rigid material. Therefore, the effective parameters porosity, permeability and tortuosity are not affected by pressure changes in the model domain. By the comparison of a rigid model versus a linear-elastic model for modeling convection-enhanced drug delivery into brain tissue, Støverud and coworkers have shown that there is no significant difference between the resulting concentration distribution within the brain tissue using the rigid or the linear-elastic model (Støverud et al. (2011) [94]).

3.4 Definition of Fluid Properties

Density

The physical quantity density is influenced by the composition of the considered phase, the temperature and the pressure. It can be distinguished between the mass density ρ_{mass} and the molar density ρ_{mol} of a phase. The mass density is defined as:

$$\rho_{mass} = \frac{m}{V}, \quad (6)$$

where m is the mass, and V is the volume. The molar density is the ratio of the number of moles n per volume V :

$$\rho_{mol} = \frac{n}{V}. \quad (7)$$

Knowing the molar density of a phase and its composition, the mass density of this phase can be obtained by the following relationship (Class (2001) [25]):

$$\rho_{mass} = \rho_{mol} \sum_{k=1}^n (x^k M^k), \quad (8)$$

where x^k represents the mole fraction of the component k in the considered phase, and M^k is the molar mass of this component k .

Viscosity

The term viscosity describes the resistance of a fluid against shear or tensile stress. The dynamic viscosity μ is defined as the ratio of the shear stress τ_s divided by the velocity gradient $\frac{dv}{dy}$. Hence, the shear stress τ_s is proportional to the velocity gradient and the proportional factor is the dynamic viscosity μ :

$$\tau_s = \mu \frac{dv}{dy}. \quad (9)$$

This equation can be obtained from an experiment. The experimental setup is outlined on the left picture in Figure 12. A fluid is arranged between two parallel plates with the distance y . The upper plate is moved with a constant velocity v due to the acting force F . It is assumed that the fluid adheres at the plates. Thus, the fluid at the border to the fixed plate has the velocity zero and the fluid at the border to the moving plate has the velocity v . This causes that the fluid shears off into single layers and a velocity gradient is generated between the two plates.

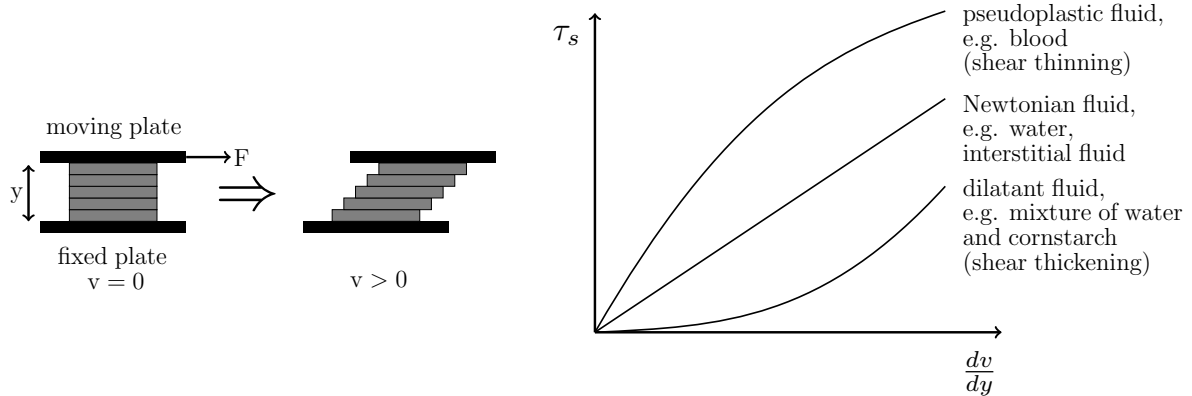


Figure 12: Left: definition of the shear stress. Right: flow behavior of different fluids.

The force F that is necessary to move the upper plate with the velocity v is proportional to the plate area A and indirectly proportional to the velocity gradient $\frac{dv}{dy}$:

$$F \sim A \frac{dv}{dy}. \quad (10)$$

The proportional constant is given by the dynamic viscosity μ and so the following equation can be obtained:

$$F = \mu A \frac{dv}{dy}. \quad (11)$$

The quotient $\frac{F}{A}$ is equal to the shear stress τ_s , and thus Equation (9) follows from the experiment. The quotient of the dynamic viscosity μ and the mass density ρ_{mass} is called kinematic viscosity ν . On the right picture in Figure 12, different kind of fluids exhibiting various flow behaviors are shown.

3.5 Definition of Processes

The main task of the conceptual model is to identify the relevant processes of the described system. In the following, a summary of all possible processes is given.

Advection

The term advection describes the transport of a substance in a stationary flow field. The transport direction during advection is determined by the direction of the flow field. The driving force for this process is a pressure gradient.

Diffusion

Diffusion is a transport process originating from a concentration gradient. The molecules move from areas of high concentration to areas of low concentration. Contrary to the advective transport, the molecules spread equally in all directions. The diffusive flux J of a solute is described by Fick's first law:

$$J = -D\nabla c, \quad (12)$$

where D represents the diffusion coefficient and c the concentration of the transported substance.

In a porous medium, there are different types of diffusion, for example, molecular diffusion, Knudsen diffusion or surface diffusion. In this thesis only molecular diffusion is considered. The molecular diffusion in a porous medium is also described by Fick's first law. However, the diffusion coefficient D is replaced by the so-called effective molecular diffusion coefficient D_{eff} . The effective molecular diffusion coefficient in porous media is always smaller than the values given in literature for common mixtures. The tortuosity τ of the considered porous medium reduces the diffusive flux. The porosity ϕ of the system itself also influences the molecular diffusion in the porous medium. The porous matrix forces the molecules to deviate from their straight diffusion paths (Shen and Chen (2007) [89]). The effective molecular diffusion coefficient D_{eff} is defined as follows:

$$D_{eff} = \hat{\tau} \phi D_{\alpha}^C \quad \text{with} \quad \hat{\tau} = \frac{1}{\tau^2}, \quad (13)$$

where D_{α}^C is the diffusion coefficient of the component C in the phase α and $\hat{\tau}$ is the tortuosity factor. The tortuosity factor is greater than zero and less than or equal to one (Yu and Neretnieks (1996) [103]).

Dispersion

The term dispersion is used to describe the transport of a component due to fluctuations in the velocity field. These fluctuations have different reasons. On the micro scale, the parabolic velocity distribution of the fluid inside the pore channels and the tortuosity of the pore space cause the fluctuations in the velocity field. On the macro scale, dispersion arises from the heterogeneous structure of the porous medium.

Reaction

The last possible process, that can be described by a conceptual model, is the reaction of the single components. The substances come into contact, react, and form a new product. In the human body, the therapeutic agent has several possibilities to react and change its chemical composition: the drug molecule can be metabolized and undergo degradation, bind non specifically to proteins and other components, or bind specifically to the target (Jain (1987) [50]).

3.6 Idea of the Multi-Scale Model

Chapter 2, dealing with the anatomy, the histology and the cardiovascular system of the lung, makes clear that the lung is a complex organ. Based on the medical knowledge about the human lung, a model concept has been developed. This model concept is specialized for an alveolar cell carcinoma. The therapeutic agent is administered via a bolus injection into the blood stream. The developed concept includes the transport of the injected therapeutic agent scFv-TRAIL through the pulmonary circulation, the transition of the dissolved drug molecules from the pulmonary capillaries into the tissue and vice versa, the processes occurring within the pulmonary tissue, and the reaction of the cancer cells to the administered drug. Hence, the description of the flow and transport processes in the lung is a multi-scale problem (see Figure 13). The following three scales are considered:

1. the pulmonary macrocirculation on the organ scale,
2. the capillary bed around an alveolus, the surrounding pulmonary tissue and the alveolar cell carcinoma on the tissue scale, and
3. the tumor cell population and the single cancer cells on the cells scale.

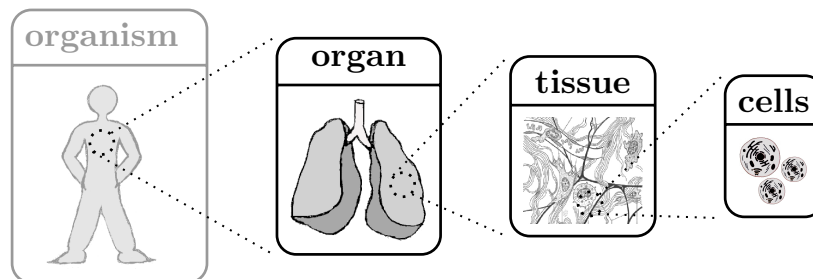


Figure 13: Relevant scales for describing cancer-therapeutic transport in the lung.

Figure 14 depicts the idea of the developed model concept for describing cancer-therapeutic transport in the lung. The relevant processes occurring on these three scales are described by three different simulators that are sequentially coupled to each other.

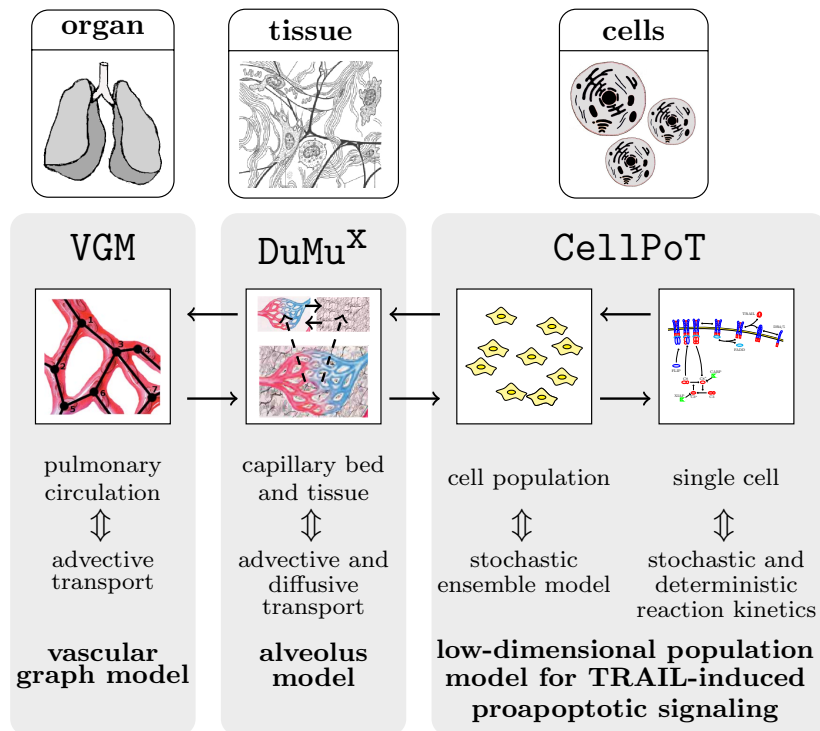


Figure 14: General model concept for describing cancer-therapeutic transport in the lung - solving a multi-scale problem.

The simulation toolbox VGM includes the vascular graph model (VGM, see Chapter 4 and Reichold et al. (2009) [81]). The advection and reaction of the blood-dissolved drug within the non-capillary part of the pulmonary vasculature (arteries, arterioles, venules and veins) are simulated using this vascular graph model. Due to the high flow velocities in the macro-circulation, the diffusive transport of the dissolved therapeutic agent through the arteries, arterioles, venules and veins is neglected. Degradation processes of the administered drug such as micturition and metabolic transformation reactions are included in the vascular graph model. The geometry of the arteries, arteriole, venules and veins is described in a discrete way.

The abundance of pulmonary capillaries (about 1800 capillary segments per alveolus (Renkin et al. (1984) [82]); total number of alveoli: $300 \cdot 10^6$ according to Weibel (1991) [102]) prevents the application of this discrete approach to the capillary bed around an alveolus due to the high computational cost incurred. Therefore, the flow, transport and reaction processes within the capillary bed and the surrounding tissue around a single alveolus are described by the so-called alveolus model instead, which is a double-continuum approach. The structure of the capillary bed and the pulmonary tissue is represented in a continuous fashion using the effective parameters defined in Section 3.3. The double-continuum model (DCM) is implemented in the simulation toolbox DuMu^x, which is a free and open-

source simulator for flow and transport processes in porous media (Flemisch et al. (2011) [36]), to represent the flow, reaction, and transport processes in the alveolar capillary bed, in the surrounding tissue and between this two compartments (see Chapter 5). The double-continuum approach is based on two separated continua: the pulmonary tissue, and the pulmonary capillaries, that are coupled by transfer functions (see Section 5.4). The tissue continuum represents the advective and diffusive transport of the dissolved drug molecules through the interstitial space of the pulmonary tissue. The influence of the lymphatic system on the flow and transport processes and the reaction of the drug molecules with the tissue cells are considered. The capillary bed continuum describes the advective and diffusive transport of the dissolved drug molecules through the microcirculation around an alveolus. As in the vascular graph model, the degradation processes of the administered drug are taken into account. The DCM is also used to represent the tumor regions in the lung.

The processes on the smallest scale, the reaction of the single cancer cell and the tumorous cell population to the administered drug, are modeled with the MATLAB toolbox CellPoT (Cell Population Toolbox; free download from [1]). CellPoT contains a low-dimensional population model for TRAIL-induced proapoptotic signaling ([PMTS]_s) that calculates the percentage of cancer cells undergoing cell death (see Chapter 6) due to the present drug concentration in the tumor cell population. The use of the [PMTS]_s gives information about the therapeutic efficacy of the administered drug.

Figure 15 depicts the scheme about the sequential coupling of the three models introduced in the paragraphs above. The vascular graph model is coupled to the alveolus model and provides the initial and boundary conditions for the pressure p and for the mole fraction of dissolved therapeutic agent x needed for the capillary bed continuum of the DCM. For the realization of the sequential coupling of the alveolus model to the vascular graph model, so-called upscaled edges and nodes are inserted into the computational lattice of the VGM,

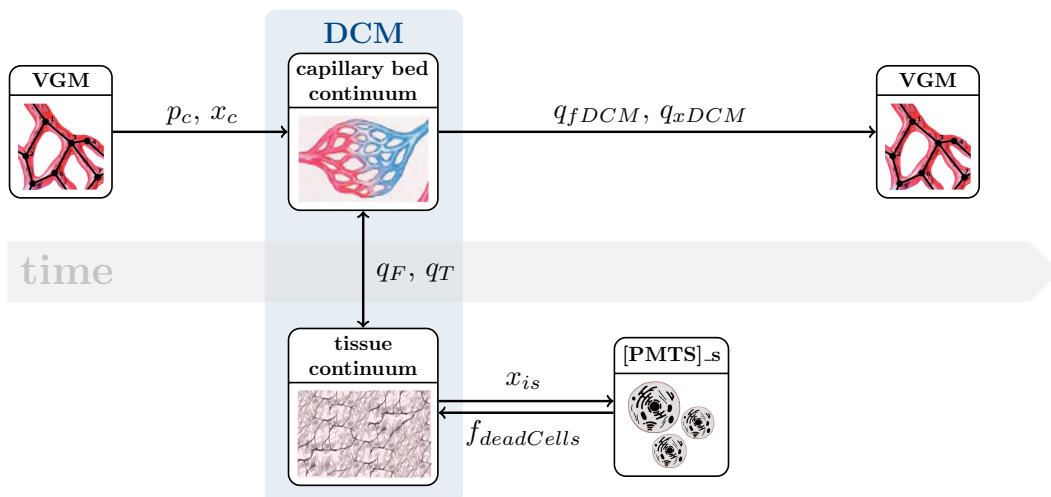


Figure 15: Sequential coupling of the three models for describing cancer-therapeutic transport in the lung.

which represent the capillary bed described by the alveolus model. For every upscaled node contained in the considered vascular graph, the VGM calls the DCM. The administered therapeutic agent can leave the blood stream through the transvascular pathways in the capillary walls. In this way, the VGM blood flow simulations have to be corrected for the loss of therapeutic agent q_{xDCM} and fluid q_{fDCM} by the transit of the dissolved drug molecules and of the blood plasma through the capillary walls into the tissue. The coupling of the alveolus model and the vascular graph model is described in more detail in Section 7.1.

The toolbox CellPoT, containing the low-dimensional population model for TRAIL-induced proapoptotic signaling, is coupled to the free and open-source simulator DuMu^x containing the alveolus model. In this way, the spatiotemporal distribution of the therapeutic agent in the pulmonary tissue is linked with the biochemical reactions occurring on the cells scale. The alveolus model provides the spatial and temporal distribution of the administered therapeutic agent $x_{i,s}$ in the tumorous tissue to the [PMTS]_s. Based on this information, the low-dimensional population model for TRAIL-induced proapoptotic signaling calculates the percentage of cancer cells undergoing cell death $f_{deadCells}$. Further, the amount of dissolved drug molecules in the pulmonary tissue is reduced by the bond of the therapeutic agent to the cancer cells. This information can be either determined by the low-dimensional population model [PMTS]_s, and is incorporated in the alveolus model as a sink term for the mole fraction of dissolved drug, or is directly calculated by the alveolus model. The decision about the model applied for the calculation of the amount of bound therapeutic agent depends on the specific application for which the multi-scale model will be used. A detailed explanation about the coupling of the low-dimensional population model for TRAIL-induced proapoptotic signaling to the double-continuum model is given in Section 7.2.

With the aim of improving the therapy of pulmonary tumors, the developed model concept is the basis for a computational simulation framework that sequentially couples a discrete vascular graph model to a double-continuum model to determine the amount of administered scFv-TRAIL that will reach the tumor cells. Knowing the concentration of therapeutic agent over a certain time interval in the pulmonary tissue, the amount of cancer cells that will undergo cell death is estimated with the help of the low-dimensional population model for TRAIL-induced proapoptotic signaling. The following Chapters 4, 5 and 6 introduce the individual models of the multi-scale model, define the decisive physical, chemical and biological processes for the transport of a therapeutic agent from the blood circuit through the pulmonary tissue to the cancer cells, explain the used system of equations and the made assumptions, and describe the numerical implementation of the mathematical models.

4 Vascular Graph Model (VGM)

The vascular graph model developed by Reichold and coworkers (Reichold et al. (2009) [81]) describes flow and transport processes in vascular networks. Here it is used to compute the spatial and temporal distribution of a therapeutic agent in the pulmonary arteries, arterioles, venules and veins. This chapter gives a brief summary of the VGM and extensions / adaptations of the vascular graph model are explained (for in-depth information see Reichold et al. (2009) [81]).

4.1 General Model Concept

The VGM treats the vasculature as a graph, i.e. a collection of vertices or nodes, connected by edges (see Figure 16). The nodes are the locations at which the vessels bifurcate or end. The edges represent the blood vessels themselves. The diameters of blood vessels vary along their length, typically they are widest at the points of bifurcation. The VGM assigns a mean diameter to each vessel and computes its conductance based on this value.

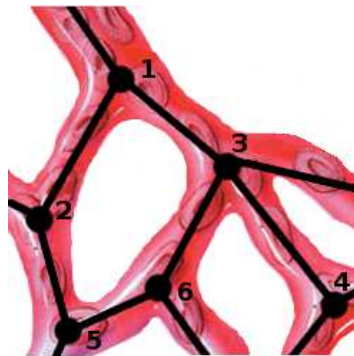


Figure 16: Schematic representation of a vascular graph: a collection of nodes i connected by edges ij .

The blood flow from the right heart ventricle to the alveolar capillaries and the backflow of blood from the capillaries to the heart are modeled using a single-phase two-component (blood and therapeutic agent) scenario. Blood and the therapeutic agent are assumed to be completely miscible and are considered as one homogeneous phase. Further, the fluid phase is assumed to be incompressible. According to Schmidt and Lang (2007) [87], blood is a heterogeneous, non-Newtonian fluid that exhibits pseudoplastic behavior. The interactions of the different blood components, which are the main origin of the blood properties, are accounted for implicitly via a non-constant viscosity that depends mainly on the vessel

diameter and the hematocrit. In-vivo data reported by Lipowsky and coworkers (Lipowsky et al. (1980) [64]) are used to determine the hematocrit in a vessel based on its diameter. In a second step, the blood viscosity within the vessel is computed from the hematocrit value using the relation derived by Pries et al. (1992) [78]. To simplify the description of the complex flow behavior within the blood vessels further, blood flow is treated as a non-pulsating flow and the influence of the vessel bifurcations on the flow is neglected. For the approximation of the flow velocity at the vessel wall, the no-slip condition is used.

4.2 Mathematical Model

If two adjacent nodes (vertices that are connected by an edge, e.g. node 1 and 2 in Figure 16) are at different blood pressure values, blood flow will be induced between them. For every node i of the vascular graph a continuity equation can be formulated:

$$\frac{\partial(\rho_{i,mol} V_i)}{\partial t} + \sum_j F_{ij} + q_{i,fDCM} = 0, \quad (14)$$

where $\rho_{i,mol}$ and V_i are the blood density and the volume term at node i , respectively. The mass flow rate through the pulmonary vessel segment ij is denoted F_{ij} and t designates the time. To a good approximation, it may be assumed that blood is an incompressible fluid. Therefore, $\rho_{i,mol}$ will remain constant unless the blood composition changes significantly. The variable $q_{i,fDCM}$ mediates the coupling of mass flow between the double-continuum model and the vascular graph model. $q_{i,fDCM}$ is zero for every node i of the vascular graph except for the so-called upscaled nodes (for details see Section 7.1).

The mass flow rate between two nodes i and j depends on their pressure difference Δp_{ij} , their geometrical distance Δz_{ij} in the direction of gravitational acceleration g (assumed to act in negative z-direction), the molar fluid density $\rho_{i,mol}$, the mass density of the fluid $\rho_{i,mass}$ and the vessel resistance R_{ij} :

$$F_{ij} = \frac{\rho_{i,mol} (\Delta p_{ij} + \rho_{i,mass} g \Delta z_{ij})}{R_{ij}}. \quad (15)$$

By inserting Equation (15) into the continuity equation (14) for all vertices, one obtains a linear system of equations whose solution yields the vertex pressures. The flow in the pulmonary vasculature can then be computed from the pressure field using Equation (15). The system of equations is linear due to the fact that the coupling variable $q_{i,fDCM}$ is known at the time of solving the equations of the VGM (see Section 7.1).

The distribution of blood in the lung is a function of the cardiac output, gravity, and pulmonary vascular resistance. An average human lung is about 30 cm long from the base (bottom of the lung) to the apex (top of the lung). The pulmonary artery enters each lung

about midway between base and apex. Due to the influence of gravity, most of the blood flows through the lower half of the lung (Des Jardins (2008) [55]). The model captures the gravitational effects, by correcting the blood pressure value of each vertex by $(\rho_{i, mass} g z_i)$, where z_i is the distance of node i to the entry of the pulmonary artery into the lung (see Figure 17). The difference in z of two nodes i and j appears as Δz_{ij} in Equation (15).

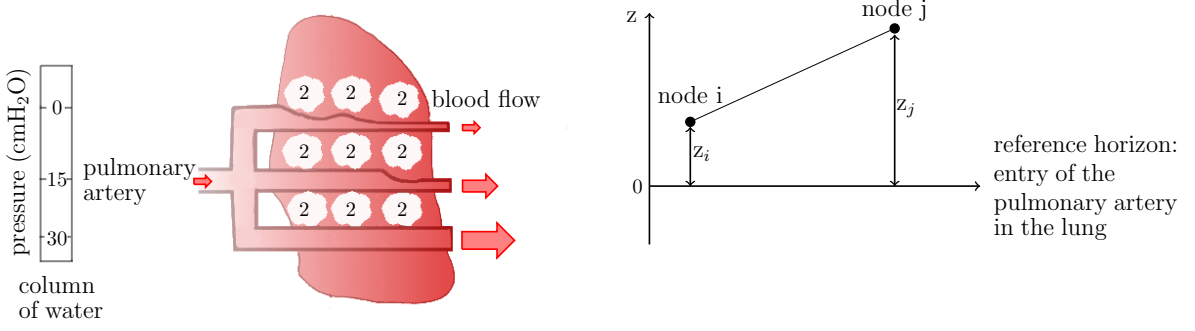


Figure 17: Gravity dependence of the pulmonary blood flow.

The resistance R_{ij} to flow within a pulmonary vessel segment ij is a result of the viscous forces, of the friction between the flowing blood and the vessel wall, as well as of the friction between the different blood components. Assuming that the flow can be described by the Hagen-Poiseuille law (neglecting wall roughness), the resistance of a vessel segment ij can be written as:

$$R_{ij} = \frac{8 \mu_{ij} L_{ij}}{r_{ij}^4 \pi}, \quad (16)$$

where μ_{ij} is the dynamic blood viscosity for the vessel segment ij calculated with the relation derived by Pries et al. (1992) [78]. L_{ij} and r_{ij} are the length and radius of the vessel segment, respectively. The Hagen-Poiseuille equation is only valid for laminar flow. In a pipe laminar flow occurs for Reynolds numbers up to 2300. Even in the large arteries and veins the critical Reynolds number of 2300 is not reached (see Table 7).

The volume V_i associated to a node i (as in Equation (14)), is defined as the sum of half the volume of all adjacent edges:

$$V_i = \sum_j \left(\frac{1}{2} A_{ij} L_{ij} \right), \quad (17)$$

where A_{ij} is the cross-sectional area of vessel ij . The diameter of the blood vessels, and consequently the vessel volume, change dynamically with the transmural pressure. The VGM takes this effect into account by making the area of the cross-sections pressure dependent. The values proposed by Li and Cheng (1993) [62] could be used to describe the cross-sectional compliance $(\partial A_{ij}) / (\partial p)$ of the different types of pulmonary vessels.

Table 7: Properties of typical vessels for an adult (modified according to Formiggia et al. (2009) [38]).

	diameter [mm]	length [cm]	peak velocity [cm/s]	wave speed [m/s]	Reynolds number
ascending aorta	15	4	1.0	5	4000
thoracic aorta	11	15	0.8	6	2500
iliac artery	5	20	0.8	6	1000
femoral artery	4	45	0.8	7	800
brachial artery	5	40	0.8	7	1000
common carotid artery	4	20	0.8	7	800
left anterior descending	3	12	0.5	12	400
small artery	2	10	0.2	20	100
arteriole	0.02	0.4	0.01	-	0.5
capillary	0.01	0.2	0.001	-	0.003
venule	0.02	0.4	0.01	-	0.5
small vein	2	10	0.6	2	100
large vein	8	50	0.8	1	1700

The transport of the dissolved drug molecules with the blood stream is modeled by the subsequent equation:

$$\frac{\partial(\rho_{i,mol} x_i V_i)}{\partial t} + \sum_j F_{ij} x_{ij} + V_i r_{i,degradation} + q_{i,xDCM} = 0, \quad (18)$$

where x_i is the mole fraction of the therapeutic agent within the volume of node i , x_{ij} represents the mole fraction of dissolved drug at the physical upstream node and $q_{i,xDCM}$ describes the coupling of the double-continuum model to the vascular graph model, taking into account the exchange of dissolved drug molecules between the two models (see Section 7.1).

The variable $r_{i,degradation}$ is the sink term that accounts for the degradation processes of the therapeutic agent, such as micturition and metabolic transformation reactions (Lüllmann et al. (2004) [67]):

$$r_{i,degradation} = \rho_{i,mol} k x_i \quad \text{with} \quad k = \frac{\ln 2}{t_{1/2}}, \quad (19)$$

where k denotes the first order rate constant of a drug administered by a bolus injection and $t_{1/2}$ is the half-life of the administered drug.

4.3 Numerical Model

The linear system of equations of the VGM (explained in Section 4.2) is numerically solved using a finite difference method for the spatial discretization, and an explicit Euler scheme for the time discretization. The system of equations of the VGM is solved for the two primary variables, the pressure p and the mole fraction of dissolved therapeutic agent x , using a decoupled scheme. First, Equation (14) is used to compute the pressure field in the vascular graph. Then the distribution of the dissolved drug can be determined using Equation (18). The simulation toolbox VGM provides Dirichlet and Neumann boundary conditions for these two primary variables. As a consequence of the explicit time discretization, the Courant-Friedrichs-Lewy (CFL) condition is applied to guarantee the convergence of the solution. The transport equation (Equation (18)) is a hyperbolic partial differential equation. Therefore, a first-order upwind scheme is applied for the discretization of the advection term. The vascular graph model is programmed in Python, while performance-critical parts are written as C-extensions using Cython. The coupling of the DCM to the VGM (see Section 7.1) is realized with the Python subprocess module. A detailed description of the numerical model of the VGM is given in the appendix of this thesis.

5 Alveolus Model - A Double-Continuum Approach (DCM)

The events occurring in the arteries, arterioles, veins and venules are described by the vascular graph model (see Chapter 4). The flow, transport, and reaction processes within the capillaries around a single alveolus and within the surrounding tissue are modeled using the alveolus model, a double-continuum approach (see Figure 18).

5.1 General Model Concept

As it has already been mentioned in Section 3.2, there are two main possibilities to describe the flow and transport processes in a biological system: the molecular approach and the continuum approach. As the inner diameter of an alveolus is in the order of $140\ \mu\text{m}$, the domain size of the alveolus model is very large compared to the size of fluid and drug molecules. The excessive number of computational particles required thus forbids the usage of a molecular approach. Therefore a continuum approach is chosen to describe the transport of the dissolved drug molecules through the pulmonary capillaries and tissue, as well as the transfer between blood vessels and tissue.

The structure of the biological system is also considered in a continuous fashion. To move from a discrete to a continuous description of the biological system, the concept of the representative elementary volume (REV), a volume averaging approach, is used (Bear (1972) [19]). The pulmonary tissue and the capillary bed are both described as two distinct continua. By means of volume averaging, the discrete properties of the capillary bed and pulmonary tissue (such as the size of the different cell types, pore-space geometry, and capillary-characteristics) are represented by a continuum with new effective parameters, e.g. porosity, tortuosity or permeability (for methodological details see Bachmann et al. (2005) [12] or Section 3.2 and Section 3.3).

As shown on the left image in Figure 18, the pulmonary capillaries are embedded in the pulmonary tissue. Flow, transport, and reaction processes in both compartments are of interest - they are, however, very different from each other. Therefore, the capillary bed around a single alveolus and the surrounding tissue are treated as two separate continua (see Figure 18). The flow and transport processes between them, i.e. the exchange of fluid and substances across the capillary walls into the pulmonary tissue and vice versa, are honored via exchange terms, the so-called transfer functions (see Section 5.4).

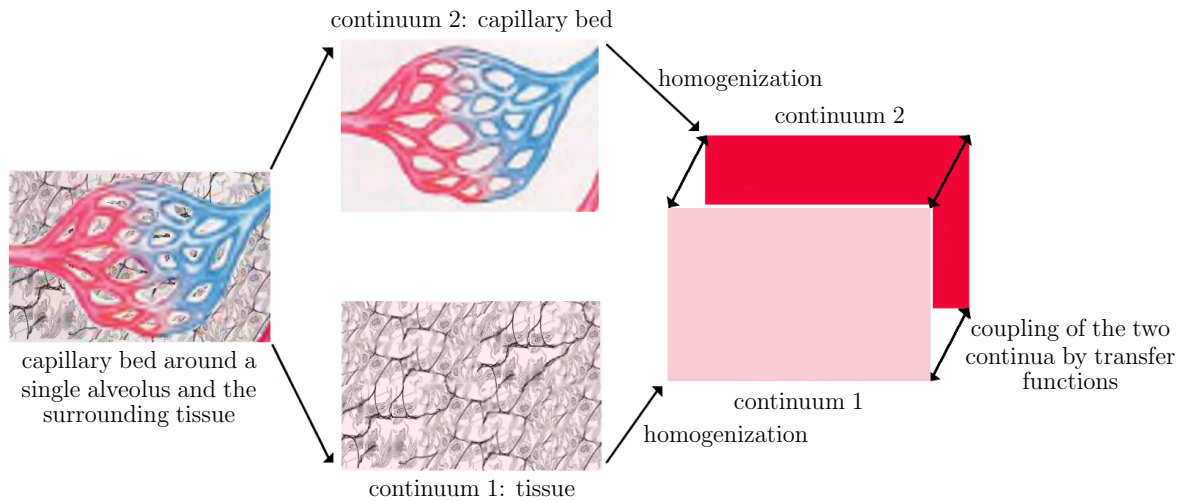


Figure 18: Explanation of the general concept of the double-continuum model.

The tissue continuum consists of cells, fibers, amorphous ground substance and interstitial fluid (a detailed description is given in Section 2.4). The individual components are not densely packed. Therefore, a fraction of the interstitial fluid can flow freely within the tissue. Hence, the pulmonary tissue can be described with a porous medium approach as it has already been done by Serikov (1991) [88].

About 1800 capillary segments, of $10\ \mu\text{m}$ average length and $8\ \mu\text{m}$ mean diameter, enwrap a human alveolus (Renkin et al. (1984) [82]). The whole lung consists of 300 million alveoli (Weibel (1991) [102]). A discrete modeling approach would therefore need to resolve $5.4 \cdot 10^{11}$ capillary segments. To avoid the high computational expense incurred, one can introduce a capillary continuum instead, which represents the pulmonary capillary bed around one alveolus as an averaged quantity.

The porous media concept requires new, effective parameters to be determined such as the permeability and porosity. The permeability expresses the ability of a porous medium to transmit fluids. In the case of the capillary continuum, this is determined by the spatial distribution and the cross linking of the individual vessel segments. The Hagen-Poiseuille law is a measure of the blood flow velocity in the vessels (Schmidt and Lang (2007) [87]) and relates it to the permeability. The volume averaging over the capillary bed results in a porosity value of one, i.e. the volume of the voids is equal to the total volume.

In summary, the double-continuum approach treats the pulmonary tissue and the capillary bed as two separate porous media continua. The interactions between them are taken into account by transfer-functions. The models of Shipley and Chapman (2010) [91] and Chapman et al. (2008) [24] also comprise a double porous medium using Darcy's law for the flow through the interstitium and the vasculature. However, the alveolus model differs from these previously presented models in that the coupling functions for the flow and transport processes between the capillary bed and the interstitium are the Starling equation (Equation (31)) and the Stavermann-Kedem-Katchalsky equation (Equation (32)) respectively. Both equations are traditionally used to describe microvascular liquid

transport in the lung (Tuma et al. (2008) [99]) and therefore ideally suited as coupling functions for the alveolus model (see Section 5.4).

5.2 Pulmonary Tissue Continuum

The phase moving within the tissue continuum consists of two components, namely the interstitial fluid and the therapeutic agent. It is assumed that the fluid phase is incompressible. Thus the movement of the dissolved drug molecules in the interstitial tissue of the lung is modeled using a single-phase two-component approach in a rigid, porous medium. The influence of the respiratory movement on the pulmonary tissue is not considered. The drug molecules are completely miscible with the interstitial fluid. The interstitial fluid is treated as a Newtonian fluid because it consists mainly of water. It has a composition similar to blood plasma, which consists of 90 percent of water, nine percent organic, and one percent inorganic substances that are dissolved in water (Schmidt and Lang (2007) [87]). With the additional assumption that the flow within the tissue is creeping, the flow velocity of the interstitial fluid can be described by Darcy's law:

$$\mathbf{v}_f = -\frac{\mathbf{K}}{\mu} (\nabla p + \rho_{mass} g \nabla z), \quad (20)$$

where \mathbf{v}_f is the Darcy velocity, \mathbf{K} is the intrinsic permeability tensor, ρ_{mass} is the mass density of the fluid, g is the gravitational acceleration, and μ is the dynamic viscosity of the fluid phase. The calculation of the flow velocity through the interstitium with Darcy's law has been done previously by Baxter and Jain (1989) [18] or Baish et al. (1997) [15], for example.

Due to the assumption of an incompressible fluid phase, a constant fraction of tissue f_T within the model domain and a constant tissue porosity, the temporal variation of the product of the porosity ϕ , the fraction of tissue f_T and the molar density ρ_{mol} does not have to be considered in the continuity equation. The following form of the continuity equation is used:

$$\nabla \cdot (f_T \rho_{mol} \mathbf{v}_f) + f_T r_{lymph} - q_F = 0. \quad (21)$$

Here, ρ_{mol} is the molar density of the fluid and q_F is the coupling variable for the flow between the two continua. The exact definition of the variable q_F is given in Section 5.4. The flow processes in the tissue and capillary continuum are calculated in the same model domain. For this reason, a factor f_T is introduced to describe the volume fraction of tissue within the model domain. The volume fraction of tissue f_T and the capillary volume fraction f_C add up to unity:

$$f_T + f_C = 1. \quad (22)$$

The exchange of fluid and dissolved components between the tissue and the capillary continuum is a surface related process. Therefore, the intercompartmental exchange rate (and thus, the coupling variable q_F) depends, among others, on the surface area of the capillaries per unit volume of tissue A_{vessel}/V_{tissue} (see Equation (31)). It is therefore not explicitly corrected with the tissue volume fraction f_T .

At the arterial side of the capillary bed, about 0.5 per cent of the plasma that flows through the capillaries is filtered out into the surrounding tissue. 90 per cent of this extravasated fluid is reabsorbed at the venous side of the capillary bed. The remaining 10 per cent of the extravasated fluid is removed by the lymphatic system from the interstitial space (Schmidt and Lang (2007) [87]). The lymphatic system carries the excess of interstitial fluid and, with it dissolved and suspended substances like macromolecules, through the lymph vessels and nodes into the great veins (Muthuchamy and Zawieja (2008) [73]). The influence of the lymphatic system on the mass balance (Equation (21)) is included by the sink term r_{lymph} (Baxter and Jain (2009) [18]):

$$r_{lymph} = L_{lymph} \frac{A_{lymph}}{V_{tissue}} (p_{is} - p_{lymph}) \rho_{mol}, \quad (23)$$

where L_{lymph} is the hydraulic conductivity of the lymphatic vessel wall, A_{lymph} is the surface area of the lymphatic vessels in the lung, V_{tissue} is the unit volume of tissue, and p_{is} and p_{lymph} are the hydrostatic pressure in the interstitial space and lymphatic system respectively. As there is no functional lymphatic system within a tumor (Jain (1998) [51]), the sink term r_{lymph} is omitted in tumor tissue.

The transport of the dissolved therapeutic agent in the pulmonary tissue is described by the following equation:

$$\begin{aligned} \frac{\partial(f_T \phi \rho_{mol} x_{is})}{\partial t} + \nabla \cdot (f_T \rho_{mol} x_{is} \mathbf{v}_f - f_T \rho_{mol} D_{eff} \nabla x_{is}) \\ + f_T r_{lymph-drug} + f_T r_{adsorption} - q_T = 0. \end{aligned} \quad (24)$$

The first term of Equation (24) is the so-called storage term. It describes the temporal variation of the product of tissue volume fraction f_T , porosity ϕ , molar density ρ_{mol} and mole fraction of the dissolved component x_{is} . The advective and diffusive transport of the therapeutic agent within the tissue are expressed by the second term. The diffusive transport of the drug depends on the effective molecular diffusion coefficient D_{eff} of the therapeutic agent (see Equation (13)). The variable q_T is the transport coupling variable. It defines the amount of dissolved drug molecules that is transported from the intravascular space across the capillary wall into the tissue and vice versa (see Section 5.4). The sink term $r_{lymph-drug}$ describes the reduction of the number of drug molecules by the lymphatic system:

$$r_{lymph-drug} = r_{lymph} \cdot x_{is}. \quad (25)$$

This sink term is defined in a similar way as the term for the flow reduction by the lymphatic system (Equation (23)), except that the mole fraction x_{is} of the dissolved therapeutic agent is additionally required.

The sink term $r_{adsorption}$ (Bongrand (1999) [22]) defines the interaction of the drug molecules with the tumor cells. The ligand-receptor interaction decreases the mole fraction of free flowing therapeutic agent:

$$r_{adsorption} = k_{on} x_{is} \rho_{mol} [R] - k_{off} [R \sim L]. \quad (26)$$

Here, $[R]$ is the receptor concentration, $[R \sim L]$ is the receptor-ligand-complex concentration, k_{on} is the kinetic constant for the forward reaction, i.e. the binding of a ligand of the drug molecule with a tumor cell receptor. The kinetic constant for the backward reaction, i.e. the splitting of the chemical bond between the therapeutic agent and the cell, is termed k_{off} . If the alveolus model is coupled to the low-dimensional population model for TRAIL-induced proapoptotic signaling (see Chapter 7 and Chapter 6) the sink term $r_{adsorption}$ will be provided by the [PMTS].s. Therefore, it is not necessary to calculate the amount of bound drug molecules by Equation (26).

The sink term $r_{adsorption}$ is only considered in tumor regions, whereas r_{lymph} and $r_{lymph-drug}$ are only included in regions of healthy pulmonary tissue.

5.3 Pulmonary Capillary Bed Continuum

The capillary continuum represents the pulmonary capillary bed around one alveolus as an averaged quantity. The movement of the dissolved drug molecules within the pulmonary capillaries is described with a single-phase two-component approach. The incompressible fluid phase consists of the two, completely miscible, components: blood and therapeutic agent. According to Beard et al. (2008) [20], the velocity within the single capillaries is constant in time. The capillaries may be treated as rigid tubes (Li and Cheng (1993) [62]) and due to the low Reynolds number within the capillaries, about 0.003 according to Formiggia et al. (2009) [38], the flow is creeping. Currently, the double-continuum model does not account for variations in capillary morphology. It assumes that the diameter of all pulmonary capillaries is constant (8 μm : the mean pulmonary capillary diameter according to Renkin et al. (1984) [82]). Consequently, a constant viscosity value of 0.0021 Pa \cdot s is assumed, which agrees with the diameter and hematocrit dependent viscosity relation developed by Pries et al. (1992) [78] that is used in the VGM.

As the capillary bed is treated as a porous media continuum, Darcy's law may be applied to determine the blood flow velocity. This has been demonstrated by Vankan et al. (1997) [100]. The method requires the computation of the continuum's intrinsic permeability tensor, which depends mainly on the connectivity of the capillary segments and their diameter. The intrinsic permeability tensor of the capillary bed can be obtained analogous to the effective conductance computation in Reichold et al. (2009) [81]. The domain is divided into a number of cuboid subvolumes. In order to compute the permeability of one such subvolume in x-direction, the integral mass flow $F_{x,REV}$ is computed between the two faces

normal to the x -axis (using the VGM and the discrete capillary network). Arbitrary (but different) pressure boundary conditions p_1 and p_2 are set at all vessel-endpoints crossing the two respective faces, and no-flow boundary conditions are set at the remaining four faces (see Figure 19). The permeability of the subvolume in x -direction now reads:

$$K_x = \frac{F_{x,REV} \mu L_{y,REV}}{|p_1 - p_2| A_{xz,REV}}, \quad (27)$$

where $L_{y,REV}$ is the length of the cuboid in y -direction and $A_{xz,REV}$ is the cross-section of the considered REV parallel to the x -axis. The permeabilities in y - and z -direction are computed analogously. Repeating this method for each subvolume yields a heterogeneous permeability field for the capillary bed around a single alveolus.

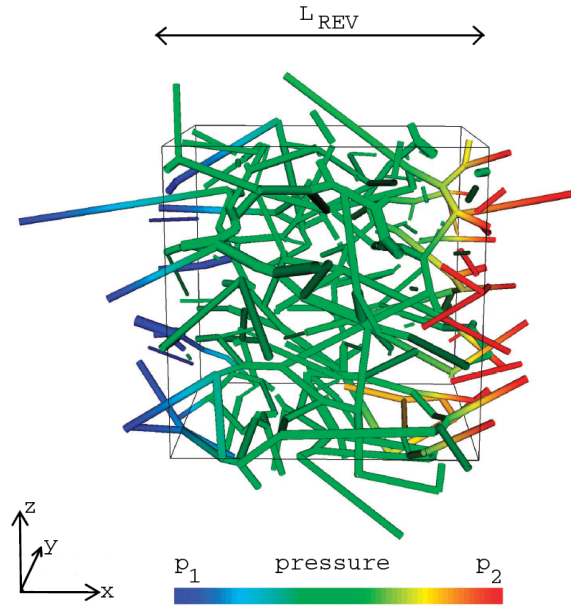


Figure 19: Computation of the effective permeability of a REV. Fixed pressures p_1 and p_2 set at all nodes crossing the left and right face normal to x respectively (no-flow boundary condition at all nodes crossing the other four faces). Effective permeability computed from pressure gradient and integral mass flow F_{REV} through the REV's capillary network (reprinted by permission from Macmillan Publishers Ltd: [Journal of Cerebral Blood Flow & Metabolism] Reichold et al. (2009) [81], copyright 2009).

Ideally, one would use a high-resolution angiography technique, such as synchrotron radiation X-ray tomographic microscopy (srXTM), to obtain the fully resolved capillary network around an alveolus. Then, the above methodology can be applied to determine a realistic intrinsic permeability tensor (see Figure 20).

As high-resolution pulmonary angiography data are not available for the present work, an artificial network is constructed instead. According to Weibel (1963) [101], the alveolar

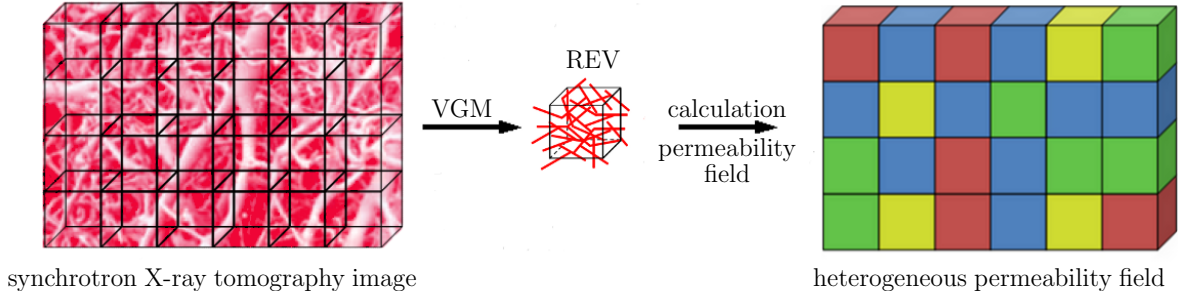


Figure 20: Generation of a realistic permeability field for the capillary continuum.

capillaries form a hexagonal network. Using the values provided by Renkin et al. [82], an artificial capillary bed is constructed consisting of 1800 capillary segments, each $8 \mu\text{m}$ in diameter and $10 \mu\text{m}$ long (see Figure 21). The intrinsic permeability tensor of the pulmonary capillary bed is obtained for the cuboid illustrated in Figure 21 by using the aforementioned method. The dimensions of the cuboid in which the hexagonal network of the capillaries is embedded depend on the size of the model domain of the alveolus model and have an influence on the permeability values (results shown in Section 8.1.3).

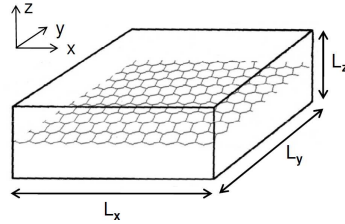


Figure 21: Determination of the permeability tensor for the capillary continuum: hexagonal mesh of pulmonary capillaries embedded in a cuboid.

With the assumptions made at the beginning of Section 5.3 and given the intrinsic permeability tensor of the capillary continuum, the flow of blood and dissolved therapeutic agent can be described with the following continuity equation:

$$\nabla \cdot (f_C \rho_{mol} \mathbf{v}_f) + q_F = 0. \quad (28)$$

The transport of the dissolved therapeutic agent is represented by the subsequent equation:

$$\frac{\partial(x_c f_C \rho_{mol})}{\partial t} + \nabla \cdot (f_C \rho_{mol} x_c \mathbf{v}_f - f_C \rho_{mol} D_{eff} \nabla x_c) + f_C r_{degradation} + q_T = 0, \quad (29)$$

where x_c is the mole fraction of drug molecules dissolved in blood. The degradation processes of the therapeutic agent are equal to those described earlier for the vascular graph model, hence $r_{degradation}$ is given by Equation (19). As the porosity ϕ of the capillary continuum is set to one, ϕ does not appear in Equation (28) and (29).

5.4 Coupling Functions for the Flow and Transport Processes between the Two Continua

The flow and transport processes between the tissue and the capillary continuum are described by the coupling functions q_F and q_T , based on the transepithelial transport via transvascular pathways. Figure 22 illustrates the different cell morphologies, which can facilitate transvascular transport, namely interendothelial clefts, fenestrae, transcellular pores and vesicles. The interendothelial or intercellular clefts are gaps between neighboring cells. Adjacent endothelial cells are connected by tight junctions. Tight junctions are small strands composed of membrane proteins. They prevent the passage of ions and molecules through the space between cells. Pores with a mean radius of 4-5 nm are formed by the tight junctions between the endothelial cells (Schmidt and Lang (2007) [87]). In some organs the endothelium of the capillaries is partly thinned so that fenestrations arise. During the generation of a fenestration, the cytoplasm is pushed away. So the cytosome consists only of two or even one plasma membrane. This plasma membrane is called diaphragm. The intracellular pores, the fenestrations, have a diameter of 50-60 nm. There are also fenestrations that are not covered by diaphragms. Transcellular pores are formed by chains of fused vesicles. Vesicles are small, membrane-enclosed sacs that transport substances through a cell. The transcellular pores only develop as a response to inflammation or injury (Petрак and Goddard (1989) [76]).

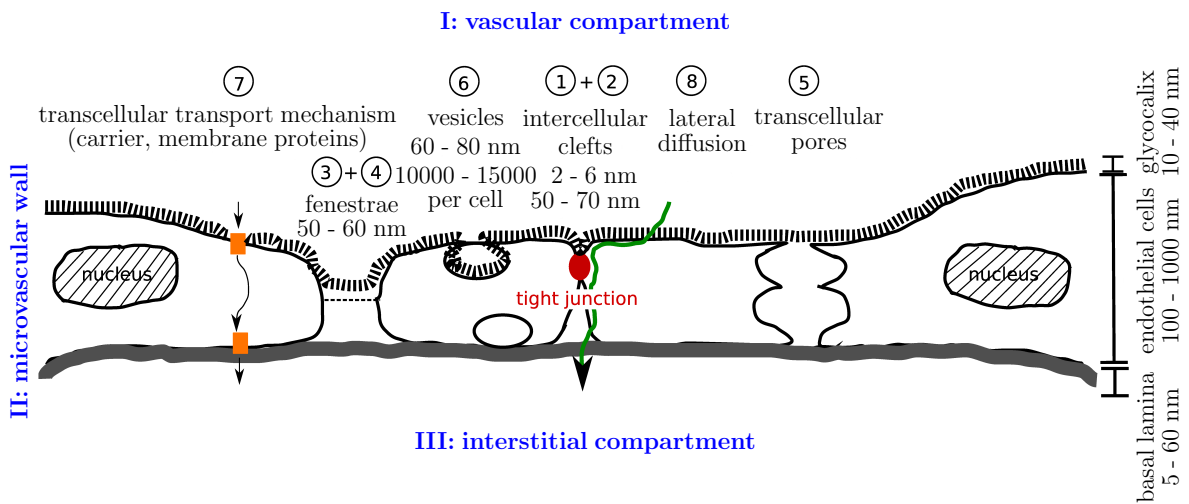


Figure 22: Paracellular and transcellular pathways (adapted from Baber (2009) [11] with kind permission of K. Baber).

There are two main ways of transport: transcellular and paracellular. The transcellular pathway crosses the apical and basolateral membrane of the endothelial cell and in most cases leads through a part of the intercellular cleft. The paracellular way spans the entire length of the intercellular cleft. The permeability of the capillary wall depends also on the type of the transported molecules. The shape, size, charge, and hydrophobicity of the molecule affect its transport across the vessel wall. According to the different properties of the single

molecules only certain transvascular pathways can be used for their transepithelial transport (see Table 8).

Table 8: Transvascular pathways (Curry (1984) [28]).

species	pathways ¹
water	1, 2, 3, 4, 7
lipophilic solutes	1, 2, 3, 4, 7, 8
hydrophilic solutes	1, 2, 3, 4, 7
macromolecules	1, 2, 3, 4, 5, 6

¹ The numbering of the pathways corresponds to the numbers in Figure 22:
 1 - small intercellular clefts, 2 - large intercellular clefts, 3 - closed fenestrae,
 4 - open fenestrae, 5 - transcellular channels of fused vesicles, 6 - vesicles,
 7 - transcellular transport mechanisms, 8 - lateral membrane diffusion.

The transport across the capillary wall mainly depends on relative pressure and concentration gradients (see Figure 23). The hydrostatic and the oncotic pressures in the capillary and the interstitial space determine the direction and the magnitude of fluid flow between the two compartments. The oncotic pressure is the sum of the colloid-osmotic pressure and an osmotic pressure caused by the Gibbs-Donnan effect. The colloid-osmotic pressure relates to

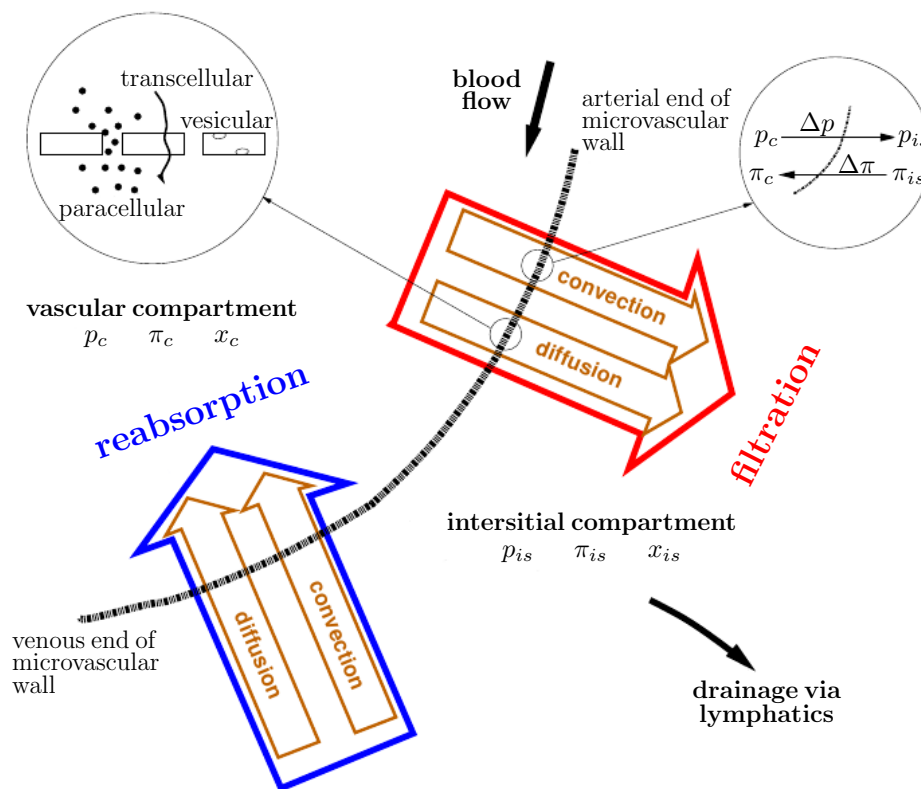


Figure 23: Processes and forces of transvascular exchange (adapted from Baber (2009) [11] with kind permission of K. Baber).

the osmotic pressure caused by macromolecules. The large anionic proteins in blood plasma cannot pass through the capillary walls. Small cations are attracted, but not bound to the large anionic proteins. Consequently, small anions will cross the capillary walls away from the plasma proteins more rapidly than small cations. This unequal distribution of permeable ions between the intravascular and the interstitial space is called Gibbs-Donnan effect and influences also the flow of water across the semipermeable capillary wall. The outflow of fluid from the capillaries into the interstitium across the microvascular wall is called filtration or extravasation. The inflow of fluid is termed reabsorption. The extravasated fluid can either be reabsorbed by the same or a different capillary, or it can leave the tissue via the lymphatic system (Kurbel et al. (2001) [59]).

The difference of the hydrostatic pressures, also called transmural pressure, and the oncotic pressures between the intravascular and the interstitial space determine the fluid transport through the capillary wall:

$$p_{eff} = \Delta p - \Delta \pi = (p_c - p_{is}) - (\pi_c - \pi_{is}). \quad (30)$$

p_{eff} is the effective filtration pressure, p_c and p_{is} are the hydrostatic pressure in capillaries and interstitial space respectively. π_c and π_{is} are the corresponding oncotic pressures. Solvent flux across the microvascular wall is proportional to the effective filtration pressure p_{eff} . According to Starling's law, net fluid flow across a vessel wall is given by (Jain (1987) [53]):

$$q_F = \rho_{mol} L_p \frac{A_{vessel}}{V_{tissue}} (p_c - p_{is} - \sigma (\pi_c - \pi_{is})), \quad (31)$$

where L_p is the hydraulic conductivity of the vessel wall, A_{vessel}/V_{tissue} is the surface area of pulmonary capillaries per unit volume of tissue. The capillary wall acts as a semipermeable membrane and thus has a strong influence on the degree of transvascular fluid flow. The reflection coefficient σ describes how well solute particles can move across the vessel wall. It can vary from zero (i.e. no reflection, all particles pass the barrier) to one (impermeable membrane). Equation (31) is used as the coupling function q_F for the fluid flow across the interface between tissue and capillary continuum.

At the arterial side of the capillary bed, the transmural pressure is higher than the osmotic pressure difference between the plasma and interstitial fluid. Therefore an outflow of fluid is observed at these locations. Due to the flow resistance in the blood vessels, the hydrostatic pressure in the capillaries decreases along their length. At the venous side of the capillary bed, the transmural pressure is equal to or often smaller than the osmotic pressure difference. This is where reabsorption of water takes place.

The Stavermann-Kedem-Katchalsky equation describes the advective and diffusive transport of the therapeutic agent across the microvascular wall (Jain (1987) [53]):

$$q_T = \rho_{mol} P \frac{A_{vessel}}{V_{tissue}} (x_c - x_{is}) + q_F (1 - \sigma_f) \bar{x}, \quad (32)$$

where P is the permeability of the capillary wall. The solvent-drag reflection coefficient σ_f describes the retardation of the therapeutic agent as it passes through the vessel wall. The variable \bar{x} represents the mean mole fraction of dissolved therapeutic agent within the pores of the capillary walls. According to Jain (1987) [53], the mean mole fraction of dissolved therapeutic agent within the pores can be calculated by the logarithmic mean: $\bar{x} = \frac{x_c - x_{is}}{\ln(x_c/x_{is})}$. In this thesis, \bar{x} is approximated by $\frac{(x_c - x_{is})}{2}$. Equation (32) is used as the coupling function q_T for the transport of the therapeutic agent between tissue and capillary continuum.

5.5 Numerical Model

The non-linear system of equations of the DCM is numerically solved using a fully upwind vertex centered finite volume method, also called fully upwind box method (see Helmig (1997) [45] and A.2.2), for the spatial discretization, and an implicit Euler scheme for the time discretization. The system of equations of the alveolus model is solved for the four primary variables, the pressures p_{is} and p_c and the mole fraction of dissolved therapeutic agent in the tissue continuum x_{is} and in the capillary continuum x_{cr} using a fully coupled scheme. Equation (21) and Equation (28) are used to compute the pressure fields in the pulmonary tissue and in the capillaries. Then, the distribution of the dissolved drug in the two continua can be determined using Equation (24) and Equation (29). The coupling of the two continua is realized by the exchange terms defined in Chapter 5.4 and numerically implemented as additional source/sink terms. The numerical model is implemented within the framework of the simulation toolbox DuMu^x. DuMu^x is a multi-scale multi-physics toolbox for the simulation of flow and transport processes in porous media. DuMu^x provides a framework for the implementation of porous media flow models. This includes several problem formulations, selection of spatial and temporal discretization schemes, nonlinear solvers and general concepts for model coupling. The toolbox DuMu^x inherits functionality from the framework DUNE. DUNE, the Distributed and Unified Numerics Environment, is a modular toolbox for solving partial differential equations with grid-based methods. It supports the easy implementation of methods like finite elements, finite differences and finite volumes (Flemisch et.al. (2007) [37] and Flemisch et al. (2011) [36]). The simulation toolbox DuMu^x provides Dirichlet, Neumann and outflow boundary conditions. A detailed description of the numerical model of the alveolus model is given in the appendix of this thesis.

6 Low-Dimensional Population Model for TRAIL-Induced Proapoptotic Signaling ([PMTS]_s)

The low-dimensional population model for TRAIL-induced proapoptotic signaling ([PMTS]_s) developed by Hasenauer and coworkers (Hasenauer et al. (2011) [42]) describes the reaction of a heterogeneous cell population to TRAIL. The low-dimensional population model is coupled to the alveolus model (see Chapter 5) to obtain information about the percentage of cancer cells that will undergo cell death due to the TRAIL concentration in the tumor tissue. This chapter gives a brief summary about the [PMTS]_s. The coupling of the [PMTS]_s to the DCM is explained in Section 7.2.

6.1 General Model Concept

The low-dimensional population model for TRAIL-induced proapoptotic signaling ([PMTS]_s) describes whether a cancer cell is or is not sensitive to a proapoptotic stimulus by TRAIL. The response of several cells to the same TRAIL stimulus is highly heterogeneous. This heterogeneous behavior of the cancer cells is also represented by the cell population model [PMTS]_s. In Section 2.6.3, a detailed overview of the induction of the programmed cell death by TRAIL is given. However, the [PMTS]_s does not include all signaling pathways explained in Section 2.6.3. It is therefore called a *low-dimensional* population model for TRAIL-induced proapoptotic signaling.

Figure 24 illustrates the reactions described by the single cell model of the [PMTS]_s. The single cell model includes the binding of TRAIL to the death receptors DR4 and DR5, the subsequent aggregation of the receptors and the formation of the death inducing signaling complex (DISC). Further, the movement of the adapter protein FADD to the DISC and the interaction with the death domain of the receptors are contained in the model. FADD binds the procaspase-8 molecules (C8). This leads to the activation of caspase-8 (C8*) and thus to the initiation of the caspase cascade and the programmed cell death by the activation of the executioner caspase, caspase-3 (C3). The concentration of activated caspase-3 (C3*) is assumed to be the decisive factor for the cell whether or not to undergo programmed cell death. If the concentration of activated caspase-3 exceeds the chosen threshold in a cell this cell will irreversibly undergo the programmed cell death. The anti-apoptotic effects of the three proteins FLIP, XIAP and CARP are also included in the single cell model of the [PMTS]_s.

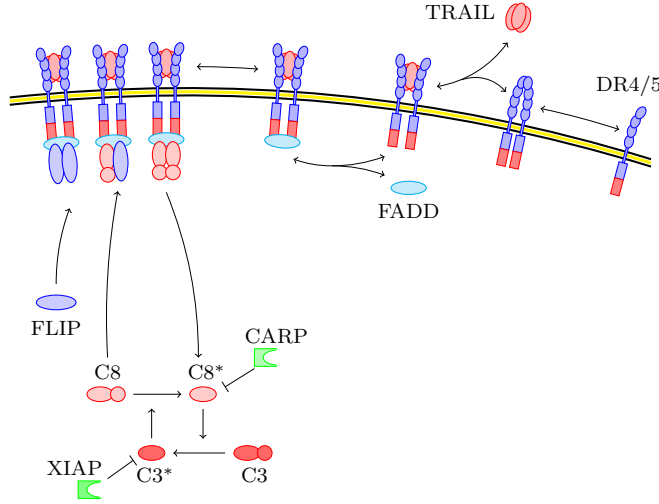


Figure 24: TRAIL signal transduction pathway as modeled by the [PMTS]_s (image from J. Hasenauer, Institute for Systems Theory and Automatic Control - University of Stuttgart).

As it has been already mentioned, [PMTS]_s considers a heterogeneous tumor cell population. The heterogeneity of the cell population is represented by differences in the parameter values and initial conditions of the single cell model for the individual cells. A multivariate probability density function is used to describe the distribution of the parameter values within the cell population. The dynamics of the single cell model are assumed to be identical in all cells and the effects of cell-cell interactions are neglected (for further details see Hasenauer et al. (2010) [43]).

6.2 Governing Equations

Table 9 shows all reactions represented by the [PMTS]_s. For each reaction of the low-dimensional population model for TRAIL-induced proapoptotic signaling one reaction rate is obtained (see Table 9). From these reaction rates, molecular balances are deduced for each species resulting in a system of 15 ordinary differential equations:

$$\frac{d[R]}{dt} = -v_1 - v_4, \quad (33)$$

$$\frac{d[C0]}{dt} = v_1 - v_2 - v_5, \quad (34)$$

$$\frac{d[C1]}{dt} = v_2 - v_3 - v_6, \quad (35)$$

$$\frac{d[C2]}{dt} = v_3 - v_7 - v_8 - v_9 + v_{10} + v_{11} + v_{12} + v_{13}, \quad (36)$$

$$\frac{d[\text{C8}]}{dt} = -v_8 - v_{10} - v_{12} - v_{16} - v_{21}, \quad (37)$$

$$\frac{d[\text{C8}^*]}{dt} = v_{10} + v_{16} - v_{18} - v_{27}, \quad (38)$$

$$\frac{d[\text{C3}]}{dt} = -v_{17} - v_{22}, \quad (39)$$

$$\frac{d[\text{C3}^*]}{dt} = v_{17} - v_{19} - v_{28}, \quad (40)$$

$$\frac{d[\text{CARP}]}{dt} = -v_{18} - v_{23}, \quad (41)$$

$$\frac{d[\text{FLIP}]}{dt} = -v_9 - v_{11} - v_{13}, \quad (42)$$

$$\frac{d[\text{XIAP}]}{dt} = -v_{19} - v_{20} - v_{24}, \quad (43)$$

$$\frac{d[\text{C2} \sim \text{C8}]}{dt} = v_8 - v_{10} - v_{11} - v_{14}, \quad (44)$$

$$\frac{d[\text{C2} \sim \text{FLIP}]}{dt} = v_9 - v_{12} - v_{13} - v_{15}, \quad (45)$$

$$\frac{d[\text{C8}^* \sim \text{CARP}]}{dt} = v_{18} - v_{25}, \quad (46)$$

$$\frac{d[\text{C3}^* \sim \text{XIAP}]}{dt} = v_{19} - v_{26}. \quad (47)$$

In Equation (33), the variable R is the receptor concentration and L is the ligand concentration. This model is specialized in the TNF-related apoptosis-inducing ligand TRAIL. Equation (34) describes the time-dependent behavior of the TRAIL-receptor complex C0. C0 is the complex consisting of the aggregated receptors DR4 and DR5 after the binding of TRAIL. If the protein FADD is bounded to the complex C0 the newly formed complex will be represented by the variable C1 (see Equation (35)). The binding of FADD to the complex C0 triggers the internalization of the receptor-ligand complexes by receptor-mediated endocytosis¹ and activates the proapoptotic signaling pathway. This configuration is denoted as C2 in Equation (36). In the Equations (33) - (47) and in Table 9, the symbol * depicts the activated form of a protein and the tilde ~ illustrates a complex consisting of two different proteins bound to each other. The reaction rates from v_1 to v_{26} in the Equations (33) - (47) are defined in Table 9. Further, the used parameter values are given in Table 9.

¹The cell absorbs the receptor-TRAIL complex. The receptor will then either be degraded or brought back to cell membrane where it is able to interact with a new ligand.

Table 9: Single cell model for TRAIL-induced proapoptotic signaling (mo = molecules, log = log-normally distributed) (parameter estimation by J. Hasenauer, Institute for Systems Theory and Automatic Control - University of Stuttgart, from experiments of M. Doseczak and P. Scheurich, Institute of Cell Biology and Immunology - University of Stuttgart).

reaction	reaction rate	parameter values
R1 $R \rightleftharpoons C0$	$v_1 = k_1 [R][L] - k_{-1}[C0]$	$k_1 = 2.0 \cdot 10^{-4} \text{ ml/min ng}$ $[R](0) = 15000 \text{ mo/cell}$ $[C0](0) = 0 \text{ mo/cell}$
R2 $C0 \rightleftharpoons C1$	$v_2 = k_2 [FADD][C0] - k_{-2}[C1]$	$k_2 = 1.0 \cdot 10^{-6} \text{ cell/min mo}$ $[FADD] = 1.0 \cdot 10^6 \text{ mo/cell}$ $k_{-2} = 6.0 \cdot 10^{-2} \text{ 1/min}$
R3 $2 C1 \rightleftharpoons C2$	$v_3 = k_3 [C1]^2 - k_{-3}[C2]$	$k_3 = 1.0 \cdot 10^{-5} \text{ cell/min mo}$ $[C1](0) = 0 \text{ mo/cell}$ $k_{-3} = 6.0 \cdot 10^{-2} \text{ 1/min}$
R4 $R \rightleftharpoons \emptyset$	$v_4 = k_4 [R] - k_{-4}$	$[C2](0) = 0 \text{ mo/cell}$ $k_{-4} = \log$
R5 $C0 \rightarrow \emptyset$	$v_5 = k_4 [C0]$	
R6 $C1 \rightarrow \emptyset$	$v_6 = k_4 [C1]$	
R7 $C2 \rightarrow \emptyset$	$v_7 = k_4 [C2]$	
R8 $C2 + C8 \rightleftharpoons C2 \sim C8$	$v_8 = k_8 [C2][C8] - k_{-8}[C2 \sim C8]$	$k_8 = 1.0 \cdot 10^{-5} \text{ cell/min mo}$ $[C8](0) = 100000 \text{ mo/cell}$ $k_{-8} = 6.0 \cdot 10^{-2} \text{ 1/min}$
R9 $C2 + \text{FLIP} \rightleftharpoons C2 \sim \text{FLIP}$	$v_9 = k_9 [C2][\text{FLIP}] - k_{-9}[C2 \sim \text{FLIP}]$	$[C2 \sim C8](0) = 0 \text{ mo/cell}$ $k_9 = 1.0 \cdot 10^{-5} \text{ cell/min mo}$ $[C2 \sim \text{FLIP}](0) = 0 \text{ mo/cell}$ $[C8^*](0) = 0 \text{ mo/cell}$
R10 $C2 \sim C8 + C8 \rightarrow C2 + C8^*$	$v_{10} = k_{10}[C2 \sim C8][C8]$	$k_{10} = 1.0 \cdot 10^{-5} \text{ cell/min mo}$
R11 $C2 \sim C8 + \text{FLIP} \rightarrow C2$	$v_{11} = k_{11}[C2 \sim C8][\text{FLIP}]$	$k_{11} = 1.0 \cdot 10^{-6} \text{ cell/min mo}$
R12 $C2 \sim \text{FLIP} + C8 \rightarrow C2$	$v_{12} = k_{12}[C2 \sim \text{FLIP}][C8]$	$k_{12} = 1.0 \cdot 10^{-6} \text{ cell/min mo}$
R13 $C2 \sim \text{FLIP} + \text{FLIP} \rightarrow 2C2$	$v_{13} = k_{13}[C2 \sim \text{FLIP}][\text{FLIP}]$	$k_{13} = 1.0 \cdot 10^{-7} \text{ cell/min mo}$
R14 $C2 \sim C8 \rightarrow \emptyset$	$v_{14} = k_{14}[C2 \sim C8]$	$k_{14} = 1.0 \cdot 10^{-1} \text{ 1/min}$
R15 $C2 \sim \text{FLIP} \rightarrow \emptyset$	$v_{15} = k_{15}[C2 \sim \text{FLIP}]$	$k_{15} = 1.0 \cdot 10^{-1} \text{ 1/min}$
R16 $C8 \rightarrow C8^*$	$v_{16} = k_{16}[C8][C3^*]$	$[C3^*](0) = 0 \text{ mo/cell}$ $k_{16} = 5.0 \cdot 10^{-5} \text{ cell/min mo}$
R17 $C3 \rightarrow C3^*$	$v_{17} = k_{16}[C3][C8^*]$	$[C3](0) = 470000 \text{ mo/cell}$ $k_{17} = 5.0 \cdot 10^{-5} \text{ cell/min mo}$
R18 $C8^* + \text{CARP} \rightleftharpoons C8^* \sim \text{CARP}$	$v_{18} = k_{18}[\text{CARP}][C8^*] - k_{-18}[C8^* \sim \text{CARP}]$	$k_{18} = 1.0 \cdot 10^{-3} \text{ cell/min mo}$ $[CARP](0) = 40000 \text{ mo/cell}$ $k_{-18} = 2.1 \cdot 10^{-1} \text{ 1/min}$
R19 $C3^* + \text{XIAP} \rightleftharpoons C3^* \sim \text{XIAP}$	$v_{19} = k_{19}[\text{XIAP}][C3^*] - k_{-19}[C3^* \sim \text{XIAP}]$	$[C8^* \sim \text{CARP}](0) = 0 \text{ mo/cell}$ $k_{19} = 1.0 \cdot 10^{-3} \text{ cell/min mo}$ $[C3^* \sim \text{XIAP}](0) = 0 \text{ mo/cell}$
R20 $\text{XIAP} \rightarrow \emptyset$	$v_{20} = k_{20}[\text{XIAP}][C3^*]$	$k_{20} = 5.0 \cdot 10^{-4} \text{ cell/min mo}$
R21 $C8 \rightleftharpoons \emptyset$	$v_{21} = k_{21}[C8] - k_{-21}$	$k_{21} = 3.9 \cdot 10^{-3} \text{ 1/min}$ $k_{-21} = \log$
R22 $C3 \rightleftharpoons \emptyset$	$v_{22} = k_{22}[C3] - k_{-22}$	$k_{22} = 3.9 \cdot 10^{-3} \text{ 1/min}$ $k_{-22} = \log$
R23 $\text{CARP} \rightleftharpoons \emptyset$	$v_{23} = k_{23}[\text{CARP}] - k_{-23}$	$k_{23} = 1.0 \cdot 10^{-3} \text{ 1/min}$ $k_{-23} = 4.0 \cdot 10^1 \text{ cell/min mo}$
R24 $\text{XIAP} \rightleftharpoons \emptyset$	$v_{24} = k_{24}[\text{XIAP}] - k_{-24}$	$k_{24} = 1.0 \cdot 10^{-3} \text{ 1/min}$ $k_{-24} = \log$
R25 $C8^* \sim \text{CARP} \rightarrow \emptyset$	$v_{25} = k_{25}[C8^* \sim \text{CARP}]$	$k_{25} = 1.0 \cdot 10^{-2} \text{ 1/min}$
R26 $C3^* \sim \text{XIAP} \rightarrow \emptyset$	$v_{26} = k_{26}[C3^* \sim \text{XIAP}]$	$k_{26} = 1.0 \cdot 10^{-2} \text{ 1/min}$
R27 $C8^* \rightarrow \emptyset$	$v_{27} = k_{27}[C8^*]$	$k_{27} = 5.8 \cdot 10^{-3} \text{ 1/min}$
R28 $C3^* \rightarrow \emptyset$	$v_{28} = k_{28}[C3^*]$	$k_{28} = 5.8 \cdot 10^{-3} \text{ 1/min}$

The system of ordinary differential equations (from Equation (33) to Equation (47)) is the same for every cell of the population. The heterogeneity within the cell population is simulated by differences in the initial conditions and parameter values between the individual cells. Experiments of M. Doszczak and P. Scheurich have shown that there is a high cell-to-cell variability for the synthesis rate of the inhibitor of apoptosis XIAP k_{-24} , for the receptor synthesis rate k_{-4} , for the synthesis rate of the caspase-8 k_{-21} , for the synthesis rate of the caspase-3 k_{-22} and for the initial condition of the FLIP concentration $[\text{FLIP}](0)$ in a cell. Therefore, these five quantities are simulated by different log-normal distributions (see Table 10) and are varied in the single cells. However, all the other reaction rates of the model remain unchanged for the individual cells of the population.

Table 10: Log-normally distributed parameters of the low-dimensional population model for TRAIL-induced proapoptotic signaling (values fitted to unpublished experimental data of M. Doszczak and P. Scheurich by J. Hasenauer).

	k_{-4}	k_{-21}	k_{-22}	k_{-24}	$[\text{FLIP}](0)$
location parameter μ_l	1318.7	315.62	1501.6	651.82	83586
minimum	0	0	0	0	0
maximum	∞	∞	∞	∞	∞
scale parameter σ_s	0.5	0.6260	0.6164	0.6833	0.5716

Log-normally distributed random variables Y for the rates k_{-4} , k_{-21} , k_{-22} , k_{-24} and for the initial condition of the FLIP concentration $[\text{FLIP}](0)$ are assigned to every cell of the population calculated with the following formula:

$$Y = e^{(\sigma_s b + \log(\mu_l))} \quad (48)$$

where b denotes a variate drawn from a normal distribution with a mean of zero and a standard deviation of one.

To solve the system of equations of the single cell model for the whole population, the initial conditions of all parameters have to be known for each cell of the population. Thus, the low-dimensional population model for TRAIL-induced proapoptotic signaling has to be always initialized before the start of the simulation. As it has been already mentioned above, the initial concentration of FLIP is drawn from a log-normal distribution for every cell. Further, it is assumed that the ligand concentration L is zero at the beginning of the simulation. All the other required initial conditions are calculated for the individual cells. For the calculation of the initial conditions for each cell of the tumor cell population, the initial conditions shown in Table 9 are taken as the starting points. Due to the assumption that there is no external stimulus of the cell population, the initial conditions that are later used for the simulation are set to the steady state values of the ordinary differential equations (33) - (47). This results in an initial concentration of zero for the parameters C_0 , C_1 , C_2 , $C_2 \sim C_8$, $C_2 \sim \text{FLIP}$, C_8^* , C_3^* , $C_8^* \sim \text{CARP}$, and $C_3^* \sim \text{XIAP}$. The remaining parameters R , FLIP , C_8 , C_3 , CARP , XIAP are not zero and their values depend on the reaction rates drawn from the log-normal distribution.

6.3 Numerical Model

The low-dimensional population model for TRAIL-induced proapoptotic signaling is programmed in MATLAB and performance-critical parts are written as C-extensions using MEX-files (for details see [2]). The system of ordinary differential equations (see Equations (33) - (47)) is implemented within the framework of the MATLAB toolbox CellPoT. CellPoT is designed for the simulation and analysis of heterogeneous cell populations. It is suitable for the simulation of large cell populations and the estimation of parameter distributions using a least-square or a maximum likelihood approach (see [1]). CellPoT is based on the Systems Biology Toolbox 2 (SBTOOLBOX2) for MATLAB and the SBPD extension package for the Systems Biology Toolbox 2 (for details see [3]). The SBTOOLBOX2 provides a mathematical analysis framework for biological and biochemical systems (Schmidt and Jirstrand (2006) [86]).

Before the system of ordinary differential equations of the [PMTS]_s is numerically solved, the reaction rates k_{-4} , k_{-21} , k_{-22} , k_{-24} and the initial condition of the FLIP concentration [FLIP](0) are drawn from their log-normal distributions for every cell of the heterogeneous cancer cell population. Then, the initialization of the low-dimensional population model for TRAIL-induced proapoptotic signaling is numerically solved using the ode45 solver of MATLAB. This solver is based on an explicit Runge-Kutta scheme, or more precisely the Dormand-Prince method (for details see Dormand and Prince (1980) [30] and Appendix A.3.1).

After the initialization of the [PMTS]_s, the simulation can be started. The model implemented within the MATLAB toolbox CellPoT is transferred to a MEX simulation function by the SBPD package. The MEX simulation function is a compiled C-code version of the model implemented in CellPoT and contains a CVODE integrator and a MATLAB interface. The CVODE integrator is provided by SUNDIALS (SUite of Nonlinear and Differential/ALgebraic equation Solvers; for details see [5]). SUNDIALS offers five different solvers and one of them is the so-called CVODE solver. The integrator CVODE is a solver for initial value problems of ordinary differential equation systems. The system of ordinary differential equations of the [PMTS]_s is numerically solved with the Backward Differentiation Formulas (BDF) method provided by the CVDENSE linear solver and Newton iterations with a Jacobian routine (for details see Cohen and Hindmarsh (1996) [26] and Appendix A.3.2). The compiled MEX simulation function generated by the SBPD package is then executed by CellPoT.

7 Coupling of the Individual Models to Each Other

As it has been already discussed in Chapter 3, the description of the flow, transport and reaction processes of a therapeutic agent administered via a bolus injection for the treatment of an alveolar cell carcinoma represents a challenging task, which includes three different scales. To account for all the different scales, three models have been introduced:

1. the vascular graph model (VGM) for describing the processes occurring in the pulmonary circulation (arteries, arterioles, venules and veins) on the organ scale (see Chapter 4),
2. the double-continuum model (DCM) for describing the processes occurring in the pulmonary microcirculation, in the surrounding pulmonary tissue, and the tumor (see Chapter 5) on the tissue scale, and
3. the low-dimensional population model for TRAIL-induced proapoptotic signaling ([PMTS]_s) for describing the reaction of the single cancer cell and the whole tumor cell population to the administered therapeutic agent (see Chapter 6) on the cells scale.

In this chapter, the numerical implementation of the coupling of the DCM to the VGM (see Section 7.1) and the coupling of the [PMTS]_s to the DCM (see Section 7.2) are explained. Further, the work flow of the multi-scale model which consists of all three models is presented in Section 7.3. The vascular graph model, the alveolus model and the low-dimensional population model for TRAIL-induced proapoptotic signaling are sequentially coupled to each other.

7.1 Coupling of the DCM to the VGM

The vascular graph model and the alveolus model have been described in Chapter 4 and in Chapter 5 respectively. This section gives an overview of the approach used to couple these two models. The coupling of the VGM and the DCM has the advantage that one obtains a discrete representation of the vasculature where it is computationally affordable (i.e. at the non-capillary level) and a continuum representation where a fully-resolved approach would be too expensive (i.e. at the level of the capillary bed and its surrounding tissue).

The vascular graph model describes the flow and transport of the therapeutic agent within the non-capillary pulmonary vasculature. Each pre-capillary arteriole and each post-capillary venule are connected via an upscaled edge to a so-called upscaled node, representing the capillary bed of a single alveolus and its associated tissue. These upscaled nodes are

in turn described by the double-continuum model. It is at these sites that the administered drugs and blood plasma can leave the blood compartment and enter the surrounding tissue. The double-continuum model is used to compute the amount of therapeutic agent and fluid leaving the bloodstream and provides this information to the VGM, where it is incorporated as additional sink terms q_{xDCM} and q_{fDCM} for the upscaled nodes. This coupling concept is illustrated in Figure 25.

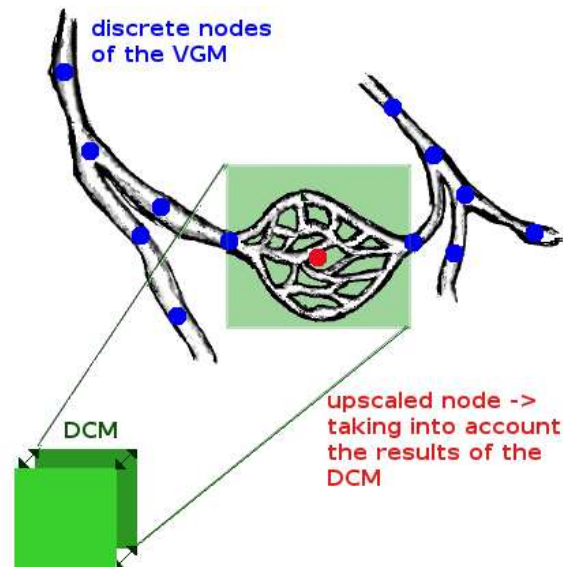


Figure 25: Coupling of the DCM to the VGM.

At each time step, the pressure and the flow field for the whole vascular graph and the distribution of the therapeutic agent in the graph are computed. Then, the additional sink terms q_{xDCM} and q_{fDCM} , also termed correction factors, are recomputed separately for each upscaled node of the vascular graph by calling the double-continuum model with the Python subprocess module (for further details see [4]). The correction factors correspond to the amount of therapeutic agent and fluid that leave the blood compartment in a time dt , which is the duration of an (explicit) time step of the VGM transport simulation. After the system of equations of the DCM has been solved for every upscaled node of the VGM to obtain the two coupling variables q_{xDCM} and q_{fDCM} for the current time step of the VGM, the pressure and the flow field of the vascular graph and the transport of the drug through the graph are corrected by the calculated sink terms.

The DCM and the VGM are linked using sequential execution and data transfer through the coupling variables q_{xDCM} and q_{fDCM} . Initial and boundary conditions of the pressure as well as the mole fraction of the dissolved therapeutic agent are required for both continua of the alveolus model, in order to solve for the additional sink terms q_{xDCM} and q_{fDCM} . The initial and the Dirichlet boundary conditions of the pressure for the capillary continuum are taken from the two VGM nodes adjacent to the upscaled node. As the VGM provides no information about the pressure in the pulmonary tissue, the initial and the Dirichlet boundary conditions for the pressure in the tissue continuum are taken from literature (Kurbel et al. (2001) [59] and Jain (1998) [52]). The two VGM nodes on the arterial and on the venous

side of the capillary bed provide the initial and the Dirichlet boundary conditions of the mole fraction of dissolved therapeutic agent in the capillary bed. The initial mole fraction of therapeutic agent in the capillary bed continuum decreases in a linear manner from the arterial side of the model domain to the venous side. The initial mole fraction of drug in the tissue is assumed to be zero. At every further time step, the final mole-fraction distribution of the previous time step is taken as initial condition. The outflow boundary condition explained in the appendix of this thesis is used for the boundary condition of the mole fraction of dissolved drug in the pulmonary tissue.

7.2 Coupling of the [PMTS]_s to the DCM

To describe the influence of the administrated drug on the cancer, the low-dimensional population model for TRAIL-induced proapoptotic signaling (see Chapter 6) is coupled to the alveolus model (see Chapter 5). The population model determines the percentage of apoptotic cancer cells and can calculate the amount of bound therapeutic agent. If the [PMTS]_s is also used for calculating the amount of bound drug the sink term $r_{adsorption}$ of the alveolus model defined in (26) and incorporated in (24) will be replaced by the amount of bound therapeutic agent calculated by the [PMTS]_s.

The realization of the coupling of the population model to the double-continuum model is shown in Figure 26. First, the [PMTS]_s needs the total number of mesh nodes of the model domain of the DCM. At every node of the finite-element mesh of the alveolus model, the number of cancer cells represented by this node has to be defined. Further, the mole fraction of therapeutic agent present in the tissue continuum has to be stored for each time step and for every mesh node of the DCM. These three pieces of information are needed as input for the [PMTS]_s. Then, the system of equations of the low-dimensional population model for TRAIL-induced proapoptotic signaling is solved and the amount of bound therapeutic agent and the percentage of apoptotic cells for each node of the DCM grid is provided to the alveolus model. The DCM and the [PMTS]_s are linked using sequential execution. The data transfer between the two models is realized by writing the needed information and calculated results to various files.

The [PMTS]_s can be called either for every time step, after certain time intervals or only at the end of the simulation of the double-continuum model. Before the low-dimensional population model for TRAIL-induced proapoptotic signaling is called by the alveolus model for the first time, the population model has to be initialized. This means that the initial conditions and the parameter vectors are generated for the simulation of the [PMTS]_s. Therefore, the information about the total number of grid nodes of the double-continuum mesh and the number of cancer cells per mesh node have to be already available at this time. The initialization of the [PMTS]_s is explained in detail in Section 6.2.

The decision, how often the population model is called by the DCM, depends on the therapeutic agent that is described by the [PMTS]_s. Until now, the parameters and the reactions of the population model are fitted to the protein TRAIL. There are other interesting forms of the therapeutic agent TRAIL, for example the bifunctional fusion protein scFv-TRAIL or nanoparticles of TRAIL. In the case of the single TRAIL molecule, the reaction of the can-

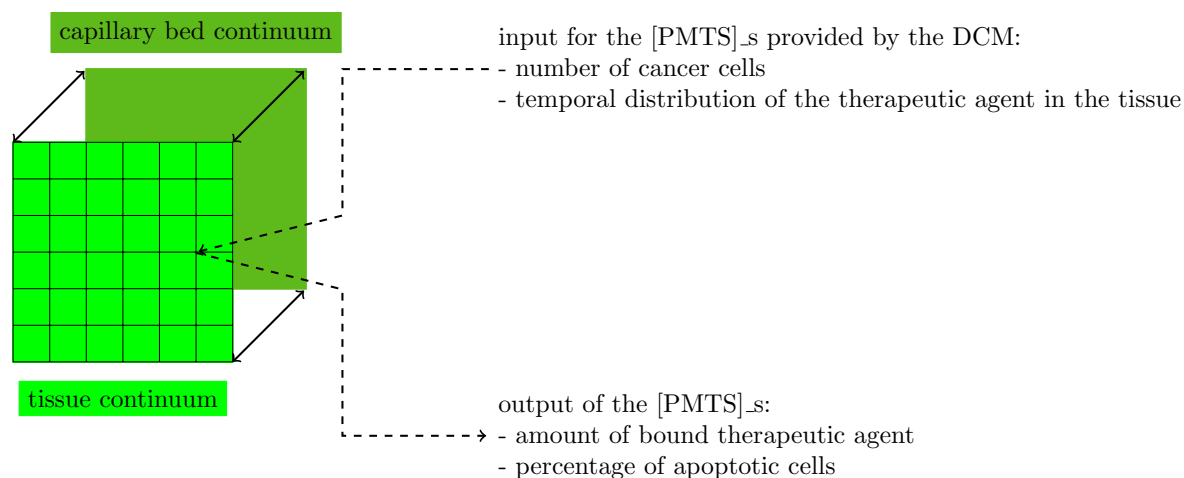


Figure 26: Coupling of the [PMTS]_s to the DCM.

cer cell to the drug can be first observed after approximately twelve hours and the amount of TRAIL that binds to the cells is negligible compared to the amount of unbound TRAIL in the tissue. In case of the bifunctional fusion protein scFv-TRAIL, the binding of the fusion proteins to the cancer cells has to be considered. Thus, the decision, how often the low-dimensional population model for TRAIL-induced proapoptotic signaling is called by the alveolus model, depends on the specific problem one wants to describe by the coupling of these two models: Which kind of TRAIL is modeled? Which period of time should be simulated?

7.3 Multi-Scale Model for Describing Cancer-Therapeutic Transport in the Lung

The model concept presented in Chapter 3 introduces the idea of a computational simulation framework for describing cancer-therapeutic transport in the lung. To comprise all relevant processes on the different scales, three models are used. For the realization of the model concept, the three individual models are sequentially coupled to each other and interfaces between the different simulation toolboxes are defined. How is the numerical implementation of the multi-scale model realized? This question will be answered in the subsequent paragraph.

Figure 27 depicts the flow chart of the multi-scale model consisting of the vascular graph model, the double-continuum model and the low-dimensional population model for TRAIL-induced proapoptotic signaling. The initialization of the multi-scale model and the sequence of the simulation is controlled by the VGM. For the initialization of the multi-scale model, the vessels building the vascular graph have to be defined: the lengths, the diameters, the connectivity and the type of the vessels. Further, the upscaled nodes and edges representing the capillary bed and the pulmonary tissue around an alveolus have to be added to the vascular graph. There are two kinds of upscaled nodes: healthy

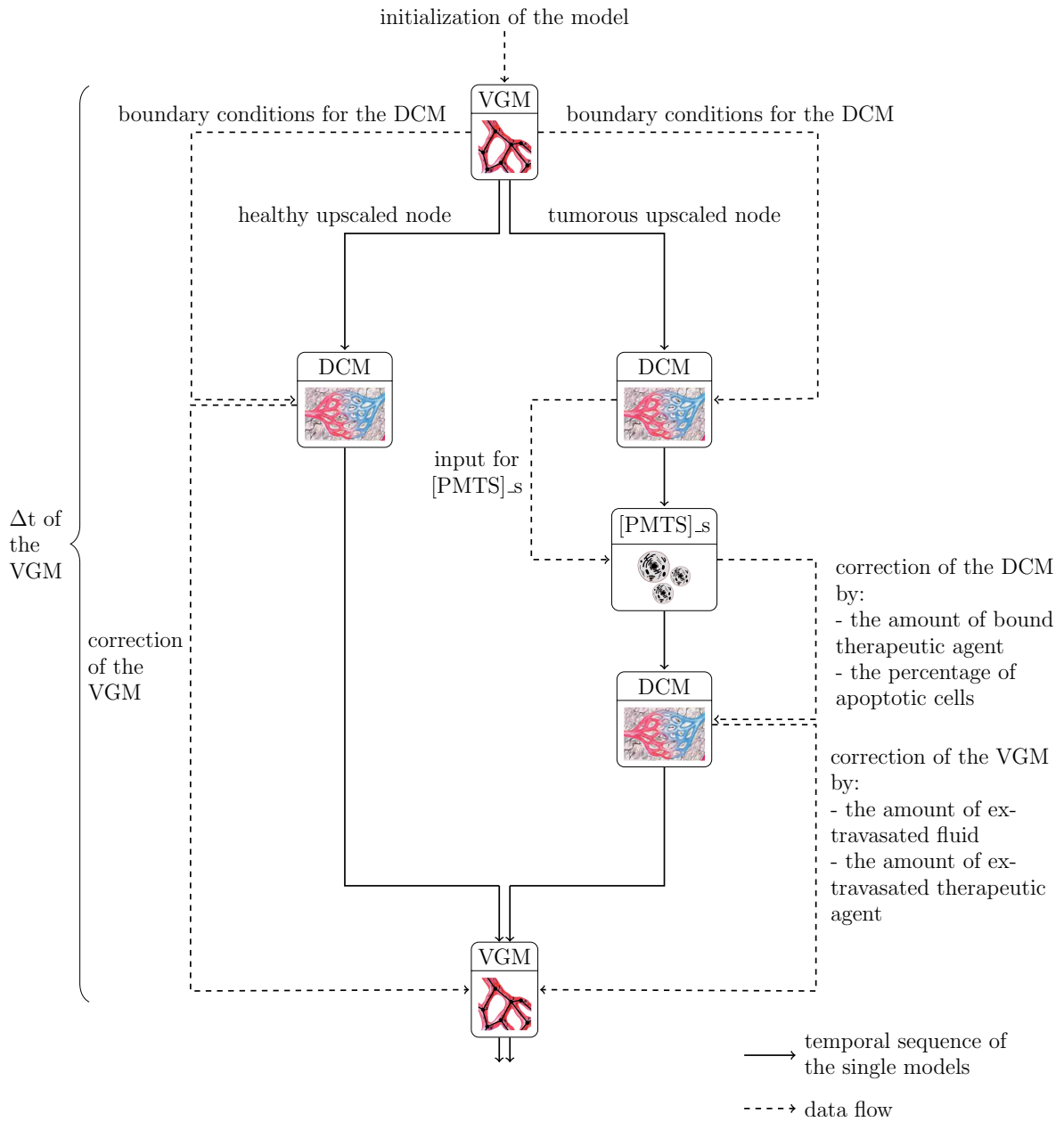


Figure 27: Work flow of the multi-scale model.

and tumorous ones. As the name tumorous upscaled node already states, the alveolar cell carcinoma is represented by this type of upscaled nodes. The difference between these two kinds of nodes lies in other parameter values and source and sink terms of the mathematical model (for details see Chapter 5). The last two necessary steps of the initialization of the multi-scale model are the definition of the initial and boundary conditions of the vascular graph model for the pressure and the concentration of administered therapeutic agent, and the specification of the total model time.

After a successful initialization of the multi-scale model, the system of equations of the vascular graph model is solved the first time for the two primary variables, the pressure and the mole fraction of dissolved therapeutic agent, using the decoupled scheme explained in the appendix of this thesis. Within this first time step of the vascular graph model, the DCM is sequentially called for every upscaled node and the fluxes and the mole-fraction distribution of the vascular graph model are corrected afterwards as it has been already explained in Section 7.1. In case of a tumorous upscaled node, the call of the DCM leads to the call of the low-dimensional population model for TRAIL-induced proapoptotic signaling. The coupling of the low-dimensional population model for TRAIL-induced proapoptotic signaling to the double-continuum model has already been explained in Section 7.2. The simulation results of the [PMTS]_s are taken into account by the DCM. If the simulations of the low-dimensional population model and the double-continuum model are finished and the results of all three models are corrected the vascular graph model starts with the second time step.

The time-step size of the multi-scale model is restricted by the use of the Courant-Friedrichs-Lewy (CFL) condition due to the explicit time discretization of the vascular graph model (for further details see Appendix A.1.1). The time-step size of the vascular graph model is in the order of tenth of seconds because the blood flow velocities are lower than 1 cm/s (see Table 7) in the vessel segments of the vascular graph. To get biologically meaningful simulation results, it is necessary to run the multi-scale model for at least twelve hours due to the fact that the response of the cancer cell population to a proapoptotic stimulus takes more than ten hours. To call the double-continuum model during every explicit time step of the VGM would mean that the total simulation time would take several years. The investigations of the multi-scale model have shown that the most calculation-intensive process is the call of the DCM by the VGM. Therefore the program cycle of the multi-scale model has been optimized and sped up for the long-time applications. The simulation time of the multi-scale model has been reduced from several years to hours. The realization of the simulation time reduction and the application of the multi-scale model to a realistic scenario are presented in the following chapter.

8 Model Applications

The simulation results of two different examples are presented in this chapter. The first example uses the vascular graph model (see Chapter 4) and the alveolus model (see Chapter 5) to describe the spatiotemporal distribution of a therapeutic agent within a subset of the human lung.

The second example consists of all three models coupled to each other: the vascular graph model, the alveolus model and the low-dimensional population model for TRAIL-induced proapoptotic signaling (see Chapter 6). Using all three models, the spatiotemporal distribution of the administered drug can be simulated as well as the reaction of the cancer cells to the administered therapeutic agent.

8.1 First Example - Simulating the Flow and the Transport of a Therapeutic Agent within the Lung

This section demonstrates how the coupled model described in Section 7.1 can be applied to simulate the spatiotemporal distribution of a therapeutic agent in the lung. The simulation demonstrates the functionality of the coupled model consisting of the discrete vascular graph model and the alveolus model which is a continuum approach. The model time of this simulation is about eleven seconds.

The computational grid is based on the literature values given in Horsfield (1978) [47] and Horsfield and Gordon (1981) [48] (see Table 11). Horsfield and coworkers studied the morphology of the human pulmonary arterial and venous trees, based on Strahler's ordering system. The Strahler algorithm defines the smallest non-capillary blood vessels as order 1. If two vessels of the same order meet, the order number of the confluent vessel will be increased by one. If a blood vessel of order n meets another vessel of an order smaller than n , the order of the confluent vessel will remain n (Huang et al. (1996) [49], see also Figure 28). The precondition that the Strahler ordering system can be used for the classification of pulmonary vessels is the dichotomous branching of the pulmonary vascular tree (Weibel (1991) [102]).

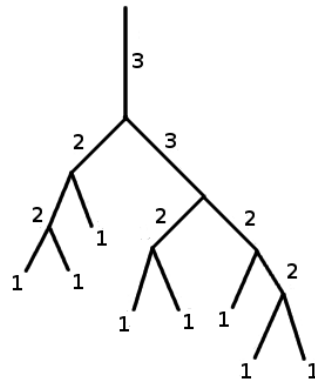


Figure 28: Classification of blood vessels according to the Strahler ordering system.

Table 11: Classification of the pulmonary arterial tree (according to Horsfield (1978) [47]) and of the pulmonary venous tree (according to Horsfield and Gordon (1981) [48]) using Strahler's ordering system.

arterial tree				venous tree			
order	number of branches	diameter [mm]	length [mm]	order	number of branches	diameter [mm]	length [mm]
17	1.000	30.000	90.50				
16	3.000	14.830	32.00				
15	8.000	8.060	10.90	15	4.000	13.88	36.7
14	$2.000 \cdot 10^1$	5.820	20.70	14	$1.400 \cdot 10^1$	5.23	39.0
13	$6.600 \cdot 10^1$	3.650	17.90	13	$5.300 \cdot 10^1$	2.90	25.4
12	$2.030 \cdot 10^2$	2.090	10.50	12	$1.580 \cdot 10^2$	1.90	18.5
11	$6.750 \cdot 10^2$	1.330	6.60	11	$4.960 \cdot 10^2$	1.21	11.0
10	$2.290 \cdot 10^3$	0.850	4.69	10	$1.842 \cdot 10^3$	0.61	3.20
9	$6.062 \cdot 10^3$	0.525	3.16	9	$7.546 \cdot 10^3$	0.39	2.54
8	$1.877 \cdot 10^4$	0.351	2.10	8	$2.384 \cdot 10^4$	0.22	1.98
7	$5.809 \cdot 10^4$	0.224	1.38	7	$7.387 \cdot 10^4$	0.14	1.34
6	$1.798 \cdot 10^5$	0.138	0.91	6	$2.331 \cdot 10^5$	0.096	0.910
5	$5.672 \cdot 10^5$	0.086	0.65	5	$7.355 \cdot 10^5$	0.064	0.617
4	$1.789 \cdot 10^6$	0.054	0.44	4	$2.321 \cdot 10^6$	0.043	0.418
3	$5.641 \cdot 10^6$	0.034	0.29	3	$7.324 \cdot 10^6$	0.029	0.283
2	$2.028 \cdot 10^7$	0.021	0.20	2	$2.311 \cdot 10^7$	0.019	0.192
1	$7.292 \cdot 10^7$	0.013	0.13	1	$7.292 \cdot 10^7$	0.013	0.130

8.1.1 Simulation Setup

A subset of the full pulmonary vasculature is chosen as the domain for the simulation. Starting from Strahler order 4, a dichotomous branching tree of arterioles is generated, leading to 21 pre-capillary arteries of order 1. These connect to as many upscaled nodes, which in turn are connected to 21 post-capillary venules of order 1. The veins dichotomously reunite until order 4 is reached (see Figure 29). The diameters and lengths of the individual vessels are assigned according to the measurement results of Horsfield (1978) [47] and Horsfield and Gordon (1981) [48], as listed in Table 11.

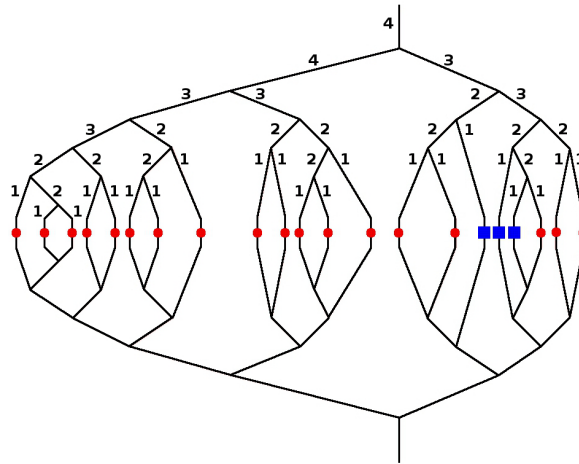


Figure 29: Visualization of the vascular graph coupled to the DCM. The black lines represent the blood vessels, which form the unstructured grid of the VGM. The red nodes and the blue rectangles symbolize the capillary bed and pulmonary tissue around an alveolus, which are simulated using the DCM. The red nodes are the healthy upscaled nodes and the blue rectangles are the tumorous ones. The blood vessels above / below the alveoli are arteries / veins of the order one to four, with a morphology according to Table 11 respectively.

Three of the 21 upscaled nodes have been assigned tumor properties, representing an alveolar cell carcinoma. These are the three upscaled nodes depicted by the blue rectangles in Figure 29. The model domain of the DCM for a healthy upscaled node represents an alveolus with its capillary bed and surrounding tissue. It is constructed as a spherical shell with an inner diameter of $140 \mu\text{m}$ (the mean diameter of a human alveolus according to Renkin et al. (1984) [82]) and an outer diameter of $364 \mu\text{m}$ (see Figure 30). On the alveolar surface, the capillaries are arranged in the form of a hexagonal network with a few interspersed pentagonal meshes to close the spherical surface (Weibel (1991) [101]). In-between the capillary segments and above the capillary mesh, the pulmonary tissue is located. The thickness of the tissue layer, $100 \mu\text{m}$, is arbitrarily chosen. The lumen of a pulmonary capillary is about $8 \mu\text{m}$ wide, and the endothelial cell wall is approximately $2 \mu\text{m}$ thick (according to Renkin et al. (1984) [82] and Schmidt and Lang (2007) [87]). The individual layers thus add up to a total thickness of $112 \mu\text{m}$. Therefore, the model domain has an outer diameter of $364 \mu\text{m}$. The model domain of the DCM for a tumorous upscaled node is a sphere with a di-

ameter of $364 \mu\text{m}$. It is assumed that the cancer cells have destroyed the alveolar walls, and have penetrated into and filled the alveolus. The tumor vasculature consists of vessels from the already existing network of the host vasculature and new vessels resulting from the angiogenesis response of the host vessels to the cancer cells (Jain (1998) [52]). There are no necrotic regions. It is assumed that the arterial input to the capillary bed is on the left side of the alveolus, and the venous drainage occurs at the right side (see Figure 30). Blood cannot enter or leave the model domain via any other pathway. According to Singhal et al. (1973) [92], the pulmonary arterioles, also termed pre-capillary vessels, give rise to the capillary networks and they number between one and two per alveolus. Therefore, the assumption of a single feeding arteriole and a single draining venule is made.

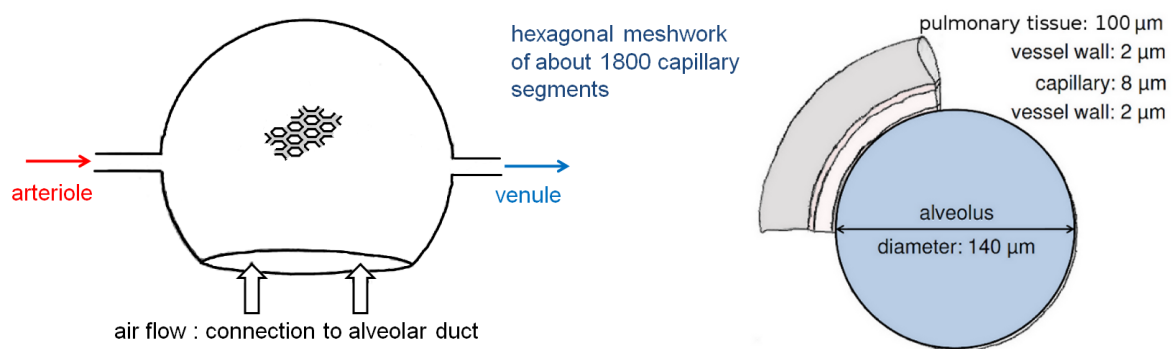


Figure 30: Left: Model domain of the alveolus model for a healthy upscaled node consisting of a spherical shell with an inner diameter of $140 \mu\text{m}$ and an outer diameter of $364 \mu\text{m}$ (according to Weibel (1991) [101]). Right: Different kind of structures comprised by the model domain of the DCM.

This setup is meant to demonstrate the functionality of the coupled model rather than being a realistic description of the spatial and temporal distribution of a therapeutic agent within the human lung for cancer therapy. Two simplifications are made. First, the cross-sectional compliance, the pressure dependent change of the cross-section of a vessel segment, is not considered in this example. Second, the influence of the gravity on the blood flow through the vessel segments is neglected. The data of Horsfield (1978) [47] and Horsfield and Gordon (1981) [48] only allow the generation of a two-dimensional graph. The distance of each single vessel segment to the entrance of the pulmonary artery into the lung cannot be determined.

8.1.2 Initial and Boundary Conditions

The systems of equations of the vascular graph model and the double-continuum model are solved for the two primary variables: the pressure p and the mole fraction of dissolved therapeutic agent x . Initial and Dirichlet pressure boundary conditions are set at the root arterial and root venous vertex. The numerical values chosen are 1067 and 200 Pa respectively, taken from Des Jardins (2008) [55]. At the root arterial vertex, the mole fraction of dissolved therapeutic agent x is set to $1.1249 \cdot 10^{-8}$.

At the outer boundaries of the model domain, the initial and boundary conditions for the upscaled nodes, where the double-continuum model's system of equations is solved, are automatically taken from the corresponding adjacent VGM nodes, as is explained in Section 7.1. In the case of a healthy upscaled node, there is an additional model domain boundary located at the inner surface of the spherical shell. There, Neumann no-flow boundary conditions are set for the primary variables. In this way, no fluid and no dissolved therapeutic agent can enter or leave the pulmonary capillary bed and the pulmonary tissue through the alveolar wall.

8.1.3 Parameters

The results, shown in Section 8.1.4, are based on the parameter values presented here. The vascular graph model requires the diameters and lengths of the vessel segments that make up the vascular graph. The numerical values of these vessel properties are taken from Table 11. Table 12 gives an overview of the parameters used in the alveolus model for the healthy and the tumorous case. Most variables are taken from literature. However, for some parameters no suitable values could be found.

Table 12: Model parameters of the alveolus model.

parameter	symbol	unit	tissue	value	ref.
tissue continuum					
diffusion coefficient ³	D	m^2/s		$5.12 \cdot 10^{-14}$	see text
dynamic viscosity ¹	μ	Pas		0.0012	[95]
hydraulic conductivity of lymphatic vessel wall ²	L_{lymph}	m/Pas	healthy	$1.9 \cdot 10^{-12}$	see text
initial receptor concentration	$[R_0]$	mol/m^3	tumorous	$1.7 \cdot 10^{-5}$	see text
kinetic constant: forward reaction	k_{on}	$\text{m}^3/(\text{mol s})$	tumorous	$1 \cdot 10^2$	see text
kinetic constant: backward reaction	k_{off}	$1/\text{s}$	tumorous	$1 \cdot 10^{-3}$	see text
interstitial fluid pressure	p_{is}	Pa	healthy	-1064	[59]
			tumorous	133	[52]
lymphatic pressure ²	p_{lymph}	Pa	healthy	-1200	see text
mass density ¹	ρ_{mass}	kg/m^3		1030	[63]
molar density ¹	ρ_{mol}	mol/m^3		303.5	[87]
intrinsic permeability	K	m^2	healthy	$4.43 \cdot 10^{-18}$	[96]
			tumorous	$2.14 \cdot 10^{-17}$	[96]
porosity	ϕ	-	healthy	0.13	[18]
			tumorous	0.27	[50]
surface area of lymph vessels per unit volume of tissue ²	$\frac{A_{lymph}}{V_{tissue}}$	$1/\text{m}$	healthy	3.0	see text
tortuosity factor	$\hat{\tau}$	-	healthy	0.28	[23]
			tumorous	0.71	[77]
volume fraction of tissue	f_T	-	healthy	0.96	see text
			tumorous	0.8	[18]
capillary continuum					
capillary volume fraction	f_C	-	healthy	0.04	see text
			tumorous	0.2	[18]
diffusion coefficient ³	D	m^2/s		$2.93 \cdot 10^{-14}$	see text
dynamic viscosity ¹	μ	Pas		0.0021	[78]
half-life of therapeutic agent	$t_{1/2}$	s		21600	see text
mass density ¹	ρ_{mass}	kg/m^3		1050	[38]
molar density ¹	ρ_{mol}	mol/m^3		284	[87]
intrinsic permeability	K	m^2	healthy	see Table 13	see text
			tumorous	$1.25 \cdot 10^{-11}$	see text
porosity ³	ϕ	-		1	see text
tortuosity factor ³	$\hat{\tau}$	-		1	see text
transfer equations					
capillary oncotic pressure	π_c	Pa	healthy	3724	[59]
			tumorous	2660	[18]
diffusive permeability	P	m/s	healthy	$2.2 \cdot 10^{-9}$	[18]
			tumorous	$1.73 \cdot 10^{-8}$	[18]
hydraulic conductivity	L_p	m/Pas	healthy	$2.71 \cdot 10^{-12}$	[18]
			tumorous	$2.11 \cdot 10^{-11}$	[18]
interstitial oncotic pressure	π_{is}	Pa	healthy	1862	[59]
			tumorous	1995	[18]
molar density ¹	ρ_{mol}	mol/m^3		293.75	see text
osmotic reflection coefficient ³	σ	-		0.8	[74]
solvent-drag reflection coefficient	σ_f	-	healthy	0.91	[18]
			tumorous	0.82	[18]
surface area of capillaries per unit volume of tissue	$\frac{A_{vessel}}{V_{tissue}}$	$1/\text{m}$	healthy	$1.9 \cdot 10^4$	see text
			tumorous	$2.0 \cdot 10^4$	[18]

¹ It is assumed that the fluid properties do not change in a tumor.² There is no lymphatic system in a tumor.³ The healthy parameter value is also taken for the tumor area.

Table 13: Calculation of permeability field of the cuboid shown in Figure 21.

	$K_x [(\mu\text{m})^2]$	$K_y [(\mu\text{m})^2]$	$K_z [(\mu\text{m})^2]$
cuboid with hexagonal network	0.15	0.22	0.00

As already discussed in Section 5.3, the processes in the alveolar capillary bed are described with a porous media approach. The results of the permeability field calculation for a healthy upscaled node are shown in Table 13. The cuboid used to compute the permeability tensor has an edge length of 364 μm in the x - and y -directions and extends 112 μm in the z -direction. The dimensions of the cuboid depend on the model domain of the DCM - a spherical shell with an inner diameter of 140 μm and an outer diameter of 364 μm . The permeability in z -direction is zero because the capillary bed forms a two-dimensional hexagonal mesh in the xy -plane (see Figure 21). As the capillary bed enwraps the spherical alveolus, it is necessary to transform the permeability tensor computed for the cuboid K_C into the coordinate system of the model domain, a spherical shell, to obtain the intrinsic permeability tensor of the capillary bed K_{CB} . This is done by setting:

$$K_{CB} = R^T K_C R, \quad (49)$$

where R is the three-dimensional rotation matrix and R^T is its transpose. The result of this transformation is the symmetric, positive semi-definite matrix K_{CB} . Due to the transformation of the permeability tensor from the coordinate system of the cuboid to the coordinate system of the spherical shell, the permeability values normal to the surface of the shell become zero (see Figure 31).

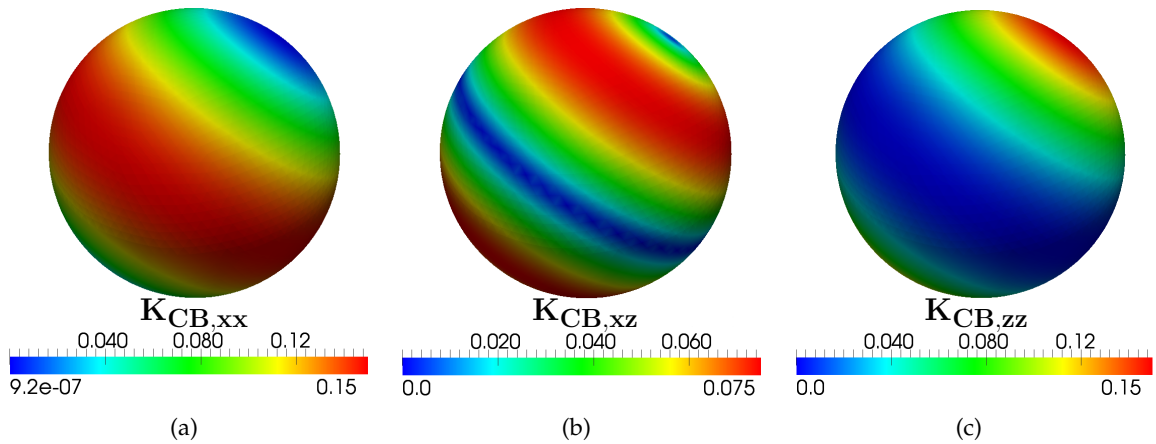


Figure 31: Visualization of the permeability field of the capillary bed in units of $(\mu\text{m})^2$ for a healthy upscaled node: (a) in x -direction, (b) in xz -direction, (c) in z -direction, in all the other directions the permeability is zero.

Solid tumors are characterized by many tortuous vessels, shunts, vascular loops, irregular intervascular distances and large avascular areas (Baish et al. (1996) [14]). Hence, the cap-

illary bed for the three tumorous upscaled nodes is not represented by a hexagonal meshwork. Due to the lack of high resolution angiography data of an alveolar cell carcinoma, the Hagen-Poiseuille equation is used to estimate the intrinsic permeability \mathbf{K} of the tumorous capillary bed. Comparing the Hagen-Poiseuille equation with Darcy's law (see Equation (20)), a relationship for the intrinsic permeability \mathbf{K} of the capillary bed of the tumor can be found:

$$\mathbf{K} = \frac{r_c^2}{8}, \quad (50)$$

where r_c is the mean capillary radius of a tumor vessel. According to Jang et al. (2003) [54], r_c is set to 10 μm .

The diffusion coefficient D of the injected therapeutic agent depends strongly on the size of the considered drug molecules. For drug molecules dissolved in blood and interstitial fluid, it can be calculated using the Stokes-Einstein-Equation:

$$D = \frac{RT}{N_A 6\pi\mu r}, \quad (51)$$

where R is the gas constant and N_A is the Avogadro number. For the body temperature T a value of 310.15 Kelvin is assumed. The radius r of the drug molecules is approximated by a mean value of 3.7 nm. The value for the dynamic viscosity μ of blood and of the interstitial fluid are assigned as listed in Table 12.

The balance equations (21) and (24) of the tissue continuum contain a sink term that considers the influence of the lymphatic system on the amount of interstitial fluid and drug molecules within the tissue. Lymph formation occurs when the lymphatic pressure p_{lymph} drops below the pressure in the interstitial space p_{is} (see Equations (23) and (25)). However, the pulmonary lymphatic pressure has not been measured until now. Experiments have merely shown that the pulmonary lymphatic pressure is at least as low as the local interstitial pressure (Negrini and Passi (2007) [74]). The values for L_{lymph} , A_{lymph}/V_{tissue} and p_{lymph} are based on assumptions.

In the case of a tumorous upscaled node, the transport equation of the tissue continuum contains a sink term that considers the interaction of the drug molecules with the cancer cells. The values for the two kinetic constants k_{on} and k_{off} and for the concentration of initially free receptors on the cell surface $[R_0]$ are based on experimental data studying the binding effect of scFv225scTRAIL fusion proteins to H460 cells (unpublished data of M. Doszczak and P. Scheurich, Institute of Cell Biology and Immunology - University of Stuttgart).

For the half-life of the drug molecules $t_{1/2}$, an arbitrary value is used. If the model is applied to a specific drug administered by bolus injection, the properties of that particular therapeutic agent need to be implemented. Further, no specific value for the molar density of blood could be found. The value listed in Table 12 is only valid for blood plasma. The values for the porosity ϕ and the tortuosity factor $\hat{\tau}$ of the capillary continuum are based on the considerations in Section 5.3.

In the case of a healthy upscaled node, the chosen values for the volume fraction of tissue f_T and for the capillary volume fraction f_C of the model domain are chosen as outlined below.

According to Effors (1984) [32], the vascular volume fraction in a 12 μm thick section of the alveolar surface is 0.9. Above this layer, we assume a 100 μm thick layer of pulmonary tissue that is not vascularized. Therefore, the overall volume fractions in the entire model domain (representing a healthy upscaled node) are $f_T = 0.96$ and $f_C = 0.04$ for tissue and capillaries respectively. The transfer equations that couple flow and transport processes between tissue and capillary continuum contain the molar density of the exchanged fluid. In the tissue continuum the considered fluid is the interstitial fluid and in the capillary continuum it is blood. Therefore, the molar density used in the transfer equations is the arithmetic mean of the molar densities of these two fluids. Additionally, the capillary surface area per unit volume of tissue A_{vessel}/V_{tissue} is included in the transfer equations. For the healthy upscaled nodes, this value is calculated based on the geometry of the model domain (a spherical shell):

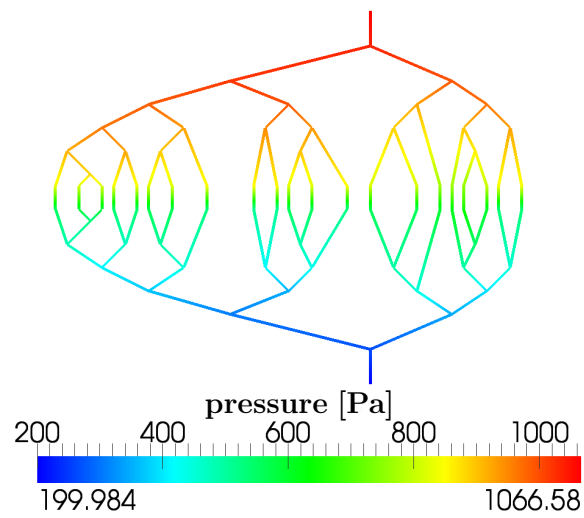
$$\frac{A_{vessel}}{V_{tissue}} = \frac{N_{vessel} 2r_{vessel} \pi l_{vessel}}{\frac{4}{3} \pi \left(r_{outer\ sphere}^3 - r_{inner\ sphere}^3 \right)}. \quad (52)$$

N_{vessel} stands for the number of vessels inside the model domain. r_{vessel} and l_{vessel} are the radius and length of the capillary segments. $r_{outer\ sphere}$ and $r_{inner\ sphere}$ are the radius of the outer and inner sphere respectively.

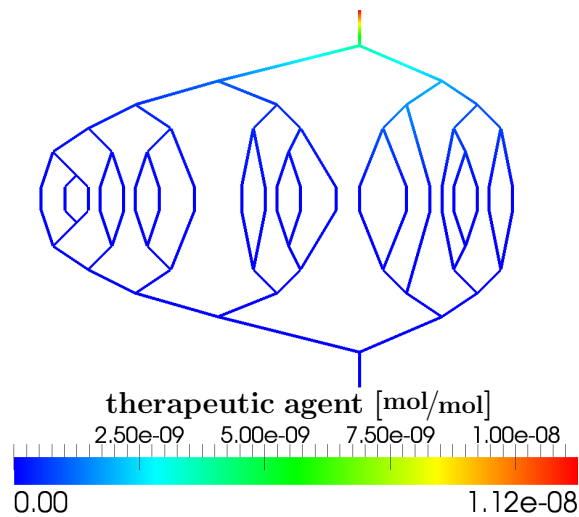
8.1.4 Simulation Results

The simulation is performed as detailed in the previous sections. Initially, the pressure and flow fields of the vascular graph are computed. A therapeutic agent is then introduced at the arterial root vertex. The dissolved drug molecules are advected through the vasculature. At the alveoli, a fraction of the blood plasma and therapeutic agent migrates into the tissue. The exchange rates and pharmacokinetics of this process differ between healthy and tumorous alveoli. Due to the inter-compartmental exchange, the pressure and flow field of the vascular graph have to be recomputed at each time step.

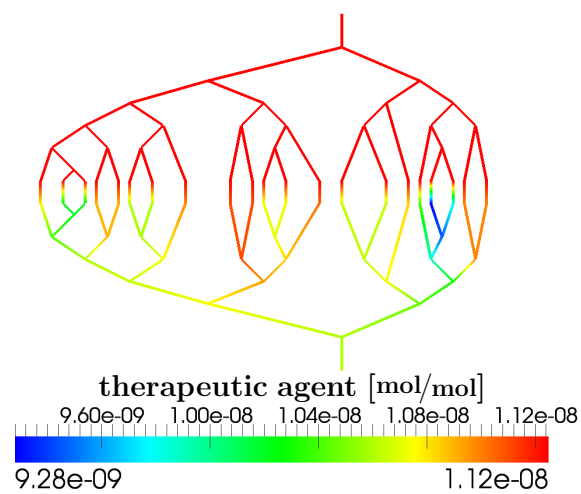
Figure 32 depicts the pressure field and the mole fraction of the drug molecules at different times during the simulation. The effective vessel resistance of a tumorous upscaled node is smaller than the vessel resistance of a healthy upscaled node. Therefore, the pressure gradient along the two edges that are connected with a tumorous upscaled node is smaller (see Figure 32 (a)). The dissolved therapeutic agent is irregularly distributed in the vascular graph (see Figure 32 (c)). The total amount of therapeutic agent that leaves the blood stream at the tumorous upscaled nodes is higher compared to the healthy upscaled nodes (see Figure 32 (c)). The maximum value for the drug concentration in the tissue is also higher for a tumorous upscaled node than for a healthy one (compare Figure 33 (d) with Figure 34 (d)). This depends on the different pressure fields in the blood and tissue continuum for the two kinds of upscaled nodes, as well as on the higher diffusive permeability and hydraulic conductivity of tumor vessels, and the increased number of blood vessels per unit volume of tissue in the tumor region.



(a)



(b)



(c)

Figure 32: Results of the vascular graph model. (a) Pressure distribution [Pa]. (b) A therapeutic agent is introduced at the arterial root vertex. Drug distribution [mol/mol] after one time step. (c) Drug distribution [mol/mol] after 11 seconds.

Figure 33 depicts the pressure and mole fraction distribution within the two continua of the double-continuum model for a single healthy upscaled node. For the visualization of the results of a healthy upscaled node, the red node situated in the leftmost position in Figure 29 is chosen. Figure 33 (a) and (b) show a cross-section through the model domain representing the pressure and mole fraction distribution for the capillary continuum. The pressures at the left side and the right side of the capillary continuum are equal to the pressures at the two adjacent nodes connected to the upscaled node. The administered therapeutic agent is distributed within the capillary bed as shown in Figure 33 (b). Figure 33 (c) and (d) show a cross-section through the model domain representing the pressure and mole fraction distribution for the pulmonary tissue continuum. According to Kurbel et al. (2001) [59], the interstitial fluid pressure in the human pulmonary tissue is -1064 Pa. Due to filtration and reabsorption processes across the capillary walls, the pressure slightly changes within the model domain (see Figure 33 (c)). The therapeutic agent is distributed within the pulmonary tissue corresponding to the pressure gradients in the pulmonary tissue. However, the amount of active ingredient is about three orders smaller compared to the capillary continuum (see Figure 33 (d)).

Figure 34 depicts the pressure and mole fraction distribution within the two continua of the double-continuum model for a tumorous upscaled node. In Figure 34 the results of the middle tumorous upscaled node are shown. For the tumorous upscaled node other parameters are used than for the healthy upscaled node (see Table 12). A further difference is that the flow and transport equations of the DCM for the tumorous upscaled node have no sink terms for describing the effects of the lymphatic system. The sink term $r_{adsorption}$ in (24) is only considered for the tumorous case. Due to the pressure distribution in the vascular graph (see Figure 32 (a)), the pressure boundary conditions for the capillary bed continuum of the healthy and the tumorous upscaled node are not the same (see Figure 33 (a) and Figure 34 (a)). The differing permeability fields used for the two kinds of upscaled nodes are a further reason for the different pressure fields in the capillary bed continuum of the tumorous upscaled node and the healthy upscaled node. The administered therapeutic agent is distributed within the capillary bed as shown in Figure 34 (b). Figure 34 (c) and (d) show a cross-section through the model domain representing the pressure and mole fraction distribution for the tumorous pulmonary tissue continuum. According to Jain (1998) [52], tumors exhibit high interstitial fluid pressures. Therefore, a Dirichlet pressure boundary condition of 133 Pa is set for the tissue continuum. Due to the lack of a functional lymphatic system and a higher filtration of fluid from the capillaries into the tumor tissue, the interstitial fluid pressure increases further in the model domain (see Figure 34 (c)). However, a certain amount of fluid is reabsorbed at the venous ends of the capillaries. Due to the higher vascular permeability and hydraulic conductivity of tumors (Jain (1998) [52]) and the presence of blood vessels in the whole model domain, the drug molecules are spread in the entire tumor tissue (see Figure 34 (d)).

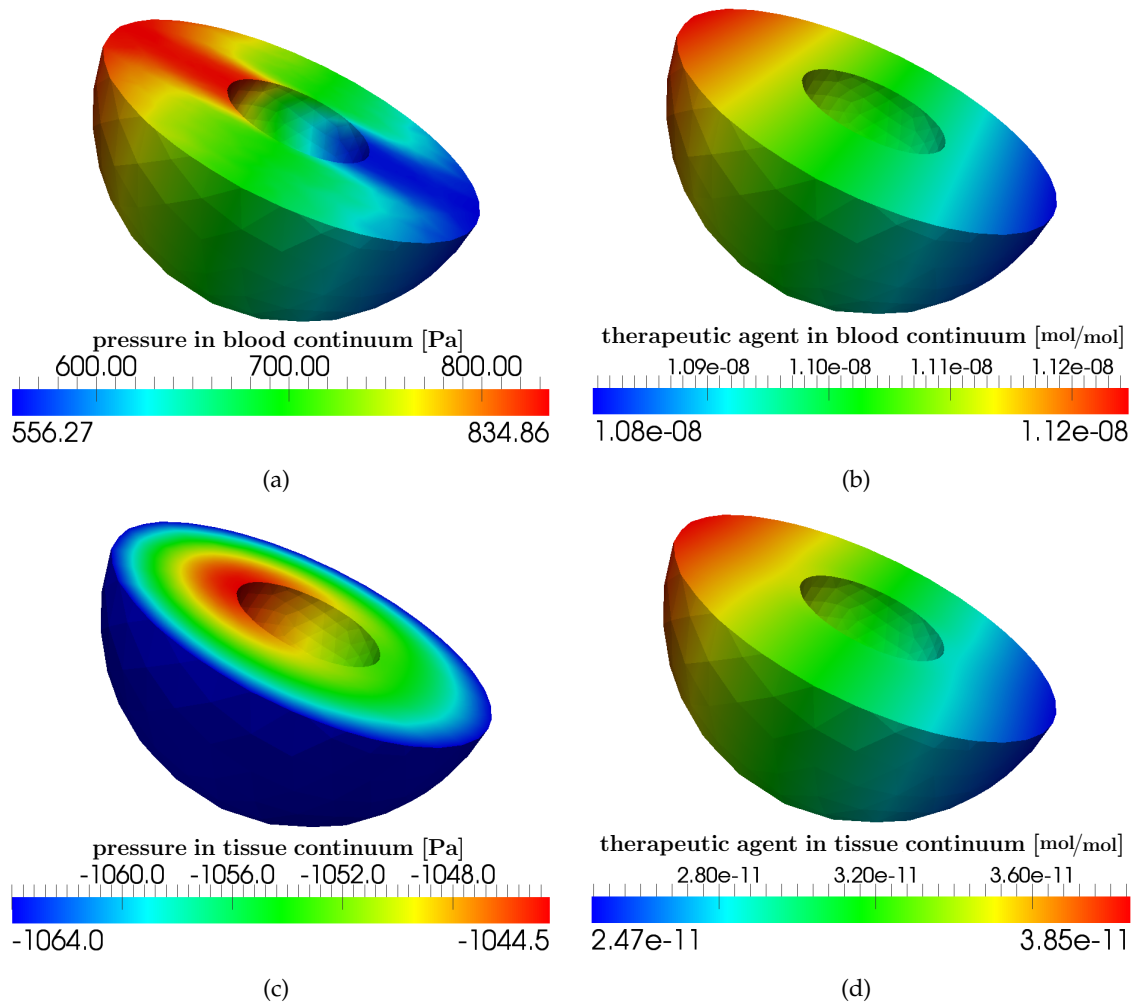


Figure 33: Results for a healthy alveolus (leftmost red node in Figure 29), at the final time step of the simulation. (a) Pressure distribution within the pulmonary capillary bed continuum [Pa]. (b) Drug distribution [mol/mol] within the pulmonary capillary bed continuum. (c) Pressure distribution within the pulmonary tissue continuum [Pa]. (d) Drug distribution [mol/mol] within the pulmonary tissue continuum.

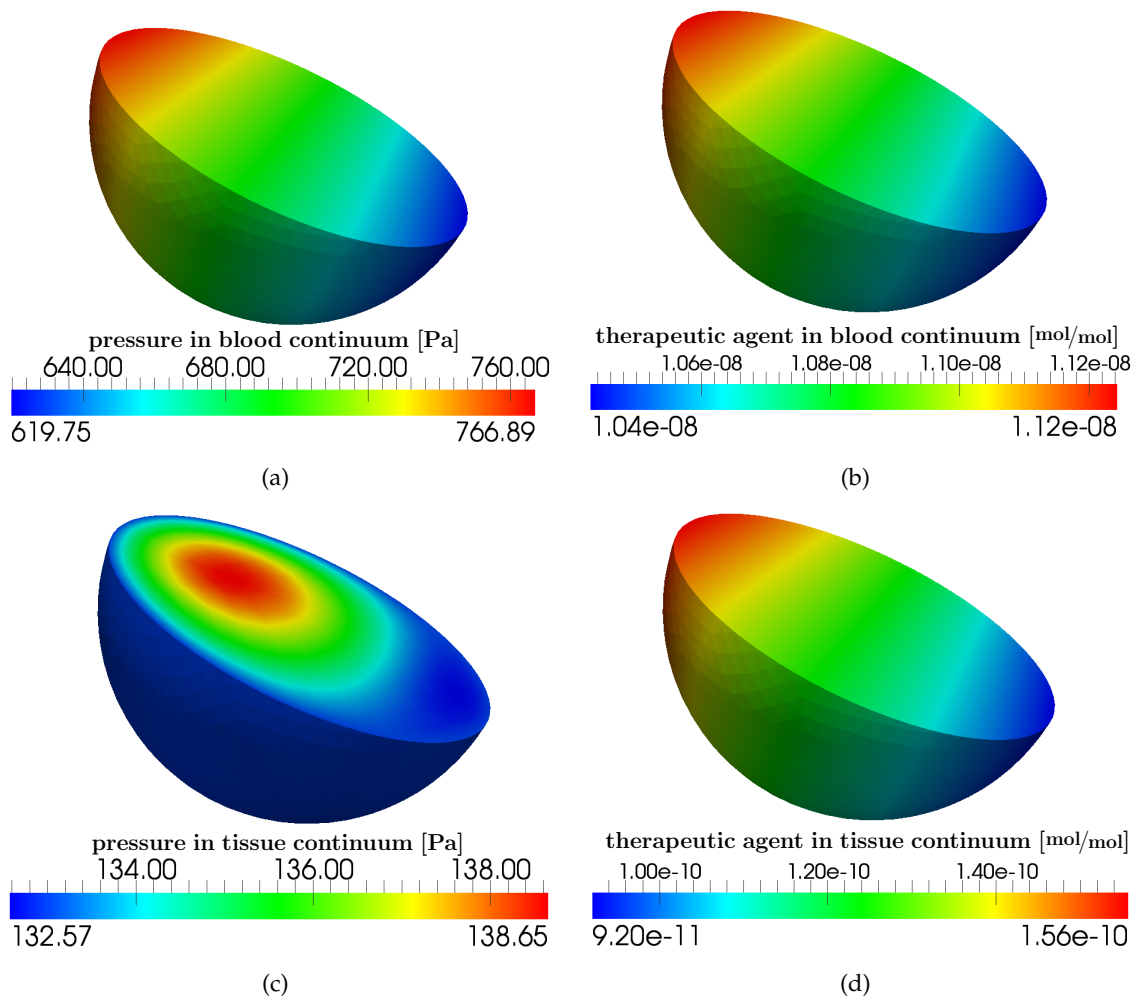


Figure 34: Results for a tumor alveolus (middle blue rectangle in Figure 29), at the final time step of the simulation. (a) Pressure distribution within the pulmonary capillary bed continuum [Pa]. (b) Drug distribution [mol/mol] within the pulmonary capillary bed continuum. (c) Pressure distribution within the pulmonary tissue continuum [Pa]. (d) Drug distribution [mol/mol] within the pulmonary tissue continuum.

8.2 Second Example - Simulating the Flow, Transport and Reaction of TRAIL Using the Multi-Scale Model

In this section, the multi-scale model described in Section 7.3 is applied to show the therapeutic efficiency of TRAIL against an alveolar cell carcinoma. The multi-scale model consists of:

- the vascular graph model for describing the spatiotemporal distribution of the drug in the pulmonary arteries, in the arterioles, in the venules and in the veins,
- the alveolus model for characterizing the spatiotemporal distribution in the alveolar capillaries, in the surrounding pulmonary tissue and in the cancer,
- and the low-dimensional population model for TRAIL-induced proapoptotic signaling for describing the reaction of the tumor cells to the administered therapeutic agent.

The model time of the second example is about twelve hours. The spatiotemporal distribution of the drug in the pulmonary blood vessels and in the pulmonary tissue lies in the order of several seconds up to minutes. However, the completion of apoptosis in the cancer cells induced by the administered therapeutic agent can take from several hours to more than 24 hours. The duration of apoptosis differs according to the type of the cell and of the tissue (Jang et al. (2003) [54]).

In addition, a local sensitivity analysis is done to identify the most important influences on the multi-scale model.

8.2.1 Simulation Setup

For the VGM, the same subset of the pulmonary vasculature (see Figure 29) is chosen as taken for the previous application in Section 8.1. There are still 18 healthy upscaled nodes and three tumorous upscaled nodes. The location of the single upscaled nodes remains unchanged. As in the first example, the cross-sectional compliance of the vessel segments and the influence of gravity on the blood flow through the vascular graph are neglected.

However, the model domains of the DCM for the different kinds of upscaled nodes are modified. In the case of a healthy upscaled node, a cube with a side length of $210\ \mu\text{m}$ is used now. Inside the cube, there is a spherical hole with a diameter of $140\ \mu\text{m}$ representing the alveolus (see Figure 35). The processes occurring within the alveolus are not considered

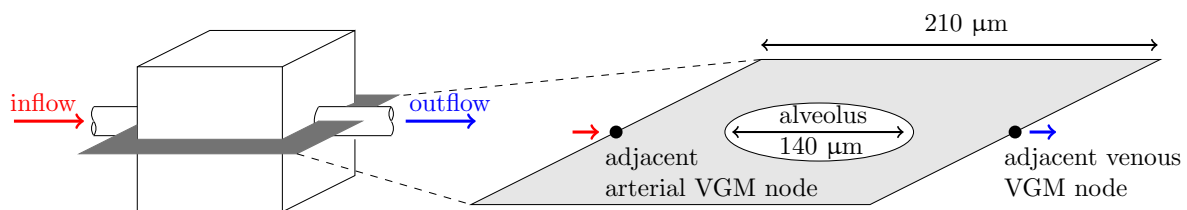


Figure 35: Model domain of a healthy upscaled node.

because the therapeutic agent is administered via a bolus injection into the blood stream. The model domain of the DCM for a tumorous upscaled node is now a cube with a side length of $364 \mu\text{m}$. As in the previous example, it is assumed that the cancer cells have destroyed the alveolar walls, and have penetrated into and filled the alveolus. The tumor vasculature consists of vessels from the already existing network of the host vasculature and new vessels resulting from the angiogenesis response of the host vessels to the cancer cells Jain (1998) [52]. There are still no necrotic regions. It is assumed that the arterial input to the capillary bed is on the left side of the alveolus, and the venous drainage occurs at the right side (see Figure 35). Blood cannot enter or leave the model domain via any other pathways. The [PMTS]_s is called for all three tumorous upscaled nodes.

8.2.2 Initial and Boundary Conditions

The system of equations of the vascular graph model is solved for the two primary variables: the pressure p and the mole fraction of dissolved therapeutic agent x . As in the previous application (see Section 8.1), the initial and the Dirichlet boundary conditions for the pressure are set at the root arterial and root venous vertex. The numerical values chosen do not differ from the one taken for the first application (see Chapter 8.1.2). At the root arterial vertex, the mole fraction of dissolved therapeutic agent x is set to $1.1249 \cdot 10^{-10}$. In this example, the initial condition for the mole fraction of dissolved therapeutic agent is two orders of magnitude smaller compared to the previous application. A too high initial mole fraction of dissolved therapeutic agent would result in the death of all cancer cells and so the heterogeneous behavior of the single tumor cells simulated with the [PMTS]_s cannot be shown.

The system of equations of the alveolus model is also solved for the two primary variables, the pressure p and the mole fraction of dissolved therapeutic agent x , in each of the two continua. The chosen initial and boundary conditions for the primary variables of the double-continuum model in the case of a healthy and a tumorous upscaled node are the same as for the first example (see Section 8.1.2)

The initial conditions for the low-dimensional population model for TRAIL-induced proapoptotic signaling are obtained by the approach that has already been described in detail in Section 6.2.

8.2.3 Parameters

For the simulation results shown in Section 8.2.5, most of the used parameter values are consistent with the parameters taken for the first example (see Section 8.1). The setup of the vascular graph is the same for the two examples presented in this chapter. Therefore, the vessel orders, the diameters and the lengths of the vessel segments that make up the vascular graph agree with the values presented in Section 8.1.3.

The parameter values used for the alveolus model are consistent with the values taken for the first application (see Table 12) except for three parameters in the case of a healthy upscaled node. These three parameters are the volume fraction of tissue f_T , the intrinsic permeability tensor \mathbf{K} in the continuum representing the capillary bed, and the surface area of

capillaries per unit volume of tissue $\frac{A_{vessel}}{V_{tissue}}$. The new values are shown in Table 14 and are caused by the change of the model domain for a healthy upscaled node.

Table 14: Changed model parameters of the alveolus model in the case of a healthy upscaled node.

parameter	symbol	unit	tissue	value	ref.
volume fraction of tissue	f_T	-	healthy	0.9	see text
intrinsic permeability	K	m ²	healthy	$2.0 \cdot 10^{-12}$	see text
surface area of capillaries per unit volume of tissue	$\frac{A_{vessel}}{V_{tissue}}$	1/m	healthy	$5.8 \cdot 10^4$	see text

It is still assumed that the alveolus is surrounded by a 12 μm thick layer which has a vascular volume fraction f_C of 0.9 (Effors (1984) [32]). Now, the volume of the non-vascularized tissue region above the 12 μm thick layer is smaller compared to the non-vascularized tissue region of the previous example. This results in a volume fraction of tissue f_T of 0.9. Due to the modified model domain volume of a healthy upscaled node, the value for the surface area of capillaries per unit volume of tissue $\frac{A_{vessel}}{V_{tissue}}$ changes from $1.9 \cdot 10^4$ 1/m to $5.8 \cdot 10^4$ 1/m. In the first example, the intrinsic permeability tensor \mathbf{K} in the continuum representing the healthy capillary bed is determined by the method described in Section 5.3. Now, the intrinsic permeability of the healthy capillary bed is determined by the relationship (50) as it is already done in the case of a tumorous capillary bed. The intrinsic permeability field of the healthy capillary bed is simplified to clearly identify the influence of \mathbf{K} on the multi-scale model by the local sensitivity analysis (see Section 8.2.6).

The model parameters of the low-dimensional population model for TRAIL-induced proapoptotic signaling for describing the reaction of the tumor cells to the administered therapeutic agent are listed in Table 9 and in Table 10. Due to the coupling of the [PMTS]_s to the DCM, the number of cancer cells represented by every node of the finite-element mesh of the alveolus model for a tumorous upscaled node has to be defined. The grid consists of 8000 cubic elements with a side length of 18.2 μm . A single human cell has an average volume of about 1000 (μm)³ (unpublished date of M. Doszczak and P. Scheurich). Thus, six cancer cells are assigned to each node of the finite element mesh. Further, the total number of grid nodes of the tumorous model domain of the DCM is required. The mesh used for the tumorous upscaled node consists of 9261 nodes.

8.2.4 Optimization of the Work Flow of the Multi-Scale Model for Long-Time Applications

To get biologically meaningful simulation results of the multi-scale model, it is necessary to run this model for at least twelve hours due to the fact that the response of the cancer cell population to a proapoptotic stimulus can take up to 24 hours (Jang et al. (2003) [54]). In the case of the multi-scale model, the maximum time-step size of all three models is given by the explicit time discretization of the VGM. The construction of the vascular graph and the assigned properties to the single vessel segments of the vascular graph used for the examples presented in this chapter result in a maximum time-step size of 0.0859512 seconds. If the DCM is called for all 21 upscaled nodes of the vascular graph and the [PMTS].s is executed for every tumorous upscaled node at every time step of the VGM this will lead to a total simulation time of the multi-scale model of about 48 years for a model time of twelve hours.

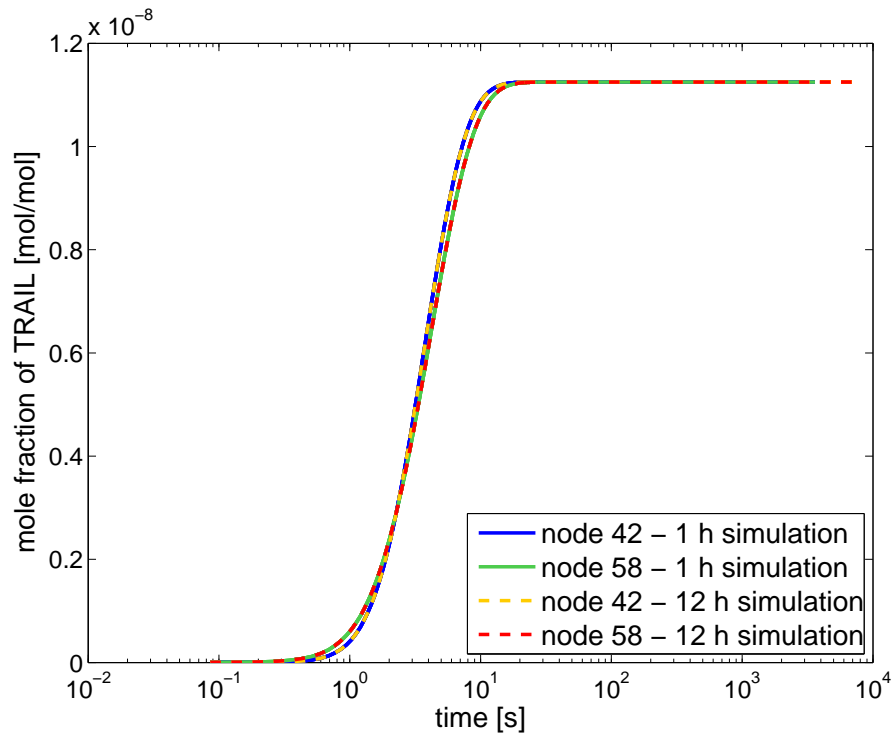
The investigations of the multi-scale model have shown that the most calculation-intensive process is the call of the DCM by the VGM. Therefore, the work flow of the multi-scale model has been optimized and sped up for the long-time application. Instead of executing the DCM for all upscaled nodes at every explicit time step of the VGM, the alveolus model is called after a previous determined time interval, for example every hour of the model time, and then the flow field and the drug distribution of the vascular graph are corrected for the length of this time interval. After the correction of the simulation results of the VGM, the vascular graph model simulates the next time period and calls the DCM afterwards to adjust the results. Now, the alveolus model provides the amount of fluid and therapeutic agent leaving the blood stream for the duration of the determined time interval to the vascular graph model. To minimize the error between the solutions of the detailed simulation and the sped up simulation, the type of the boundary condition for the mole fraction of dissolved therapeutic agent x_c in the capillary bed continuum is modified for the sped up case. Now, the Dirichlet boundary condition for x_c changes with time. For every upscaled node of the vascular graph, the mole fractions of dissolved therapeutic agent x_{in} and x_{out} at the two nodes connected with the arterial and venous side of the considered upscaled node (see small picture in Figure 37) are written to two different files for each time step of the vascular graph model. Thus, the mole fractions of dissolved therapeutic agent at the two adjacent nodes of the considered upscaled node are known at each time point of the simulation of the DCM. When the alveolus model is executed x_{in} and x_{out} are taken as initial and Dirichlet boundary condition on the left and on the right side of the model domain of the alveolus model. A linear decrease of the mole fraction of dissolved therapeutic agent x_c between x_{in} and x_{out} provide the initial and the boundary conditions for the remaining sides of the model domain. The initial and boundary condition for x_c are looked up in the two files written by the VGM and adapted at each time step of the simulation of the alveolus model.

The above described approach can only be applied if the error done by the speed up of the work flow of the multi-scale model is negligibly small. For the application presented in this section, the DCM should be executed at every full hour of the total model time. A model time of twelve hours for a model consisting only of the alveolus model coupled to the vascular graph model would result in a simulation time of about 20 years. To determine

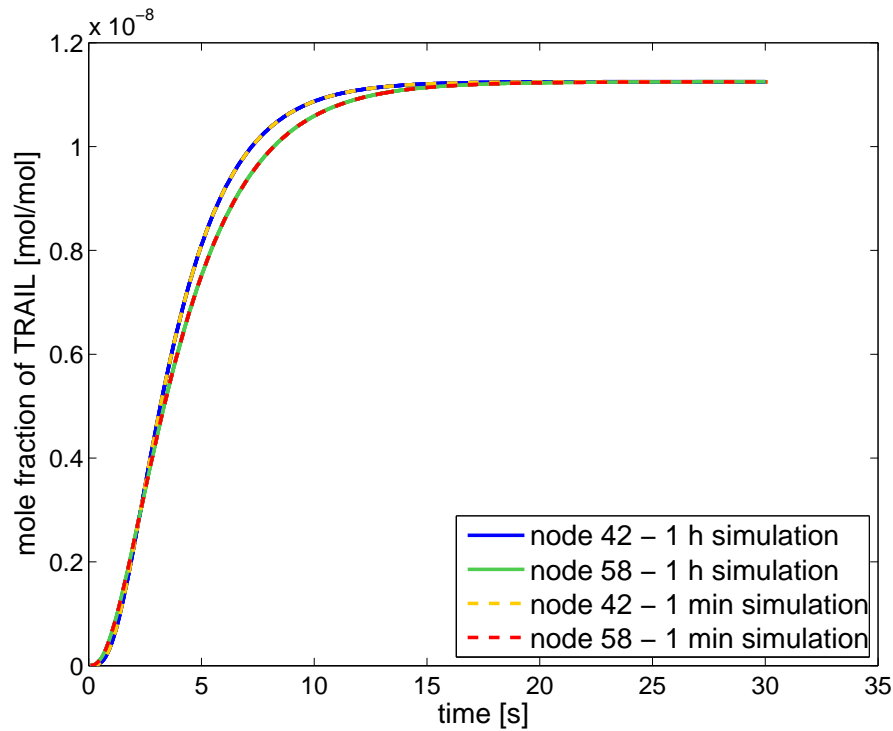
the error done by the speed up of the work flow of the multi-scale model, three different simulations have been performed and have been compared against one another. The result of the *twelve hours simulation* (coupling of the DCM to the VGM in one hour steps; total model time of twelve hours) is compared with the *one hour simulation* (coupling of the DCM to the VGM in one minute steps; total model time of one hour). If there is a good agreement between the two simulations the *one hour simulation* will be compared with the *one minute simulation* (coupling of the DCM to the VGM at every explicit vascular graph time step; total model time of one minute). The simulation results of the three scenarios, the *twelve hours simulation*, the *one hour simulation* and the *one minute simulation*, are tested and controlled for every upscaled node of the considered asymmetric vascular graph. However, the findings of this simulation study are only shown for one healthy upscaled node, namely the red node situated in the leftmost position in Figure 29 called node 42, and for one tumorous upscaled node, namely the middle tumorous upscaled node in Figure 29 called node 58. Figure 36 (a) depicts the comparison of the simulation results of the *twelve hours simulation* with the results of the *one hour simulation*. There is no difference between the solutions of the two scenarios for the two types of upscaled nodes. The same applies to the comparison of the simulation results of the *one hour simulation* with the results of the *one minute simulation* (see Figure 36 (b)). The results of the remaining upscaled nodes also show the same agreements between the *twelve hours simulation* and the *one hour simulation* and between the *one hour simulation* and the *one minute simulation*. From this it follows that it is acceptable to execute the alveolus model at hourly intervals of the total model time.

For the tumorous upscaled nodes, the low-dimensional population model for TRAIL-induced proapoptotic signaling is also not called for every explicit time step of the vascular graph model. The [PMTS]_s is only executed at the last time step of the simulation. However, the simulation of the [PMTS]_s takes into account the temporal distribution of the administered therapeutic agent in the tumor tissue over the total model time. There are two reasons for executing the low-dimensional population model for TRAIL-induced proapoptotic signaling only once at the end of the simulation. First, the whole interest is to know the per cent of the apoptotic cell fraction at the end of the simulation. The intermediate results of the [PMTS]_s are not of interest. Changes of the drug transport in the tumor occur after a 16- to 24-hours time lag after the first treatment due to a decreased tumor cell density and an expanded interstitial space (Jang et al. (2003) [54]). The structural changes within the tumor caused by the drug-induced apoptosis are not covered by the multi-scale model until now. Second it is omitted to calculate the amount of bound therapeutic agent with the [PMTS]_s to reduce the simulation time of the multi-scale model further. The reduction of the free available therapeutic agent in the cancer by the binding of the drug molecules to the tumor cells is already taken into account by the sink term (26) in the system of equations of the alveolus model.

A third approach to speed up the simulation time of the multi-scale model is applied. If an upscaled node has the same initial and boundary conditions and equal properties as its adjacent upscaled node in the vascular graph the DCM will not be called again by the vascular graph model. The results of the simulation of the corresponding adjacent upscaled node are taken as correction factors for the VGM for the considered upscaled node.



(a)



(b)

Figure 36: (a) Comparison of the simulation results of the *twelve hours simulation* with the results of the *one hour simulation* for the healthy upscaled node 42 and the tumorous upscaled node 58. (b) Comparison of the simulation results of the *one hour simulation* with the results of the *one minute simulation* for the healthy upscaled node 42 and the tumorous upscaled node 58.

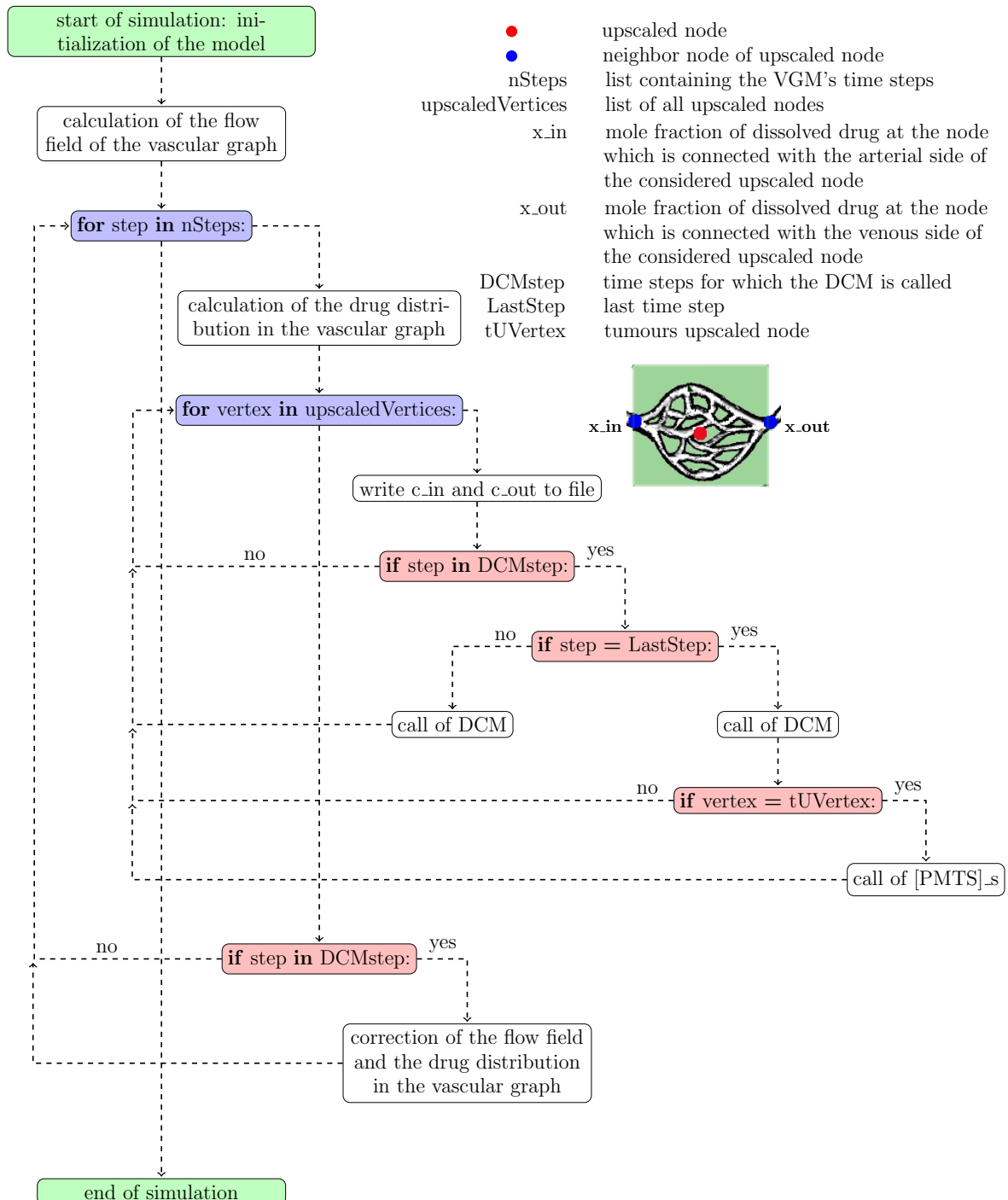


Figure 37: Work flow of the multi-scale model for a long-time application.

The above described methods reduce the simulation time of the multi-scale model from several years to hours. Figure 37 depicts the modified work flow of the multi-scale model for the long-time application. After the initialization of the coupled model, Equation (14) is solved the first time to determine the flow field in the vascular graph. Then, a for loop over all time steps of the VGM is executed. First, the distribution of the administered therapeutic agent is calculated using Equation (18). Afterwards, a second for loop over all upscaled nodes of the vascular graph is entered. For every upscaled node, the mole fraction of dissolved therapeutic agent at the arterial and at the venous side of the considered upscaled node are written to two different files. If the actual time step of the VGM is a so-called *DCMstep* the alveolus model will be called for the considered upscaled node. A *DCMstep* is defined as such a time step for which the double-continuum model should be executed. The duration of the simulation of the alveolus model is equivalent to the length of the time interval between two *DCMsteps*. For each time step of the simulation of the DCM, the boundary conditions for the capillary bed continuum are adapted by the values provided by the vascular graph model (see Figure 38). If the actual time step is also the last time step of the current simulation, the so-called *LastStep*, and the considered upscaled node is a tumorous upscaled node the [PMTS]_s will be executed. As it is depicted in Figure 38, the [PMTS]_s takes into account all time steps of the DCM's simulations.

After the successful execution of the second for loop, the flow field and the spatial drug distribution of the VGM will be corrected if the actual time step of the vascular graph model is a *DCMstep*. Then, the calculations for the next time step of the vascular graph model start. This work flow is used for the generation of the simulation results shown in the subsequent section.

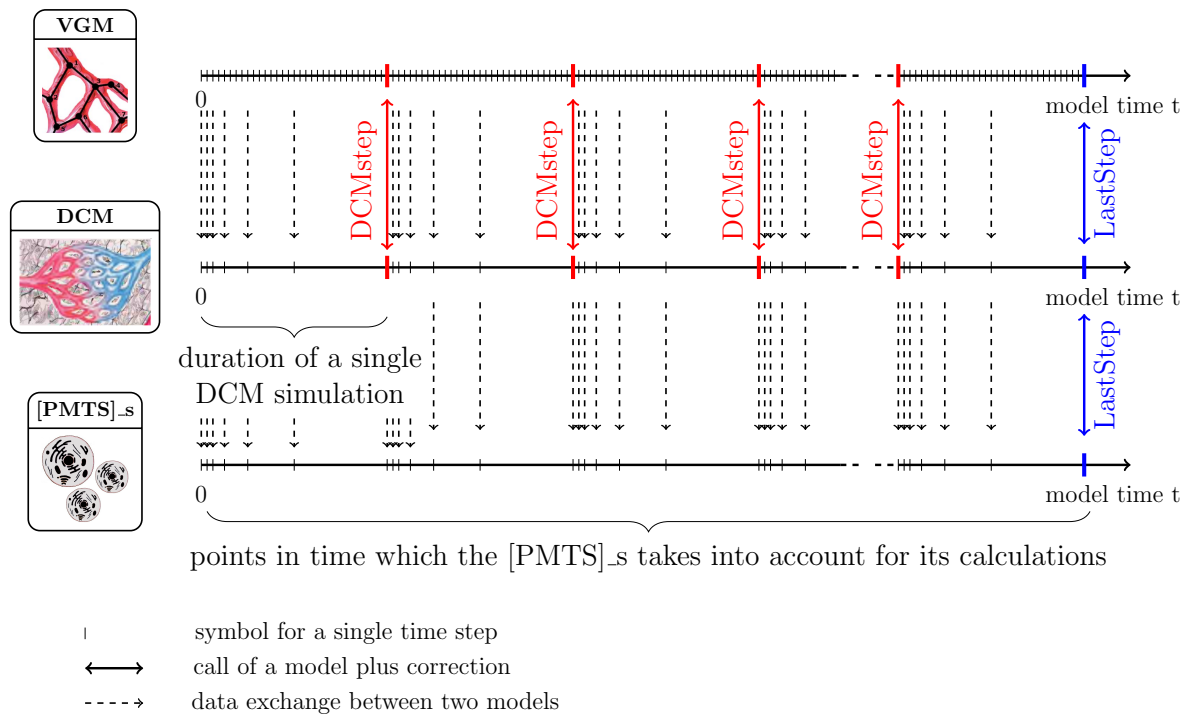


Figure 38: Different time scales of the multi-scale model for the long-time application.

8.2.5 Simulation Results

The multi-scale model is applied to simulate the therapeutic efficiency of TRAIL against an alveolar cell carcinoma. The drug is administered by a continuous bolus injection of twelve hours. The simulation is performed using the simulation setup explained in Section 8.2.1, the initial and boundary conditions defined in Section 8.2.2, the parameter values presented in Section 8.2.3 and the work flow described in Section 8.2.4.

As the setup of the vascular graph is the same as for the first example presented in this chapter, the pressure field of the vascular graph remains unchanged. Therefore, it is not depicted again. The pressure distribution of the first example has been shown in Figure 32 (a). The correction of the pressure field of the VGM after the execution of the DCM lead to no significant changes of the pressure distribution in the vascular graph.

In Figure 39 the drug distribution over the total model time of twelve hours is illustrated for three nodes of the considered asymmetric vascular graph, namely the healthy upscaled node 42, the tumorous upscaled node 58 and the root venous vertex. The effective resistance of the upscaled edges connected with the tumorous upscaled node 58 is smaller than the

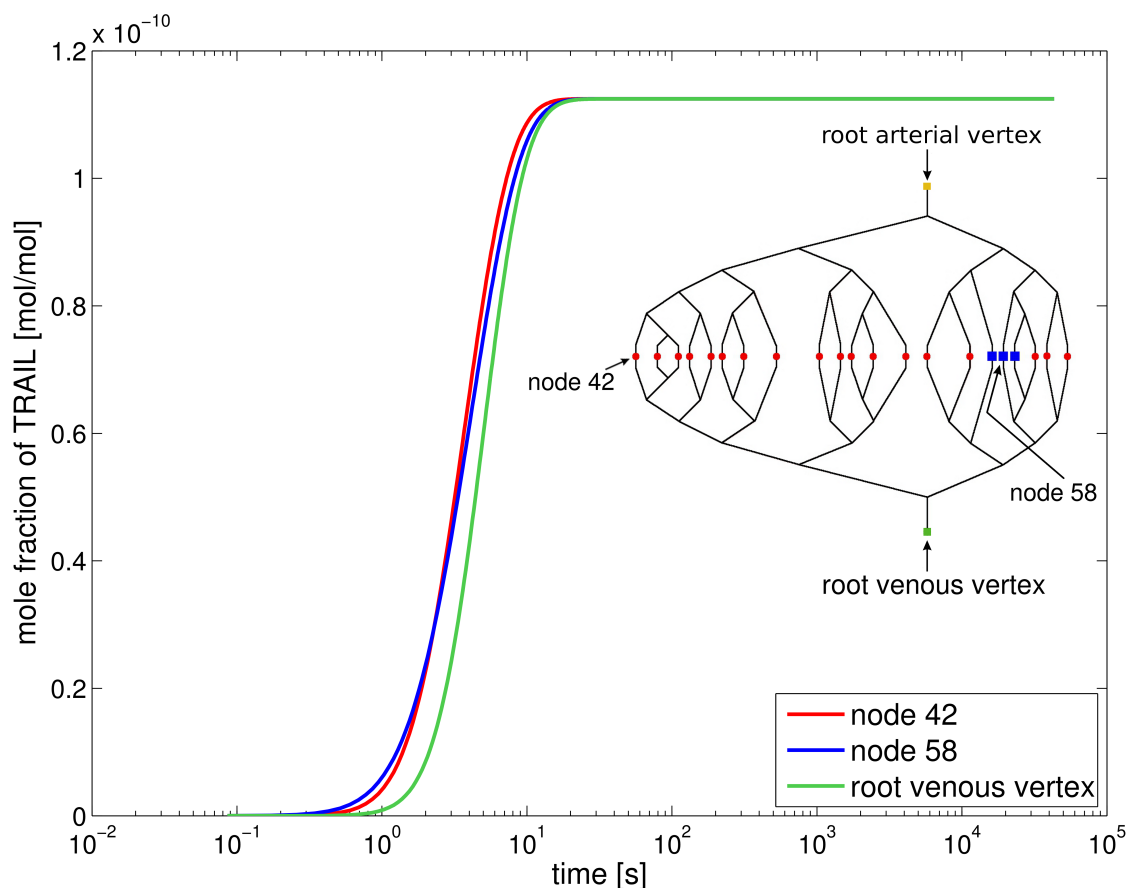


Figure 39: Drug distribution over the model time of twelve hours shown at three different nodes of the vascular graph: the healthy upscaled node 42, the tumorous upscaled node 58 and the root venous node.

resistance of the upscaled edges connected with the healthy upscaled node 42. The reason for this is the larger radius of the tumor capillaries r_c . According to Jang et al. (2003) [54], r_c is set to 10 μm for the tumor blood vessels and to 4 μm for the healthy capillaries according to Renkin et al. (1984) [82]. Due to the lower resistance of the tumorous upscaled edges, the flow rate through this segments of the vascular graph is faster. So, the therapeutic agent will reach these parts earlier. However, the effective volume of the tumorous upscaled edges is higher than the effective volume of the healthy upscaled edges. The consequence is that the dissolved drug molecules are transported faster to the tumor nodes of the vascular graph and need longer time to pass through those nodes (see Figure 39). After about ten seconds, the initial mole fraction of dissolved therapeutic agent x of $1.1249 \cdot 10^{-10}$ set at the root arterial vertex reaches the root venous vertex.

Figure 40 depicts the pressure and the mole fraction distribution within the two continua of the double-continuum model for the healthy upscaled node 42 after one hour. Figure 40 (a) and (b) depict a cross-section through the model domain representing the pressure and the mole fraction distribution for the capillary bed continuum. The pressures at the left side and the right side of the capillary continuum are equal to the pressures at the two adjacent nodes connected to the upscaled node 42. In the capillary bed continuum, the mole fraction of dissolved therapeutic agent x_c has reached its maximum value (see Figure 40 (b)). Figure 40 (c) and (d) show a cross-section through the model domain representing the pressure and the mole fraction distribution for the pulmonary tissue continuum. According to Kurbel et al. (2001) [59], the interstitial fluid pressure in the human pulmonary tissue is set to -1064 Pa. Due to filtration and reabsorption processes across the capillary walls, the pressure slightly changes within the model domain (see Figure 40 (c)). At the arterial side of the model domain, the pressure difference between the capillary bed continuum and the pulmonary tissue continuum is much higher than on the venous side of the model domain. According to Starling's law (see Equation (31)), more fluid filtrates into the tissue continuum on the arterial side of the model domain than on the venous side. Therefore, there is a higher pressure increase on the left side of the model domain of the tissue continuum. The therapeutic agent is distributed within the pulmonary tissue corresponding to the pressure gradients in the pulmonary tissue. However, the amount of active ingredient is still smaller compared to the capillary continuum after one hour of the total model time of twelve hours (see Figure 40 (d)).

Figure 41 depicts the pressure and the mole fraction distribution within the two continua of the double-continuum model for the tumorous upscaled node 58 after one hour model time. Due to the pressure distribution in the vascular graph, the pressure boundary conditions for the capillary bed continuum of the healthy and the tumorous upscaled nodes are not the same (compare Figure 40 (a) with Figure 41 (a)). The administered therapeutic agent is distributed within the capillary bed as shown in Figure 41 (b) and has reached its maximum value as in the case of the healthy upscaled node 42. Figure 41 (c) and (d) show a cross-section through the model domain representing the pressure and the mole fraction distribution for the tumorous pulmonary tissue continuum. According to Jain (1998) [52], a Dirichlet pressure boundary condition of 133 Pa is set for the tissue continuum. Due to the lack of a functional lymphatic system and an higher filtration of

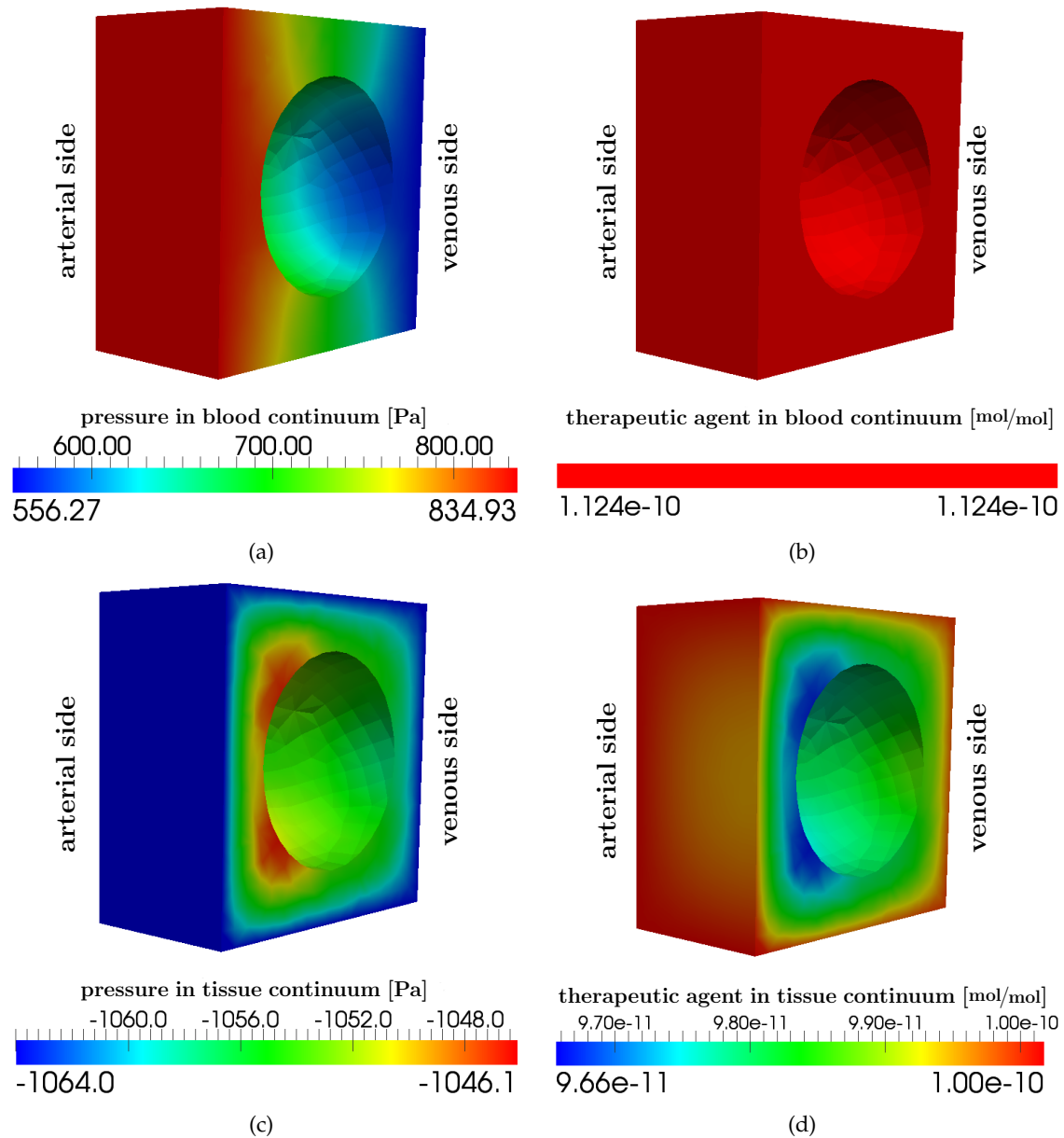


Figure 40: Results for the healthy alveolus (leftmost red node in Figure 29; node 42) after one hour. (a) Pressure distribution within the pulmonary capillary bed continuum [Pa]. (b) Drug distribution [mol/mol] within the pulmonary capillary bed continuum. (c) Pressure distribution within the pulmonary tissue continuum [Pa]. (d) Drug distribution [mol/mol] within the pulmonary tissue continuum.

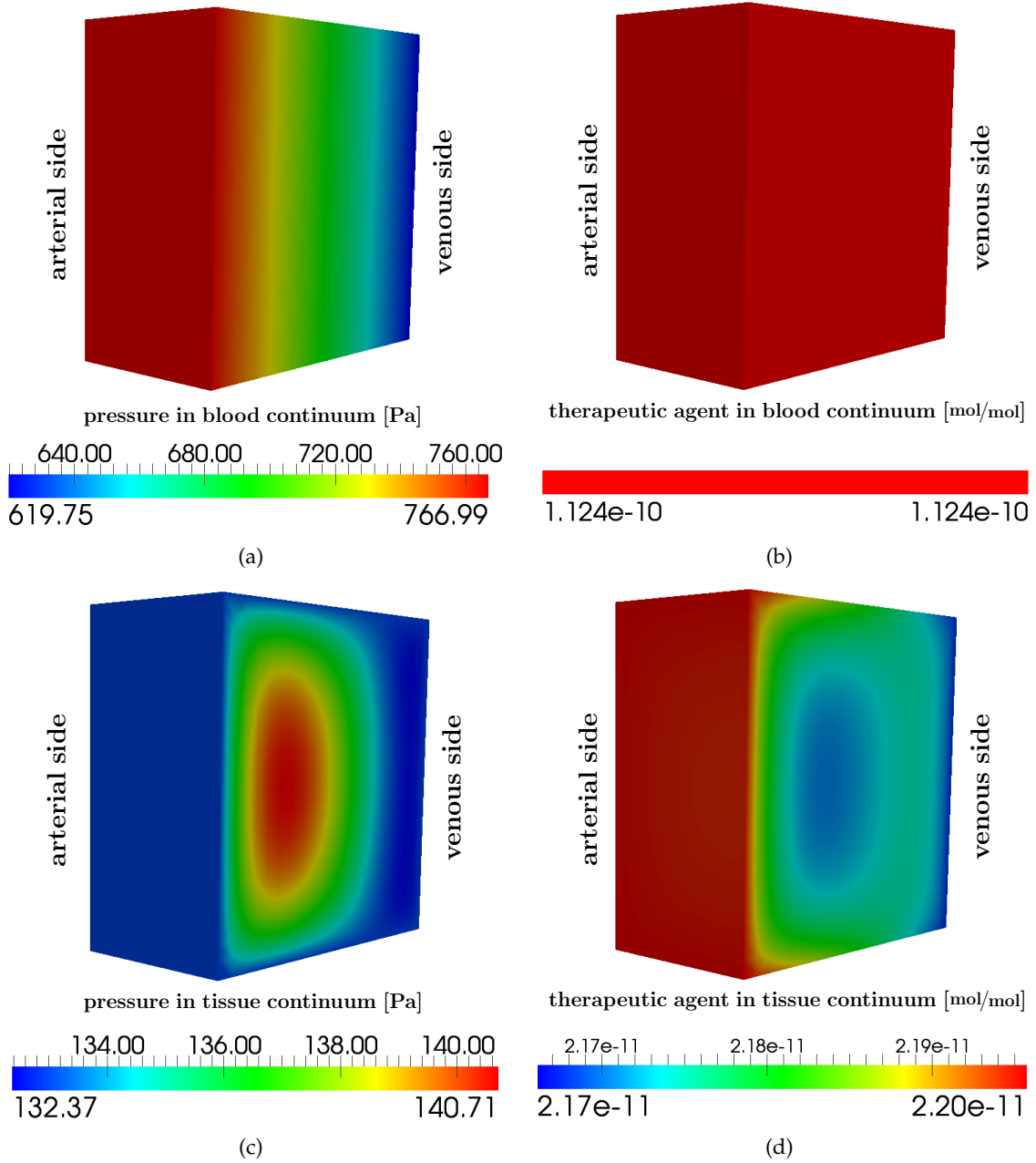


Figure 41: Results for the tumorous alveolus (middle blue rectangle in Figure 29; node 58) after one hour. (a) Pressure distribution within the pulmonary capillary bed continuum [Pa]. (b) Drug distribution [mol/mol] within the pulmonary capillary bed continuum. (c) Pressure distribution within the pulmonary tissue continuum [Pa]. (d) Drug distribution [mol/mol] within the pulmonary tissue continuum.

fluid from the capillaries into the tumor tissue, the interstitial fluid pressure increases further in the model domain (see Figure 41 (c)). However, a certain amount of fluid is reabsorbed at the venous ends of the capillaries. Due to the higher vascular permeability and hydraulic conductivity of tumors (Jain (1998) [52]) and the presence of blood vessels in the whole model domain, the drug molecules are spread in the entire tumor tissue (see Figure 41 (d)).

By the comparison of Figure 40 (d) with Figure 41 (d) it becomes visible that after one hour model time the average amount of therapeutic agent in the healthy pulmonary tissue of the upscaled node 42 is higher than in the tumor tissue of the upscaled node 58. The first example presented in this chapter has shown that the average amount of therapeutic agent in the healthy pulmonary tissue of the upscaled node 42 is smaller than in the tumor tissue of the upscaled node 58 after a model time of eleven seconds (compare Figure 33 (d) with Figure 34 (d)). Figure 42 proves the observations made by the comparison of Figure 33 (d) with Figure 34 (d) and Figure 40 (d) with Figure 41 (d). For the first 100 seconds of the simulation the mole fraction of dissolved therapeutic agent is higher in the tumor tissue. Afterwards, the situation changes. Finally, the mole fraction of dissolved therapeutic agent in the tissue continuum of the upscaled node 42 is six times higher than in the tumor tissue of the upscaled node 58. Neither in the tissue continuum of the tumorous upscaled node 57, of the tumorous upscaled node 58, nor of the tumorous upscaled node 59 is a higher maximum value

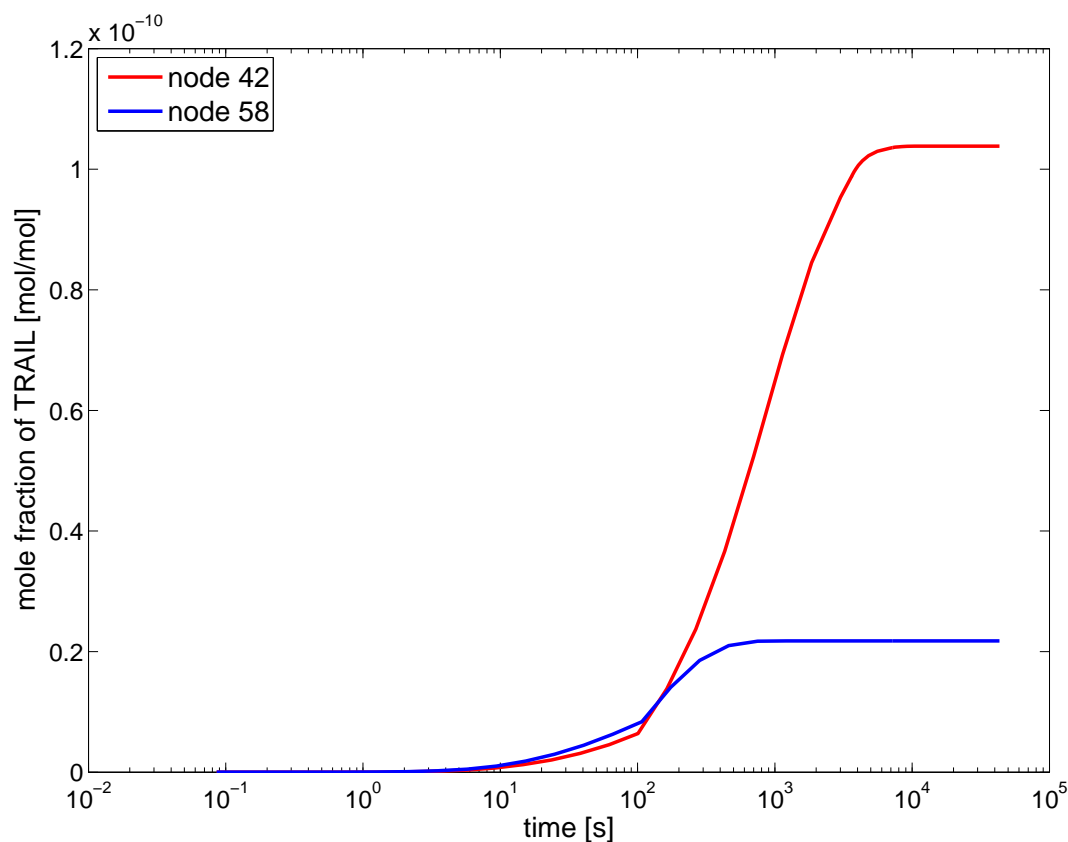


Figure 42: Average drug distribution in the tissue continuum over the model time of twelve hours for the healthy upscaled node 42 and for the tumorous upscaled node 58.

for the mole fraction of TRAIL reached (see Figure 43). The higher diffusive permeability P , the higher hydraulic conductivity L_p and the lower solvent-drag reflection coefficient σ_f of the tumorous capillary walls cause the faster enrichment of the therapeutic agent in the tissue continuum of the upscaled node 58. The maximum mole fraction of TRAIL that can be reached in the tissue continuum is mainly determined by the pressure gradients and the concentration gradients between the capillary bed and the tissue continuum of the alveolus model (see Stavermann-Kedem-Katchalsky equation (32)). The maximum mole fraction of dissolved therapeutic agent in the capillary bed continuum is identical for the healthy and the tumorous upscaled nodes. However, the pressure gradients between the two continua of the DCM are different for the two kinds of upscaled nodes. This explains the higher maximal mole fraction of dissolved therapeutic agent in the tissue continuum of a healthy upscaled node. Further, the increased pressure gradients in the tumor interstitium (see Figure 41 (c) or Jain (1987) [50]) cause an outflow of interstitial fluid and dissolved therapeutic agent.

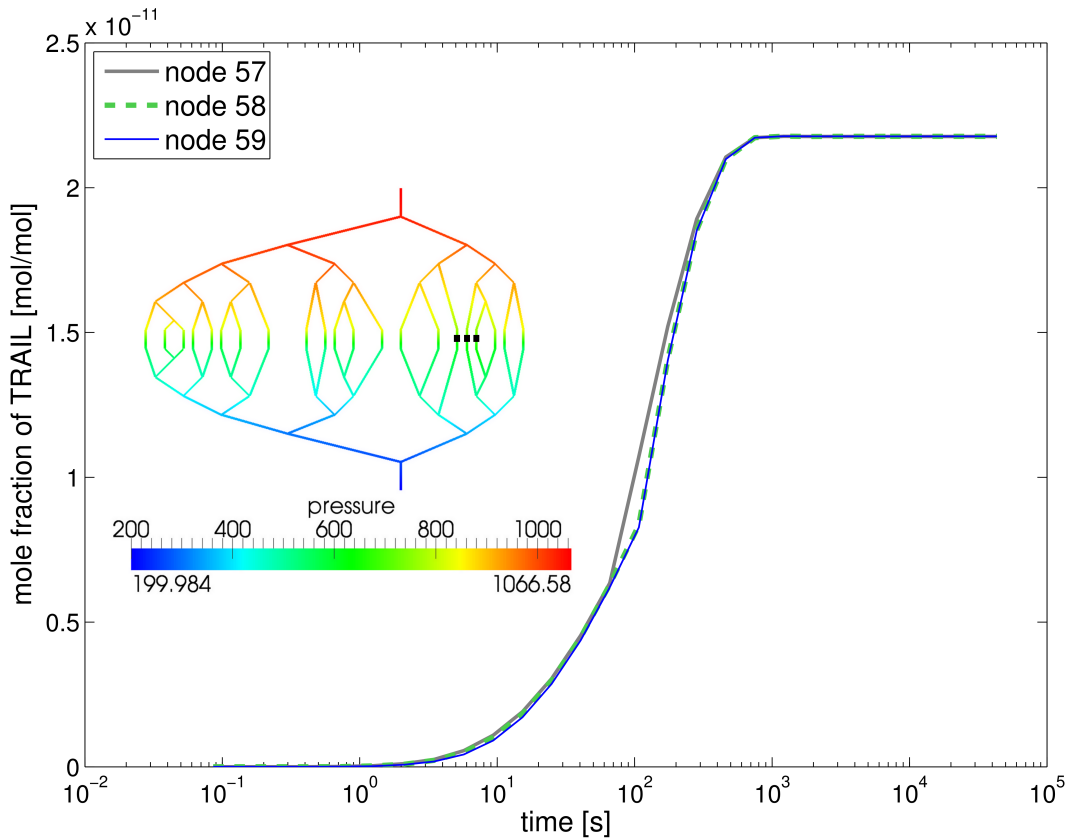


Figure 43: Average drug distribution in the tissue continuum over the model time of twelve hours shown for all three tumorous upscaled nodes (left black rectangle = node 57, middle black rectangle = node 58, right black rectangle = node 59).

When the double-continuum model is executed for the last time, the simulation of the low-dimensional population model for TRAIL-induced proapoptotic signaling is started for all three tumorous upscaled nodes of the vascular graph model: node 57, node 58 and node 59. For the upscaled node 58, Figure 44 depicts the percent of cancer cells that irreversibly undergo the programmed cell death after a continuous bolus injection of the therapeutic agent TRAIL over twelve hours. The response of the cells to the TRAIL stimulus is highly heterogeneous. There are two sources for this heterogeneous behavior of the alveolar cell carcinoma to the administered therapeutic agent: the variability of the individual cancer cells in the tumor and the spatial difference in the TRAIL concentration over the model domain.

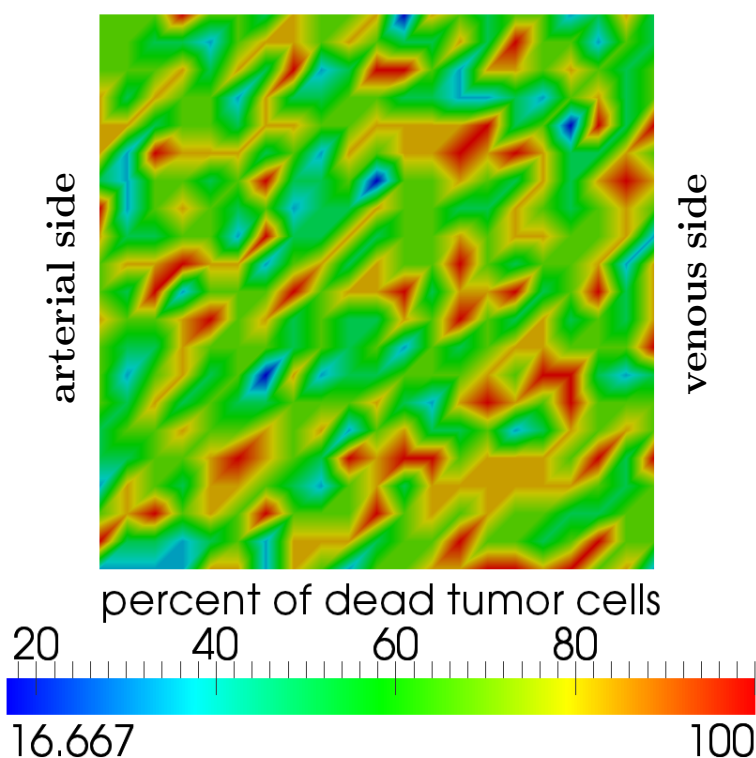


Figure 44: Percent of dead cancer cells at the upscaled node 58 (top view on the horizontal cross section through the middle of the model domain).

8.2.6 Local Sensitivity Analysis of the Multi-Scale Model

To apportion the uncertainty in the output variables to the uncertainty in all used model parameters in other words to identify the most important influences on the multi-scale model, a local sensitivity analysis¹ is done. The local sensitivity analysis helps to determine:

¹According to Saltelli et al. (2000) [83], the different sensitivity analysis methods can be grouped into three classes: local, global and screening. The choice of the method is a decision between the computational cost and the information gained by the applied sensitivity analysis.

- the factors that mainly contribute to the output variability and that require additional investigations to strengthen the understanding of the model and
- the parameters or the mathematical terms of the system of equations of the multi-scale model that are irrelevant and so can be eliminated from the final model (Saltelli et al. (2000) [83]).

The local sensitivity matrix \mathbf{S} of the multi-scale model is determined using the finite-difference approximation. The elements of the sensitivity matrix $S_{o_j}^y(t)$ at the time t are calculated by:

$$\left. \frac{\partial \mathbf{y}}{\partial o_j} \right|_{o,t} \approx \frac{\mathbf{y}(t, o_j + \Delta o_j) - \mathbf{y}(t, o_j)}{\Delta o_j}, \quad j = 1, \dots, m, \quad (53)$$

where o_j is the varied parameter of the m -vector of parameters \mathbf{o} , \mathbf{y} is the n -vector of output variables and Δo_j is the parameter change (Saltelli et al. (2000) [83]). To make the local sensitivity matrix \mathbf{S} independent of the physical units of the parameters and variables of the multi-scale model, the normalized local sensitivity matrix $\tilde{\mathbf{S}}$ defined as:

$$\tilde{\mathbf{S}}(t) = \left\{ \frac{o_j}{y_i(t)} \frac{\partial y_i(t)}{\partial o_j} \right\} \quad (54)$$

for the time t is used (Saltelli et al. (2000) [83]). In contrast to the coefficients of the local sensitivity matrix \mathbf{S} , the normalized sensitivity coefficients can be compared with each other. The local sensitivity analysis presented in this section consists of 44 realizations, namely the baseline case plus the variation of 43 different parameters. For a single run, one parameter out of the 43 is changed by five per cent of its nominal value and all the other model parameters are kept constant (see Table 15). According to Saltelli et al. (2000) [83], a parameter change of five per cent is the upper limit for the assumption of the local linearity in the case of a nonlinear model. The model is run repeatedly for each realization to get the output variables for the parameters of interest. The vector \mathbf{y} consists of the following output variables:

- the pressure p_c in the capillary bed continuum,
- the pressure p_{is} in the interstitial space of the tissue continuum,
- the mole fraction of dissolved therapeutic agent x_c in the capillary bed continuum,
- the mole fraction of dissolved therapeutic agent x_{is} in the tissue continuum,
- the fluid flow q_F across the pulmonary capillary walls (defined by Equation (31)),
- the transport of dissolved drug molecules q_T through the capillaries into the tissue and vice versa (defined by Equation (32)) and
- the percentage of cancer cells undergoing cell death after a treatment of the tumor tissue with TRAIL for twelve hours $f_{deadCells}$.

In this thesis, the findings of the sensitivity analysis are depicted for the healthy upscaled node 42 (see Figure 45) and for the tumorous upscaled node 58 (see Figure 46). Due to the non-linearity of the multi-scale model and the different conditions at the individual upscaled nodes of the considered asymmetric vascular graph, the coefficients of the normalized local sensitivity matrix vary slightly from one upscaled node to another. However, the same parameters are of importance for all healthy upscaled nodes and for all tumorous ones. The multi-scale model is a time-dependent problem. Therefore, Figure 45 and Figure 46 represent the maximal normalized local sensitivity matrix over the total model time of twelve hours. On the x-axis all varied parameters are plotted. The considered output variables are depicted on the y-axis. Both figures illustrate that only a few of the parameters listed in Table 15 are of great importance.

In the case of the healthy upscaled node 42, as well as in the case of the tumorous upscaled node 58, the radius of the healthy and the tumorous capillary vessels, $r_{vessel,h}$ and $r_{vessel,t}$ are relevant. An increase of $r_{vessel,h}$ or $r_{vessel,t}$ leads to a decreased vessel resistance R_{ij} (see Equation (16)) for the upscaled edges of the affected upscaled nodes in the vascular graph and a higher intrinsic permeability \mathbf{K} (see Equation (50)) in the capillary bed continuum. A smaller vessel resistance for the upscaled edges results in a higher mass flow rate through these vessel segments. Thus, more therapeutic agent is transported to the upscaled nodes. This is confirmed by the high local sensitivity coefficients for the two output variables q_T and x_c (see Figure 45 and Figure 46). Looking at the healthy upscaled node 42 (Figure 45), the variation of the radius of the healthy capillary vessels $r_{vessel,h}$ affects the pressure p_c in the capillary bed continuum and the pressure p_{is} in the tissue continuum. A change of the radius of the tumor blood vessels $r_{vessel,t}$ also has an influence on p_c and p_{is} of the upscaled node 42. This behavior of the multi-scale model is caused by the modification of the pressure field in the vascular graph by the variation of the vessel resistance R_{ij} of the upscaled edges by changing $r_{vessel,h}$ or $r_{vessel,t}$. The same is valid for the tumorous upscaled node 58. For the tumorous upscaled node 58, the parameters $r_{vessel,h}$ and $r_{vessel,t}$ are the only two parameters of the parameter vector \mathbf{o} that significantly influence the percentage of cancer cells undergoing cell death after a treatment of the tumor tissue with TRAIL for twelve hours (see output variable $f_{deadCells}$ in Figure 46). As Figure 46 depicts, the initial mole fraction of therapeutic agent x_{co} set at the root arterial vertex of the considered asymmetric vascular graph is of less importance for the output variable $f_{deadCells}$. The flow rate through the vascular graph determined by the parameters $r_{vessel,h}$ and $r_{vessel,t}$ seems to have a higher influence on the amount of therapeutic agent reaching the cancer cells than the parameter x_{co} . This assumption is strengthened by the sensitivity coefficients of the output variable x_{is} for the parameters $r_{vessel,h}$, $r_{vessel,t}$ and x_{co} . The variation of the molar density ρ_{mol} of blood and of the interstitial fluid, of the surface area of tumor blood vessels per unit volume of tumor tissue $A_{vessel,t}/V_{tissue,t}$, of the diffusive permeability P_t of the capillary wall, of the volume fraction of tumor tissue $f_{T,t}$, of the initial receptor concentration $[R_0]$ in the tumor tissue, and of the kinetic constant k_{on} describing the binding of the TRAIL molecules with the receptors of the cancer cells influence the output variable x_{is} in the same order of magnitude as the parameter x_{co} . Figure 46 illustrates that every parameter which is significant for the mole fraction of dissolved therapeutic agent x_{is} in the tissue continuum of the tumorous upscaled node also affects the percentage of cancer cells undergoing cell death represented by the output variable $f_{deadCells}$.

The parameter A_{vessel}/V_{tissue} regulates the fluid flow q_F as well as the advective and diffusive transport q_T between the two continua of the alveolus model. In contrast to the variable q_F defined by the Starling equation (31), the output variable q_T calculated with the Stavermann-Kedem-Katchalsky equation (32) contains the surface area of capillaries per unit volume of tissue A_{vessel}/V_{tissue} twice. Therefore, the variable q_T is more sensitive with respect to a change of A_{vessel}/V_{tissue} than the variable q_F (see Figure 45 and Figure 46). However, the mole fraction of dissolved therapeutic agent x_{is} in the tissue continuum is neither strongly affected by the ratio A_{vessel}/V_{tissue} nor by all the other parameters of the transfer equations of the double-continuum model: the Starling equation (31) and the Stavermann-Kedem-Katchalsky equation (32). The surface area of capillaries per unit volume of tissue A_{vessel}/V_{tissue} , the diffusive permeability P of the capillary wall and the hydraulic conductivity L_p of the vessel wall can be seen as weighting factors for the mass flow rates and the transport processes between the capillary bed continuum and the tissue continuum. These parameters have no impact on the balance between the inflow and outflow into a continuum. A change of the capillary oncotic pressure π_c , of the interstitial oncotic pressure π_{is} , of the osmotic reflection coefficient σ , or of the solvent-drag reflection coefficient σ_f of the administered therapeutic agent influences the pressure gradients between the two continua of the alveolus model. These four parameters therefore determine the balance between the outflow and inflow into a continuum. However, a variation of 5 per cent of π_c , π_{is} , σ or σ_f does also not result in significant changes of the output variables x_c , x_{is} , p_c , p_{is} and $f_{deadCells}$.

The influences of the lymphatic system (Equation (23) and Equation (25) of the alveolus), represented by the parameters p_{lymph} , L_{lymph} and A_{vessel}/V_{tissue} , and of the degradation processes (Equation (19) used by the vascular graph model and by the alveolus model) represented by the parameter $t_{1/2}$ on the considered output variables seem to be small. The lymphatic system is only considered in the case a of healthy upscaled node. The degradation processes are taken into account by both kind of upscaled nodes. For the considered output variables, the significance of the sink term $r_{adsorption}$ (see Equation (26)) that represents the interaction of the drug molecules with the cancer cells in the pulmonary tissue continuum in the case of a tumorous upscaled node is expressed by the parameters $[R_0]$, k_{off} and k_{on} in Figure 46. This sink term has a higher, however not a significant, impact on the output variables than the other two sink terms of the multi-scale model.

A change of the molecular radius of TRAIL r_{TRAIL} results in new values for the diffusion coefficient D of the injected therapeutic agent in both continua of the alveolus model. The diffusion coefficient D is obtained by Equation (51). The considered output variables are not very sensitive with regard to the variation of the parameter r_{TRAIL} (see Figure 45 and Figure 46). So, diffusion is not the dominant transport mechanism in the two continua of the DCM.

Summing up, the local sensitivity analysis of the multi-scale model shows that the the radius of the healthy and the tumorous capillary vessels, $r_{vessel,h}$ and $r_{vessel,t}$ contribute the most to the variability of the considered output variables. The sink terms describing the influences of the lymphatic system and the degradation processes are irrelevant. The variation of the parameters π_c , π_{is} , σ or σ_f results in more significant changes of the output variables q_F and q_T than of the output variables x_c , x_{is} , p_c , p_{is} and $f_{deadCells}$.

Table 15: Model parameters varied for the local sensitivity analysis.

parameter	symbol	unit		nominal value	variation of 5 %
capillary continuum					
dynamic viscosity	μ	Pas		$2.1 \cdot 10^{-3}$	$2.205 \cdot 10^{-3}$
mass density	ρ_{mass}	kg/m ³		1050	11025.5
molar density	ρ_{mol}	mol/m ³		284	298.2
vessel radius	$r_{vessel,h}$	m ²	healthy	$4.0 \cdot 10^{-12}$	$4.2 \cdot 10^{-12}$
	$r_{vessel,t}$	m ²	tumorous	$10.0 \cdot 10^{-12}$	$10.5 \cdot 10^{-12}$
half-life of therapeutic agent	$t_{1/2}$	s		21600	22680
transfer equations					
surface area of capillaries per unit volume of tissue	$\frac{A_{vessel,h}}{V_{tissue,h}}$	1/m	healthy	$5.8 \cdot 10^4$	$6.09 \cdot 10^4$
	$\frac{A_{vessel,t}}{V_{tissue,t}}$	1/m	tumorous	$2.0 \cdot 10^4$	$2.1 \cdot 10^4$
capillary oncotic pressure	$\pi_{c,h}$	Pa	healthy	3724	3910.2
	$\pi_{c,t}$	Pa	tumorous	2660	2793
diffusive permeability	P_h	m/s	healthy	$2.2 \cdot 10^{-9}$	$2.31 \cdot 10^{-9}$
	P_t	m/s	tumorous	$1.73 \cdot 10^{-8}$	$1.8165 \cdot 10^{-8}$
hydraulic conductivity	$L_{p,h}$	m/Pas	healthy	$2.71 \cdot 10^{-12}$	$2.8455 \cdot 10^{-12}$
	$L_{p,t}$	m/Pas	tumorous	$2.11 \cdot 10^{-11}$	$2.2155 \cdot 10^{-11}$
interstitial oncotic pressure	$\pi_{is,h}$	Pa	healthy	1862	1955.1
	$\pi_{is,t}$	Pa	tumorous	1995	2094.75
osmotic reflection coefficient	σ_h	-	healthy	0.8	0.84
	σ_t	-	tumorous	0.8	0.84
solvent-drag reflection coefficient	$\sigma_{f,h}$	-	healthy	0.91	0.9555
	$\sigma_{f,t}$	-	tumorous	0.82	0.861
tissue continuum					
dynamic viscosity	μ	Pas		$1.2 \cdot 10^{-3}$	$1.26 \cdot 10^{-3}$
interstitial fluid pressure	$p_{is,h}$	Pa	healthy	-1064	-1117.2
	$p_{is,t}$	Pa	tumorous	133	139.65
mass density ¹	ρ_{mass}	kg/m ³		1030	1081.5
molar density ¹	ρ_{mol}	mol/m ³		303.5	318.675
intrinsic permeability	K_h	m ²	healthy	$4.43 \cdot 10^{-18}$	$4.6515 \cdot 10^{-18}$
	K_t	m ²	tumorous	$2.14 \cdot 10^{-17}$	$2.247 \cdot 10^{-17}$
porosity	ϕ_h	-	healthy	0.13	0.1365
	ϕ_t	-	tumorous	0.27	0.2835
molecular radius of TRAIL	r_{TRAIL}	m		$3.7 \cdot 10^{-9}$	$3.885 \cdot 10^{-9}$
tortuosity factor	$\hat{\tau}_h$	-	healthy	0.28	0.294
	$\hat{\tau}_t$	-	tumorous	0.71	0.7455
volume fraction of tissue	$f_{T,h}$	-	healthy	0.9	0.945
	$f_{T,t}$	-	tumorous	0.8	0.84
initial receptor concentration	$[R_0]$	mol/m ³		$1.7 \cdot 10^{-5}$	$1.785 \cdot 10^{-5}$
kinetic constant: forward reaction	k_{on}	m ³ /(mol s)		$1.0 \cdot 10^2$	$1.05 \cdot 10^2$
kinetic constant: backward reaction	k_{off}	1/s		$1.0 \cdot 10^{-3}$	$1.05 \cdot 10^{-3}$
lymphatic pressure	p_{lymph}	Pa		-1200	-1260
hydraulic conductivity of lymphatic vessel wall	L_{lymph}	m/Pas		$1.9 \cdot 10^{-12}$	$1.995 \cdot 10^{-12}$
surface area of lymph vessels per unit volume of tissue	$\frac{A_{lymph}}{V_{tissue}}$	1/m		3.0	3.15
VGM					
initial mole fraction of therapeutic agent	x_{co}	mol/mol		$1.1249 \cdot 10^{-10}$	$1.181145 \cdot 10^{-10}$
pressure at arterial root vertex	$p_{0,artery}$	Pa		1067	1120.35
pressure at venous root vertex	$p_{0,vein}$	Pa		200	210

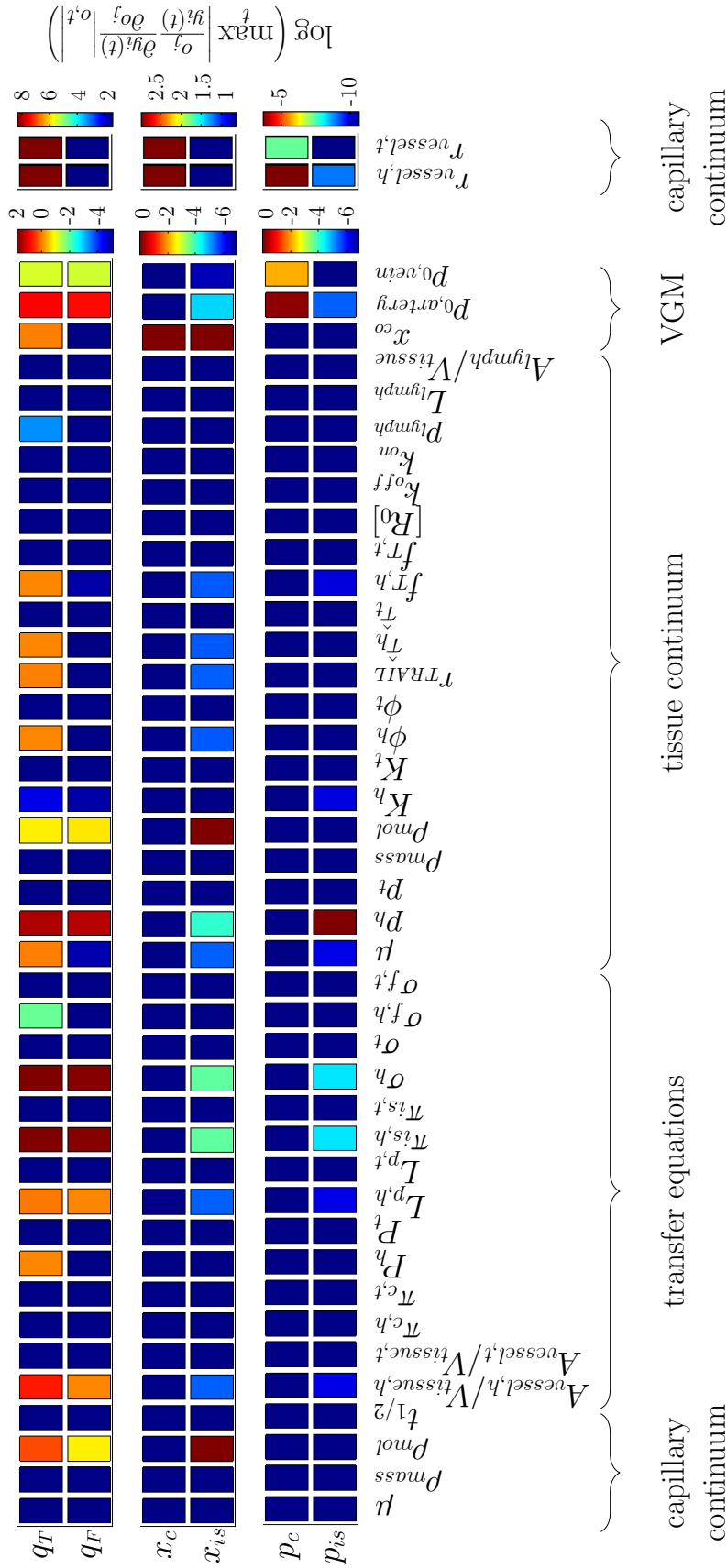


Figure 45: Visualization of the maximal normalized local sensitivity matrix for the healthy upscaled node 42. The processes in the capillary continuum are described by the Equations (28) and (29). The transfer equations are defined by the Starling equation (31) and the Stavermann-Kedem-Katchalsky equation (32). The processes in the tissue continuum are described by the Equations (21) and (24). The flow and the transport of TRAIL through the vascular graph is calculated using the Equations (14) and (18).

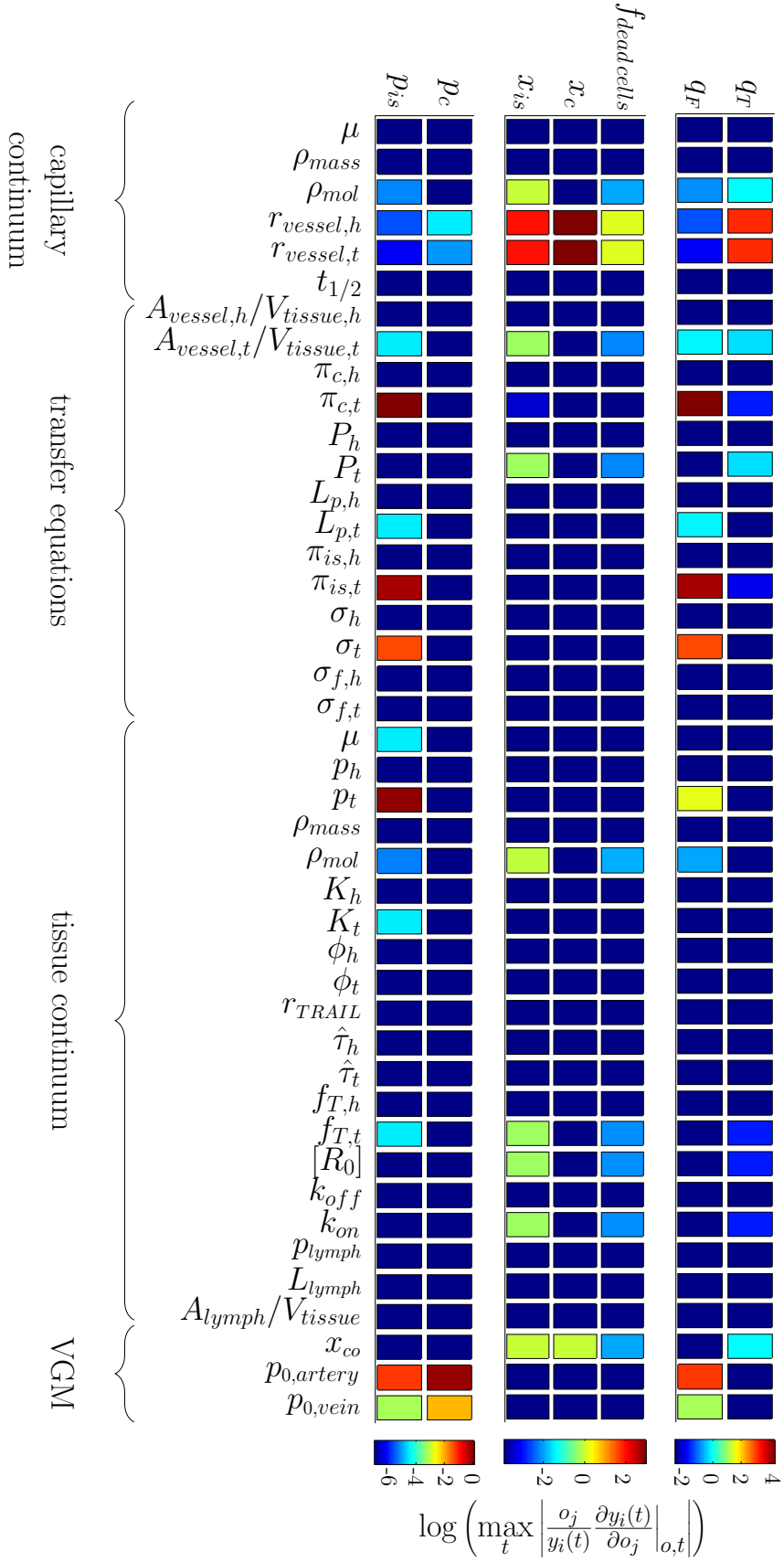


Figure 46: Visualization of the maximal normalized local sensitivity matrix for the tumorous upscaled node 58. The processes in the capillary continuum are described by the Equations (28) and (29). The transfer equations are defined by the Starling equation (31) and the Stavermann-Kedem-Katchalsky equation (32). The processes in the tissue continuum are described by the Equations (21) and (24). The flow and the transport of TRAIL through the vascular graph is calculated using the Equations (14) and (18).

8.3 Conclusions

The first example simulates the spatiotemporal distribution of a therapeutic agent using the vascular graph model and the alveolus model in a small part of the human lung affected by an alveolar cell carcinoma for a model time of eleven seconds. It accounts for the influence of micturition and metabolic transformation reactions on the agent concentration. Moreover, the role of the lymphatic system as well as the binding of the drug molecules to tumor cells are captured.

The second example uses the vascular graph model, the alveolus model and the low-dimensional population model for TRAIL-induced proapoptotic signaling to describe the spatiotemporal distribution of the therapeutic agent and the reaction of the alveolar cell carcinoma to the administered therapeutic agent TRAIL after a treatment time of twelve hours. The modified work flow of the multi-scale model for this long-time application shows that it is not necessary to couple all three models for every explicit time step of the VGM to each other. The flow and transport processes in the considered vascular graph are hardly affected by the coupling to the alveolus model. However, new coupling conditions between the three models will be required if the initial mole fraction of therapeutic agent in the vascular graph is increased or the exchange processes between the two continua of the DCM become more relevant. Further, an increase of the model time to several days or the simulation of a complete treatment schedule for alveolar cell carcinoma might affect the coupling between the models. Depending on the special application, the coupling between the three individual models of the developed multi-scale model has to be reconsidered again.

The local sensitivity analysis of the multi-scale model shows that it is important to know the physical properties of the vessel segments considered by the vascular graph model and the alveolus models. A small variation of the capillary diameter has a significant influence on the amount of therapeutic agent that will reach the cancer cells and so on the per cent of tumor cells undergoing cell death after the applied treatment. Therefore the developed approach for calculating the intrinsic permeability field of the healthy capillary bed continuum should be extended to the capillary bed continuum of the tumor. Furthermore, high resolution angiography data should provide the basis for the determination of the intrinsic permeability tensor of the capillary continuum of the alveolus model.

Further, the longer model time of the second example unveils the inhibition of the TRAIL distribution in the tumor tissue due to the increased interstitial fluid pressure. The inhibited drug penetration of solid tumors caused by an increased interstitial fluid pressure has been already reported, for example by Trédan et al. (2007) [98], Minchinton and Tannock (2006) [72] or Jain (1987) [50].

As blood is a heterogeneous, non-Newtonian fluid that exhibits pseudoplastic behavior (Schmidt and Lang (2007) [87]), the VGM determines the blood viscosity within the vessel segments of the considered vascular graph from the hematocrit value using the relation derived by Pries et al. (1992) [78]. Currently, the DCM does not account for variations in the capillary morphology. It is assumed that all capillaries have the same

physical properties. Consequently, a constant viscosity value is taken. According to Obrist et al. (2010) [75], models treating capillaries as a spatial continuum with a given permeability which is based on the local morphology of the capillary network neglect the role of the red blood cells on the flow and transport processes through this network of capillaries. As it is already stated in the paragraph above, high resolution angiography data are required for the pulmonary capillary bed and the alveolar cell carcinoma to determine the intrinsic permeability tensor for Darcy's law. The approach explained in Section 5.3 should be extended by the continuum model for red blood cell transport in capillary networks presented in Obrist et al. (2010) [75] and Reichold (2011) [80] to account for the influence of the red blood cells on the vessel resistance of capillaries.

9 Final Remarks - Summary and Outlook

As already mentioned in the motivation of this thesis, lung cancer kills more people than any other type of cancer and is responsible for 1.4 million deaths worldwide yearly [6]. Often, drug treatments employ a trial and error procedure to determine the most effective dosage. A predictive mathematical model suitable to guide cancer-therapeutic strategies is still lacking. There exist plenty of publications about the modeling of fluid flow and delivery of macromolecules in solid tumors, for example: Baxter and Jain (1989) [18], Baxter and Jain (1990) [16], Baxter and Jain (1991) [17], Chapman et al. (2008) [24], Eikenberry (2009) [33] or Shipley and Chapman (2010) [91]. Further, there are several publications about blood flow simulations in vascular networks, for example: Boas et al. (2008) [21], Reichold et al. (2009) [81], Guibert et al. (2010) [40], Lorthois et al. (2011) [65] and Lorthois et al. (2011) [66]. There exist also a lot of publications about the modeling of the pathway of apoptosis in a single cell or in a cell population, for example: Bagci et al. (2006) [13], Eißing et al. (2009) [34] or Hasenauer et al. (2010) [43]. While the application of these models is restricted to tumor tissue, to vascular networks or to cell populations, the modeling concept presented here is designed for the simulation of the fluid and drug transport in the entire organ affected by the cancer (the macrocirculation, the microcirculation, the tissue and the tumor) as well as for the simulation of the reaction of the tumor cells to the administered therapeutic agent.

In this thesis, a computational simulation framework for describing cancer-therapeutic transport in the lung has been developed. The mathematical models and the numerical models presented in this thesis couple three different spatial scales and the corresponding physical processes of each scale with each other. The developed model concept is based on the above mentioned publications. However, the coupling of a model for the macrocirculation to two further models, one model for the microcirculation and the surrounding tissue and a second model for the process of apoptosis in the heterogeneous cancer cell population and so the representation of a whole organ affected by a tumor are new. The discrete vascular graph model is coupled to the double-continuum model to determine the amount of administered therapeutic agent that will reach the cancer cells. The low-dimensional population model for TRAIL-induced proapoptotic signaling is coupled to the alveolus model to know the percent of cancer cells undergoing cell death. The system of equations of the coupled model contains terms that account for degradation processes of the therapeutic agent, the reduction of the number of drug molecules by the lymphatic system and the interaction of the drug with the tissue cells. The numerical implementation of the fully coupled model has the advantage of very flexible numerical interfaces between the three single models. Each model can be improved and adapted to the new requirements without changing the already defined numerical interfaces.

This thesis shows the process of the development of a mathematical and a numerical model for describing cancer-therapeutic transport in the human lung, and its application to two artificial scenarios. The fully coupled model includes the transport of the injected therapeutic agent through the pulmonary circulation, the transition of the dissolved drug molecules from the blood vessels into the tissue and the processes occurring within the pulmonary tissue and the tumor. However, there remains room for improvement.

Future work should include the acquisition of high-resolution angiography data of the pulmonary circulation (e.g. via srXTM) to generate a realistic vascular graph. A fully resolved capillary bed around a single alveolus and of the alveolar cell carcinoma are the prerequisite to determining the accurate permeability tensor of the capillary continuum in the case of a healthy or a tumorous upscaled node. Once these data are available, the simulation results can be compared with existing measurements to verify the developed numerical model. The presented concept is chiefly based on theoretical considerations and thus requires validation by comparison with experimental results.

Currently, the focus of the model is on predicting the spatiotemporal distribution and the therapeutic efficacy of therapeutic agents. Until now, the proposed model is not sufficient to guide cancer-therapeutic strategies because the influence of the tumor is not completely covered by the model. The absence of the lymphatic system within a tumor and the interaction / reaction of the drug molecules with / to the cancer cells are described. Angiogenesis, tumor growth, decreased tumor cell density and expanded interstitial space caused by the drug-induced apoptosis are currently not considered. These effects occur at timescales that are much larger than those of drug transport and adsorption (Baxter and Jain (1989) [18]). Jang et al. (2003) [54] report of changes of the drug transport in tumors after a 16- to 24-hours time delay of the cancer treatment. Therefore, the next necessary step would be the implementation of a tumor-growth model. One can use the vascular graph model coupled to the alveolus model as described in this thesis to compute the evolution of blood flow and drug distribution. After several hours, the vascular and the tissue configuration in the cancerous region change slightly, according to the progression of tumor growth and the angiogenesis (needs to be implemented) and due to the completion of apoptosis in the cancer cells induced by the administered drug (already implemented by the coupling of the DCM to the [PMTS]_s).

Further, it would be interesting to simulate different treatment schedules of the alveolar cell carcinoma. Jang et al. (2003) [54] have already shown the influence of varying treatment schedules on the apoptotic cell fraction in tumors.

Until now, the simplifying assumption of a non-pulsating flow through the vessel segments of the vascular graph and the capillary bed of the alveolus model is made. However, the arterial blood pressure rises and falls due to the phases of the cardiac cycle (Des Jardins (2008) [55]). In the future, the vascular graph model and the double-continuum model should include the cyclic pressure changes in the blood vessels.

The numerical simulation concept presented here is a first step towards a predictive mathematical and numerical model that is suitable to guide pulmonary cancer-therapeutic strategies. It should be the goal to further improve the accuracy of the model by the extensions outlined above such that the model can be of clinical value.

Bibliography

- [1] Download CellPoT. <http://sourceforge.net/projects/cellpot/>. Accessed 2012 January 24.
- [2] MathWorks. <http://www.mathworks.com>. Accessed 2012 January 24.
- [3] Sbtoolbox2. <http://www.sbtoolbox2.org>. Accessed 2012 January 24.
- [4] Subprocess management. <http://docs.python.org/library/subprocess.html>. Accessed 2012 January 24.
- [5] Sundials. <https://computation.llnl.gov/casc/sundials/main.html>. Accessed 2012 January 24.
- [6] WHO. <http://www.who.int/mediacentre/factsheets/fs297/en/index.html>. Accessed 2012 January 24.
- [7] Alberts, B., Bray, D., Hopkin, K., Johnson, A., Lewis, J., Raff, M., Roberts, K., and Walter, P. *Essential Cell Biology*. Garland Science, 2004.
- [8] Alberts, B., Johnson, A., Lewis, J., Raff, M., Roberts, K., and Walter, P. *Molekularbiologie der Zelle*. Wiley-VCH Verlag, 2004.
- [9] Ascher, U. M. and Petzold, L. R. *Computer Methods for Ordinary Differential Equations and Differential-Algebraic Equations*. SIAM, 1998.
- [10] Baber, K., Mosthaf, K., Flemisch, B., Helmig, R., and Müthing, S. Numerical scheme for coupling two-phase compositional porous-media flow and one-phase compositional free flow. *IMA Journal of Applied Mathematics*, submitted, 2011.
- [11] Baber, K. Modeling the transfer of therapeutic agents from the vascular space to the tissue compartment (a continuum approach). master thesis, Universität Stuttgart, 2009.
- [12] Bachmann, D., Bumle, R., Baraka-Lokmane, S., Brauchler, R., Dietrich, P., Eichel, H., Helmig, R., Htzl, H., Imig, M., Jansen, D., Kngeter, J., Lagendijk, V., Leven, C., Liedl, R., McDermott, C. I., Neunhuserer, L., Rubin, Y., Sauter, M., Silberhorn-Hemming, A., Sinclair, B., S, M., Teutsch, G., Thringer, C., Vogel, T., Weede, M., and Witthser, K. *Flow and Transport in Fractured Porous Media*. Springer, 2005.
- [13] Bagci, E., Vodovotz, Y., Billiar, T., Ermentrout, G., and Bahar, I. Bistability in apoptosis: Roles of bax, bcl-2, and mitochondrial permeability transition pores. *BIOPHYSICAL JOURNAL*, 90:1546–1559, 2006.

- [14] Baish, J. W., Gazit, Y., Berk, D. A., Nozue, M., Baxter, L. T., and Jain, R. K. Role of tumor vascular architecture in nutrient and drug delivery: An invasion percolation-based network model. *Microvascular Research*, 51:327–346, 1996.
- [15] Baish, J. W., Netti, P. A., and Jain, R. K. Transmural coupling of fluid flow in microcirculatory network and interstitium in tumors. *Microvascular Research*, 53:128–141, 1997.
- [16] Baxter, L. T. and Jain, R. K. Transport of fluid and macromolecules in tumors ii. role of heterogeneous perfusion and lymphatics. *Microvascular Research*, 40:246–263, 1990.
- [17] Baxter, L. T. and Jain, R. K. Transport of fluid and macromolecules in tumors iii. role of binding and metabolism. *Microvascular Research*, 41:5–23, 1991.
- [18] Baxter, L. T. and Jain, R. K. Transport of fluid and macromolecules in tumors: I. role of interstitial pressure and convection. *Microvascular Research*, 37:77–104, 1989.
- [19] Bear, J. *Dynamics of Fluids in Porous Media*. Courier Dover Publications, 1972.
- [20] Beard, D. A., Wu, F., Cabrera, M. E., and Dash, R. K. Modeling of cellular metabolism and microcirculatory transport. *Microcirculation*, 15:777–793, 2008.
- [21] Boas, D., Jones, S., Devor, A., Huppert, T., and Dale, A. A vascular anatomical network model of the spatio-temporal response to brain activation. *NeuroImage*, 40:1116–1129, 2008.
- [22] Bongrand, P. Ligand-receptor interactions. *Rep. Prog. Phys.*, 62:921–968, 1999.
- [23] Brown, B., Primhak, R., Smallwood, R., Milnes, P., Narracott, A., and Jackson, M. Neonatal lungs: maturational changes in lung resistivity spectra. *Medical & Biological Engineering & Computation*, 40:506–511, 2002.
- [24] Chapman, S. J., Shipley, R. J., and Jawad, R. Multiscale modeling of fluid transport in tumors. *Bulletin of Mathematical Biology*, 70:2334–2357, 2008.
- [25] Class, H. *Theorie und numerische Modellierung nichtisothermer Mehrphasenprozesse in NAPL-kontaminierten porösen Medien*. PhD thesis, Institut für Wasserbau, Universität Stuttgart, 2001.
- [26] Cohen, S. D. and Hindmarsh, A. C. Cvode, a stiff/nonstiff ode solver in c. *Computers in Physics*, 10:138–143, 1996.
- [27] Cretney, E., Takeda, K., and Smyth, M. J. Cancer: Novel therapeutic strategies that exploit the tnfr-related apoptosis-inducing ligand (trail)/trail receptor pathway. *The International Journal of Biochemistry & Cell Biology*, 39:280–286, 2007.
- [28] Curry, F.-R. E. Mechanics and thermodynamics of transcapillary exchange. In Renkin, E. M., Michel, C., and Geiger, S., Ed., *Handbook of Physiology*, Band IV. American Physiological Society, 1984.
- [29] Dingermann, T., Hänsel, R., and Zündorf, I. *Pharmazeutische Biologie - Molekulare Grundlagen und klinische Anwendungen*. Springer-Verlag, 2002.

- [30] Dormand, J. R. and Prince, P. J. A family of embedded runge-kutta formulae. *Journal of Computational and Applied Mathematics*, 6:19–26, 1980.
- [31] Dreher, M. and Chilkoti, A. Toward a systems engineering approach to cancer drug delivery. *oxford journal*, 983–985, 2007.
- [32] Effors, R. Pulmonary microcirculation and exchange. In Renkin, E. M., Michel, C., and Geiger, S., Ed., *Handbook of Physiology*, Band IV. American Physiological Society, 1984.
- [33] Eikenberry, S. A tumor cord model for doxorubicin delivery and dose optimization in solid tumors. *Theoretical biology and Medical Modelling*, 6:16, 2009.
- [34] Eißing, T., Chaves, M., and Allgöwer, F. Live and let die - a systems biology view on cell death. *Computers and Chemical Engineering*, 33:583–589, 2009.
- [35] Falschlehner, C., Emmerich, C. H., Gerlach, B., and Walczak, H. Trail signalling: Decisions between life and death. *The International Journal of Biochemistry & Cell Biology*, 39:1462–1475, 2007.
- [36] Flemisch, B., Darcis, M., Erbertseder, K., Faigle, B., Lauser, A., Mosthaf, K., Müthing, S., Nuske, P., Tatomir, A., Wolff, M., and Helmig, R. Dumux: Dune for multi-(phase, component, scale, physics, ...) flow and transport in porous media. *Advances in Water Resources*, 34:1102–1112, 2011.
- [37] Flemisch, B., Fritz, J., Helmig, R., Niessner, J., and Wolmuth, B. Dumux: A multi-scale, multi-physics toolbox for flow and transport processes in porous media. In *ECOMAS Thematic Conference on Multi-Scale Computational Methods for Solids and Fluids*, 2007.
- [38] Formaggia, L., Quarteroni, A., and Veneziani, A. *Cardiovascular Mathematics - Modelling and simulation of the circulatory system*. Springer-Verlag, 2009.
- [39] Frommhold, W. and Gerhardt, P. *Tumoren der Lunge klinisch-radiologisches Seminar*, Band 17. Georg Thieme Verlag Stuttgart, 1987.
- [40] Guibert, R., Fonta, C., and Plouraboue, F. Cerebral blood flow modeling in primate cortex. *Journal of Cerebral Blood Flow & Metabolism*, 30:1860–1873, 2010.
- [41] Hanahan, D. and Weinberg, R. A. The hallmarks of cancer. *CELL*, 100:57–70, 2000.
- [42] Hasenauer, J., Waldherr, S., and Allgöwer, F. Low-dimensional population model for trail-induced propapoptotic signaling. unpublished.
- [43] Hasenauer, J., Waldherr, S., Doszczak, M., Scheurich, P., and Allgöwer, F. Density-based modeling and identification of biochemical networks in cell populations. In *Int. Symp. Dyn. Cont. Proc. Syst. (DYCOPS)*, 306–311, July 2010.
- [44] Hehlhans, T. and Pfeffer, K. The intriguing biology of the tumour necrosis factor/tumour necrosis factor receptor superfamily: players, rules and the games. *Immunology*, 115:1–20, 2004.
- [45] Helmig, R. *Multiphase Flow and Transport Processes in the Subsurface - A Contribution to the Modeling of Hydrosystems*. Springer-Verlag, 1997.

- [46] Helmig, R. Modellkonzepte und simulationenmethoden für ein und mehrphasenströmungen. Institut für Wasserbau, Universität Stuttgart, 2008.
- [47] Horsfield, K. Morphometry of the small pulmonary arteries in man. *Circulation Research*, 42:593–597, 1978.
- [48] Horsfield, K. and Gordon, W. I. Morphometry of pulmonary veins in man. *Lung*, 159:211–218, 1981.
- [49] Huang, W., Yen, R. T., McLaurine, M., and Bledsoe, G. Morphometry of the human pulmonary vasculature. *Journal of Applied Physiology*, 81:2123–2133, 1996.
- [50] Jain, R. Transport of molecules in the tumor interstitium: A review. *Cancer Research*, 47:3039–3051, 1987.
- [51] Jain, R. Delivery of molecular and cellular medicine to solid tumors. *Journal of Controlled Release*, 53:49–67, 1998.
- [52] Jain, R. K. Delivery of molecular and cellular medicine to solid tumors. *Journal of Controlled Release*, 53:49–67, 1998.
- [53] Jain, R. Transport of molecules across tumor vasculature. *Cancer and Metastasis Reviews*, 6:559–593, 1987.
- [54] Jang, S., Wientjes, M., Lu, D., and Au, J. Drug delivery and transport to solid tumors. *Pharmaceutical Research*, 1337–1350, 2003.
- [55] Jardins, T. D. *Cardiopulmonary Anatomy & Physiology - Essentials of Respiratory Care*. Cengage Learning, 2008.
- [56] Junqueira, L., Carneiro, J., and Kelley, R. *Histologie*. Springer, Berlin, 5. edition, 2002.
- [57] Komietzko, N., Wiesner, B., and Wendel, H. *Erkrankungen der Lunge*. de Gruyter, 1994.
- [58] Koolman, J. and Röhm, K. *Taschenatlas der Biochemie des Menschen*. Georg Thieme Verlag Stuttgart, 2009.
- [59] Kurbel, S., Kurbel, B., Belovari, T., Marić, S., Steiner, R., and Božić, D. Model of interstitial pressure as a result of cyclical changes in the capillary wall fluid transport. *Medical Hypotheses*, 57(2):161–166, 2001.
- [60] Larsen, R. and Ziegenfuß, T. *Beatmung*. Springer, 2009.
- [61] LeBlanc, H. and Ashkenazi, A. Apo2l/trail and its death and decoy receptors. *Cell Death and Differentiation*, 10:66–75, 2003.
- [62] Li, C. W. and Cheng, H. D. A nonlinear fluid model for pulmonary blood circulation. *Journal of Biomechanics*, 6:653–664, 1993.
- [63] Liepsch, D. *Strömungsuntersuchungen an Modellen menschlicher Blutgefäß-Systeme*. Reihe 7: Stroemungsmechanik. VDI Verlag, Dsseldorf, 1987.
- [64] Lipowsky, H. H., Usami, S., and Chien, S. In vivo measurements of apparent viscosity and microvessel hematocrit in the mesentery of the cat. *Microvascular Research*, 19:297–319, 1980.

- [65] Lorthois, S., Cassot, F., and Lauwers, F. Simulation study of brain blood flow regulation by intra-cortical arterioles in an anatomically accurate large human vascular network: Part i: Methodology and baseline flow. *NeuroImage*, 54:1031–1042, 2011.
- [66] Lorthois, S., Cassot, F., and Lauwers, F. Simulation study of brain blood flow regulation by intra-cortical arterioles in an anatomically accurate large human vascular network. part ii: Flow variations induced by global or localized modifications of arteriolar diameters. *NeuroImage*, 54:2840–2853, 2011.
- [67] Lüllmann, H., Mohr, K., and Hein, L. *Taschenatlas Pharmakologie*. Thieme, Stuttgart, 5. edition, 2004.
- [68] Marcovitch, H. *Black's Medical Dictionary*, Band 41. A and C Black, 2005.
- [69] McDonald, E. R. and El-Deiry, W. A. Suppression of caspase-8- and -10-associated ring proteins results in sensitization to death ligands and inhibition of tumor cell growth. *PNAS*, 101:6170–6175, 2004.
- [70] McDougall, S. R., Anderson, A. R., and Chaplain, M. A. Mathematical modelling of dynamic adaptive tumour-induced angiogenesis: Clinical implications and therapeutic targeting strategies. *Journal of Theoretical Biology*, 241:564–589, 2006.
- [71] Milnor, W. R. *Cardiovascular Fluid Dynamics*, Kapitel Pulmonary Hemodynamics, 299–340. Academic Press, 1972.
- [72] Minchinton, A. I. and Tannock, I. F. Drug penetration in solid tumours. *NATURE REVIEWS CANCER*, 6:583–592, 2006.
- [73] Muthuchamy, M. and Zawieja, D. Molecular regulation of lymphatic contractility. *Ann. N.Y. Acad. Sci.*, 1131:89–99, 2008.
- [74] Negrini, D. and Passi, A. Interstitial matrix and transendothelial fluxes in normal lung. *Respiratory Physiology and Neurobiology*, 159:301–310, 2007.
- [75] Obrist, D., Weber, B., Buck, A., and Jenny, P. Red blood cell distribution in simplified capillary networks. *PHILOSOPHICAL TRANSACTIONS OF THE ROYAL SOCIETY A-MATHEMATICAL PHYSICAL AND ENGINEERING SCIENCES*, 368:2897–2918, 2010.
- [76] Petrak, K. and Goddard, P. Transport of macromolecules across the capillary walls. *Advanced Drug Delivery Reviews*, 3:191–214, 1989.
- [77] Pluen, A., Boucher, Y., Ramanujan, S., McKee, T., Gohongi, T., Brown, E., Izumi, Y., Campbell, R., Berk, D., and Jain, R. Role of tumor-host interactions in interstitial diffusion of macromolecules: Cranial vs. subcutaneous tumors. *Proceedings of the National Academy of Sciences*, 98:4628–4633, 2001.
- [78] Pries, A. R., Neuhaus, D., and Gaehtgens, P. Blood viscosity in tube flow: dependence on diameter and hematocrit. *AMERICAN JOURNAL OF PHYSIOLOGY*, 263:H1770–H1778, 1992.
- [79] Reiche, D. *Roche Lexikon der Medizin*, Band 5. Urban and Fischer, 2003.

- [80] Reichold, J. *Cerebral Blood Flow Modeling*. PhD thesis, ETH Zurich, 2011.
- [81] Reichold, J., Stampanoni, M., Keller, A. L., Buck, A., Jenny, P., and Weber, B. Vascular graph model to simulate the cerebral blood flow in realistic vascular networks. *Journal of Cerebral Blood Flow & Metabolism*, 29:1429–1443, 2009.
- [82] Renkin, E., Goresky, C., Groom, A., Rose, C., Lundgren, O., Effros, R., Levick, J., Rosell, S., Fenstermacher, J., Rapoport, S., Bill, A., Henderson, J., Daniel, P., and Movat, H. *HANDBOOK OF PHYSIOLOGY Section 2: The Cardiovascular System Volume IV. Microcirculation, Part 2*. American Physiological Society, 1984.
- [83] Saltelli, A., Chan, K., and Scott, E. M., Ed. *Sensitivity Analysis*. Wiley, 2000.
- [84] Schiebler, T., Schmidt, W., and Zilles, K. *Anatomie*. Springer-Verlag, 1999. Achte Auflage.
- [85] Schiebler, T. H. and Korf, H. *Anatomie - Histologie, Entwicklungsgeschichte, makroskopische und mikroskopische Anatomie, Topographie*. STEINKOPF VERLAG, 2007.
- [86] Schmidt, H. and Jirstrand, M. Systems biology toolbox for matlab: a computational platform for research in systems biology. *Bioinformatics*, 22:514–515, 2006.
- [87] Schmidt, R. and Lang, F. *Physiologie des Menschen - mit Pathophysiologie*. Springer, 30. edition, 2007.
- [88] Serikov, V. B. Porous phase model of the lung interstitial fluid motion. *Microvascular Research*, 42:1–16, 1991.
- [89] Shen, L. and Chen, Z. Critical review of the impact of tortuosity on diffusion. *Chemical Engineering Science*, 3748–3755, 2007.
- [90] Shijubo, N., Kojima, H., Nagata, M., Ohchi, T., Suzuki, A., Abe, S., and Sato, N. Tumor angiogenesis of non-small cell lung cancer. *Microscopy Research and Technique*, 60:186–198, 2003.
- [91] Shipley, R. J. and Chapman, S. J. Multiscale modelling of fluid and drug transport in vascular tumours. *Bulletin of Mathematical Biology*, 72:1464–1491, 2010.
- [92] Singhal, S., Henderson, R., Horsfield, K., Harding, K., and Cumming, G. Morphometry of the human pulmonary arterial tree. *Circulation Research*, 33:190–197, 1973.
- [93] Spencer, S. L. and Sorger, P. K. Measuring and modeling apoptosis in single cells. *Cell*, 144:926–939, 2011.
- [94] Støverud, K., Darcis, M., Helmig, R., and Hassanizadeh, S. M. Modeling concentration distribution and deformation during convection-enhanced drug delivery into brain tissue. *Transport in Porous Media*, 1–25, 2011.
- [95] Sugihara-Seki, M. and Fu, B. Blood flow and permeability in microvessels. *Fluid Dynamic Research*, 37:82–132, 2005.
- [96] Swabb, E. A., Wei, J., and Gullino, P. M. Diffusion and convection in normal and neoplastic tissues. *Cancer Research*, 34:2814–2822, 1974.

-
- [97] Tillmann, B. *Atlas der Anatomie des Menschen*. Springer-Verlag, 2005.
- [98] Trédan, O., Galmarini, C. M., Patel, K., and Tannock, I. F. Drug resistance and the solid tumor microenvironment. *JOURNAL OF THE NATIONAL CANCER INSTITUTE*, 99:1441–1454, 2007.
- [99] Tuma, R. F., Duran, W. N., and Ley, K., Ed. *Microcirculation*. Academic Press, 2008.
- [100] Vankan, W. J., Huyghe, J. M., Janssen, J. D., Huson, A., Hacking, W. J. G., and Schreiner, W. Finite element analysis of blood flow through biological tissue. *International Journal of Engineering Science*, 35:375–385, 1997.
- [101] Weibel, E. R. *Morphometry of the Human Lung*. Springer-Verlag, 1963.
- [102] Weibel, E. R. Fractal geometry: a design principle for living organisms. *AMERICAN JOURNAL OF PHYSIOLOGY*, 261:L361–L369, 1991.
- [103] Yu, J. and Neretnieks, I. Modelling of transport and reaction processes in a porous medium in an electrical field. *Chemical Engineering Science*, 51:4355–4368, 1996.

A Numerical Model

In general, mathematical models can only be solved analytically under the assumption of special initial and boundary conditions. Therefore, mathematical models are strongly restricted in their applications. The equations have to be solved with the help of a numerical method. A numerical model transforms the associated mathematical model into numerical algorithms. The numerical model has to be chosen in such a way that the mathematical equations can be solved for different geometries, initial and boundary conditions with regard to the chosen primary variables. The obtained numerical algorithms are implemented into a software to calculate the processes that are described by the conceptual and mathematical model (Helmig (2008) [46]).

The quality of a discretization method depends on three criteria: the consistency of the discretization, the stability of the solution and the convergence of the solution. The consistency of the discretization means that the discretization matches the original differential equation of the mathematical model for the limit $\Delta t, \Delta x \rightarrow 0$. Therefore, it is ensured that the correct problem is solved. A numerical solution will be stable if the error does not increase with time and thus the error is bounded. The numerical solution has to converge to the exact solution for the limit $\Delta t, \Delta x \rightarrow 0$. The fulfillment of these three criteria is the basis for a good numerical model.

Initial and Boundary Conditions: A differential equation describes a time and spatially dependent problem. To solve a system of differential equations, an adequate set of initial and boundary conditions is required. The initial conditions provide the values for all primary variables at each point in the model domain at the beginning of the simulation. Additionally, boundary conditions have to be defined to link the solution within the model domain to the situation at the boundary. The multi-scale multi-physics toolbox DuMu^x provides three different types of boundary conditions:

1. Dirichlet Boundary Condition

The Dirichlet boundary condition is necessary to get an unique solution of the system of equations. The value of the primary variable u_p is fixed at the boundary of the model domain Γ :

$$u_p = u_D \text{ on } \Gamma_D.$$

2. Neumann Boundary Condition

The flux of a primary variable perpendicular to the model domain boundary is described. The Neumann Boundary Condition is understood as the normal derivative of the primary variable u_p at the boundary Γ :

$$\frac{\partial u_p}{\partial \mathbf{n}} = u_N \text{ on } \Gamma_N.$$

3. Outflow Boundary Condition

The outflow boundary condition describes the flux of a primary variable u_p perpendicular to a boundary of the model domain where this primary variable is unknown previous to the solution of the problem. The value for the primary variable at the boundary will be calculated from the interior.

The simulation toolbox VGM supports Dirichlet and Neumann boundary conditions.

A.1 Vascular Graph Model

In the following, the numerical method and the discretization employed in this thesis for the vascular graph model (see Chapter 4) are explained in detail. The VGM describes a transient problem. Therefore, a discretization in time and space is necessary.

A.1.1 Time Discretization

For the time discretization an explicit Euler scheme is used (see Figure 47). The known solution of the old time step t is used to calculate the unknowns, the primary variables, of the algebraic system of the new time step $t + \Delta t$:

$$\frac{\partial u_p}{\partial t} \approx \frac{u_p^{t+\Delta t} - u_p^t}{\Delta t} = f(u_p)^t. \quad (55)$$

The expression $f(u_p)^t$ represents the system of equations that is evaluated at the old time level t . To guarantee the convergence of the solution, the time-step size is restricted according to the Courant-Friedrichs-Lewy (CFL) condition:

$$\frac{|v|}{\Delta x / \Delta t} \leq 1 \quad \rightarrow \quad \Delta t \leq \frac{\Delta x}{|v|} \quad (56)$$

where v is the average flow velocity, Δx the dimension of the grid cell and Δt the maximum time-step size. In the case of the vascular graph model, the Courant-Friedrichs-Lewy (CFL) condition is implemented as follows:

$$\Delta t = \left| \frac{V_{ij}}{2F_{ij}} \right|, \quad (57)$$

where V_{ij} is the volume of a single edge ij , the cross-section A_{ij} times the length L_{ij} of this vessel segment, and F_{ij} is the flow along the considered edge ij . To determine the maximum allowed time-step size for the vascular graph, the Courant-Friedrichs-Lewy (CFL) condition is applied to every edge of the graph and the smallest calculated Δt is chosen for the current time step of the simulation.

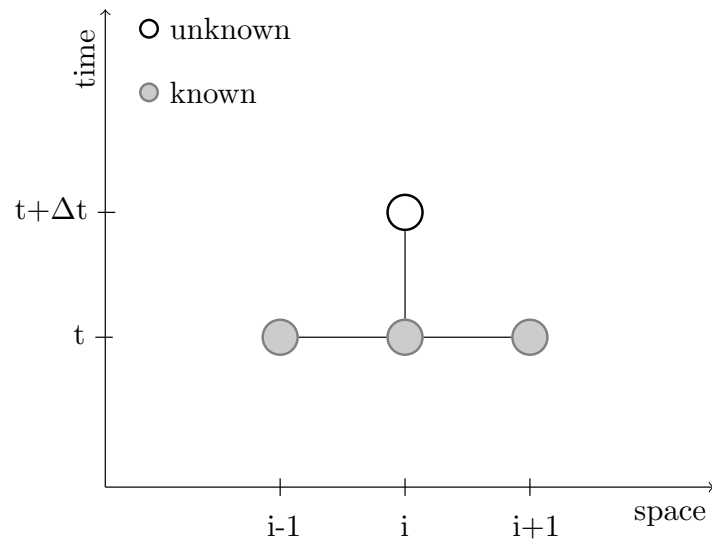


Figure 47: Explicit time discretization.

A.1.2 Spatial Discretization

The method for the spatial discretization of the vascular graph model is a fully upwind finite difference method. The numerical implementation of the mathematical model described in Chapter 4 is explained using the example of the vascular graph shown in Figure 48.

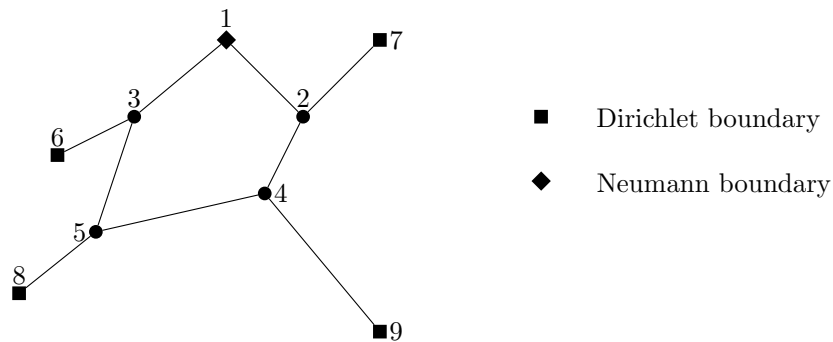


Figure 48: Example of a vascular graph.

Every vascular graph is treated as a zero-dimensional problem in space. First of all, a linear system of the following form $\mathbf{A} \cdot \mathbf{u}_p = \mathbf{b}$ is defined. The matrix \mathbf{A} contains the information about the conductance of the considered graph. The conductance T_{ij} of a vessel segment ij is $1/R_{ij}$ where R_{ij} is the vessel resistance (see Equation (16)). The vector \mathbf{u}_p comprises the pressures at the nodes of the vascular graph for which the system needs to be solved. The vector \mathbf{b} contains the boundary conditions and source and sink terms.

For the vascular graph shown in Figure 48, the following linear system of equations needs to be solved to get the pressure at every node i :

$$\begin{bmatrix} \sum_{i=1}^n T_{1,n} & -T_{1,2} & -T_{1,3} & 0 & 0 \\ -T_{2,1} & \sum_{i=1}^n T_{2,n} & 0 & -T_{2,4} & 0 \\ -T_{3,1} & 0 & \sum_{i=1}^n T_{3,n} & 0 & -T_{3,5} \\ 0 & -T_{4,2} & 0 & \sum_{i=1}^n T_{4,n} & -T_{4,5} \\ 0 & 0 & -T_{5,3} & -T_{5,4} & \sum_{i=1}^n T_{5,n} \end{bmatrix} \begin{bmatrix} p_1 \\ p_2 \\ p_3 \\ p_4 \\ p_5 \end{bmatrix} = \begin{bmatrix} q_1 \\ T_{2,7}p_7 \\ T_{3,6}p_6 \\ T_{4,9}p_9 \\ T_{5,8}p_8 \end{bmatrix}. \quad (58)$$

The linear system of equations (58) is solved using the Gauss-Seidel algorithm. Knowing the pressures at every vertex of the graph, the flow through all vessel segments ij is calculated:

$$F_{ij} = \frac{\rho_{i,mol}(p_i - p_j)}{R_{ij}}. \quad (59)$$

In case of the coupling of the DCM to the VGM for an upscaled node u , the flow field of the vascular graph has to be corrected by the mass flow between the two models $q_{u,fDCM}$:

$$F_{uj} = \frac{\rho_{u,mol}(p_u - p_j)}{R_{uj}} - q_{u,fDCM}. \quad (60)$$

The correction of the flow field requires the recalculation of the pressure field.

After the determination of the flow field for the whole graph, the distribution of a therapeutic agent in the considered vascular graph can be identified. The transport of the dissolved therapeutic agent is described by a hyperbolic differential equation (see (18)). For the numerical implementation of this equation, a first-order upwind scheme is used. The amount of a therapeutic agent x at a node i is determined with the help of the subsequent equation:

$$x_i^{t+\Delta t} = \begin{cases} x_i^t - \frac{\Delta t}{\rho_{i,mol}V_i} \left(\sum_{j=1}^n F_{ij}x_j^t + V_i r_{i,degradation}^t + q_{i,xDCM}^t \right) & \text{for } F_{ij} > 0, \\ x_i^t - \frac{\Delta t}{\rho_{i,mol}V_i} \left(\sum_{j=1}^n F_{ij}x_j^t + V_i r_{i,degradation}^t + q_{i,xDCM}^t \right) & \text{for } F_{ij} < 0. \end{cases} \quad (61)$$

$x_i^{t+\Delta t}$ is the amount of dissolved drug molecules at the node i for the new time level and x_i^t for the old time level. The result further depends on the sum of all fluxes from the considered node i to all neighboring nodes j and vice versa $\sum_{j=1}^n F_{ij}$.

A.2 Alveolus Model

In this section, the numerical method and the discretization applied for the alveolus model (see Chapter 5) are introduced. The alveolus model also describes a transient problem. Therefore, a discretization in time and space has to be applied.

A.2.1 Time Discretization

For the time discretization, the implicit Euler scheme is used. An implicit method evaluates the system of equations on the new time level (see Figure 49). The implicit Euler scheme has no stability-motivated restriction of the time-step size and is unconditionally stable (Helmig (1997) [45]). For the two transport equations (24) and (29) of the single continua, the time discretization with the implicit Euler method leads to:

$$\frac{\partial u_p}{\partial t} \approx \frac{u_p^{t+\Delta t} - u_p^t}{\Delta t} = f(u_p)^{t+\Delta t}. \quad (62)$$

The expression $f(u_p)^{t+\Delta t}$ represents the system of equations that is evaluated at the new time level $t + \Delta t$.

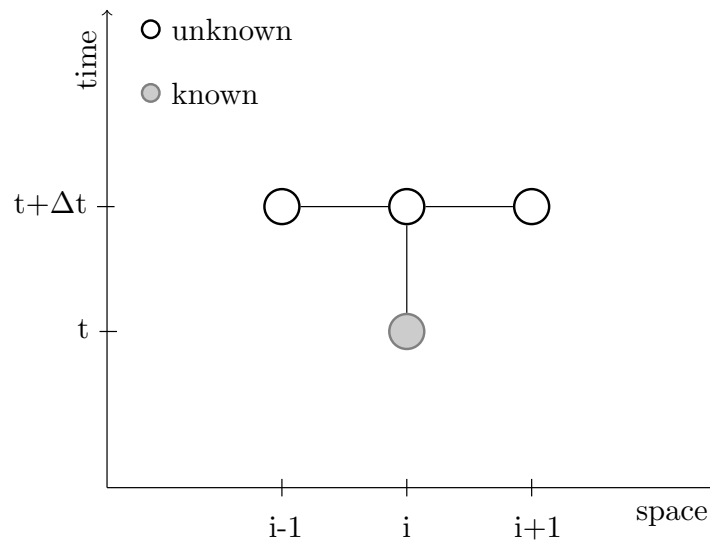


Figure 49: Implicit time discretization.

A.2.2 Spatial Discretization

The method for the spatial discretization is a fully upwind vertex centered finite volume method, also called fully upwind box method (see Figure 50). The model domain is discretized by a finite element mesh and an additional finite volume mesh. For each node of the finite element mesh, a control volume (box B_i) is constructed with its corners at the edge

midpoints and on the centers of gravity of the finite elements surrounding the node (see Figure 50 a)). Thus, each node of the finite element mesh is surrounded by a box B_i of the finite volume mesh. As shown in Figure 50 b), the boxes B_i are divided into subcontrol volumes V_i^k by the finite element mesh. The fluxes are computed on the subcontrol-volume faces f at the integration points X_f (see Figure 50 c)). However, the chosen primary variables are evaluated at the nodes of the finite element mesh. The implementation of the discretized equations is done element-wise and it is looped over all subcontrol volumes V_k^i inside the considered element E_k . The method is locally mass conservative at each control volume. This means that the numerical flux cannot produce non-physical sources or sinks (Helmig (1997) [45]).

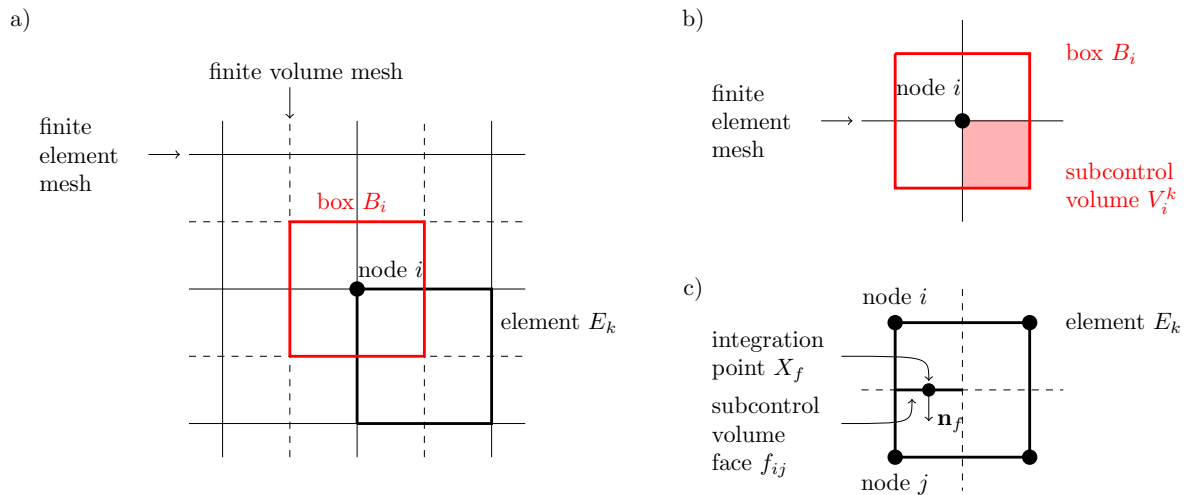


Figure 50: Vertex centered finite volume method (box method). a) Construction of the grid. b) Division of the box B_i into subcontrol volumes V_k^i . c) computation of the fluxes (according to Baber et al. (2011) [10]).

The spatial discretization is shown on the example of the transport equation (24) for the tissue continuum. The spatial discretization of all the other equations of the alveolus model has to be done similarly and the discretized form of these equations is shown at the end of this chapter.

The first step is the integration of (24) over the discretized domain G :

$$\begin{aligned}
& \int_G \frac{\partial(f_T \phi \rho_{mol} x_{is})}{\partial t} dG - \int_G \nabla \cdot \left(\frac{f_T \mathbf{K} \rho_{mol} x_{is}}{\mu} (\nabla p_{is} + \rho_{mass} g \nabla z) \right) dG \\
& - \int_G \nabla \cdot (f_T \rho_{mol} D_{eff} \nabla x_{is}) dG + \int_G f_T L_{lymph} \frac{A_{lymph}}{V_{lymph}} (p_{is} - p_{lymph}) \rho_{mol} x_{is} dG \\
& + \int_G f_T (k_{on} x_{is} \rho_{mol} [R] - k_{off} [R - L]) dG - \int_G \rho_{mol} P \frac{A_{vessel}}{V_{tissue}} (x_c - x_{is}) \\
& + \left(\rho_{mol} L_p \frac{A_{vessel}}{V_{tissue}} (p_c - p_{is} - \sigma (\pi_c - \pi_{is})) \right) \frac{(x_c - x_{is})}{2} (1 - \sigma_f) dG = 0.
\end{aligned} \tag{63}$$

Until now, the primary variables u_p (e.g. pressure p_{is} , pressure p_c and mole fraction of dissolved therapeutic agent x_{is} and x_c) are only described exactly at the nodes of the finite element mesh. The next step includes the introduction of the shape function N_i at each discrete nodal point i of the finite element mesh to approximate the primary variables between these nodes. For this model, linear shape functions $N_i(u_{p,k})$ are applied with the following additional restriction:

$$N_i(u_{p,k}) = \delta_{ik} = \begin{cases} 1 & \text{for } i = k, \\ 0 & \text{for } i \neq k. \end{cases} \tag{64}$$

δ_{ik} stands for the Kronecker symbol. Due to the applied restriction (64), the shape function $N_i(u_{p,k})$ is one at the respective node and zero at all other nodes.

The primary variables are now expressed as follows:

$$x_{is} = \sum_{i=1}^{n_{nodes}} \hat{x}_{is,i} N_i, \quad p_{is} = \sum_{i=1}^{n_{nodes}} \hat{p}_{is,i} N_i, \quad x_c = \sum_{i=1}^{n_{nodes}} \hat{x}_{c,i} N_i, \quad p_c = \sum_{i=1}^{n_{nodes}} \hat{p}_{c,i} N_i, \tag{65}$$

where n_{nodes} is the number of nodes in the discretized domain G and $\hat{x}_{is,i}$, $\hat{p}_{is,i}$, $\hat{x}_{c,i}$ and $\hat{p}_{c,i}$ represent discrete values of the primary variables at the node i of the finite element mesh.

The insertion of (65) into the transport equation (63) generates an error ϵ on the right hand side, the so called residuum:

$$\begin{aligned}
& \int_G \frac{\partial \left(f_{T,i} \phi_i \rho_{mol,i} \left(\sum_{i=1}^{n_{nodes}} \hat{x}_{is,i} N_i \right) \right)}{\partial t} dG \\
& - \int_G \nabla \cdot \left(\frac{f_{T,i} \mathbf{K}_{ij} \rho_{mol,i} \left(\sum_{i=1}^{n_{nodes}} \hat{x}_{is,i} N_i \right)}{\mu_i} \left(\nabla \left(\sum_{i=1}^{n_{nodes}} \hat{p}_{is,i} N_i \right) + \rho_{mass,i} g_i \nabla z_i \right) \right) dG \\
& - \int_G \nabla \cdot \left(f_{T,i} \rho_{mol,i} D_{eff,ij} \nabla \left(\sum_{i=1}^{n_{nodes}} \hat{x}_{is,i} N_i \right) \right) dG \\
& + \int_G f_{T,i} L_{lymph,i} \frac{A_{lymph,i}}{V_{lymph,i}} \left(\left(\sum_{i=1}^{n_{nodes}} \hat{p}_{is,i} N_i \right) - p_{lymph,i} \right) \rho_{mol,i} \left(\sum_{i=1}^{n_{nodes}} \hat{x}_{is,i} N_i \right) dG \quad (66) \\
& + \int_G f_{T,i} (k_{on,i} \left(\sum_{i=1}^{n_{nodes}} \hat{x}_{is,i} N_i \right) \rho_{mol,i} [R]_i - k_{off,i} [R - L]_i) dG \\
& - \int_G \rho_{mol,i} P_i \frac{A_{vessel,i}}{V_{tissue,i}} \left(\left(\sum_{i=1}^{n_{nodes}} \hat{x}_{c,i} N_i \right) - \left(\sum_{i=1}^{n_{nodes}} \hat{x}_{is,i} N_i \right) \right) \\
& + \left(\rho_{mol,i} L_{p,i} \frac{A_{vessel,i}}{V_{tissue,i}} \left(\left(\sum_{i=1}^{n_{nodes}} \hat{p}_{c,i} N_i \right) - \left(\sum_{i=1}^{n_{nodes}} \hat{p}_{is,i} N_i \right) - \sigma_i (\pi_{c,i} - \pi_{is,i}) \right) \right) \\
& \frac{\left(\left(\sum_{i=1}^{n_{nodes}} \hat{x}_{c,i} N_i \right) - \left(\sum_{i=1}^{n_{nodes}} \hat{x}_{is,i} N_i \right) \right)}{2} (1 - \sigma_{f,i}) dG = \int_G \epsilon dG.
\end{aligned}$$

The intrinsic permeability \mathbf{K}_{ij} is defined as the harmonic mean of the intrinsic permeabilities of the neighboring nodes i and j . The harmonic mean is also applied to the calculation of the effective diffusion coefficient $D_{eff,ij} = (\hat{\tau} \phi D)_{ij}$. All the other parameters are determined at the node of the considered box.

The residuum ϵ has to become zero so that the transport equation is fulfilled exactly over the discretized domain G . This is achieved by the use of the weighted residual method. For further details see Helmig (1997) [45]. The weighting function W_i is introduced for every node i . The characteristic of the weighted residual method is that the integral of the residuum over G is set to zero:

$$\int_G W_i \epsilon dG = 0 \quad i = 1, 2, \dots, n_{nodes}. \quad (67)$$

In addition, it is required that $\sum_{i=1}^{n_{nodes}} W_i = 1$ for a node i within the domain G and that the

weighting functions are linearly independent. Therefore, the weighting function W_i is one in the respective box volume B_i and zero in all other boxes:

$$W_i = \delta_{ik} = \begin{cases} 1 & \text{if } i \in \text{box } B_i, \\ 0 & \text{if } i \notin \text{box } B_i. \end{cases} \quad (68)$$

Inserting (67) and the weighting function W_i into (66) the following equation is obtained:

$$\begin{aligned} & \int_G W_i \frac{\partial \left(f_{T,i} \phi_i \rho_{mol,i} \left(\sum_{i=1}^{n_{nodes}} \hat{x}_{is,i} N_i \right) \right)}{\partial t} dG \\ & - \int_G W_i \nabla \cdot \left(\frac{f_{T,i} \mathbf{K}_{ij} \rho_{mol,i} \left(\sum_{i=1}^{n_{nodes}} \hat{x}_{is,i} N_i \right)}{\mu_i} \left(\nabla \left(\sum_{i=1}^{n_{nodes}} \hat{p}_{is,i} N_i \right) + \rho_{mass,i} g_i \nabla z_i \right) \right) dG \\ & \quad - \int_G W_i \nabla \cdot \left(f_{T,i} \rho_{mol,i} D_{eff,ij} \nabla \left(\sum_{i=1}^{n_{nodes}} \hat{x}_{is,i} N_i \right) \right) dG \\ & + \int_G W_i f_{T,i} L_{lymph,i} \frac{A_{lymph,i}}{V_{lymph,i}} \left(\left(\sum_{i=1}^{n_{nodes}} \hat{p}_{is,i} N_i \right) - p_{lymph,i} \right) \rho_{mol,i} \left(\sum_{i=1}^{n_{nodes}} \hat{x}_{is,i} N_i \right) dG \\ & \quad + \int_G W_i f_{T,i} (k_{on,i} \left(\sum_{i=1}^{n_{nodes}} \hat{x}_{is,i} N_i \right) \rho_{mol,i} [R]_i - k_{off,i} [R - L]_i) dG \\ & \quad - \int_G W_i \rho_{mol,i} P_i \frac{A_{vessel,i}}{V_{tissue,i}} \left(\left(\sum_{i=1}^{n_{nodes}} \hat{x}_{c,i} N_i \right) - \left(\sum_{i=1}^{n_{nodes}} \hat{x}_{is,i} N_i \right) \right) \\ & + W_i \left(\rho_{mol,i} L_{p,i} \frac{A_{vessel,i}}{V_{tissue,i}} \left(\left(\sum_{i=1}^{n_{nodes}} \hat{p}_{c,i} N_i \right) - \left(\sum_{i=1}^{n_{nodes}} \hat{p}_{is,i} N_i \right) - \sigma_i (\pi_{c,i} - \pi_{is,i}) \right) \right. \\ & \quad \left. \frac{\left(\left(\sum_{i=1}^{n_{nodes}} \hat{x}_{c,i} N_i \right) - \left(\sum_{i=1}^{n_{nodes}} \hat{x}_{is,i} N_i \right) \right)}{2} (1 - \sigma_{f,i}) \right) dG = 0. \end{aligned} \quad (69)$$

The third step is the application of the mass lumping technique to the storage term and to the source/sink terms. Mass lumping allows the transformation of a finite element discretization to a finite volume form (Helmig (1997) [45]). Based on this technique the following condition:

$$\int_G W_i N_j dG = \begin{cases} V_i & \text{for } i = j, \\ 0 & \text{for } i \neq j, \end{cases} \quad (70)$$

where V_i is a single volume of the finite volume mesh, a box volume B_i , is inserted into (69):

$$\begin{aligned}
& V_i \frac{\partial (f_{T,i} \phi_i \rho_{mol,i} \hat{x}_{is,i})}{\partial t} \\
& - \int_G W_i \nabla \cdot \left(\frac{f_{T,i} \mathbf{K}_{ij} \rho_{mol,i} \sum_{i=1}^{n_{nodes}} \hat{x}_{is,i} N_i}{\mu_i} \left(\nabla \left(\sum_{i=1}^{n_{nodes}} \hat{p}_{is,i} N_i \right) + \rho_{mass,i} g_i \nabla z_i \right) \right) dG \\
& - \int_G W_i \nabla \cdot \left(f_{T,i} \rho_{mol,i} D_{eff,ij} \nabla \left(\sum_{i=1}^{n_{nodes}} \hat{x}_{is,i} N_i \right) \right) dG \\
& + V_i f_{T,i} L_{lymph,i} \frac{A_{lymph,i}}{V_{lymph,i}} (\hat{p}_{is,i} - p_{lymph,i}) \rho_{mol,i} \hat{x}_{is,i} \\
& + V_i f_{T,i} (k_{on,i} \hat{x}_{is,i} \rho_{mol,i} [R]_i - k_{off,i} [R - L]_i) \\
& - V_i \rho_{mol,i} P_i \frac{A_{vessel,i}}{V_{tissue,i}} (\hat{x}_{c,i} - \hat{x}_{is,i}) \\
& - V_i \rho_{mol,i} L_{p_i} \frac{A_{vessel,i}}{V_{tissue,i}} (\hat{p}_{c,i} - \hat{p}_{is,i} - \sigma_i (\pi_{c,i} - \pi_{is,i})) \frac{(\hat{x}_{c,i} - \hat{x}_{is,i})}{2} (1 - \sigma_{f,i}) = 0.
\end{aligned} \tag{71}$$

Further, the Green-Gaussian integral is applied on the integrals of the advective and diffusive term. In this thesis the Green-Gaussian integral is exemplified for the diffusive term:

$$\begin{aligned}
& \int_G W_i \nabla \cdot \left(f_{T,i} \rho_{mol,i} D_{eff,ij} \nabla \left(\sum_{i=1}^{n_{nodes}} \hat{x}_i N_i \right) \right) dG \\
& = \int_G \nabla \cdot \left(W_i f_{T,i} \rho_{mol,i} D_{eff,ij} \nabla \left(\sum_{i=1}^{n_{nodes}} \hat{x}_i N_i \right) \right) dG \\
& - \int_G \nabla W_i \cdot \left(f_{T,i} \rho_{mol,i} D_{eff,ij} \nabla \left(\sum_{i=1}^{n_{nodes}} \hat{x}_i N_i \right) \right) dG \\
& = \int_{\Gamma} \left(W_i f_{T,i} \rho_{mol,i} D_{eff,ij} \nabla \left(\sum_{i=1}^{n_{nodes}} \hat{x}_i N_i \right) \right) \cdot \mathbf{n} d\Gamma \\
& - \int_G \nabla W_i \cdot \left(f_{T,i} \rho_{mol,i} D_{eff,ij} \nabla \left(\sum_{i=1}^{n_{nodes}} \hat{x}_i N_i \right) \right) dG.
\end{aligned} \tag{72}$$

The diffusive term is expressed as the difference of two integrals where the minuend can be simplified with the Gaussian integral theorem. A volume integral of the divergence of a

function is transformed into a surface integral. This function times the normal vector \mathbf{n} is integrated along the boundary of the discretized domain Γ .

In the same way it is done for the advective term:

$$\begin{aligned} & \int_G W_i \nabla \cdot \left(\frac{f_{T,i} \mathbf{K}_{ij} \rho_{mol,i} \sum_{i=1}^{n_{nodes}} \hat{x}_{is,i} N_i}{\mu_i} \left(\nabla \left(\sum_{i=1}^{n_{nodes}} \hat{p}_{is,i} N_i \right) + \rho_{mass,i} g_i \nabla z_i \right) \right) dG = \\ & \int_{\Gamma} \left(W_i \frac{f_{T,i} \mathbf{K}_{ij} \rho_{mol,i} \sum_{i=1}^{n_{nodes}} \hat{x}_{is,i} N_i}{\mu_i} \left(\nabla \left(\sum_{i=1}^{n_{nodes}} \hat{p}_{is,i} N_i \right) + \rho_{mass,i} g_i \nabla z_i \right) \right) \cdot \mathbf{n} d\Gamma \quad (73) \\ & - \int_G \nabla W_i \cdot \left(\frac{f_{T,i} \mathbf{K}_{ij} \rho_{mol,i} \sum_{i=1}^{n_{nodes}} \hat{x}_{is,i} N_i}{\mu_i} \left(\nabla \left(\sum_{i=1}^{n_{nodes}} \hat{p}_{is,i} N_i \right) + \rho_{mass,i} g_i \nabla z_i \right) \right) dG. \end{aligned}$$

For the box method the weighting functions are piecewise constant in the individual boxes and are chosen according to the definition of (68) which leads to $\nabla W_i = 0$. If the transport equation is only integrated over the control volume of one box B_i of the discretized domain G the volume integral in (72) and (73) will vanish.

Combining the time and the spatial discretization and the fully upwinding for the advective term, the following discretized form for the transport equation (24) is obtained:

$$\begin{aligned}
& \frac{(V_i f_{T,i} \phi_i \rho_{mol,i} \hat{x}_{is,i})^{t+\Delta t} - (V_i f_{T,i} \phi_i \rho_{mol,i} \hat{x}_{is,i})^t}{\Delta t} \\
& - \int_{\Gamma_{B_i}} \left(\frac{f_{T,i} \mathbf{K}_{ij} \rho_{mol,up(i,j)} x_{is,up(i,j)}}{\mu_{up(i,j)}} \left(\nabla \left(\sum_{i=1}^{n_{nodes}} \hat{p}_{is,i} N_i \right) + \rho_{mass,i} g_i \nabla z_i \right) \right)^{t+\Delta t} \cdot \mathbf{n} d\Gamma_{B_i} \\
& - \int_{\Gamma_{B_i}} \left(f_{T,i} \rho_{mol,i} D_{eff,ij} \nabla \left(\sum_{i=1}^{n_{nodes}} \hat{x}_i N_i \right) \right)^{t+\Delta t} \cdot \mathbf{n} d\Gamma_{B_i} \\
& + \left(V_i f_{T,i} L_{lymph,i} \frac{A_{lymph,i}}{V_{lymph,i}} (\hat{p}_{is,i} - p_{lymph,i}) \rho_{mol,i} \hat{x}_{is,i} \right)^{t+\Delta t} \\
& + (V_i f_{T,i} (k_{on,i} \hat{x}_{is,i} \rho_{mol,i} [R]_i - k_{off,i} [R - L]_i))^{t+\Delta t} \\
& - \left(V_i \rho_{mol,i} P_i \frac{A_{vessel,i}}{V_{tissue,i}} (\hat{x}_{c,i} - \hat{x}_{is,i}) \right)^{t+\Delta t} \\
& - \left(V_i \rho_{mol,i} L_{p,i} \frac{A_{vessel,i}}{V_{tissue,i}} (\hat{p}_{c,i} - \hat{p}_{is,i} - \sigma (\pi_{c,i} - \pi_{is,i})) \frac{(\hat{x}_{c,i} - \hat{x}_{is,i})}{2} (1 - \sigma_{f,i}) \right)^{t+\Delta t} = 0,
\end{aligned} \tag{74}$$

where $up(i, j)$ is the physical upstream node of the two neighboring nodes i and j . The discretization of the continuity equation of the tissue continuum (see (21)) is done in the same way as shown for the transport equation. The discretized continuity equation of the tissue continuum is defined as follows:

$$\begin{aligned}
& - \int_{\Gamma_{B_i}} \left(\frac{f_{T,i} \mathbf{K}_{ij} \rho_{mol,up(i,j)}}{\mu_{up(i,j)}} \nabla \left(\sum_{i=1}^{n_{nodes}} \hat{p}_{is,i} N_i \right) + \rho_{mass,i} g_i \nabla z_i \right)^{t+\Delta t} \cdot \mathbf{n} d\Gamma_{B_i} \\
& + \left(V_i f_{T,i} L_{lymph,i} \frac{A_{lymph,i}}{V_{lymph,i}} (\hat{p}_{is,i} - p_{lymph,i}) \rho_{mol,i} \right)^{t+\Delta t} \\
& - \left(V_i \rho_{mol,i} L_{p,i} \frac{A_{vessel,i}}{V_{tissue,i}} (\hat{p}_{c,i} - \hat{p}_{is,i} - \sigma (\pi_{c,i} - \pi_{is,i})) \right)^{t+\Delta t} = 0.
\end{aligned} \tag{75}$$

Applying the above explained discretization scheme for the continuity equation (28) and the transport equation (29) of the capillary bed continuum, the following two discretized equations are obtained:

1) Continuity equation

$$\begin{aligned}
& - \int_{\Gamma_{B_i}} \left(\frac{f_{C,i} \mathbf{K}_{ij} \rho_{mol,up(i,j)}}{\mu_{up(i,j)}} \nabla \left(\sum_{i=1}^{n_{nodes}} \hat{p}_{c,i} N_i \right) + \rho_{mass,i} g_i \nabla z_i \right)^{t+\Delta t} \cdot \mathbf{n} d\Gamma_{B_i} \\
& + \left(V_i \rho_{mol,i} L_{p,i} \frac{A_{vessel,i}}{V_{tissue,i}} (\hat{p}_{c,i} - \hat{p}_{is,i} - \sigma (\pi_{c,i} - \pi_{is,i})) \right)^{t+\Delta t} = 0,
\end{aligned} \tag{76}$$

2) Transport equation

$$\begin{aligned}
& \frac{(V_i f_{C,i} \phi_i \rho_{mol,i} \hat{x}_{c,i})^{t+\Delta t} - (V_i f_{C,i} \phi_i \rho_{mol,i} \hat{x}_{c,i})^t}{\Delta t} \\
& - \int_{\Gamma_{B_i}} \left(\frac{f_{C,i} \mathbf{K}_{ij} \rho_{mol,up(i,j)} x_{c,up(i,j)}}{\mu_{up(i,j)}} \left(\nabla \left(\sum_{i=1}^{n_{nodes}} \hat{p}_{c,i} N_i \right) + \rho_{mass,i} g_i \nabla z_i \right) \right)^{t+\Delta t} \cdot \mathbf{n} d\Gamma_{B_i} \\
& - \int_{\Gamma_{B_i}} \left(f_{C,i} \rho_{mol,i} D_{eff,ij} \nabla \left(\sum_{i=1}^{n_{nodes}} \hat{x}_{c,i} N_i \right) \right)^{t+\Delta t} \cdot \mathbf{n} d\Gamma_{B_i} \tag{77} \\
& + \left(V_i \hat{x}_{c,i} \rho_{mol,i} \frac{\ln 2}{t_{1/2}} \right)^{t+\Delta t} \\
& + \left(V_i \rho_{mol,i} P_i \frac{A_{vessel,i}}{V_{tissue,i}} (\hat{x}_{c,i} - \hat{x}_{is,i}) \right)^{t+\Delta t} \\
& + \left(V_i \rho_{mol,i} L_{p,i} \frac{A_{vessel,i}}{V_{tissue,i}} (\hat{p}_{c,i} - \hat{p}_{is,i} - \sigma_i (\pi_{c,i} - \pi_{is,i})) \frac{(\hat{x}_{c,i} - \hat{x}_{is,i})}{2} (1 - \sigma_{f,i}) \right)^{t+\Delta t} = 0.
\end{aligned}$$

A.2.3 Solving the Non-Linear Problem

The discretized balance equations (74), (75), (76) and (77) for all control volumes B_i of the model domain G form a system of equations of the following type:

$$f(\mathbf{u}_p) = 0. \tag{78}$$

f is a non-linear function of \mathbf{u}_p and \mathbf{u}_p is a vector composed of the primary variables. To linearize the non-linear system of equations, the Newton-Raphson method is used (for further details see Helmig (1997) [45]):

$$\mathbf{u}_{p,n+1} = \mathbf{u}_{p,n} - \left(\frac{\partial f}{\partial \mathbf{u}_{p,n}} \right)^{-1} \cdot f(\mathbf{u}_{p,n}), \tag{79}$$

where the index n is the iteration step and $\frac{\partial f}{\partial \mathbf{u}_{p,n}}$ is the Jacobi matrix. The Jacobi matrix is determined by numerical differentiation. For the solution of the linearized problem at each

Newton iteration step, the simulation toolbox DuMu^x offers various direct and iterative linear solvers. In this case a BiCGStab Solver with an ILU preconditioner is used.

A.3 Low-Dimensional Population Model for TRAIL-Induced Proapoptotic Signaling

In this section, the numerical methods used for the solution of the initial value problem of the low-dimensional population model for TRAIL-induced proapoptotic signaling (see Chapter 6) are explained in detail. The Dormand-Prince method is applied to determine the initial conditions for the system of ordinary differential equations (ODEs) of the [PMTS]_s. Afterwards, this system of ordinary differential equations is numerically solved using the Backward Differentiation Formulas (BDF) method.

A.3.1 Explicit Runge-Kutta Scheme - The Dormand-Prince Method

The initial conditions for the system of ordinary differential equations of the [PMTS]_s for every cell of the heterogeneous cancer cell population are obtained by calculating the steady-state solutions of the Equations (33) - (47) with the initial conditions shown in Table 9. The system of ODEs is numerically solved using an explicit Runge-Kutta scheme, the so-called Dormand-Prince method (Dormand and Prince (1980) [30]). As every method belonging to the family of Runge-Kutta methods, the Dormand-Prince method is a single-step procedure. This means that only the actual solution t_n is used to determine the solution of the next time step t_{n+1} . Every explicit Runge-Kutta method approximates the solution of an initial value problem $\dot{y} = f(t, y)$ with $y(t_0) = y_0$ at the new time step $t_{n+1} = t_n + h_n$ by:

$$y_{n+1} = y_n + \sum_{i=1}^s b_i d_i \quad \text{with} \quad d_i = h_n f(t_n + c_i h_n, y_n + \sum_{j=1}^{i-1} a_{ij} d_j) \quad (80)$$

where h_n is the step size, s is the number of stages, the different b_i are named weights and the coefficients a_{ij} are summarized to the matrix **A**. All coefficients a_{ij} , and b_i and c_i are usually arranged in a so-called Butcher tableau that has the following form for an explicit Runge-Kutta method:

A.3 Low-Dimensional Population Model for TRAIL-Induced Proapoptotic Signaling 119

$$\begin{array}{c|cccccc}
 0 & 0 & 0 & \cdots & 0 & 0 \\
 c_2 & a_{21} & 0 & \cdots & 0 & 0 \\
 c_3 & a_{31} & a_{32} & \cdots & 0 & 0 \\
 \vdots & \vdots & \vdots & \ddots & \vdots & \vdots \\
 c_s & a_{s1} & a_{s2} & \cdots & a_{s,s-1} & 0 \\
 \hline
 & b_1 & b_2 & \cdots & b_{s-1} & b_s
 \end{array}$$

In case of an explicit Runge-Kutta method, the matrix \mathbf{A} is strictly lower triangular. To specify a certain explicit approach out of the family of the Runge-Kutta methods, the number of stages s and the coefficients a_{ij} for $1 \leq j < i \leq s$, b_i and c_i for $i = 1, 2, 3, \dots, s$ have to be determined.

The Butcher table of the Dormand-Prince method is defined in Dormand and Prince (1980) [30]. For the Dormand-Prince method, the number of stages s is equal to seven. The Dormand-Prince approach is an embedded explicit Runge-Kutta method. An embedded Runge-Kutta technique consists of two Runge-Kutta formulas of orders p_o and q_o (usually $q_o = p_o + 1$) which share the same coefficients c_i and function evaluations a_{ij} but use different weights b_i :

$$\begin{array}{c|cccccc}
 0 & 0 & 0 & \cdots & 0 & 0 \\
 c_2 & a_{21} & 0 & \cdots & 0 & 0 \\
 c_3 & a_{31} & a_{32} & \cdots & 0 & 0 \\
 \vdots & \vdots & \vdots & \ddots & \vdots & \vdots \\
 c_s & a_{s1} & a_{s2} & \cdots & a_{s,s-1} & 0 \\
 \hline
 & b_1 & b_2 & \cdots & b_{s-1} & b_s \\
 & \tilde{b}_1 & \tilde{b}_2 & \cdots & \tilde{b}_{s-1} & \tilde{b}_s
 \end{array}$$

where \tilde{b}_i is the weight of the lower-order Runge-Kutta formula. An embedded Runge-Kutta method results in two solutions (Dormand and Prince (1980) [30]):

$$y_{n+1} = y_n + \sum_{i=1}^s b_i d_i \quad \text{and} \quad \tilde{y}_{n+1} = y_n + \sum_{i=1}^s \tilde{b}_i d_i, \quad (81)$$

where \tilde{y}_{n+1} is the calculated solution for the time step t_{n+1} with the lower-order Runge-Kutta formula. Due to the two solutions for one time-step, it is possible to estimate the local truncation error e_{n+1} of the Runge-Kutta time step t_{n+1} by (Dormand and Prince (1980) [30]):

$$e_{n+1} = y_{n+1} - \tilde{y}_{n+1} = h_n \sum_{i=1}^s (b_i - \tilde{b}_i) d_i. \quad (82)$$

By calculating the local truncation error, the selection of the new time-step size h_{n+1} can be controlled with the following formula (Dormand and Prince (1980) [30]):

$$h_{n+1} = 0.9 h_n \left[\frac{\psi}{\|e_{n+1}\|} \right]^{\frac{1}{p_o+1}}. \quad (83)$$

where ψ is the maximum allowable local error. The Dormand-Prince method calculates fourth- and fifth-order accurate solutions based on seven function evaluations (short form for the Dormand-Prince technique: RK5(4)). However, this technique uses only six different function evaluations. The first evaluation at the n th step is equal to the last evaluation at the previous step. This property of the Dormand-Prince approach is called FSAL (First Same As Last). A further characteristic of the Dormand-Prince method is that this technique has a small principal truncation error in the fifth order formula (Dormand and Prince (1980) [30]).

A.3.2 Backward Differentiation Formulas Method

The Backward Differentiation Formulas (BDF) method belongs to the linear multistep methods for the numerical solution of ordinary differential equations. In contrast to the single-step methods such as the Euler method or the different Runge-Kutta techniques that refer to only one previous integration step for the calculation of the solution of the current value, the multistep methods use the information from several previous integration steps (Ascher and Petzold (1998) [9]). For a linear multistep method as the BDF approach, a linear combination of the prior values and derivatives is chosen. According to Cohen and Hindmarsh (1996) [26], the Backward Differentiation Formulas technique approximates the solution of an initial value problem $\dot{y} = f(t, y)$ with $y(t_0) = y_0$ at the new time step $t_n = t_{n-1} + h_n$ by:

$$y_n = \sum_{i=0}^{n_{steps}} \alpha_i y_{n-i} + h_n \beta_0 \dot{y}_n. \quad (84)$$

Here, h_n is the time-step size and n_{steps} is the number of steps. In case of the BDF method, the used order p_o of the BFD method is equal to the number of steps n_{steps} . The values for the coefficients α_i and β_0 depending on the two parameters p_o and n_{steps} are shown in Table 16.

Table 16: Coefficients of the Backward Differentiation Formulas method up to the order 6 (Ascher and Petzold (1998) [9]).

p_o	n_{steps}	β_0	α_0	α_1	α_2	α_3	α_4	α_5	α_6
1	1	1	1	-1					
2	2	$\frac{2}{3}$	1	$-\frac{4}{3}$	$\frac{1}{3}$				
3	3	$\frac{6}{11}$	1	$-\frac{18}{11}$	$\frac{9}{11}$	$-\frac{2}{11}$			
4	4	$\frac{12}{25}$	1	$-\frac{48}{25}$	$\frac{36}{25}$	$-\frac{16}{25}$	$\frac{3}{25}$		
5	5	$\frac{60}{137}$	1	$-\frac{300}{137}$	$\frac{300}{137}$	$-\frac{200}{137}$	$\frac{75}{137}$	$-\frac{12}{137}$	
6	6	$\frac{60}{147}$	1	$-\frac{360}{147}$	$\frac{450}{147}$	$-\frac{400}{147}$	$\frac{225}{147}$	$-\frac{72}{147}$	$\frac{10}{147}$

If the coefficient β_0 is zero the linear multistep method is explicit. An implicit linear multistep method uses for the method's coefficient β_0 a value different from zero. The Backward Differentiation Formulas method is thus an implicit linear multistep method (Ascher and Petzold (1998) [9]).

A.3 Low-Dimensional Population Model for TRAIL-Induced Proapoptotic Signaling 121

For the solution of the system of ordinary differential equations of the [PMTS].s, the CVODE solver uses the BDF method. The order p_o is set to five. The nonlinear system at each time step is numerically solved with a modified Newton method. The following nonlinear system:

$$G(y_n) \equiv y_n - h_n \beta_0 \dot{y}_n - \sum_{i>0} (\alpha_i y_{n-i}) = 0 \quad (85)$$

has to be numerically solved at each time step. The Newton iterations m for a single time step solve the equation $M(y_{n(m+1)} - y_{n(m)}) = -G(y_{n(m)})$ in which $M \approx I - h_n \beta_{n,0} \frac{\partial f}{\partial y}$ (Cohen and Hindmarsh (1996) [26]).

Lebenslauf

Persönliche Daten

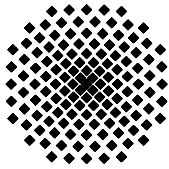
Name: Karin Maria Erbertseder
Anschrift: Engelboldstraße 84, 70569 Stuttgart
Telefon: 0711 / 685 - 64600
E-Mail: karin.erbertseder@iws.uni-stuttgart.de
Geburtsdatum: 08.11.1983
Geburtsort: Pfarrkirchen
Staatsangehörigkeit: deutsch
Familienstand: ledig

Ausbildung

10/2003 - 10/2008 Studium der Werkstoffwissenschaften an der Friedrich-Alexander Universität Erlangen Nürnberg,
Masterprogramm „Advanced Materials and Processes“ des Elitenetzwerks Bayerns
Abschluss: Diplom-Ingenieur Werkstoffwissenschaften - Advanced Materials and Processes
09/2007 Teilnahme an der Ferienakademie der Universitäten Erlangen-Nürnberg, München und Stuttgart (Sarntal, Italien)
09/1994 - 05/2003 Gymnasium Pfarrkirchen
Abschluss: Allgemeine Hochschulreife

Berufliche Tätigkeit

seit 11/2008 Wissenschaftliche Mitarbeiterin am Institut für Wasser- und Umweltsystemmodellierung, Lehrstuhl für Hydromechanik und Hydrosystemmodellierung, Universität Stuttgart



**Institut für Wasser- und
Umweltsystemmodellierung
Universität Stuttgart**

Pfaffenwaldring 61
70569 Stuttgart (Vaihingen)
Telefon (0711) 685 - 64717/64749/64752/64679
Telefax (0711) 685 - 67020 o. 64746 o. 64681
E-Mail: iws@iws.uni-stuttgart.de
<http://www.iws.uni-stuttgart.de>

Direktoren

Prof. Dr. rer. nat. Dr.-Ing. András Bárdossy
Prof. Dr.-Ing. Rainer Helmig
Prof. Dr.-Ing. Silke Wieprecht

Vorstand (Stand 01.04.2009)

Prof. Dr. rer. nat. Dr.-Ing. A. Bárdossy
Prof. Dr.-Ing. R. Helmig
Prof. Dr.-Ing. S. Wieprecht
Jürgen Braun, PhD
Dr.-Ing. H. Class
Dr.-Ing. S. Hartmann
Dr.-Ing. H.-P. Koschitzky
PD Dr.-Ing. W. Marx
Dr. rer. nat. J. Seidel

Emeriti

Prof. Dr.-Ing. habil. Dr.-Ing. E.h. Jürgen Giesecke
Prof. Dr.h.c. Dr.-Ing. E.h. Helmut Kobus, PhD

**Lehrstuhl für Wasserbau und
Wassermengenwirtschaft**

Leiter: Prof. Dr.-Ing. Silke Wieprecht
Stellv.: PD Dr.-Ing. Walter Marx, AOR

Versuchsanstalt für Wasserbau

Leiter: Dr.-Ing. Sven Hartmann, AOR

**Lehrstuhl für Hydromechanik
und Hydrosystemmodellierung**

Leiter: Prof. Dr.-Ing. Rainer Helmig
Stellv.: Dr.-Ing. Holger Class, AOR

Lehrstuhl für Hydrologie und Geohydrologie

Leiter: Prof. Dr. rer. nat. Dr.-Ing. András Bárdossy
Stellv.: Dr. rer. nat. Jochen Seidel

**VEGAS, Versuchseinrichtung zur
Grundwasser- und Altlastensanierung**

Leitung: Jürgen Braun, PhD
Dr.-Ing. Hans-Peter Koschitzky, AD

Verzeichnis der Mitteilungshefte

- 1 Röhnisch, Arthur: *Die Bemühungen um eine Wasserbauliche Versuchsanstalt an der Technischen Hochschule Stuttgart*, und Fattah Abouleid, Abdel: *Beitrag zur Berechnung einer in lockeren Sand gerammten, zweifach verankerten Spundwand*, 1963
- 2 Marotz, Günter: *Beitrag zur Frage der Standfestigkeit von dichten Asphaltbelägen im Großwasserbau*, 1964
- 3 Gurr, Siegfried: *Beitrag zur Berechnung zusammengesetzter ebener Flächen-tragwerke unter besonderer Berücksichtigung ebener Stauwände, mit Hilfe von Randwert- und Lastwertmatrizen*, 1965
- 4 Plica, Peter: *Ein Beitrag zur Anwendung von Schalenkonstruktionen im Stahlwasserbau*, und Petrikat, Kurt: *Möglichkeiten und Grenzen des wasserbaulichen Versuchswesens*, 1966

- 5 Plate, Erich: *Beitrag zur Bestimmung der Windgeschwindigkeitsverteilung in der durch eine Wand gestörten bodennahen Luftschicht, und*
Röhnisch, Arthur; Marotz, Günter: *Neue Baustoffe und Bauausführungen für den Schutz der Böschungen und der Sohle von Kanälen, Flüssen und Häfen; Gesteungskosten und jeweilige Vorteile, sowie Unny, T.E.: Schwingungsuntersuchungen am Kegelstrahlschieber, 1967*
- 6 Seiler, Erich: *Die Ermittlung des Anlagenwertes der bundeseigenen Binnenschiffahrtsstraßen und Talsperren und des Anteils der Binnenschifffahrt an diesem Wert, 1967*
- 7 *Sonderheft anlässlich des 65. Geburtstages von Prof. Arthur Röhnisch mit Beiträgen von* Benk, Dieter; Breitling, J.; Gurr, Siegfried; Haberhauer, Robert; Honekamp, Hermann; Kuz, Klaus Dieter; Marotz, Günter; Mayer-Vorfelder, Hans-Jörg; Miller, Rudolf; Plate, Erich J.; Radomski, Helge; Schwarz, Helmut; Vollmer, Ernst; Wildenhahn, Eberhard; 1967
- 8 Jumikis, Alfred: *Beitrag zur experimentellen Untersuchung des Wassernachschubs in einem gefrierenden Boden und die Beurteilung der Ergebnisse, 1968*
- 9 Marotz, Günter: *Technische Grundlagen einer Wasserspeicherung im natürlichen Untergrund, 1968*
- 10 Radomski, Helge: *Untersuchungen über den Einfluß der Querschnittsform wellenförmiger Spundwände auf die statischen und rammtechnischen Eigenschaften, 1968*
- 11 Schwarz, Helmut: *Die Grenztragfähigkeit des Baugrundes bei Einwirkung vertikal gezogener Ankerplatten als zweidimensionales Bruchproblem, 1969*
- 12 Erbel, Klaus: *Ein Beitrag zur Untersuchung der Metamorphose von Mittelgebirgsschneedecken unter besonderer Berücksichtigung eines Verfahrens zur Bestimmung der thermischen Schneequalität, 1969*
- 13 Westhaus, Karl-Heinz: *Der Strukturwandel in der Binnenschifffahrt und sein Einfluß auf den Ausbau der Binnenschiffskanäle, 1969*
- 14 Mayer-Vorfelder, Hans-Jörg: *Ein Beitrag zur Berechnung des Erdwiderstandes unter Ansatz der logarithmischen Spirale als Gleitflächenfunktion, 1970*
- 15 Schulz, Manfred: *Berechnung des räumlichen Erddruckes auf die Wandung kreiszylindrischer Körper, 1970*
- 16 Mobasseri, Manoutschehr: *Die Rippenstützmauer. Konstruktion und Grenzen ihrer Standsicherheit, 1970*
- 17 Benk, Dieter: *Ein Beitrag zum Betrieb und zur Bemessung von Hochwasserrückhaltebecken, 1970*

- 18 Gál, Attila: *Bestimmung der mitschwingenden Wassermasse bei überströmten Fischbauchklappen mit kreiszylindrischem Staublech*, 1971, vergriffen
- 19 Kuz, Klaus Dieter: *Ein Beitrag zur Frage des Einsetzens von Kavitationserscheinungen in einer Düsenströmung bei Berücksichtigung der im Wasser gelösten Gase*, 1971, vergriffen
- 20 Schaak, Hartmut: *Verteilleitungen von Wasserkraftanlagen*, 1971
- 21 *Sonderheft zur Eröffnung der neuen Versuchsanstalt des Instituts für Wasserbau der Universität Stuttgart mit Beiträgen von* Brombach, Hansjörg; Dirksen, Wolfram; Gál, Attila; Gerlach, Reinhard; Giesecke, Jürgen; Holthoff, Franz-Josef; Kuz, Klaus Dieter; Marotz, Günter; Minor, Hans-Erwin; Petrikat, Kurt; Röhnisch, Arthur; Rueff, Helge; Schwarz, Helmut; Vollmer, Ernst; Wildenhahn, Eberhard; 1972
- 22 Wang, Chung-su: *Ein Beitrag zur Berechnung der Schwingungen an Kegelstrahlschiebern*, 1972
- 23 Mayer-Vorfelder, Hans-Jörg: *Erdwiderstandsbeiwerte nach dem Ohde-Variationsverfahren*, 1972
- 24 Minor, Hans-Erwin: *Beitrag zur Bestimmung der Schwingungsanfachungsfunktionen überströmter Stauklappen*, 1972, vergriffen
- 25 Brombach, Hansjörg: *Untersuchung strömungsmechanischer Elemente (Fluidik) und die Möglichkeit der Anwendung von Wirbelkammerelementen im Wasserbau*, 1972, vergriffen
- 26 Wildenhahn, Eberhard: *Beitrag zur Berechnung von Horizontalfilterbrunnen*, 1972
- 27 Steinlein, Helmut: *Die Eliminierung der Schwebstoffe aus Flußwasser zum Zweck der unterirdischen Wasserspeicherung, gezeigt am Beispiel der Iller*, 1972
- 28 Holthoff, Franz Josef: *Die Überwindung großer Hubhöhen in der Binnenschifffahrt durch Schwimmerhebwerke*, 1973
- 29 Röder, Karl: *Einwirkungen aus Baugrundbewegungen auf trog- und kastenförmige Konstruktionen des Wasser- und Tunnelbaues*, 1973
- 30 Kretschmer, Heinz: *Die Bemessung von Bogenstaumauern in Abhängigkeit von der Talform*, 1973
- 31 Honekamp, Hermann: *Beitrag zur Berechnung der Montage von Unterwasserpipelines*, 1973
- 32 Giesecke, Jürgen: *Die Wirbelkammertriode als neuartiges Steuerorgan im Wasserbau*, und Brombach, Hansjörg: *Entwicklung, Bauformen, Wirkungsweise und Steuereigenschaften von Wirbelkammerverstärkern*, 1974

- 33 Rueff, Helge: *Untersuchung der schwingungserregenden Kräfte an zwei hintereinander angeordneten Tiefschützen unter besonderer Berücksichtigung von Kavitation*, 1974
- 34 Röhnisch, Arthur: *Einpreßversuche mit Zementmörtel für Spannbeton - Vergleich der Ergebnisse von Modellversuchen mit Ausführungen in Hüllwellrohren*, 1975
- 35 *Sonderheft anlässlich des 65. Geburtstages von Prof. Dr.-Ing. Kurt Petrikat mit Beiträgen von:* Brombach, Hansjörg; Erbel, Klaus; Flinspach, Dieter; Fischer jr., Richard; Gàl, Attila; Gerlach, Reinhard; Giesecke, Jürgen; Haberhauer, Robert; Hafner Edzard; Hausenblas, Bernhard; Horlacher, Hans-Burkhard; Hutarew, Andreas; Knoll, Manfred; Krummet, Ralph; Marotz, Günter; Merkle, Theodor; Miller, Christoph; Minor, Hans-Erwin; Neumayer, Hans; Rao, Syamala; Rath, Paul; Rueff, Helge; Ruppert, Jürgen; Schwarz, Wolfgang; Topal-Gökceli, Mehmet; Vollmer, Ernst; Wang, Chung-su; Weber, Hans-Georg; 1975
- 36 Berger, Jochum: *Beitrag zur Berechnung des Spannungszustandes in rotations-symmetrisch belasteten Kugelschalen veränderlicher Wandstärke unter Gas- und Flüssigkeitsdruck durch Integration schwach singulärer Differentialgleichungen*, 1975
- 37 Dirksen, Wolfram: *Berechnung instationärer Abflußvorgänge in gestauten Gerinnen mittels Differenzenverfahren und die Anwendung auf Hochwasserrückhaltebecken*, 1976
- 38 Horlacher, Hans-Burkhard: *Berechnung instationärer Temperatur- und Wärmespannungsfelder in langen mehrschichtigen Hohlzylindern*, 1976
- 39 Hafner, Edzard: *Untersuchung der hydrodynamischen Kräfte auf Baukörper im Tiefwasserbereich des Meeres*, 1977, ISBN 3-921694-39-6
- 40 Ruppert, Jürgen: *Über den Axialwirbelkammerverstärker für den Einsatz im Wasserbau*, 1977, ISBN 3-921694-40-X
- 41 Hutarew, Andreas: *Beitrag zur Beeinflußbarkeit des Sauerstoffgehalts in Fließgewässern an Abstürzen und Wehren*, 1977, ISBN 3-921694-41-8, vergriffen
- 42 Miller, Christoph: *Ein Beitrag zur Bestimmung der schwingungserregenden Kräfte an unterströmten Wehren*, 1977, ISBN 3-921694-42-6
- 43 Schwarz, Wolfgang: *Druckstoßberechnung unter Berücksichtigung der Radial- und Längsverschiebungen der Rohrwandung*, 1978, ISBN 3-921694-43-4
- 44 Kinzelbach, Wolfgang: *Numerische Untersuchungen über den optimalen Einsatz variabler Kühlsysteme einer Kraftwerkskette am Beispiel Oberrhein*, 1978, ISBN 3-921694-44-2
- 45 Barczewski, Baldur: *Neue Meßmethoden für Wasser-Luftgemische und deren Anwendung auf zweiphasige Auftriebsstrahlen*, 1979, ISBN 3-921694-45-0

- 46 Neumayer, Hans: *Untersuchung der Strömungsvorgänge in radialen Wirbelkammerverstärkern*, 1979, ISBN 3-921694-46-9
- 47 Elalfy, Youssef-Elhassan: *Untersuchung der Strömungsvorgänge in Wirbelkammerdioden und -drosseln*, 1979, ISBN 3-921694-47-7
- 48 Brombach, Hansjörg: *Automatisierung der Bewirtschaftung von Wasserspeichern*, 1981, ISBN 3-921694-48-5
- 49 Geldner, Peter: *Deterministische und stochastische Methoden zur Bestimmung der Selbstdichtung von Gewässern*, 1981, ISBN 3-921694-49-3, vergriffen
- 50 Mehlhorn, Hans: *Temperaturveränderungen im Grundwasser durch Brauchwassereinleitungen*, 1982, ISBN 3-921694-50-7, vergriffen
- 51 Hafner, Edzard: *Rohrleitungen und Behälter im Meer*, 1983, ISBN 3-921694-51-5
- 52 Rinnert, Bernd: *Hydrodynamische Dispersion in porösen Medien: Einfluß von Dichteunterschieden auf die Vertikalvermischung in horizontaler Strömung*, 1983, ISBN 3-921694-52-3, vergriffen
- 53 Lindner, Wulf: *Steuerung von Grundwasserentnahmen unter Einhaltung ökologischer Kriterien*, 1983, ISBN 3-921694-53-1, vergriffen
- 54 Herr, Michael; Herzer, Jörg; Kinzelbach, Wolfgang; Kobus, Helmut; Rinnert, Bernd: *Methoden zur rechnerischen Erfassung und hydraulischen Sanierung von Grundwasserkontaminationen*, 1983, ISBN 3-921694-54-X
- 55 Schmitt, Paul: *Wege zur Automatisierung der Niederschlagsermittlung*, 1984, ISBN 3-921694-55-8, vergriffen
- 56 Müller, Peter: *Transport und selektive Sedimentation von Schwebstoffen bei gestautem Abfluß*, 1985, ISBN 3-921694-56-6
- 57 El-Qawasmeh, Fuad: *Möglichkeiten und Grenzen der Tropfbewässerung unter besonderer Berücksichtigung der Verstopfungsanfälligkeit der Tropfelemente*, 1985, ISBN 3-921694-57-4, vergriffen
- 58 Kirchenbaur, Klaus: *Mikroprozessorgesteuerte Erfassung instationärer Druckfelder am Beispiel seegangbelasteter Baukörper*, 1985, ISBN 3-921694-58-2
- 59 Kobus, Helmut (Hrsg.): *Modellierung des großräumigen Wärme- und Schadstofftransports im Grundwasser*, Tätigkeitsbericht 1984/85 (DFG-Forschergruppe an den Universitäten Hohenheim, Karlsruhe und Stuttgart), 1985, ISBN 3-921694-59-0, vergriffen
- 60 Spitz, Karlheinz: *Dispersion in porösen Medien: Einfluß von Inhomogenitäten und Dichteunterschieden*, 1985, ISBN 3-921694-60-4, vergriffen
- 61 Kobus, Helmut: *An Introduction to Air-Water Flows in Hydraulics*, 1985, ISBN 3-921694-61-2

- 62 Kaleris, Vassilios: *Erfassung des Austausches von Oberflächen- und Grundwasser in horizontalebene Grundwassermodellen*, 1986, ISBN 3-921694-62-0
- 63 Herr, Michael: *Grundlagen der hydraulischen Sanierung verunreinigter Porengrundwasserleiter*, 1987, ISBN 3-921694-63-9
- 64 Marx, Walter: *Berechnung von Temperatur und Spannung in Massenbeton infolge Hydratation*, 1987, ISBN 3-921694-64-7
- 65 Koschitzky, Hans-Peter: *Dimensionierungskonzept für Sohlbelüfter in Schußbrinnen zur Vermeidung von Kavitationsschäden*, 1987, ISBN 3-921694-65-5
- 66 Kobus, Helmut (Hrsg.): *Modellierung des großräumigen Wärme- und Schadstofftransports im Grundwasser*, Tätigkeitsbericht 1986/87 (DFG-Forschergruppe an den Universitäten Hohenheim, Karlsruhe und Stuttgart) 1987, ISBN 3-921694-66-3
- 67 Söll, Thomas: *Berechnungsverfahren zur Abschätzung anthropogener Temperaturanomalien im Grundwasser*, 1988, ISBN 3-921694-67-1
- 68 Dittrich, Andreas; Westrich, Bernd: *Bodenseeufererosion, Bestandsaufnahme und Bewertung*, 1988, ISBN 3-921694-68-X, vergriffen
- 69 Huwe, Bernd; van der Ploeg, Rienk R.: *Modelle zur Simulation des Stickstoffhaushaltes von Standorten mit unterschiedlicher landwirtschaftlicher Nutzung*, 1988, ISBN 3-921694-69-8, vergriffen
- 70 Stephan, Karl: *Integration elliptischer Funktionen*, 1988, ISBN 3-921694-70-1
- 71 Kobus, Helmut; Zilliox, Lothaire (Hrsg.): *Nitratbelastung des Grundwassers, Auswirkungen der Landwirtschaft auf die Grundwasser- und Rohwasserbeschaffenheit und Maßnahmen zum Schutz des Grundwassers*. Vorträge des deutsch-französischen Kolloquiums am 6. Oktober 1988, Universitäten Stuttgart und Louis Pasteur Strasbourg (Vorträge in deutsch oder französisch, Kurzfassungen zweisprachig), 1988, ISBN 3-921694-71-X
- 72 Soyeaux, Renald: *Unterströmung von Stauanlagen auf klüftigem Untergrund unter Berücksichtigung laminarer und turbulenter Fließzustände*, 1991, ISBN 3-921694-72-8
- 73 Kohane, Roberto: *Berechnungsmethoden für Hochwasserabfluß in Fließgewässern mit überströmten Vorländern*, 1991, ISBN 3-921694-73-6
- 74 Hassinger, Reinhard: *Beitrag zur Hydraulik und Bemessung von Blocksteinrampen in flexibler Bauweise*, 1991, ISBN 3-921694-74-4, vergriffen
- 75 Schäfer, Gerhard: *Einfluß von Schichtenstrukturen und lokalen Einlagerungen auf die Längsdispersion in Porengrundwasserleitern*, 1991, ISBN 3-921694-75-2
- 76 Giesecke, Jürgen: *Vorträge, Wasserwirtschaft in stark besiedelten Regionen; Umweltforschung mit Schwerpunkt Wasserwirtschaft*, 1991, ISBN 3-921694-76-0

- 77 Huwe, Bernd: *Deterministische und stochastische Ansätze zur Modellierung des Stickstoffhaushalts landwirtschaftlich genutzter Flächen auf unterschiedlichem Skalenniveau*, 1992, ISBN 3-921694-77-9, vergriffen
- 78 Rommel, Michael: *Verwendung von Klufdaten zur realitätsnahen Generierung von Klufnetzen mit anschließender laminar-turbulenter Strömungsberechnung*, 1993, ISBN 3-92 1694-78-7
- 79 Marschall, Paul: *Die Ermittlung lokaler Stofffrachten im Grundwasser mit Hilfe von Einbohrloch-Meßverfahren*, 1993, ISBN 3-921694-79-5, vergriffen
- 80 Ptak, Thomas: *Stofftransport in heterogenen Porenaquiferen: Felduntersuchungen und stochastische Modellierung*, 1993, ISBN 3-921694-80-9, vergriffen
- 81 Haakh, Frieder: *Transientes Strömungsverhalten in Wirbelkammern*, 1993, ISBN 3-921694-81-7
- 82 Kobus, Helmut; Cirpka, Olaf; Barczewski, Baldur; Koschitzky, Hans-Peter: *Versuchseinrichtung zur Grundwasser und Altlastensanierung VEGAS, Konzeption und Programmrahmen*, 1993, ISBN 3-921694-82-5
- 83 Zang, Weidong: *Optimaler Echtzeit-Betrieb eines Speichers mit aktueller Abflußregenerierung*, 1994, ISBN 3-921694-83-3, vergriffen
- 84 Franke, Hans-Jörg: *Stochastische Modellierung eines flächenhaften Stoffeintrages und Transports in Grundwasser am Beispiel der Pflanzenschutzmittelproblematik*, 1995, ISBN 3-921694-84-1
- 85 Lang, Ulrich: *Simulation regionaler Strömungs- und Transportvorgänge in Karst-aquiferen mit Hilfe des Doppelkontinuum-Ansatzes: Methodenentwicklung und Parameteridentifikation*, 1995, ISBN 3-921694-85-X, vergriffen
- 86 Helmig, Rainer: *Einführung in die Numerischen Methoden der Hydromechanik*, 1996, ISBN 3-921694-86-8, vergriffen
- 87 Cirpka, Olaf: *CONTRACT: A Numerical Tool for Contaminant Transport and Chemical Transformations - Theory and Program Documentation -*, 1996, ISBN 3-921694-87-6
- 88 Haberlandt, Uwe: *Stochastische Synthese und Regionalisierung des Niederschlages für Schmutzfrachtberechnungen*, 1996, ISBN 3-921694-88-4
- 89 Croisé, Jean: *Extraktion von flüchtigen Chemikalien aus natürlichen Lockergesteinen mittels erzwungener Luftströmung*, 1996, ISBN 3-921694-89-2, vergriffen
- 90 Jorde, Klaus: *Ökologisch begründete, dynamische Mindestwasserregelungen bei Ausleitungskraftwerken*, 1997, ISBN 3-921694-90-6, vergriffen
- 91 Helmig, Rainer: *Gekoppelte Strömungs- und Transportprozesse im Untergrund - Ein Beitrag zur Hydrosystemmodellierung-*, 1998, ISBN 3-921694-91-4, vergriffen

- 92 Emmert, Martin: *Numerische Modellierung nichtisothermer Gas-Wasser Systeme in porösen Medien*, 1997, ISBN 3-921694-92-2
- 93 Kern, Ulrich: *Transport von Schweb- und Schadstoffen in staugeregelten Fließgewässern am Beispiel des Neckars*, 1997, ISBN 3-921694-93-0, vergriffen
- 94 Förster, Georg: *Druckstoßdämpfung durch große Luftblasen in Hochpunkten von Rohrleitungen* 1997, ISBN 3-921694-94-9
- 95 Cirpka, Olaf: *Numerische Methoden zur Simulation des reaktiven Mehrkomponententransports im Grundwasser*, 1997, ISBN 3-921694-95-7, vergriffen
- 96 Färber, Arne: *Wärmetransport in der ungesättigten Bodenzone: Entwicklung einer thermischen In-situ-Sanierungstechnologie*, 1997, ISBN 3-921694-96-5
- 97 Betz, Christoph: *Wasserdampfdestillation von Schadstoffen im porösen Medium: Entwicklung einer thermischen In-situ-Sanierungstechnologie*, 1998, ISBN 3-921694-97-3
- 98 Xu, Yichun: *Numerical Modeling of Suspended Sediment Transport in Rivers*, 1998, ISBN 3-921694-98-1, vergriffen
- 99 Wüst, Wolfgang: *Geochemische Untersuchungen zur Sanierung CKW-kontaminierter Aquifere mit Fe(0)-Reaktionswänden*, 2000, ISBN 3-933761-02-2
- 100 Sheta, Hussam: *Simulation von Mehrphasenvorgängen in porösen Medien unter Einbeziehung von Hysterese-Effekten*, 2000, ISBN 3-933761-03-4
- 101 Ayros, Edwin: *Regionalisierung extremer Abflüsse auf der Grundlage statistischer Verfahren*, 2000, ISBN 3-933761-04-2, vergriffen
- 102 Huber, Ralf: *Compositional Multiphase Flow and Transport in Heterogeneous Porous Media*, 2000, ISBN 3-933761-05-0
- 103 Braun, Christopherus: *Ein Upscaling-Verfahren für Mehrphasenströmungen in porösen Medien*, 2000, ISBN 3-933761-06-9
- 104 Hofmann, Bernd: *Entwicklung eines rechnergestützten Managementsystems zur Beurteilung von Grundwasserschadensfällen*, 2000, ISBN 3-933761-07-7
- 105 Class, Holger: *Theorie und numerische Modellierung nichtisothermer Mehrphasenprozesse in NAPL-kontaminierten porösen Medien*, 2001, ISBN 3-933761-08-5
- 106 Schmidt, Reinhard: *Wasserdampf- und Heißluftinjektion zur thermischen Sanierung kontaminierter Standorte*, 2001, ISBN 3-933761-09-3
- 107 Josef, Reinhold: *Schadstoffextraktion mit hydraulischen Sanierungsverfahren unter Anwendung von grenzflächenaktiven Stoffen*, 2001, ISBN 3-933761-10-7

- 108 Schneider, Matthias: *Habitat- und Abflussmodellierung für Fließgewässer mit unscharfen Berechnungsansätzen*, 2001, ISBN 3-933761-11-5
- 109 Rathgeb, Andreas: *Hydrodynamische Bemessungsgrundlagen für Lockerdeckwerke an überströmbaren Erddämmen*, 2001, ISBN 3-933761-12-3
- 110 Lang, Stefan: *Parallele numerische Simulation instationärer Probleme mit adaptiven Methoden auf unstrukturierten Gittern*, 2001, ISBN 3-933761-13-1
- 111 Appt, Jochen; Stumpp Simone: *Die Bodensee-Messkampagne 2001, IWS/CWR Lake Constance Measurement Program 2001*, 2002, ISBN 3-933761-14-X
- 112 Heimerl, Stephan: *Systematische Beurteilung von Wasserkraftprojekten*, 2002, ISBN 3-933761-15-8, vergriffen
- 113 Iqbal, Amin: *On the Management and Salinity Control of Drip Irrigation*, 2002, ISBN 3-933761-16-6
- 114 Silberhorn-Hemminger, Annette: *Modellierung von Kluftaquifersystemen: Geostatistische Analyse und deterministisch-stochastische Kluftgenerierung*, 2002, ISBN 3-933761-17-4
- 115 Winkler, Angela: *Prozesse des Wärme- und Stofftransports bei der In-situ-Sanierung mit festen Wärmequellen*, 2003, ISBN 3-933761-18-2
- 116 Marx, Walter: *Wasserkraft, Bewässerung, Umwelt - Planungs- und Bewertungsschwerpunkte der Wasserbewirtschaftung*, 2003, ISBN 3-933761-19-0
- 117 Hinkelmann, Reinhard: *Efficient Numerical Methods and Information-Processing Techniques in Environment Water*, 2003, ISBN 3-933761-20-4
- 118 Samaniego-Eguiguren, Luis Eduardo: *Hydrological Consequences of Land Use / Land Cover and Climatic Changes in Mesoscale Catchments*, 2003, ISBN 3-933761-21-2
- 119 Neunhäuserer, Lina: *Diskretisierungsansätze zur Modellierung von Strömungs- und Transportprozessen in geklüftet-porösen Medien*, 2003, ISBN 3-933761-22-0
- 120 Paul, Maren: *Simulation of Two-Phase Flow in Heterogeneous Porous Media with Adaptive Methods*, 2003, ISBN 3-933761-23-9
- 121 Ehret, Uwe: *Rainfall and Flood Nowcasting in Small Catchments using Weather Radar*, 2003, ISBN 3-933761-24-7
- 122 Haag, Ingo: *Der Sauerstoffhaushalt staugeregelter Flüsse am Beispiel des Neckars - Analysen, Experimente, Simulationen -*, 2003, ISBN 3-933761-25-5
- 123 Appt, Jochen: *Analysis of Basin-Scale Internal Waves in Upper Lake Constance*, 2003, ISBN 3-933761-26-3

- 124 Hrsg.: Schrenk, Volker; Batereau, Katrin; Barczewski, Baldur; Weber, Karolin und Koschitzky, Hans-Peter: *Symposium Ressource Fläche und VEGAS - Statuskolloquium 2003, 30. September und 1. Oktober 2003*, 2003, ISBN 3-933761-27-1
- 125 Omar Khalil Ouda: *Optimisation of Agricultural Water Use: A Decision Support System for the Gaza Strip*, 2003, ISBN 3-933761-28-0
- 126 Batereau, Katrin: *Sensorbasierte Bodenluftmessung zur Vor-Ort-Erkundung von Schadensherden im Untergrund*, 2004, ISBN 3-933761-29-8
- 127 Witt, Oliver: *Erosionsstabilität von Gewässersedimenten mit Auswirkung auf den Stofftransport bei Hochwasser am Beispiel ausgewählter Stauhaltungen des Oberrheins*, 2004, ISBN 3-933761-30-1
- 128 Jakobs, Hartmut: *Simulation nicht-isothermer Gas-Wasser-Prozesse in komplexen Kluft-Matrix-Systemen*, 2004, ISBN 3-933761-31-X
- 129 Li, Chen-Chien: *Deterministisch-stochastisches Berechnungskonzept zur Beurteilung der Auswirkungen erosiver Hochwasserereignisse in Flusstauhaltungen*, 2004, ISBN 3-933761-32-8
- 130 Reichenberger, Volker; Helmig, Rainer; Jakobs, Hartmut; Bastian, Peter; Niessner, Jennifer: *Complex Gas-Water Processes in Discrete Fracture-Matrix Systems: Upscaling, Mass-Conservative Discretization and Efficient Multilevel Solution*, 2004, ISBN 3-933761-33-6
- 131 Hrsg.: Barczewski, Baldur; Koschitzky, Hans-Peter; Weber, Karolin; Wege, Ralf: *VEGAS - Statuskolloquium 2004*, Tagungsband zur Veranstaltung am 05. Oktober 2004 an der Universität Stuttgart, Campus Stuttgart-Vaihingen, 2004, ISBN 3-933761-34-4
- 132 Asie, Kemal Jabir: *Finite Volume Models for Multiphase Multicomponent Flow through Porous Media*. 2005, ISBN 3-933761-35-2
- 133 Jacoub, George: *Development of a 2-D Numerical Module for Particulate Contaminant Transport in Flood Retention Reservoirs and Impounded Rivers*, 2004, ISBN 3-933761-36-0
- 134 Nowak, Wolfgang: *Geostatistical Methods for the Identification of Flow and Transport Parameters in the Subsurface*, 2005, ISBN 3-933761-37-9
- 135 Süß, Mia: *Analysis of the influence of structures and boundaries on flow and transport processes in fractured porous media*, 2005, ISBN 3-933761-38-7
- 136 Jose, Surabhin Chackiath: *Experimental Investigations on Longitudinal Dispersive Mixing in Heterogeneous Aquifers*, 2005, ISBN: 3-933761-39-5
- 137 Filiz, Fulya: *Linking Large-Scale Meteorological Conditions to Floods in Mesoscale Catchments*, 2005, ISBN 3-933761-40-9

- 138 Qin, Minghao: *Wirklichkeitsnahe und recheneffiziente Ermittlung von Temperatur und Spannungen bei großen RCC-Staumauern*, 2005, ISBN 3-933761-41-7
- 139 Kobayashi, Kenichiro: *Optimization Methods for Multiphase Systems in the Sub-surface - Application to Methane Migration in Coal Mining Areas*, 2005, ISBN 3-933761-42-5
- 140 Rahman, Md. Arifur: *Experimental Investigations on Transverse Dispersive Mixing in Heterogeneous Porous Media*, 2005, ISBN 3-933761-43-3
- 141 Schrenk, Volker: *Ökobilanzen zur Bewertung von Altlastensanierungsmaßnahmen*, 2005, ISBN 3-933761-44-1
- 142 Hundecha, Hirpa Yesheatesfa: *Regionalization of Parameters of a Conceptual Rainfall-Runoff Model*, 2005, ISBN: 3-933761-45-X
- 143 Wege, Ralf: *Untersuchungs- und Überwachungsmethoden für die Beurteilung natürlicher Selbstreinigungsprozesse im Grundwasser*, 2005, ISBN 3-933761-46-8
- 144 Breiting, Thomas: *Techniken und Methoden der Hydroinformatik - Modellierung von komplexen Hydrosystemen im Untergrund*, 2006, 3-933761-47-6
- 145 Hrsg.: Braun, Jürgen; Koschitzky, Hans-Peter; Müller, Martin: *Ressource Untergrund: 10 Jahre VEGAS: Forschung und Technologieentwicklung zum Schutz von Grundwasser und Boden*, Tagungsband zur Veranstaltung am 28. und 29. September 2005 an der Universität Stuttgart, Campus Stuttgart-Vaihingen, 2005, ISBN 3-933761-48-4
- 146 Rojanschi, Vlad: *Abflusskonzentration in mesoskaligen Einzugsgebieten unter Berücksichtigung des Sickerraumes*, 2006, ISBN 3-933761-49-2
- 147 Winkler, Nina Simone: *Optimierung der Steuerung von Hochwasserrückhaltebecken-systemen*, 2006, ISBN 3-933761-50-6
- 148 Wolf, Jens: *Räumlich differenzierte Modellierung der Grundwasserströmung alluvialer Aquifere für mesoskalige Einzugsgebiete*, 2006, ISBN: 3-933761-51-4
- 149 Kohler, Beate: *Externe Effekte der Laufwasserkraftnutzung*, 2006, ISBN 3-933761-52-2
- 150 Hrsg.: Braun, Jürgen; Koschitzky, Hans-Peter; Stuhmann, Matthias: *VEGAS-Statuskolloquium 2006*, Tagungsband zur Veranstaltung am 28. September 2006 an der Universität Stuttgart, Campus Stuttgart-Vaihingen, 2006, ISBN 3-933761-53-0
- 151 Niessner, Jennifer: *Multi-Scale Modeling of Multi-Phase - Multi-Component Processes in Heterogeneous Porous Media*, 2006, ISBN 3-933761-54-9
- 152 Fischer, Markus: *Beanspruchung eingeeerdeter Rohrleitungen infolge Austrocknung bindiger Böden*, 2006, ISBN 3-933761-55-7

- 153 Schneck, Alexander: *Optimierung der Grundwasserbewirtschaftung unter Berücksichtigung der Belange der Wasserversorgung, der Landwirtschaft und des Naturschutzes*, 2006, ISBN 3-933761-56-5
- 154 Das, Tapash: *The Impact of Spatial Variability of Precipitation on the Predictive Uncertainty of Hydrological Models*, 2006, ISBN 3-933761-57-3
- 155 Bielinski, Andreas: *Numerical Simulation of CO₂ sequestration in geological formations*, 2007, ISBN 3-933761-58-1
- 156 Mödinger, Jens: *Entwicklung eines Bewertungs- und Entscheidungsunterstützungssystems für eine nachhaltige regionale Grundwasserbewirtschaftung*, 2006, ISBN 3-933761-60-3
- 157 Manthey, Sabine: *Two-phase flow processes with dynamic effects in porous media - parameter estimation and simulation*, 2007, ISBN 3-933761-61-1
- 158 Pozos Estrada, Oscar: *Investigation on the Effects of Entrained Air in Pipelines*, 2007, ISBN 3-933761-62-X
- 159 Ochs, Steffen Oliver: *Steam injection into saturated porous media – process analysis including experimental and numerical investigations*, 2007, ISBN 3-933761-63-8
- 160 Marx, Andreas: *Einsatz gekoppelter Modelle und Wetterradar zur Abschätzung von Niederschlagsintensitäten und zur Abflussvorhersage*, 2007, ISBN 3-933761-64-6
- 161 Hartmann, Gabriele Maria: *Investigation of Evapotranspiration Concepts in Hydrological Modelling for Climate Change Impact Assessment*, 2007, ISBN 3-933761-65-4
- 162 Kebede Gurmessa, Tesfaye: *Numerical Investigation on Flow and Transport Characteristics to Improve Long-Term Simulation of Reservoir Sedimentation*, 2007, ISBN 3-933761-66-2
- 163 Trifković, Aleksandar: *Multi-objective and Risk-based Modelling Methodology for Planning, Design and Operation of Water Supply Systems*, 2007, ISBN 3-933761-67-0
- 164 Götzinger, Jens: *Distributed Conceptual Hydrological Modelling - Simulation of Climate, Land Use Change Impact and Uncertainty Analysis*, 2007, ISBN 3-933761-68-9
- 165 Hrsg.: Braun, Jürgen; Koschitzky, Hans-Peter; Stuhmann, Matthias: *VEGAS – Kolloquium 2007*, Tagungsband zur Veranstaltung am 26. September 2007 an der Universität Stuttgart, Campus Stuttgart-Vaihingen, 2007, ISBN 3-933761-69-7
- 166 Freeman, Beau: *Modernization Criteria Assessment for Water Resources Planning; Klamath Irrigation Project, U.S.*, 2008, ISBN 3-933761-70-0

- 167 Dreher, Thomas: *Selektive Sedimentation von Feinstschwebstoffen in Wechselwirkung mit wandnahen turbulenten Strömungsbedingungen*, 2008, ISBN 3-933761-71-9
- 168 Yang, Wei: *Discrete-Continuous Downscaling Model for Generating Daily Precipitation Time Series*, 2008, ISBN 3-933761-72-7
- 169 Kopecki, Ianina: *Calculational Approach to FST-Hemispheres for Multiparametrical Benthos Habitat Modelling*, 2008, ISBN 3-933761-73-5
- 170 Brommundt, Jürgen: *Stochastische Generierung räumlich zusammenhängender Niederschlagszeitreihen*, 2008, ISBN 3-933761-74-3
- 171 Papafotiou, Alexandros: *Numerical Investigations of the Role of Hysteresis in Heterogeneous Two-Phase Flow Systems*, 2008, ISBN 3-933761-75-1
- 172 He, Yi: *Application of a Non-Parametric Classification Scheme to Catchment Hydrology*, 2008, ISBN 978-3-933761-76-7
- 173 Wagner, Sven: *Water Balance in a Poorly Gauged Basin in West Africa Using Atmospheric Modelling and Remote Sensing Information*, 2008, ISBN 978-3-933761-77-4
- 174 Hrsg.: Braun, Jürgen; Koschitzky, Hans-Peter; Stuhmann, Matthias; Schrenk, Volker: *VEGAS-Kolloquium 2008 Ressource Fläche III*, Tagungsband zur Veranstaltung am 01. Oktober 2008 an der Universität Stuttgart, Campus Stuttgart-Vaihingen, 2008, ISBN 978-3-933761-78-1
- 175 Patil, Sachin: *Regionalization of an Event Based Nash Cascade Model for Flood Predictions in Ungauged Basins*, 2008, ISBN 978-3-933761-79-8
- 176 Assteerawatt, Anongnart: *Flow and Transport Modelling of Fractured Aquifers based on a Geostatistical Approach*, 2008, ISBN 978-3-933761-80-4
- 177 Karnahl, Joachim Alexander: *2D numerische Modellierung von multifraktionalem Schwebstoff- und Schadstofftransport in Flüssen*, 2008, ISBN 978-3-933761-81-1
- 178 Hiester, Uwe: *Technologieentwicklung zur In-situ-Sanierung der ungesättigten Bodenzone mit festen Wärmequellen*, 2009, ISBN 978-3-933761-82-8
- 179 Laux, Patrick: *Statistical Modeling of Precipitation for Agricultural Planning in the Volta Basin of West Africa*, 2009, ISBN 978-3-933761-83-5
- 180 Ehsan, Saqib: *Evaluation of Life Safety Risks Related to Severe Flooding*, 2009, ISBN 978-3-933761-84-2
- 181 Prohaska, Sandra: *Development and Application of a 1D Multi-Strip Fine Sediment Transport Model for Regulated Rivers*, 2009, ISBN 978-3-933761-85-9

- 182 Kopp, Andreas: *Evaluation of CO₂ Injection Processes in Geological Formations for Site Screening*, 2009, ISBN 978-3-933761-86-6
- 183 Ebigo, Anozie: *Modelling of biofilm growth and its influence on CO₂ and water (two-phase) flow in porous media*, 2009, ISBN 978-3-933761-87-3
- 184 Freiboth, Sandra: *A phenomenological model for the numerical simulation of multiphase multicomponent processes considering structural alterations of porous media*, 2009, ISBN 978-3-933761-88-0
- 185 Zöllner, Frank: *Implementierung und Anwendung netzfreier Methoden im Konstruktiven Wasserbau und in der Hydromechanik*, 2009, ISBN 978-3-933761-89-7
- 186 Vasin, Milos: *Influence of the soil structure and property contrast on flow and transport in the unsaturated zone*, 2010, ISBN 978-3-933761-90-3
- 187 Li, Jing: *Application of Copulas as a New Geostatistical Tool*, 2010, ISBN 978-3-933761-91-0
- 188 AghaKouchak, Amir: *Simulation of Remotely Sensed Rainfall Fields Using Copulas*, 2010, ISBN 978-3-933761-92-7
- 189 Thapa, Pawan Kumar: *Physically-based spatially distributed rainfall runoff modeling for soil erosion estimation*, 2010, ISBN 978-3-933761-93-4
- 190 Wurms, Sven: *Numerische Modellierung der Sedimentationsprozesse in Retentionsanlagen zur Steuerung von Stoffströmen bei extremen Hochwasserabflussergebnissen*, 2011, ISBN 978-3-933761-94-1
- 191 Merkel, Uwe: *Unsicherheitsanalyse hydraulischer Einwirkungen auf Hochwasserschutzdeiche und Steigerung der Leistungsfähigkeit durch adaptive Strömungsmodellierung*, 2011, ISBN 978-3-933761-95-8
- 192 Fritz, Jochen: *A Decoupled Model for Compositional Non-Isothermal Multiphase Flow in Porous Media and Multiphysics Approaches for Two-Phase Flow*, 2010, ISBN 978-3-933761-96-5
- 193 Weber, Karolin (Hrsg.): *12. Treffen junger WissenschaftlerInnen an Wasserbauinstituten*, 2010, ISBN 978-3-933761-97-2
- 194 Bliedernicht, Jan-Geert: *Probability Forecasts of Daily Areal Precipitation for Small River Basins*, 2011, ISBN 978-3-933761-98-9
- 195 Hrsg.: Koschitzky, Hans-Peter; Braun, Jürgen: *VEGAS-Kolloquium 2010 In-situ-Sanierung - Stand und Entwicklung Nano und ISCO -*, Tagungsband zur Veranstaltung am 07. Oktober 2010 an der Universität Stuttgart, Campus Stuttgart-Vaihingen, 2010, ISBN 978-3-933761-99-6

- 196 Gafurov, Abror: *Water Balance Modeling Using Remote Sensing Information - Focus on Central Asia*, 2010, ISBN 978-3-942036-00-9
- 197 Mackenberg, Sylvia: *Die Quellstärke in der Sickerwasserprognose: Möglichkeiten und Grenzen von Labor- und Freilanduntersuchungen*, 2010, ISBN 978-3-942036-01-6
- 198 Singh, Shailesh Kumar: *Robust Parameter Estimation in Gauged and Ungauged Basins*, 2010, ISBN 978-3-942036-02-3
- 199 Doğan, Mehmet Onur: *Coupling of porous media flow with pipe flow*, 2011, ISBN 978-3-942036-03-0
- 200 Liu, Min: *Study of Topographic Effects on Hydrological Patterns and the Implication on Hydrological Modeling and Data Interpolation*, 2011, ISBN 978-3-942036-04-7
- 201 Geleta, Habtamu Itefa: *Watershed Sediment Yield Modeling for Data Scarce Areas*, 2011, ISBN 978-3-942036-05-4
- 202 Franke, Jörg: *Einfluss der Überwachung auf die Versagenswahrscheinlichkeit von Staustufen*, 2011, ISBN 978-3-942036-06-1
- 203 Bakimchandra, Oinam: *Integrated Fuzzy-GIS approach for assessing regional soil erosion risks*, 2011, ISBN 978-3-942036-07-8
- 204 Alam, Muhammad Mahboob: *Statistical Downscaling of Extremes of Precipitation in Mesoscale Catchments from Different RCMs and Their Effects on Local Hydrology*, 2011, ISBN 978-3-942036-08-5
- 205 Hrsg.: Koschitzky, Hans-Peter; Braun, Jürgen: *VEGAS-Kolloquium 2011 Flache Geothermie - Perspektiven und Risiken*, Tagungsband zur Veranstaltung am 06. Oktober 2011 an der Universität Stuttgart, Campus Stuttgart-Vaihingen, 2011, ISBN 978-3-933761-09-2
- 206 Haslauer, Claus: *Analysis of Real-World Spatial Dependence of Subsurface Hydraulic Properties Using Copulas with a Focus on Solute Transport Behaviour*, 2011, ISBN 978-3-942036-10-8
- 207 Dung, Nguyen Viet: *Multi-objective automatic calibration of hydrodynamic models – development of the concept and an application in the Mekong Delta*, 2011, ISBN 978-3-942036-11-5
- 208 Hung, Nguyen Nghia: *Sediment dynamics in the floodplain of the Mekong Delta, Vietnam*, 2011, ISBN 978-3-942036-12-2
- 209 Kuhlmann, Anna: *Influence of soil structure and root water uptake on flow in the unsaturated zone*, 2012, ISBN 978-3-942036-13-9

- 210 Tuthan, Jeff: *Including the Second Law Inequality in Aquatic Ecodynamics: A Modeling Approach for Alpine Rivers Impacted by Hydropeaking*, 2012, ISBN 978-3-942036-14-6
- 211 Tolossa, Habtamu: *Sediment Transport Computation Using a Data-Driven Adaptive Neuro-Fuzzy Modelling Approach*, 2012, ISBN 978-3-942036-15-3
- 212 Tatomir, Alexandru-Bodgan: *From Discrete to Continuum Concepts of Flow in Fractured Porous Media*, 2012, ISBN 978-3-942036-16-0
- 213 Erbertseder, Karin Maria: *A Multi-Scale Model for Describing Cancer-Therapeutic Transport in the Human Lung*, 2012, ISBN 978-3-942036-17-7

Die Mitteilungshefte ab der Nr. 134 (Jg. 2005) stehen als pdf-Datei über die Homepage des Instituts: www.iws.uni-stuttgart.de zur Verfügung.